Multiscale experimental characterisation and modelling of transverse cracking in thin-ply composites

Thèse N° 9132

Présentée le 11 février 2019

à la Faculté des sciences et techniques de l'ingénieur
Laboratoire de mécanique appliquée et d'analyse de fiabilité
Programme doctoral en mécanique

pour l'obtention du grade de Docteur ès Sciences

par

Sébastien KOHLER

Acceptée sur proposition du jury

Dr M. Farhat, président du jury
Prof. J. Botsis, Prof. J. Cugnoni, directeurs de thèse
Prof. J. Costa, rapporteur
Dr Y. Swolfs, rapporteur
Prof. V. Michaud, rapporteuse

2019

ÉCOLE POLYTECHNIQUE
FÉDÉRALE DE LAUSANNE

It’s not about waiting for the storm to pass, it’s about learning how to dance in the rain!
as repeated by my dear friend, Iain McGrory (1959-2019)

Abstract

Driven by the industry requirement for materials exhibiting high strength and stiffness to weight ratios, carbon-fibre reinforced polymers (CFRP) have been increasingly used in recent years. Their usage is however subjected to some caveats, as their damage modes and failure mechanisms are hard to predict. Furthermore, the multi-axial laminates used in industrial applications often exhibit a first ply failure as low as 30% of the theoretical fibre strength, seriously hampering the theoretical weight savings.
The recent introduction of tow-spreading techniques to the market allowed the emergence of the so-called *thin-ply* laminates, where the individual laminae thicknesses are typically comprised between 20µm and 150µm. The design space that this new class of materials offers is much larger than the one of traditional thicker plies and is of particular interest when applied to very thin structures such as sandwich skins. Additionally, these materials exhibit outstanding strength properties thanks to a ply confinement effect allowing certain laminates to reach the ultimate translaminar fracture of the 0° plies with no premature sign of damage.

Unfortunately, the full potential of these new materials is currently not exploited due to the lack of accurate prediction of this strength increase with respect to ply thickness for very light plies, as well as its dependency on the constituents of the composite. This work therefore focuses on the understanding and the modelling of the damage mechanism encountered in thin-ply CFRP composite laminates to understand and characterise the cause responsible for the discrepancy observed between LEFM strength predictions and experimental results.

To this effect, the damage dependency on ply thickness is investigated experimentally for three different thin-ply CFRP quasi-isotropic laminates, with constituents spanning a large range of properties. It is shown that free edge damage mechanisms, observed with in-situ microscopy, change with decreasing ply thickness. Whilst free-edge delamination dominates the damage behaviour when thicker plies are used, transverse cracking (TC) dominates the free edge behaviour of thinner plies with an increasing onset of damage with decreasing ply thickness. With some material constituents, this onset is increased so much that the translaminar fracture of the 0° plies precedes it and no transverse cracking is detected any more.
Bulk damage, recorded by acoustic emission, is linked to major propagation of TC from the free edge through the width of the sample. It is shown to happen at higher strains than the free edge damage for all but the thickest plies tested, where free edge delamination prevails. Its onset is also shown to scale differently with respect to ply thickness than what is observed

at the free edge.
Assuming LEFM hypotheses, a critical ERR associated with transverse cracking is identified by inverting the in-situ strength model. A ply dependency of this apparent toughness is shown for all material tested with a decrease of its value with decreasing ply thickness.

A multiscale embedded-cell FE model is developed to gain more insight in the intricate damage mechanisms present at the micro-scale. All material properties used are obtained or derived from experimental tests, save for the fibre-matrix interface. A good agreement with the obtained experimental onset of TC in the bulk as well as at the free edge is achieved. A dominance of the interface properties on the TC development is demonstrated, and its appearance is shown to be triggered by debonding coalescence, leading to matrix micro-filament bridging. The crucial effect of thermal residual stresses is highlighted, as values leading to debonding or matrix failure after curing can be reached at the micro-scale for high temperature curing composites. An inversely proportional influence of the curing temperature on the onset of TC under the assumed modelling hypotheses is shown.
Using this calibrated model to identify a TC-related critical ERR, the same trend of a decreasing apparent toughness with decreasing ply thickness than in the semi-experimental case is observed.

In light of these results, a mesoscale model is proposed with all the damage lumped into a single TC modelled using two superposed cohesive element zones, the first one representing debonding and the second one representing matrix micro bridging. An optimisation scheme is used to identify the two linear traction-separation laws implemented to match the experimentally measured AE onsets. The maximum cohesive stresses thus identified as well as critical ERR predictions are in good agreement with the values obtained from the micromechanical model.
It was noticed that a simple linear cohesive law could predict the observed scaling of TC onset with respect to ply thickness with enough accuracy, which opens the way for new, improved in-situ strength models that could properly account for the finite size of the process zone without requiring a much larger experimental dataset.

Keywords:

Carbon fibre reinforced polymers, Thin-ply composites, In-situ microscopy, X-ray computed tomography, Transverse cracking, Interface properties, Size effects, Toughness, Multiscale FE modelling, Cohesive elements.

Résumé

De par la demande industrielle croissante pour des matériaux alliant haute résistance et excellente rigidité spécifique, les matériaux polymères renforcés de fibres de carbone (CFRP) sont employés de manière croissante ces dernières années. Leur utilisation présente toutefois certaines difficultés, en raison de leurs modes d'endommagement ainsi que de leur point de rupture qui sont tous deux difficiles à prévoir. Du plus, les stratifiés multi-axiaux souvent employés en pratique peuvent présenter un endommagement du premier pli dès 30% de la résistance théorique des fibres, réduisant d'autant les allègements théoriquement possibles grâce à ces matériaux.
L'apparition récente des techniques d'étalement de fibres sur le marché a permis le développement des stratifiés *thin-ply*, dans lesquels l'épaisseur des couches individuelles sont typiquement comprises entre 20µm et 150µm. L'espace de conception offert par de tels matériaux est nettement plus grand que ce qui est traditionnellement possible, ce qui est particulièrement intéressant pour des structures minces telles que les peaux de structures sandwich. De plus, ces matériaux présentent une résistance exceptionnelle grâce à un plus grand confinement des plis hors axe, permettant à certains stratifiés d'atteindre la limite de rupture translaminaire des plis à 0° sans signe précurseur de dommage.

Malheureusement, le potentiel de ces nouveaux matériaux ne peut être pleinement exploité pour l'instant. En effet, les modèles permettant la prédiction de cette augmentation de résistance liée à la diminution de l'épaisseur des plis manquent de précision pour les plus légers grammages, et la dépendance aux constituants du composite est méconnue. De ce fait, ce travail se concentre sur la compréhension et la modélisation des mécanismes d'endommagement rencontrés dans des stratifiés de CFRP afin de comprendre les causes sous-jacentes aux différences observées entre les prédictions de résistance obtenues par mécanique de la rupture linéaire élastique (LEFM) et les résultats expérimentaux.

Pour ce faire, la dépendance de l'endommagement à l'épaisseur des plis est étudiée expérimentalement pour trois différents stratifiées quasi-isotropes de CFRP, dont les constituants couvrent une large palette de propriétés. Il est démontré que les mécanismes d'endommagement observés par microscopie in-situ aux bords des échantillons varient en fonction de l'épaisseur des plis. Si la délamination des bords de l'échantillon domine le comportement des échantillons aux plis les plus épais, c'est la fissuration transverse qui domine lorsque l'épaisseur des plis est réduite, avec une apparition de plus en plus tardive de ce type de

dommage au fur et à mesure que l'épaisseur des plis est réduite. Avec certains constituants, cette apparition est tellement retardée que la rupture translaminaire des plis à 0° mène à la ruine des échantillons avant même que la fissuration transverse ne puisse être observée.
Le dommage au cœur de l'échantillon, étudié par émission acoustique, a pu être lié à la propagation massive de fissures transverses du bord de l'échantillon vers son centre. Il est montré que cela se produit à de plus grandes déformations appliquées que le dommage au bord des échantillons pour toutes les épaisseurs de plis à l'exception des plus grandes, épaisseurs auxquelles la délamination domine l'endommagement des échantillons. Il est également démontré que l'augmentation de la résistance en fonction de l'épaisseur de pli est différente au bord et au cœur des échantillons étudiés.
En acceptant les hypothèses sous-jacentes à la LEFM, un taux de restitution d'énergie critique (ERR) associé à la fissuration transverse a été identifié en inversant le modèle de résistance in-situ. Une dépendance de cette ténacité apparente à l'épaisseur des plis est démontrée pour tous les matériaux étudiés, avec une diminution de sa valeur quand l'épaisseur de pli est réduite.

Un modèle élément finis multi-échelle a été développé afin de mieux comprendre les mécanismes d'endommagement complexes présents à l'échelle micrométrique. Toutes les propriétés de matériaux employées ont été obtenues expérimentalement ou dérivées d'expériences à l'exception des propriétés d'interface fibre-matrice. Une bonne correspondance de ce modèle avec l'apparition de fissures transverses observées expérimentalement au bord ainsi qu'au cœur des échantillons est atteinte. Une dominance des propriétés d'interface sur le développement final des fissures transverses est démontré, et il est prouvé que celui-ci est déclenché par la coalescence de décohésions fibres-matrice menant à du micro-pontage de ligaments de matrice. Les effets cruciaux des contraintes thermiques résiduelles sont soulignés, des valeurs menant à un endommagement par décohésion d'interface ou cavitation de la matrice pouvant être atteintes à l'échelle micrométrique dans certains cas de figure. Une relation de proportionnalité inverse entre la température de cuisson et le début de l'endommagement sous les hypothèses de modélisation retenues est démontrée.
En utilisant ce modèle recalé afin d'identifier un ERR lié à la fissuration transverse, une diminution de la ténacité apparente lors de la diminution de l'épaisseur des plis est observée, tout comme cela était le cas avec la méthode semi-expérimentale.

A la lumière de ces résultats, un modèle à l'échelle du pli est proposé, dans lequel tout le dommage est groupé dans une seule fissure transverse, modélisée à l'aide de deux zones d'éléments cohésifs superposées, l'une représentant la décohésion fibre-matrice et la seconde représentant le micro-pontage de la résine. Une stratégie d'optimisation est utilisée afin de déterminer les deux lois de traction-séparation linéaires implémentées, afin de reproduire les débuts d'endommagements obtenus expérimentalement par émission acoustique. Les contraintes cohésives maximales ainsi que les ERR critiques obtenues de cette façon sont en accord avec ceux obtenus à l'aide du modèle multi-échelle. De plus, il est montré qu'une seule loi linéaire de traction-séparation pourrait être employée afin de prédire l'apparition des fissures transverses avec une précision acceptable, ce qui ouvre une perspective pour l'élaboration d'un nouveau modèle amélioré de résistance in-situ qui serait en mesure de tenir compte de la taille non négligeable de la zone de développement de dommage sans requérir d'avantage de caractérisation expérimentale.

Mots-clés :

Polymères renforcés de fibres de carbone, Stratifiés à plis fins, Microscopie in-situ, Tomographie à rayons X, Fissuration transverse, Propriétés d'interface, Effets d'échelle, Ténacité, Simulation par éléments finis multi-échelle, Éléments cohésifs.

Acknowledgements

I would like to express my gratitude to my PhD thesis directors Prof. John Botsis and Prof. Joël Cugnoni for the opportunity offered to work at the Laboratory of applied mechanics and reliability analysis (LMAF) on this project. Their support, interest, availability and involvement throughout the project is laudable. Joël's seemingly endless knowledge and invaluable technical advice was a great help and powerful motivator. Like many before me, I found him a great example to look up to, both on a scientific and on a human level.
Most of the funding for this project was granted by the Swiss National Science Foundation (FNS grant 200021_156207) for which I am most grateful.

I want to thank the jury committee members of my defence, Prof. Josep Costa, Dr. Yentl Swolfs and Prof. Véronique Michaud for kindly accepting to evaluate this work. Their expert remarks and suggestions have without any doubt improved the present document.

My great colleagues and friends of the "thin-ply" team, Guillaume Frossard and Robin Amacher, have to be thanked for the great time we spent together in and out of work, the lengthy technical discussions and the wealth of knowledge they shared with me upon my arrival. It has been a pleasure and an honour to spend this time with you.
Work at LMAF would not be the same without our lunches and especially coffee breaks, where great scientific discussions could be followed (or preceded for that matter) by great banter and rubbish talk. I have to thank all those who shared these moments with me during the past four years, including Joël, Robin, Guillaume, Maurice Ammann, Ebrahim Farmand-Ashtiani, Matteo Galli, Thomas Gmür, Bruno Giuntoli, Miguel Herráez, my first-class office mate Mathieu Janier, Simon Joncas, Anne Legrand, Alexandre Mordasini, Fernando Naya, Alain Prenleloup and Helena Teixido.
I would also like to thank fellow car freak Marco Borotto as well as Charlie Blondeau, Luis Canal, Georgios Pappas, and Niels Pichler for the nice and helpful working environment.
Finally, I wish to thank Viviane Magnenat for her patience and kindness in sorting out all my administrative issues, during my master projects and throughout these four years.

I need to acknowledge the work of the master students who kindly accepted to work under my supervision in relation to this thesis. Thank you to Felix Oberlé, John Stevenson and Simon Hayoz, who was mad enough to come back for a second one.

For their help and support in the manufacturing of my testing contraptions, as well as for the many totally unrelated discussions that we had, I'd like to thank the team of the ATME workshop, and especially Romain Baumer, Laurent Chevalley, Marc Jeanneret and Christophe Zurmühle. Many thanks also to the ATMX workshop for the frequent use of their equipment, and to Yves Ruschetta more specifically for putting up with me there.
For the many technical discussions we had, for their expertise and support, I would like to thank Yannick Prioux and Olivier Thomassin from our material supplier NTPT™, without whom this work would not have been possible.

Beyond the friends and colleagues, I am grateful to my parents for their love and steadfast support, both moral and material, throughout these four PhD years and during all my studies before that. Finally, the last person I wish to thank from the bottom of my heart is Catherine, whom I was fortunate enough to marry during the first year of my PhD. She supported me in my desire to work on this research, and put up with me all the way through it. Now that this chapter closes, we have many more adventures to look forward to, and I can't wait to share them with her!

Lausanne, 28 January 2019 S. K.

Contents

List of Figures

List of Tables

List of Symbols

a	TC crack extension (chap. 7)
a	Drucker-Prager material parameter (chap. 3-6)
b	Drucker-Prager material parameter
n	Stacking sequence repetition number
p	Equivalent pressure stress ($-\frac{1}{3}\,\mathrm{trace}\,(\boldsymbol{\sigma})$)
p_t	Hydrostatic tensile strength
q	Von Mises equivalent stress
s	Simulation step time
t	Ply thickness
E	Young's modulus
G	Shear modulus
G_{app}	Apparent toughness (=$G_{\mathrm{1c}}^{\mathrm{is}}$)
G_{1c}	Critical Energy release rate in mode 1
$G_{\mathrm{1c}}^{\mathrm{is}}$	In-situ critical Energy release rate in mode 1
G_i	Fibre-matrix interface toughness
G_B	Cohesive element toughness for bridging
G_D	Cohesive element toughness for debonding
T	Temperature
V^f	Fibre volume fraction
V_n^f	Effective fibre volume fraction (of a sample)
V^m	Matrix volume fraction
W_e	Elastic energy (nano-indentation)
W_t	Total energy (nano-indentation)
Y_T^{is}	In-situ transverse tensile strength
Y_r	Reduced (normalised) in-situ strength
α	Coefficient of thermal expansion
β	Drucker-Prager friction angle
δ	Crack opening displacement (also COD)
δ_B	Maximum opening of cohesive element for bridging
δ_D	Maximum opening of cohesive element for debonding
δ	Crack opening displacement (also COD)
ε_p	Equivalent plastic strain
ε_p^D	Equivalent plastic strain at damage onset

ε_s^C	Compressive strain at damage onset
ε_s^C	Shear strain at damage onset
ε_t^C	Tensile strain at damage onset
ϵ_t^n	Strain at TC onset for ply thickness t in simulations (chap. 7)
ϵ_t^n	Strain at AE onset for ply thickness t in experiments (chap. 7)
ϵ_f^{UTS}	Fibre ultimate tensile strength (chap. 7)
η	Triaxiality of the stress-state ($-p/q$)
ν	Poisson's ratio
ξ	Error vector
$\boldsymbol{\sigma}$	Stress tensor
σ	Normalised stress reported from experiments
σ_n	Stress measured during the experiments
σ^y	Yield stress
σ_t^y	Uniaxial tensile yield stress
σ_c^y	Uniaxial compressive yield stress
σ_{COH}	Cohesive stress
σ_B	Cohesive bridging strength
σ_D	Cohesive debonding strength
τ_i	Fibre-matrix interface strength
τ_i^n	Fibre-matrix normal interface strength
τ_i^s	Fibre-matrix shear interface strength
Φ	Yield function
ϕ	Transverse crack angle at the free edge
ψ	Drucker-Prager dilatation angle

List of Abbreviations

AE	Acoustic emission
AFM	Atomic force microscope
ASTM	American Society for Testing and Materials
ATL	Automated tape layup
CDM	Continuum damage mechanics
CFRP	Carbon fibre reinforced polymer
CLT	Classical laminate theory
CMM	Computational micromechanics
CNC	Computer numerical control
COD	Crack opening displacement (also δ)
CP	Cross-ply laminate layup
CSDMG	Cohesive damage variable (Abaqus output)
CTE	Coefficient of Thermal Expansion
DIC	Digital image correlation
EDP	Energy dissipation potential
EIT	Young's modulus measured by nano-indentation
ERR	Energy release rate
FE	Finite Element
GFRP	Glass fibre reinforced polymer
DIC	Digital image correlation
ISM	In-situ microscopy
LEFM	Linear elastic fracture mechanics
LMAF	Laboratory of Applied Mechanics and Reliability Analysis
MCID	Matrix cracking induced delamination
NTPT	North Thin Ply Technology (NTPT™)
OHT	Open-hole tensile test
PAN	Polyacrylonitrile
PEEQ	Equivalent plastic strain (Abaqus output)
PVA	Polyvinyl acetate
PIXE	Interdisciplinary Platform for X-ray micro-tomography
PSI	Paul Scherrer Institute (Villigen, Switzerland)
QI	Quasi-isotropic laminate layup
R-curve	Resistance curve (ERR vs crack length)

RVE	Representative Volume Element
SDEG	Material damage variable (Abaqus output)
SE	Secondary electron
SEM	Scanning electron microscopy
SENB	Single Edge Notched Bend
TC	Transverse cracking
TCID	Transverse cracking induced delamination
UD	Unidirectional laminate layup
UNT	Unnotched tensile test
UNT90	Transverse tensile (test/strength/model/...)
UTS	Ultimate tensile strength
Prepreg	Pre-impregnated fibre tape
2D	Two dimensional
3D	Three dimensional

1 Introduction

1.1 Motivation

The demand for lighter and stronger structures is as high as it has ever been, owing to the increasing economic and societal pressure to reduce the carbon footprint of the transportation systems in order to answer the major world issue that global warming represents. At the same time, the emergence of a wealthy middle class in developing parts of the world is boosting the demand for a continuous development of leisure and sporting goods into performance territories that just cannot be achieved with classical materials. Fibre reinforced composites, and especially carbon reinforced composites (CFRP) represent an excellent alternative for this quest of lightness and rigidity thanks to their exceptional strength and stiffness to weight ratio. The demand for such materials as a whole has therefore been on a strong annual rise of 10-12% [1, 2, 3], and this trend is expected to last as shown on Fig. 1.1.

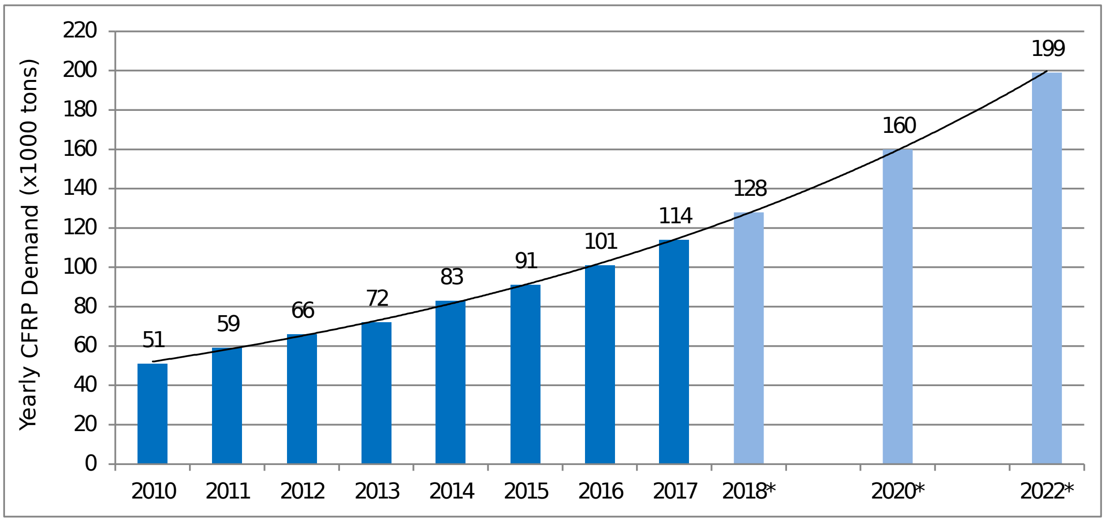

Figure 1.1: CFRP Market growth (* denotes an estimate) [3]

The aerospace market is perhaps the most prominent user of such high performance materials due to its very nature, the weight of the aircraft being much more penalizing to fuel efficiency than on non-airborne transportation means. For this reason, the latest aircraft generation (Airbus A350XWB, Boeing 787, Bombardier C-series/ Airbus A220) feature as much as 70% of such advanced materials including both the wings and the fuselage, increasing the weight savings as much as 15% over the previous generation of aircrafts such as the Airbus A380 which already incorporated about 25% of these materials [4]. Together with improvements in engine technology and advances in aerodynamics, the weight reduction permitted by such materials was one of the three main contributors to the 80% improvement in fuel efficiency in today's fleet compared to the one of the early 1960's.

This aerospace and associated defence industry is currently the largest CFRP customer by revenue, representing more than half of the CFRP industry at over 10 billion US $, as shown on Fig. 1.2b. This explains the large R&D effort put into products suitable for this use, despite the fact that it only represents 30% of the industry by volume (Fig. 1.2a) as their cost by mass is over three times that of products for other industries.

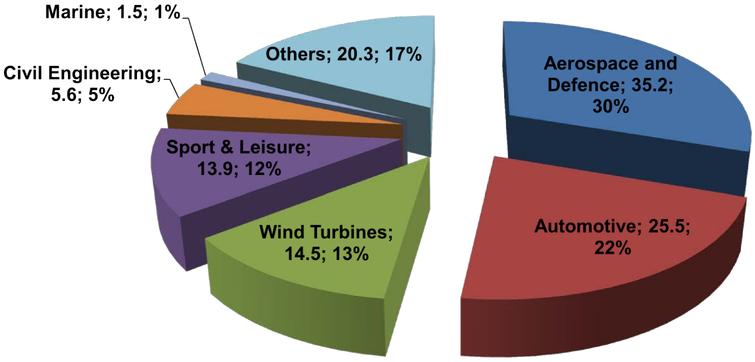

(a) Demand by mass (thousand tonnes)

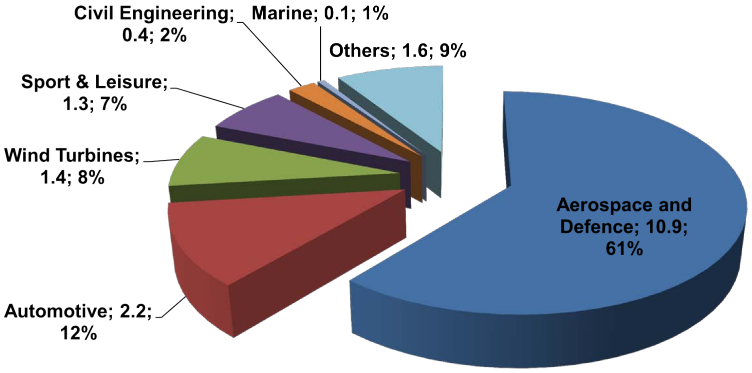

(b) Revenue in billion US$

Figure 1.2: 2015 Demand and revenue for CFRP by application [1]

The use of CFRP for these highly demanding customers is however hampered by the difficulty to predict their failure behaviour. Delamination and transverse cracking interact in ways that are difficult to predict, leading to critical design stresses as low as 30% to 50% of the actual fibre strength [5]. Transverse cracking is of special concern as it is difficult to detect, and drastically reduces both the fatigue life of the part and its ability to sustain of-axis loadings.
In a bid to raise these design limit, increasingly advanced fibre and matrices are used, with corresponding increased individual mechanical properties and price. This unfortunately drives the final component's prices up, which does therefore not improve the cost/performance ratio. A better use of these expensive constituents could be made if the design envelope of a given material could be increased by delaying the first ply failure and delaminations that are currently dominating the design criteria. A very promising development for such high-performance composites is the development of so-called thin-ply composites, where the individual plies are typically thinner than 150 µm. Such materials allow a much increased design space, which is especially interesting for thin structures or sandwich skins, where QI or orientated laminates can advantageously replace previously used stacking sequences without compromising the requirement for symmetric and balanced laminates [6].

For the aerospace industry, where certain percentages of fibres are required at given angles, it is not unusual for a single traditional ply to far exceed the requirement, leading to an unnecessary weight increase to comply with design rules. Thin-ply composites can therefore contribute to lightening structures within existing design procedures by their very nature. Furthermore, this new class of material presents other benefits such as better strength properties and fatigue life at the expense of a reduced toughness. This latter disadvantage can however be partly mitigated by the use of toughened resin systems and interlayer toughening techniques to compensate the drop in inter- and intralaminar toughness [7, 8]. Ply-level hybridization has also been shown to increase the translaminar toughness and can be used to create a pseudo-ductile behaviour [9].

The increase of damage onset warranted by thin-ply composites could significantly contribute to the structural lightening effort, but unfortunately the accurate prediction of this increase with respect to ply thickness, as well as its dependence on the constituents of the composite, is not yet well understood. Consequently, unless significant prototyping and experimental characterisation is undertaken prior to market release, the industry cannot rely on these better properties and the potential of thin-ply composites is therefore partly wasted. This work is therefore an attempt to contribute to the understanding and modelling of the mechanisms responsible for the increased damage onset of these materials in order to unleash their full potential.

1.2 Objectives

The first observation of a ply-thickness effect is by far not new, as a study on this topic for GFRP laminates can be found as early as 1978 with the work of Parvizi et al. [10]. However, the appearance of new manufacturing techniques allowing fast and controllable fibre tow spreading and thus the commercial production of thin-ply laminae about 15 years ago was responsible for a renewed interest in this area. Since the pioneering experimental work of Sihn et al. [11] and the application of a linear elastic fracture mechanics (LEFM) criterion based on Dvorák's work [12] to the constraining effect of a thin 90° ply by Camanho [13], the now called "in-situ strength effect", encountered in thin-ply composites has been the subject of much research which will be discussed in detail in chapter 2.

Research performed previously at EPFL [5, 6] did raise interesting questions, as the observed onset of damage scaling with respect to ply thickness t, defined using acoustic emission measurements (AE) and validated by open-hole tensile fatigue tests coupled with ultrasonic C-scans, differed strongly from the $1/\sqrt{t}$ law expected by a modelling based on LEFM hypothesis. Considering that this expected scaling was validated by previous experimental observations, though mostly for larger ply thicknesses than in [5], the question of whether different failure mechanisms were at play at very small ply thicknesses was raised. Alternatively, considering that the acoustic emission is a bulk measurement whereas in-situ microscopy of the free edge (ISM) is limited to this site, where the stress state is highly tridimensional and therefore not representative of the whole sample, it can be questioned whether the observations performed there are representative of a bulk behaviour.

If this difference in onset of damage between the AE measurements and the expected LEFM-based scaling can be both validated and explained mechanistically in the present work, a modelling of the identified effects at a higher scale ought to be attempted in order to allow the prediction of the ply thickness effect for very thin-ply composites. In summary, in order to be able to use thin-ply composites at their full potential in real applications, a detailed understanding and accurate prediction methodology of the in-situ strength effect must be developed. Starting at the microscale to understand the mechanisms, they should account for the specific damage processes encountered at very small ply thicknesses before being extrapolated at the lamina-level for ease of use and reduced computational cost.

From the interrogation presented above, a set of questions to address in this work can be derived:

- **Macroscale characterisation:** How do the macroscopically observable onset of damage in the bulk (AE) and at the free edge (ISM) compare for given fibre/matrix system and ply thicknesses?

- **Damage mechanism identification:** What are the microscopically observable damage mechanisms at play both at the free edge and in the bulk?
- **Damage modelling:** Can the microscopically observed damage mechanisms be replicated in a computational micromechanical finite element framework, and does it end up producing the same response as the macroscopically observed onset of damage? If so, this model should be used to deepen the knowledge gained with the experimental characterisation at the microscale.
- **Higher scale modelling:** Once understood, can the damage mechanism observed be modelled in a continuum damage mechanics model of some sort?

Considering the many advantages of thin-ply composites mentioned in section 1.1, it is a priority to fully understand the damage mechanisms at play and their ply thickness dependency. To this effect, unnotched tensile testing performed on quasi-isotropic laminates was selected as an appropriate experiment to qualify the macroscale response due to its representativity of the behaviour of a wide class of multi axial laminates. It was decided to complement the AE onset of damage measurements with optical in-situ damage observation at the free edges. Repeated for several fibre-matrix systems manufactured in plies of varying thickness, these observations should yield a good understanding of the influence of the composite's constituents and the effect of ply thickness.

Combining the macroscopic observations at the free edge with microscopic observations performed in a scanning electron microscope and x-ray tomographic imaging of partially loaded samples should contribute to the damage mechanism identification. To compliment the experimental results and in order to gain a better insight in the damage processes as well as validate the mechanistic conclusions drawn from the experiments, a computational micromechanics (CMM) finite element model was developed and implemented in the form of an embedded cell model, effectively coupling a CMM model with a homogenized, linear elastic model. The microstructures used were based on real micrographic observations of the actual samples, used for a better representation of their micro-structural inhomogeneity than with computer-generated ones. Finally, a mesoscale continuum damage mechanics (CDM) modelling based on the identified R-curve behaviour of the in-situ toughness of thin-ply composited was be proposed.

1.3 Thesis Outline

Following this introductory chapter, this thesis will be structured as follows:

- **Chapter 2** will present a state of the art regarding thin-ply composites in general, as well as the in-situ strength concept, its characterisation, and its modelling. Various relevant references for sub-parts of the thesis such as specific observation or modelling techniques will also be mentioned.
- **Chapter 3** details both the materials used throughout the thesis as well as all the experimental methods used for the different damage mechanism characterisation and other material properties identifications. The latter are used to obtain the values required to feed the developed numerical models of this work.
- **Chapter 4** is dedicated to the presentation of the experimental tests results and their analysis.
- **Chapter 5** is the pendent of chapter 3 for the numerical techniques used for the CMM modelling.
- **Chapter 6** presents the results obtained using the CMM modelling, and analyses them in order to contribute to the understanding of the mechanism at play and thus allow the modelling of the in-situ strength behaviour at a higher scale.
- **Chapter 7** concentrates on the presentation of the method used to model the identified mechanisms at the lamina level and discusses its application to the two materials modelled at the micro-scale.
- **Chapter 8** summarizes the knowledge gained throughout this work and presents future research avenues and outlook.

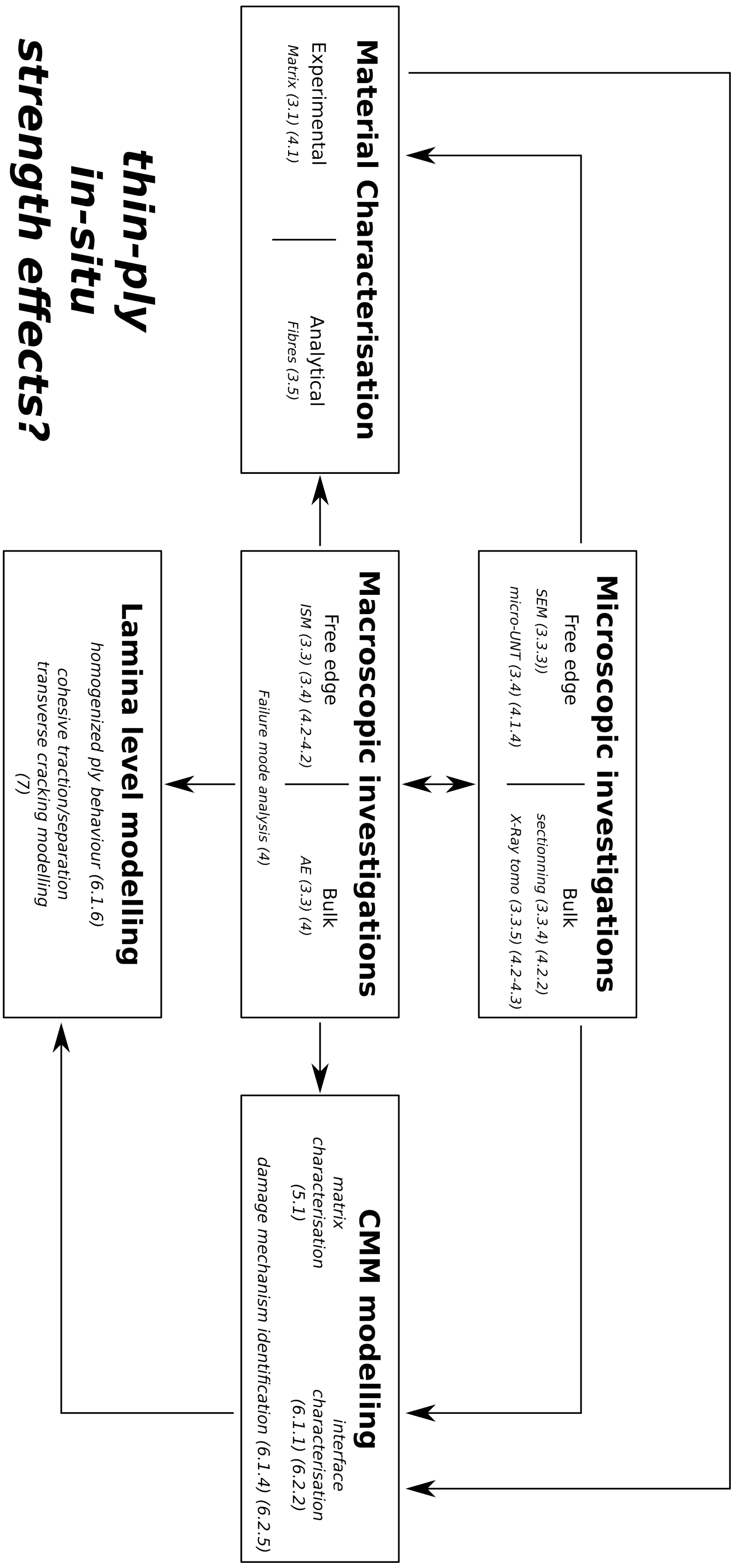

Figure 1.3: Thesis flowchart

2 State of the art

2.1 Thin-ply emergence and manufacturing

High performance industrial applications require to enlarge the design space of laminates and improve the performance of very thin parts such as sandwich skins. Interested by the increasing strength properties with reduced ply thickness shown in early experimental work such as Parvizi and Bailey et al. [10, 14], several methods were proposed in the literature regarding the manufacturing of thin-ply composite laminae. The conventional lower ply weight limit is usually regarded as being set between t=150 µm and t=125 µm. To reduce the fibre areal weight further than what was possible at the time, the spreading of individual fibre tows was required. To this effect, a technique making use of mechanical gears with perpendicular teeth was patented [15]. Besides mechanical tow spreading, many other techniques were proposed, with working principles such as electrostatic, vibration and acoustic working principles [16]. Another method was developed by Kawabe et al. [17], where the aerodynamic forces created by an airflow are used to spread the fibre tows as shown on Fig. 2.1, allowing a continuous and non-damaging process to take place.
Development of thin-ply composites is becoming a strong trend today with several composite manufacturers developing solutions alongside the UD prepregs of NTPT™, such as Chomarat C-Ply non-crimp fabric, Oxeon Textreme woven textile, special products from Sakai Ovex, Mitsubishi and Fukui R&D in Japan, as well as the offerings of several Chinese manufacturers.

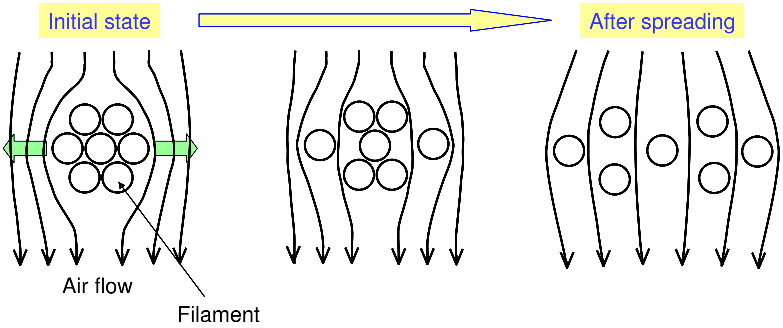

Figure 2.1: Aerodynamic tow spreading process [11]

2.2 Ply thickness effect and modelling

As mentioned in the previous section, the early observation of a ply thickness effect on the transverse tensile strength of the 90° ply of laminates was of great interest to some researchers. Dvorak and Laws [12] proposed a criterion based on LEFM, where considering plies of any thickness $2a$, the strength of the transverse layer $(\overline{\sigma}_{22})_{cr}$ was expressed as

$$(\overline{\sigma}_{22})_{cr} = \left(\frac{4G_{\mathrm{Ic}}(L)}{\pi\xi_I\Lambda_{22}^0 a}\right)^{0.5} \tag{2.2.1}$$

with $G_{\mathrm{Ic}}(L)$ the critical energy release rate (ERR) related to transverse cracking, Λ_{ij}^0 the non-vanishing components of the crack tensor and ξ_I a crack geometrical factor in their notation. Using G_{Ic} as a fitting parameter, a good agreement was shown with E-glass/Epoxy GFRP and T300/934 CFRP experimental free edge transverse cracks measurements, as shown on Fig. 2.2.

If a good agreement can be observed with the GFRP data set, it must be mentioned with hindsight that the CFRP does seem to behave more linearly for the thinnest plies. This model was later on expanded upon and formulated as a function of ply thickness by Camanho et al. [13], where the nomenclature of *in-situ* strength was proposed, and its $1/\sqrt{t}$ dependency highlighted. However, the discrepancy for very thin ply thicknesses remained until very recently, when following a discussion with the author a further modification to this model was proposed by Catalanotti [18], with the goal to tackle the issue of the "unrealistic asymptotic behaviour".

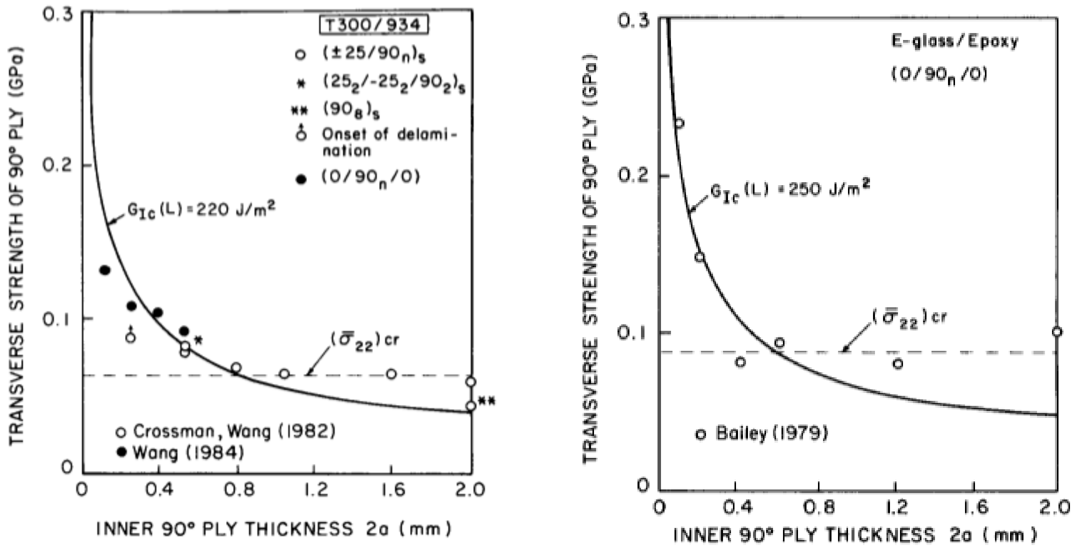

(a) CFRP experimental fitting

(b) GFRP experimental fitting

Figure 2.2: Strength of a constrained ply, taken from Dvorak [12]

2.3 Thin-ply experimental characterisation

To prove that the development of such thin-ply materials was successful, researchers embarked upon testing and characterising laminates made with the newly developed spread tow laminae. Taking on from Kawabe, Sihn et al. [11] performed the first study on tow spread thin-ply CFRP, comparing laminates made with 40 µm and 200 µm ply thickness, obtained by sub-laminate or ply-block stacking of 5 of the thinner plies. A 10% higher strength in UNT testing of QI laminates that were sub-laminate stacked was observed, paired with a change of failure behaviour to a brittle fracture compared to the usual progressive damage accumulation exhibited by such materials. The fatigue life of thin-ply laminates was shown to be improved thanks to reduced free edge damage, but this same effect lead to earlier failure in open-hole tensile tests as the tested specimen were unable to reduce the stress concentrators before catastrophic failure. A higher resistance to delamination upon impact was also exhibited by thin-ply laminates, thus also improving their compression after impact strength.

Wisnom et al. [19] performed tensile tests of unidirectional and quasi-isotropic specimen of varying specimen and ply thickness. If a small increase in strength was noted when increasing the thickness of quasi-isotropic specimen by sub-laminate stacking, a much larger detrimental effect was observed when varying the ply thickness by ply-block stacking, accompanied by a change in failure mechanism from fibre failure after partial delamination with the thinner ply-blocks (250 µm or less) to delamination only with the thicker ones (500 µm or more).

More recently, Amacher et al. [20, 5, 6] performed a comprehensive experimental macroscale characterisation of several thin-ply composites using various constituents. The improved properties of thin-ply laminates both at the component level (by means of bolted-joint bearing test including hot-wet conditions) and at the lamina level (by means of compressive and tensile fatigue tests) were confirmed. Furthermore, a linear increase of the stress at onset of damage with respect to ply thickness (Fig. 2.3) was reported, as opposed to the $1/\sqrt{t}$ scaling predicted by LEFM. This onset of damage was determined as the stress at which the cumulative acoustic energy reaches a 10^{-15}J threshold, as acquired by a Mistras-2001 measurement equipment, using a 65dB minimum acquisition threshold and an appropriate ΔT-front-end filter to reject acoustic activity taking place out of the gauge length. The value of this threshold was determined by a sensitivity analysis and validated by performing fatigue tests and C-scans. No AE event clustering was attempted and further work of the author along those lines proved unsuccessful as was also reported by Kötter et al. [21]. However, the attribution of a specific mechanism to certain AE characteristic features was shown to be notably complicated in the case of QI laminates, with AE signatures varying depending on the plies orientation and on their relative position in the laminate [22], which explains this pitfall. The results obtained in [5] were replicated on many different CFRP systems in [7] with similar conclusions drawn.

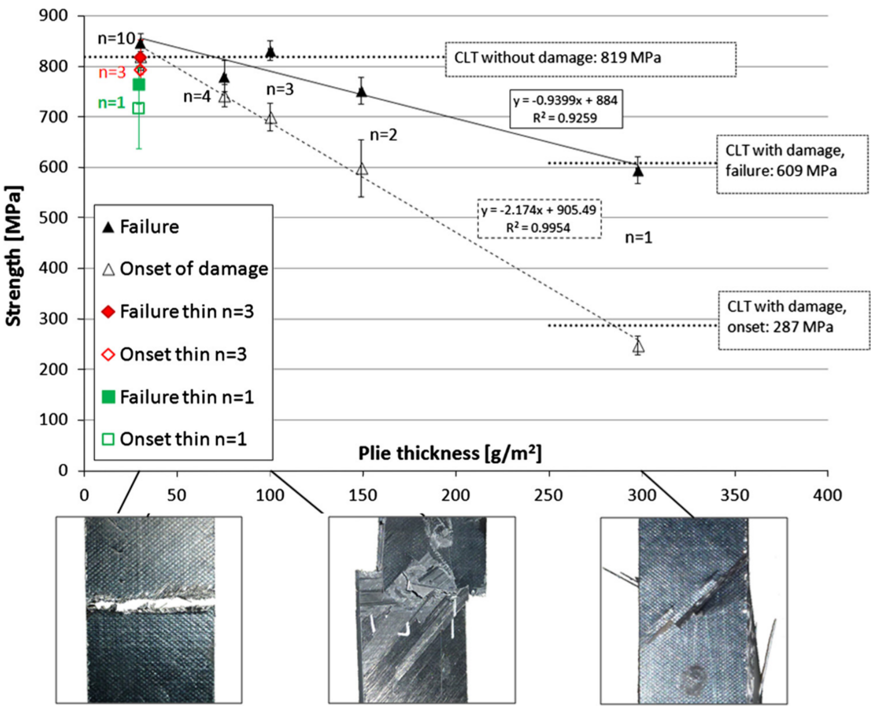

Figure 2.3: Onset of damage and ultimate tensile strength in unnotched QI specimen as a function of ply thickness [5]

This discrepancy in onset of damage scaling with respect to ply thickness compared to LEFM predictions is the main motivation for this work, and raised in its wake questions pertaining to the difference between free edge and bulk damage. For instance, Saito et al. [23, 24] studied the transverse crack propagation in 90° layers of variable thickness embedded between 0° plies and reported the existence of a transverse crack suppression effect for the thinner plies. They related it numerically to a decrease in energy release rate at the crack tip with decreasing ply thickness. The fibre-matrix debonding would appear at similar strains, but the coalescence of these into formed transverse cracks and their propagation through the thickness of the ply were delayed with thinner plies. They also related the higher crack density observed in the thinner plies at high strains (Fig. 2.4b) to the reduced stress relaxation obtained with smaller transverse cracks. Similar observations regarding the crack density (Fig. 2.4a) as well as a dependency to the adjacent ply stiffness were reported by Sebaey et al. [25], though on relatively larger plies of 183 μm minimum, by using an in-situ optical observation of the tested specimens' polished free edges. However, Yokozeki et al. [26] reported a retardation of matrix cracking accumulation in specimen made of thinner plies coupled with a decreased crack density in the bulk of their samples (Fig. 2.4c) when observing them by means of x-ray radiography.

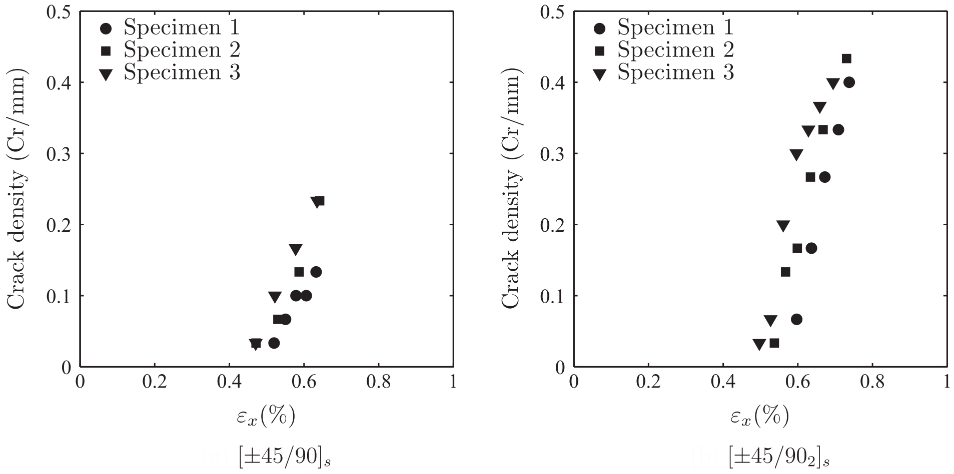

(a) Free edge TC density for two constrained ply thicknesses ([25])

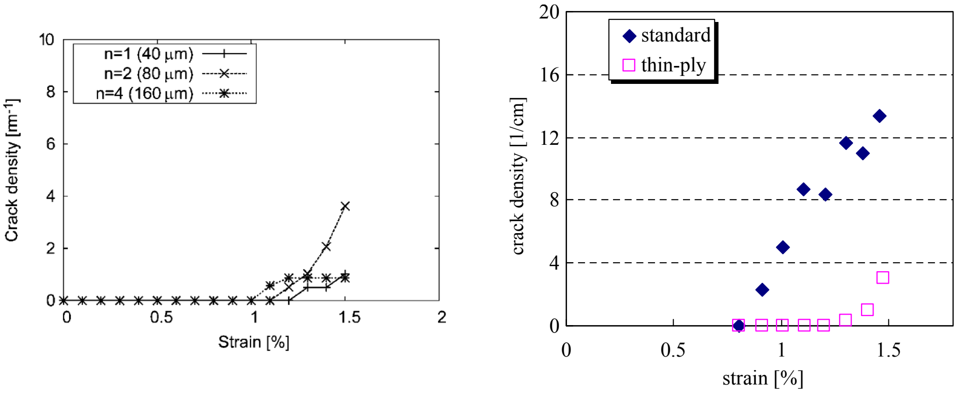

(b) Fully extended free edge TC density [23]

(c) Bulk TC density ([26])

Figure 2.4: Difference in TC density dependence on ply thickness between free edge and bulk

Other works confirmed experimentally the radically different failure modes compared to standard composites, with limited or suppressed damage development before failure. Apart from the transverse crack density in the bulk of the samples, Yokezeki et al. [26] compared 75g/m^2 and 145g/m^2 toughened epoxy CFRP and have observed up to 20% increase in UNT and compressive strength, open-hole compressive strength as well as fatigue life. An onset of damage increased by over 50% was also detected by AE and found to correlate well with their crack density measurements mentioned above. The same researchers also compared the out-of-plane transverse response (indentation) of thin and thick ply composites and showed that fibre fracture could develop within a thin ply because of limited delamination development [27]. Using a similar approach to Sebaey et al.[25], Guillamet et al. [28] measured the crack density, onset of transverse cracking (TC), free edge delamination and matrix cracking induced delamination (MCID) in the 90° ply of quasi-isotropic laminates containing both thick-ply (t=150 µm) and thin-ply (t=75 µm) regions. A systematic delay of TC was observed in the thin region compared to the thick one. The effect of loading direction was also shown to have a strong influence both on the strength of the tested laminates and on the development of micro damages therein. The notched response of non-crimp thin-ply fabric composites was shown by Arteiro et al. [29] by using a FFM approach to be largely similar to traditional laminates for ply thicknesses ranging from 75 µm to 150 µm.

Unfortunately, the improved strength properties of thin-ply laminates were shown by Frossard et al. [30, 31, 8] to be achieved at the cost of reduced mode 1 interlaminar and intralaminar steady state fracture toughness as well as reduced translaminar fracture toughness for both quasi-isotropic and cross-ply laminates. This effect was attributed to the higher ply homogeneity for the inter- and intralaminar fracture toughnesses, and to diminishing of the pull-out length with decreasing ply thickness for the translaminar one. This explains why the impact resistance properties of ultra-thin ply composites can be less advantageous than those of laminates made with slightly thicker plies [32, 5]. The early fibre fracture during impact on thin-ply laminates was shown to play a key role [27], although the hybridisation of thick and thin plies in a laminate was shown by Sebaey and Mahdi [33] to yield beneficial effects. Interlayer toughening and fibre hybridisation were considered to counter this detrimental effect [34], which also allowed the appearance of a certain pseudo-ductility in the failure behaviour of CFRP laminates by controlling the progressive fragmentation of certain layers [34, 35, 9, 36, 37, 38, 39].

2.4 Experimental observation techniques for composite damage

To better understand the damage mechanism at play as well as their differences between the free edge and the bulk, several observation techniques can be applied. The use of video microscopy on a polished free edge [23, 25, 28] has already been mentioned for the observation of formed cracks at the free edge, and DIC can be used in a similar way to obtain full field measurements [40]. When lower scale damage leading to the formation of these cracks such as fibre-matrix debonding is required, SEM observations can be performed in-situ [41, 42, 43] to enhance the magnification, including DIC measurements [44].

The observation of damage in the bulk of the material is somewhat more delicate. The use of AE is possible [10, 14, 26, 5] but the obtained data cannot easily be directly correlated to a given damage type in CFRP, especially in multi-angle laminates. Alternatively, X-ray radiography [26] or micro-tomography [45] allow damage visualisation in the bulk of tested samples, but these techniques are more costly and in-situ experiments are complicated to set-up with strong limitations on testing apparatus. The limited resolution of standard micro X-ray tomography, typically 1 μm to 10 μm per voxel, as well as the low absorption contrast between fibres and matrix has to be considered, especially when observing constrained micro-cracks that have very small crack openings. This limitation can be overcome by the use of a contrastant such as zinc iodide [46] allowing the detection of features 5% to 10% of the size of the voxel, or by using synchrotron tomography [47]. To increase the interface detection, the combination of high and low energy images [48] in conventional micro-tomographs can be used, like simultaneous phase and amplitude extraction from a single defocused image [49] is used in synchrotron tomography. Finally, if contrasting micro-particles can be included in the matrix, digital volume correlation can also be performed from X-ray CT scans [50], allowing the full strain field to be reconstructed in the different plies of the laminate as well as crack openings and potentially crack opening displacements of the micro-cracks present during thin-ply laminate damage. The local strain distribution profile in an embedded ply could also be measured via an embedded optical Fibre Bragg Grating sensor, as has been used to monitor interlaminar cracking by Farmand Ashtiani et al. [51, 52].

2.5 Composite micromechanical modelling

Over the last 15 years, FE micromechanical modelling and homogenisation schemes have been increasingly applied to model the characteristic multiscale damage mechanisms of fibre reinforced polymers. Due to computational cost, many of these rely on the 2D plane-strain hypothesis, using an RVE with periodic boundary conditions. Such is the case for instance for the work of Gonzalez and Llorca [42], where the compression of a UD ply was studied by modelling the matrix using a Mohr-Coulomb plasticity model and the fibre-matrix interface using cohesive elements, demonstrating a convergence for an RVE of about 70 fibres. Canal et al. followed a similar approach to model transverse tension and out of plane shear [53] using a matrix model developed by Jeong [54] which combines the Drucker-Prager yield function with a Gurson plasticity model to represent the toughening particles in the epoxy. They later used this model to replicate an in-situ SEM three point bending test on a notched beam with an excellent agreement between experimental and numerical data, by making use of an embedded cell that naturally couples microscale and macroscale. The damage sequence, starting with fibre-matrix debonding, coalescence of damage and finally crack propagation observed experimentally could be replicated numerically [43]. A similar damage sequence was shown by Vaughan and McCarthy [55, 56] where the sensitivity of transverse fracture to the fibre-matrix

interface, matrix ductility, thermal residual stresses and matrix rich zones was established for their RVE and compared to the SEM experimental data of [41]. A micromechanical constitutive model of UD composites using periodic boundary conditions on its RVE was developed by Melro et al. [57] who applied it to transverse tensile and compressive loading scenarios, as well as longitudinal and transverse shear loadings [58].
Naya et al. [59] studied the behaviour of UD plies in transverse and shear loadings including environmental effects by using a statistically equivalent RVE obtained by the application of the Random Sequential Adsorption algorithm [60], with fibres modelled as linear elastic and transversally isotropic solids, and the matrix modelled as an isotropic solid relying on the concrete-plasticity model implemented in Abaqus [61]. The latter is a modification of the Drucker–Prager plasticity yield surface [62] including a damage variable in order to capture the quasi-brittle behaviour of the polymer under dominant tensile loads. A good agreement with experimental data was reported, and the requirement to include fibre-matrix interface considerations in ply failure criteria relying only on ply properties [63] which traditionally assume a perfect interface was highlighted. The same framework was later used by these authors to model fibre kinking in FRP's [64].

Due to computational cost, multiple ply orientation are usually not included in a micromechanical RVE, but Soni et al. did model two plies of a CP laminate with discrete fibre and interfaces to study the in-plane shear of [±45°] and [0°/90°] laminates [65] and the localised damage evolution in double V-notch rail shear tests [66].

The issue with fully periodic boundary conditions is that they represent an infinite domain, and therefore cannot be used for simulations where ply constraining plays a role, such as for the study of the "thin-ply" effect. They are also unable to capture free edge effects. The application of such models to a constrained ply subjected to transverse tension was therefore performed by Herraez et al. [67] using the same framework as Naya et al.[59, 68, 64] and by Arteiro et al. [69] applying the constitutive model of Melro et al. [57], both using 2D plane strain semi-periodic embedded cell approaches. In such a case, only the edges of the RVE perpendicular to the loading direction make use of periodic boundary conditions, and the ones parallel to the loading are bonded to adjacent homogenized plies as they would be in an embedded cell [43].
The results of Herraez et al. [67] were in good agreement with LEFM predictions. The ones of Arteiro et al. [69] captured the same change of mechanism with decreasing ply thickness as observed experimentally, and predicted a quasi-linear increase of in-situ strength with decreasing ply thickness (see Fig. 2.5). More recently, these researchers published an overview of the current approaches used to predict damage and failure of CFRP thin-ply composites and their limitations, from numerical micromechanical model at the smaller scale to finite fracture mechanic approaches at the component scale, thus highlighting the intrinsically multiscale nature of this subject [70].

Regarding the free edge effect, Zubillaga et al. [71, 72] and Guillamet et al. [73] have proposed two modelling strategies to predict free-edge delamination and matrix cracking induced delamination in thin-ply composites. The analytical matrix-cracking induced delamination criterion of Zubillaga is based on a simple energetic criterion and classical laminate theory whereas the free edge delamination predictions in the work of Guillamet are performed using 2D plane strain finite element models with a cohesive model to represent the damage at the interfaces between plies. Good agreement with experiments was shown in terms of strain at onset of free edge delamination.

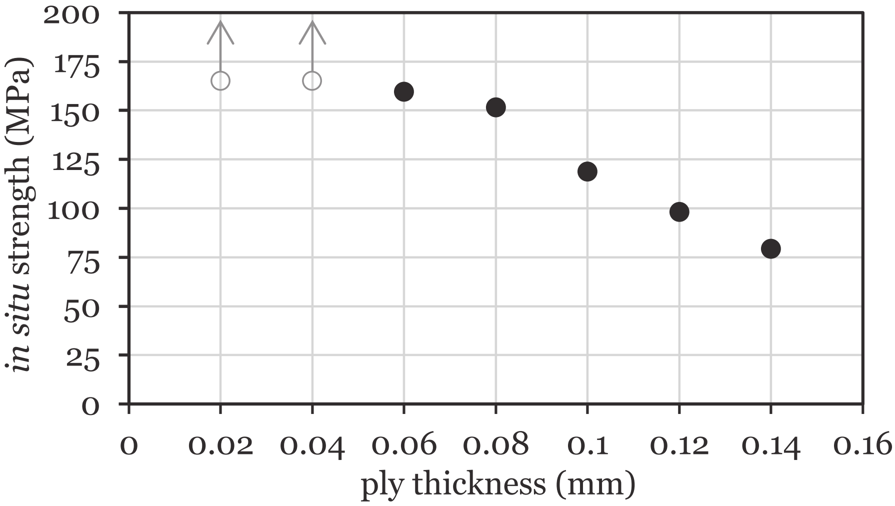

Figure 2.5: FE prediction of the in-situ strength of thin-ply laminates ([69])

2.5.1 Material properties at the microscale

The mechanical properties measured during macroscopic testing cannot always be used directly in micromechanical models. The epoxy matrix especially was shown by Fiedler et al., Hobbiebrunken et al. and Misumi et al. [74, 75, 76] to exhibit a strong size effect during experimental testing, and the requirement for a strain-hardening behaviour of the matrix to accurately predict the location of plastic zones in highly debonded areas was shown numerically by Romanowicz [77]. Consequently, the strain to failure in tension advertised in manufacturer's specifications for such a resin grossly underestimates the true ductility capability of the material when constrained between closely packed fibres. This was demonstrating numerically by Chevalier et al. [78] when applying their newly developed pressure dependent failure model for highly cross-linked epoxy resins [79] to several loading scenarios and comparing it with experimental data.

If the modelling of the resin can be troublesome, obtaining meaningful mechanical properties for the fibre-matrix interface is even more complicated. Rodriguez et al.[80], who developed a methodology to obtain two out of triplet of matrix material properties using nano-indentation tests, proposed a methodology to determine the fibre-matrix interface shear strength by fibre push-in tests performed on a nano-indenter which was expanded upon by Naya et al. [81, 68]. A possible relation to relate interface normal strength to the shear strength thus measured is proposed by Ogihara and Koyanagi [82].

At this scale, the fibres are modelled as linear elastic, transversally isotropic solids. However, very few studies have measured the transverse properties, and quite often an inverse homogenisation technique, be it analytical or based on a numerical FE-homogenisation model [83] is used. Some direct measurements exist for the validation of properties thus obtained, like the nano-indentation performed by Maurin et al. [84], the single fibre compression tests performed by Fujita et al. [85] or the Raman spectroscopy experiments performed by Miyagawa et al. [86], from which transverse Young's moduli ranging from 8 GPa to 15 GPa can be obtained. The transverse stiffness is also shown to be inversely proportional to the longitudinal one for different fibre types.

2.6 Mesoscale models and simulation

The computational cost of micromechanical FE models can be borne by research institutions to understand physical phenomena, but it is unsuitable for use by the industry for large scale applications. There is therefore a strong drive to propose ply level models, such as the LaRC03 [63] or the newly proposed consistent anisotropic damage model proposed by Reinoso et al. [87]. To carry the mechanisms observed at the microscale to the mesoscale, analytical or numerical models can be used. Whilst many different strength criteria have been implemented based on micro scale failure consideration or homogenization, fracture toughness prediction and extrapolation from microscale to mesoscale is a much more difficult task. To this effect, the work of Herráez et al. [88] demonstrated how the actual fracture mechanism in a single notch end beam modelled in an embedded cell could be transferred at a lamina level for use in a continuum damage scheme. The crack initiation is shown in the micromechanical model to be due to the coalescence of fibre-matrix debonding, followed by the extension of matrix ligaments that bridge the forming crack until final failure (small-scale bridging). It was shown that the R-curve behaviour exhibited during fracture could be replicated by lumping the two damage processes in an equivalent bilinear cohesive law [89] with a very good agreement.

At a lamina level, Okabe et al. [90] developed a continuum damage mechanics model for predicting the stiffness reduction of composite laminates including transverse cracks, formulated as a function of crack density. This model is able to compute the local stress distribution in a ply including transverse cracks as a function of crack density.

Following discussions with the author, the idea of a R-curve behaviour effect in the transverse cracking of constrained ply was recently implemented by Catalanoti [18] to provide a correction of the in-situ strength model which accounts for a finite limit of transverse strength when decreasing ply thickness.

3 Experimental materials and methods

This chapter will first present the three different carbon fibre / epoxy systems used throughout this work. Their processing as well as the whole sample preparation will then be discussed. The experimental testing performed, including all the observation techniques used, will finally be introduced. Previously characterized properties will be presented and all the additional experimental characterisation of individual components required for the numerical modelling will also be discussed.

3.1 Prepreg Materials used

The prepreg carbon-epoxy composite materials used in this work are all manufactured by North Thin Ply Technology (NTPT™) in Renens, Switzerland. Prepreg is the name used in the industry for materials where the fibres have been pre-impregnated with the resin, which is then subsequently partially cured to maintain the fibres together. The resulting product is a tape of extremely reproducible fibre volume fraction, which is therefore largely used in all demanding applications to ensure good manufacturing tolerances and reproducibility. In the present case, the prepregs used were unidirectional (UD) ones, meaning that all the fibres are placed along the tape length and only held together by the partially cured resin. Such material has to be stored at freezing temperature (typically −18 °C) to slow down the already initiated matrix reaction, and in hermetically closed bags to avoid the appearance of condensation upon thawing, as this would lead to all sorts of undesirable effects during the part's curing, resulting in unacceptable porosity levels and in some cases even delaminated plies.

In order to cover a wide range of material properties, two different epoxy matrices and two different fibre types were used throughout this work. For the fibres, it was chosen to use Toray Torayca® M40JB fibres, with a high modulus (377 GPa) and a limited elongation to fracture (1.2%), and T800 fibres from the same manufacturer, with a lower modulus (292 GPa) but with a maximal elongation of up to 2% which makes them one of the fibres that is able to absorb the most elastic energy on the market. For the matrices, TP80ep is an NTPT™ proprietary resin mainly used for naval applications nowadays, with a curing temperature of 80 °C. It is a first generation epoxy, fairly brittle and subject to viscous deformation (both viscoelastic and viscoplastic) due to the partial cross-linking inherent to the low curing temperature. The TP175 resin also used in this work, developed jointly between NTPT™ and Huntsman in collaboration with EPFL and FHNW [7], is a new last generation epoxy which cures at 180 °C, is highly toughened and much more cross-linked than the TP80ep, making it a very good candidate for current and future aerospace applications. Viscous effects are much less pronounced with this formulation.

3.1.1 Composite systems description and available data

The four components previously described were used in three different combinations in this work:

- **M40JB-TP80ep** is one of the first systems brought to market by NTPT™ and was extensively characterized at EPFL in previous work [20, 5, 6], making it the reference system of this work. Fortunately, enough material of the exact same batch as used by Amacher et al. [5, 6] and Frossard et al. [30, 91, 31, 8] was available for this work, and the results obtained can therefore be directly compared to previously obtained data with no bias.
- **T800-TP80ep** is exploring the influence of the fibre properties on the studied mechanisms compared to the reference M40JB-TP80ep system. However, the formulation of the resin was slightly changed between the production of the reference system and this one. Furthermore, the base resin was already expired when the tape for this system was produced, raising some questions as to the ability to directly compare it to the reference system. Nevertheless, the resulting system represent a low Tg carbon epoxy system with an intermediate modulus, high elongation carbon fibre which contrasts with the two other systems.
- **T800-TP175** is the latest system developed by NTPT™ and is typical of a third generation aerospace material. Compared to the T800-TP80ep system, the influence of the matrix properties on the mechanisms studied should be highlighted. Due to elevated curing temperatures and high content of toughening agents, this system contrasts significantly with the two other low temperature curing systems.

Previously characterized lamina properties of two of these composites systems can be found in Tables 3.1 and 3.2.

This choice allows a good coverage of the possible material spectrum, with the TP80ep resin being used with both the M40JB high modulus fibres and the T800 high strength ones, highlighting any fibre-induced effect. Any matrix-induced effect ought to be revealed by having both the TP80ep and TP175 resins used with the T800 fibres.

Table 3.1: M40JB-TP80ep lamina properties [5, 30, 31]. Thick plies are made of 2 blocked 150gsm plies.

All results normalized for 55% v^f		Thin	Intermediate	Thick
Property	Unit	30 gsm	100 gsm	300 gsm
Tensile modulus @ 0°	(GPa)	222 ± 14	223 ± 12	229 ± 11
Ultimate tensile strength @ 0°	(MPa)	2250 ± 139	2350 ± 130	2360 ± 150
Tensile onset of damage @ 0°	(MPa)	1644 ± 430	2019± 184	1391 ± 382
Poisson's ratio ν_{12}	–	0.314 ± 0.017	0.274 ± 0.02	0.266 ± 0.022
Tensile modulus @ 90°	(GPa)	7.01 ± 0.14		
Ultimate tensile strength @ 90°	(MPa)	23 ± 4		
Compressive modulus @ 0°	(GPa)	213 ± 7.3	201 ± 5	208 ± 4.9
Ultimate compressive strength @ 0°	(MPa)	1052 ± 89	869 ± 217	848 ± 150
Compressive modulus @ 90°	(GPa)	8.04 ± 0.41		
Ultimate compressive strength @ 90°	(MPa)	117 ± 7		
Interlaminar shear strength	(Mpa)	79.1 ± 2	79.9 ± 3	76.7 ± 2
In-plane shear modulus	(GPa)	4.661 ± 0.142		
Maximum in-plane shear stress	(MPa)	88.26 ± 1.83		
In-plane shear stress at 0.2% offset	(MPa)	50.23 ± 1.00		
Critical interlaminar mode 1 ERR	(J/m^2)	140 ± 11 (initiation value)		
Critical interlaminar mode 2 ERR	(J/m^2)	400 (initiation value)		
Critical intralaminar mode 1 ERR	(J/m^2)	138.6 ± 20(initiation value)		

Table 3.2: T800-TP175 lamina properties [34, 7]

All results normalized for 55% v^f		
Property	Unit	67 gsm
Tensile modulus @90°	(GPa)	9.57 ± 0.43
Ultimate tensile strength @90°	(MPa)	41.5 ± 2.6
Interlaminar shear strength	(MPa)	110.3 ± 1.7
Critical interlaminar mode 1 ERR	(J/m^2)	277 ± 15 (initiation value)
Critical interlaminar mode 2 ERR	(J/m^2)	728 ± 111 (initiation value)

3.1.2 Manufacturing specificities

These three systems were produced in UD-prepregs of several fibre areal weights. Coincidentally, the weight of the plies in gsm (g/m^2) is nearly equivalent to the ply thickness in µm, explaining why the two nomenclatures can easily be interchanged for ply thickness designation. The ply thicknesses used were t=300 µm, 150 µm, 75 µm, and 30 µm for the two systems using the TP80ep resin, and t=268 µm, 134 µm, 67 µm, and 34 µm for the system using the TP175 resin. These tapes were stacked into "complexes" of the chosen stacking sequence using an automated tape layup (ATL) system and delivered as "complexes" of 4 pre-stacked plies already cut to the desired production plate size, which then only required to be stacked on top of each other by hand for most cases. This procedure ensured that the layup angles chosen were perfectly respected as the stacking of more rigid square "plates" on top of each other is much less subjected to human error and imperfection than if each individual ply had to be laid down by hand at its correct angle. However, the whole T800-TP80ep system as well as the 34gsm T800-TP175 material could only be obtained as UD roll because no ATL time slot was available at the time, which means that these were entirely stacked by hand.

For the M40JB-TP80ep system, three different fibre batches were used depending on production times, with a tensile modulus of 377 ± 1 GPa and an elongation at break of 1.205±0.015% according to the manufacturer's batch fibre certificates. Considering the very small spread of properties, the mean value will be used throughout this work without further consideration given to fibre batch effect.

In the case of all but one specific tape, the T800-TP80ep system tapes were manufactured with a single fibre batch, with a 298 GPa modulus and an elongation at break of 2.0% according to the manufacturer's batch fibre certificate. Only the T800-TP80ep 30gsm tape was produced with two batches of another fibre type due to manufacturing constraints. However, the change for this tape was quite a major one, with a change from T800S to T800H fibres, which meant that the two commingled batches used had a very similar Young's modulus to the thicker tapes at 292 GPa, but an elongation at break drastically reduced to 1.835±0.065%, meaning that the translaminar fracture of the 0° plies will happen much earlier than for the other ply thicknesses of the same composite system, leading to a reduced ultimate strength. This will most definitely have to be considered when analysing the results. The reason for the difference between the two fibre types is a different spinning method, leading to different coarseness of their surfaces, different fibril sizes, different growth and compactness of the graphite micro-crystals as well as different micro-pore sizes and graphite ribbon toughness [92].

Finally, for the T800-TP175 system, a single fibre batch was used for all the ply thicknesses used, with a Young's modulus of 292 GPa and an elongation at break of 1.96% according to the manufacturer's fibre batch certificate, making it directly comparable to the T800-TP80ep system but for the 30gsm ply thickness of the latter.

The M40JB-TP80ep system has UD plies that were specifically manufactured for each ply thickness, but for the 300gsm. In this latter case, two 150gsm plies were "restacked" (stacked together in a ply-block stacking) to make a ply of double thickness. Due to production rationalization, the T800-TP80ep system was similarly made by restacking 75gsm tape for all ply thicknesses equal or superior to t=75µm. Only the 30gsm tape was manufactured separately. In the case of the T800-TP175 system, a single 67gsm tape was once again used as the base of all the plies produced but for the 34gsm tape which was produced specifically for this study. This procedure was shown to have very little impact on the performances of the specimen compared to plies manufactured at a specific ply thickness [5] and reduces the spread-tow processing variability.

3.2 Bulk Matrix Characterisation

Although the matrix is often considered as the "weak link" in composites, its material characterisation is actually crucial. Where ply-level experimental characterisations have not been performed, the Young's modulus E^m and Poisson's ratio ν^m of the matrices in the respective laminae are used to obtain homogenized ply properties. More importantly than the isotropic material parameters, though, the elasto-plastic properties and ultimate strength of the epoxy matrices play a major role in the behaviour of the final composites and thus have to be characterized for proper numerical modelling of these materials at the microscale.
The coefficient of thermal expansion (CTE) of the matrix should also not be neglected as it needs to be considered to evaluate internal residual stresses when working with high temperature curing systems such as the TP175.

3.2.1 Available material data

The two epoxy matrices used, TP80ep and TP175, are both proprietary products of NTPT™who provided the material information summarized in Table 3.3 as well as the actual stress-strain curves (shown on Fig. 3.1) obtained from standard ISO 527-2/93 [93] tensile tests .

Table 3.3: Bulk matrix properties as provided by NTPT™

Matrix type	TP80ep	TP175
Young's Modulus E (MPa)	3261.45	4240
Tensile yield strength σ_t^y (MPa)	59.93	101.8

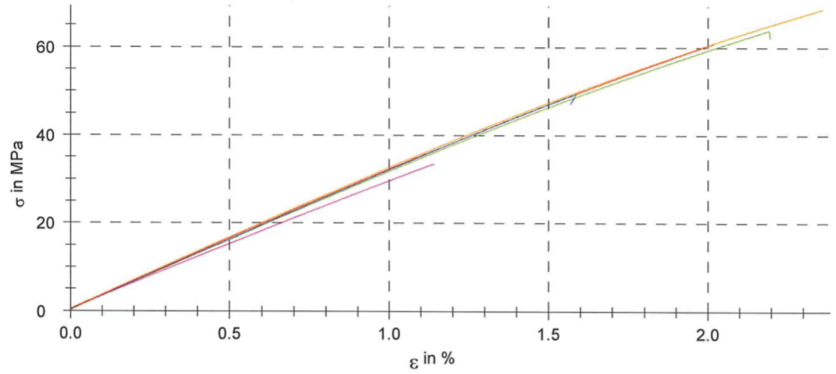

(a) Tensile tests TP80ep

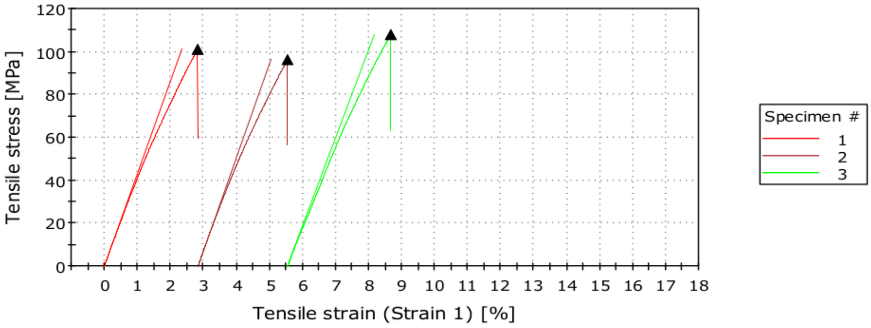

(b) Tensile tests TP175 (the curves for each samples are shifted)

Figure 3.1: Experimental tensile tests results for both resins used, as provided to the author by NTPT™.

3.2.2 Ductility extension

The ultimate tensile stress of an epoxy is notably smaller than its compressive counterpart. Two main reason can explain this asymmetrical behaviour:

- An epoxy is inherently sensitive to tensile loadings approaching a triaxial stress-state. During tensile testing in a standardized tensile test such as the ones performed by NTPT™ for the characterisation of the two resins used in this work, the specimen itself is in a stress state with triaxiality $\eta < -1/3$ (with $\eta = -p/q$ and p the hydrostatic stress and q the Von Mises equivalent Stress) due to its geometry even though the applied loading is truly uniaxial ($\eta = -1/3$).

- A strong size effect in strength [74, 75] is present due to the presence of internal defects such as micro-voids, which leads typical tensile test samples such as the ones used in the tests performed for NTPT™ to grow local damage at lower stresses which quickly lead to localization and early specimen failure.

Table 3.4: Matrix properties after ductility extension

Matrix type	TP80ep	TP175
Plastic strain at damage onset ε_p^D (%)	1.72	3.74
Tensile yield strength σ_t^y (MPa)	40	45
Hardening data	Determined from curve	

These two reasons explain why the values given in section 3.2.1 cannot be used directly in the FE models, where the micro scale uniaxial stress/strain curves are required. As it was demonstrated by Fiedler et al. [74], the stress-strain curve of epoxy matrix remains relatively similar when decreasing the specimen size but due to the reduction of specimen size, the small specimens exhibit a much larger ductility. Consequently, the experimental stress-strain curves were extended by a least-square fitting of a second order polynomial in the present work, and the curves thus obtained used until a perfectly plastic behaviour (horizontal tangent) is reached. The resulting curves are shown on Figs. 3.2a and 3.2b and the properties deduced thereof, which are in good agreement with [74, 75], are shown in Table 3.4.

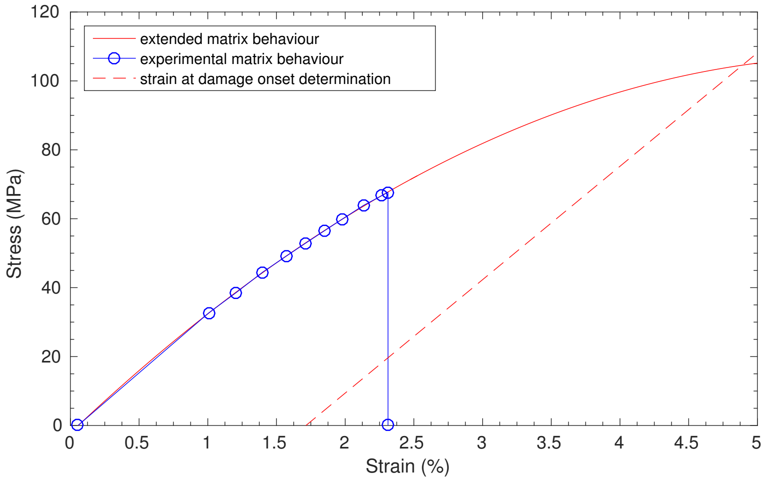

(a) TP80ep resin

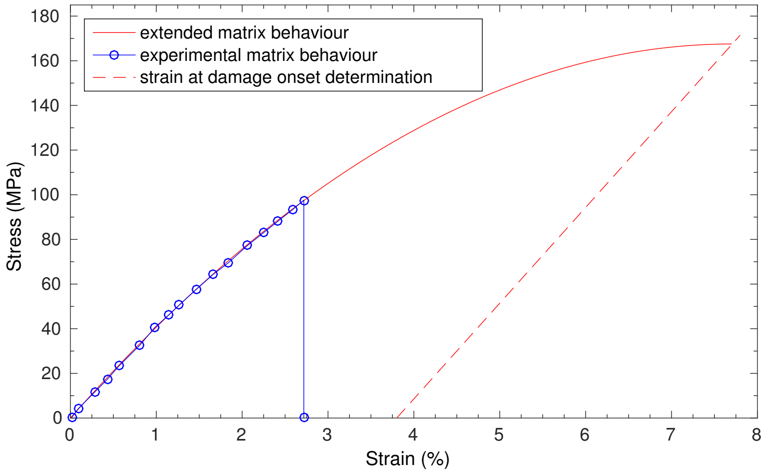

(b) TP175 resin

Figure 3.2: Ductility extension for both resins used. The strain at onset of damage in tension ε_t^C is chosen equal to the ultimate plastic strain ε_p^D, defined by a regression using the initial elastic Young's modulus from the strain at failure until 0 Stress (red interrupted lines)

3.2.3 Plasticity model identification - experimental testing

The behaviour of epoxy is known to be pressure dependent and many models based on Mohr-Coulomb or Drucker-Prager type of constitutive law have been proposed in the literature, as discussed in chapter 2. For the purpose of this work, it was decided to use the general exponent Drucker-Prager model offered in Abaqus [61], the implementation of which is discussed in detail in section 5.1. The yield function of this model is formulated as

$$\Phi = aq^b - p - p_t = 0 \tag{3.2.1}$$

where a and b are material parameters independent of plastic deformation, p denotes the hydrostatic pressure, q the equivalent von Mises stress and p_t is the hardening parameter that represents the hydrostatic tensile strength of the material , as shown on Fig. 3.3. In such a model, the

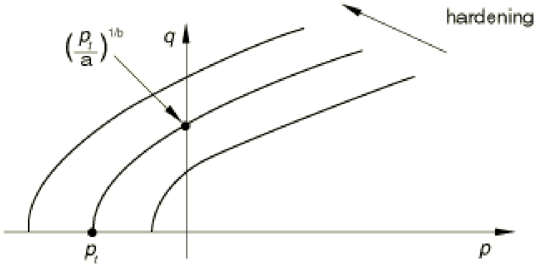

Figure 3.3: General exponent Drucker-Prager yield surface definition [61]

This yield function has a very similar shape to the one used by Melro et al. [57, 58] based on the paraboïdal yield criterion by Tschoegl [94] where the yield function is defined as

$$\Phi(\boldsymbol{\sigma}, \sigma_t^y, \sigma_c^y) = 2q^2 - 6p(\sigma_c^y - \sigma_t^y) - 2\sigma_c^y \sigma_t^y = 0 \tag{3.2.2}$$

where σ_c^y and σ_t^y denote the uniaxial compressive and tensile yield stresses, respectively. In a triaxial tensile stress state where $q = 0$ and $p = p_t$, this reduces to

$$\Phi(\boldsymbol{\sigma}, \sigma_t^y, \sigma_c^y) = -6p_t(\sigma_c^y - \sigma_t^y) - 2\sigma_c^y \sigma_t^y = 0 \tag{3.2.3}$$

which means that knowing σ_t^y and σ_c^y, p_t can easily be obtained. This calculation is in good agreement for both matrices with the experimentally validated void initiation failure criterion [95] stating that p_t could be estimated as a third of the ultimate uniaxial tensile strength.

To identify the parameters a and b, a least-square fitting approach was used for equation 3.2.1, with the objective of matching the experimentally determined yield points in uniaxial tension and compression σ_t^y, σ_c^y as well as the estimated yield point in triaxial tension p_t.

Consequently, the uniaxial tensile σ_t^y and compressive σ_c^y yield stresses for both matrices of our composite systems required an experimental characterisation.

The tensile yield stresses could easily be extracted from the stress-strain curves of the tensile tests provided by NTPT™, by defining the yield point as 0.05% plastic strain. The compressive values required uniaxial compressive test to be performed, which are discussed below in section 3.2.3.1. Finally, nano-indentation tests, which are presented in section 3.2.3.2 were performed on neat resin specimen in order to obtain the Drucker-Prager dilation angle ψ, which controls the amount of volumetric strain developed during plastic shearing, as it is well known that the flow of an epoxy matrix is non-associative. Although not used directly in this formulation, the friction angle β of the traditional linear Drucker-Prager model, which defines the sensitivity of the material to the hydrostatic stresses, can be calculated by using the tangent of the resulting yield function at high confining pressures.

3.2.3.1 Uniaxial compression tests

A couple of very small (10x10x5 mm) cast samples of both resins used in this work could be obtained from NTPT™. One of them for each resin type was used for a uniaxial compressive test which were performed as closely as possible to the ASTM D595 standard [96]. As the available samples were dimensionally close enough to the recommended alternative specimen dimension (0.5in x 0.5in x material thickness) the only machining work performed was to straighten the edges.

The specimen were loaded between two thick, flat plates mounted on a MTS 809 tensile testing machine, using a 10kN load cell. Despite the application of a Teflon film between the loading apparatus and the samples, remaining friction might cause a deviation of the desired uniaxial stress state in the sample, especially close to the edges contacting the loading plates. For this reason, the strain was measured using DIC in the central zone of the specimen, as shown on Fig. 3.5.
To make sure that these measures were sufficient, an FE simulation of the worst case scenario of perfect adhesion at the contact surface was performed, and even there the measured triaxiality value in the zone of interest did not notably deviate from the expected $\eta = -1/3$ as shown on Fig. 3.4.
The speckle pattern was applied by hand using a paint spray and the image acquisition performed at 20Hz using a Guppy F-146 CCD camera. The data reduction was performed with VIC-2D™ , and just like for the its tensile pendant, σ_c^y was defined as 0.05% plastic strain. The compressive strain was calculated by averaging the local strains measured in the region of interest.

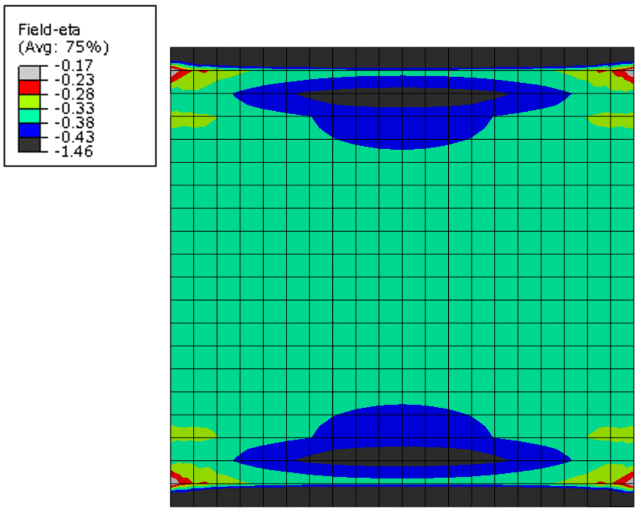

Figure 3.4: FE simulation of an elastic TP80ep resin block compressed uniaxially with perfect adhesion to the loading fixture at 2% strain. The contours plots represent the triaxiality η of the stress state under the assumed modelling hypothesis

Due to the 2D nature of the data reduction, the validity of the strain values obtained is limited by the occurrence of a barrelling effect at higher strains. However, as the only value of interest was the compressive yield strength σ_c^y, which is reached before barrelling appears, this was not deemed to be an issue for the application of the chosen 2D analysis.

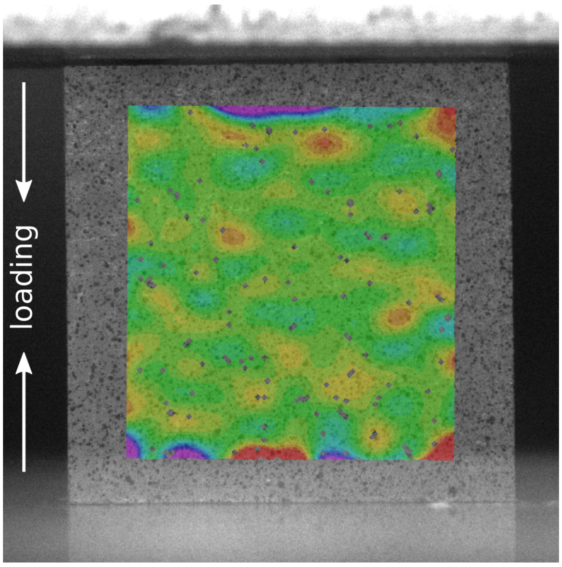

Figure 3.5: Zone of interest for the DIC analysis (strains in the loading direction shown)

3.2.3.2 Nano-indentation

Rodriguez et al. [80] performed nano-indentation test on several materials, including the well known 8552 epoxy matrix, and showed that it was possible to determine the constitutive response of the material from the indentation curve based on the universal hardness equation. In an initial bid to replicate this experiment and obtain the constitutive response of the two epoxy matrices used in this work, nano-indentation tests were performed on the remaining cast sample of each matrix. An Anton Paar NHT2 with a Berkovitch indenter tip was used, and several loading speeds and holding times tried on both systems.

Unfortunately, the master-curve approach proposed in [80] can not be directly applied in our case as the ratio of elastic to total energy W_e/W_t was measured to be smaller than 0.5 for all the different loading scenarios, preventing the use of the Oliver and Pharr method [97] to determine the contact area. Unlike [80] where this ratio was measured at around 0.52 for the 8552 epoxy matrix, an actual measurement of the indenter's contact area would have been required in our case. the viscous effects did however prevent a meaningful measurement to be taken using the optical microscope fitted to the nano-indenter, and no practical access to an atomic force microscope was possible. Furthermore, even if this approach had been successful, the theoretical framework is actually limited to non-hardening material behaviours, which from the discussion in section 3.2.2 is clearly not the case for the epoxies used in this work.

Considering the pitfall of the method envisaged, the alternate approach of determining the constitutive response by a direct inverse-identification of experimentally determined points of an assumed yield function (equation 3.2.1) exposed earlier in this section is deemed more suitable. However, the work of Rodriguez et al. described above was an inspiration to use the indentation curve to determine the Drucker-Prager dilatation angle ψ, as discussed in detail in section 5.1.1, when it was noticed that the simulated response of the indentation test was sensitive to this parameter. As ψ could not have been otherwise determined with the experimental tests performed, it turned out most useful.

3.3 Unnotched tension test (UNT)

3.3.1 Material Processing

The chosen stacking sequence for the quasi-isotropic (QI) samples was $[45/90/\text{-}45/0]_{\mathrm{Ns}}$ to be consistent with Amacher et al. [5, 6] who characterized this material using this exact sequence, but also because the 45° angle between adjacent plies provides an adequate balance between the ply constraining required for an in-situ strength effect to appear and the reduction of shear stresses between laminae responsible for edge delaminations [19]. Furthermore, the widely studied cross-ply (CP)laminates are seldom used in practice, whereas the 0°, ±45° and 90° ply orientations are the main ones used in aerospace, with minimum percentages of each one often imposed by design rules.

Considering that the focus of the present work lies on the ply thickness effect, n was varied between samples made of different ply thicknesses to warrant a nearly constant specimen thickness across all of the samples. It was also of prime importance to ensure that the plies laying on the sample's symmetry plane were 0° ones and not 90° ones, as a doubled transverse ply in the center of the specimen would have dominated its damage behaviour. Having the symmetry plane in the middle of a central 0° ply would have been even better, but this would have complicated the material supply, as some complexes (see section 3.1.2) would have had to be manufactured with 3 plies instead of 4 and the idea was therefore discarded.

Once stacked, the plates were cured in the autoclave of LMAF. As shown on Fig. 3.6, spacers of specified thickness ensured that the desired compaction was reached, whilst a 25 mm counter-plate ensured a good flatness and smooth finish on both sides of the curing plates. The manufacturer's recommended curing cycles were adhered to and can be found on Fig. 3.7a for the TP80ep resin and on Fig. 3.7b for the TP175 one. It is important to not forget that most usual autoclave consumables are usually only rated to 3 Bars and 120 °C, meaning that specific ones have to be used for aerospace grade matrices such as TP175 lest issues arise.

For the T800-TP175 system, due to the different fibre areal weights used, the compacted plate thickness differed from the previously targeted one and this was compensated for by the use of high temperature siliconed paper laid in the mould instead of re-machining a set of spacers.

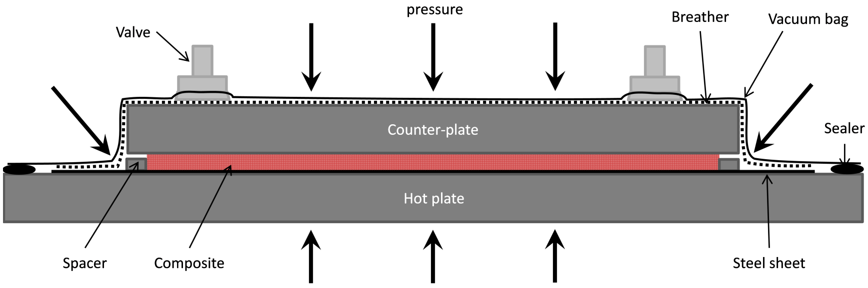

Figure 3.6: Autoclave curing setup [8]

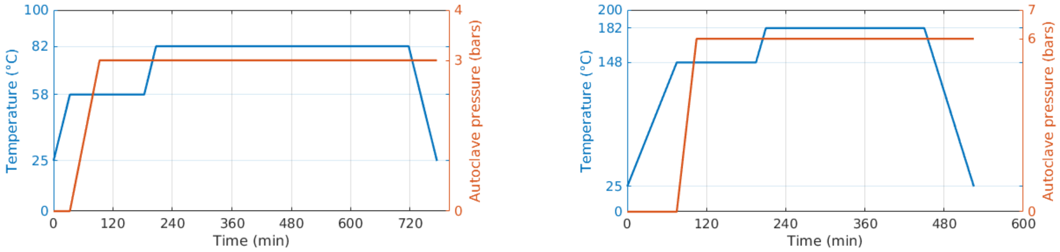

(a) Curing Cycle TP80ep

(b) Curing Cycle TP175

Figure 3.7: Curing cycles for both epoxy resins following NTPT™ recommendations

The targeted fibre volume fraction of all the plates produces was 55%, which was always reached with less than 5% deviation for the systems using the TP80ep resin. The plates made with the 67gsm T800-TP175 system were closer to 61% due to the supply of a tape that was not quite resin rich enough to reach the target. However, considering the relatively small discrepancy, the stress measurements reported in this work have all been normalized to 55% volume fraction to account for these differences according to the formula

$$\sigma = \frac{55\%}{V_n^f}\sigma_n \tag{3.3.1}$$

where σ is the normalised stress reported, V_n^f the effective volume fraction of each plate in percent and σ_n the stress actually measured during the experiment

Regarding the integrity of the T800-TP175 plates, optical microscopy performed on the free edge of multiple samples did not reveal large voids in the laminate. Very small ones could be seen, though, especially within the outermost plies of the laminates but not at the interface between different plies. The fairly dry tape received is blamed for that, though it is not deemed detrimental to the mechanical properties of the produced specimen.

3.3.2 Sample production

The experimental UNT tests performed were set-up accordingly to the ASTM D3039 [98] standard. Consequently, the samples were designed for the dimensions shown on Fig. 3.8. The pre-tapered, 2 mm thick ±45° GFRP tabs were glued on the produced 280x300 mm plates with a carbon charged epoxy resin, leaving 20 mm on every side of the plate to be cut off, ensuring that no defects could be due to the plate's edge. A 3 mm wide diamond bladed disc saw was then used to cut the samples to their nominal width b of 24 mm. No visible cutting damage resulted from this procedure as the feed rate of the blade was kept low enough compared to its rotational speed.

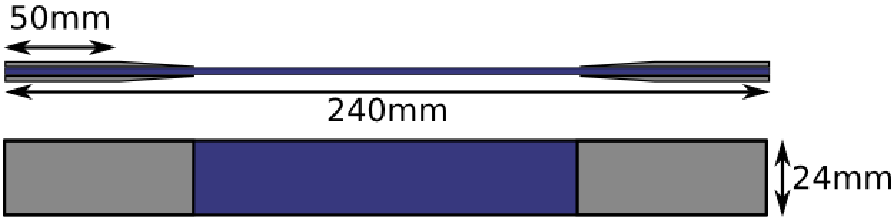

Figure 3.8: UNT samples dimensions, following ASTM D3039 [98]

Samples used for in-situ microscopic observation of their free edge had to have one of them polished. On top of the surface finish itself, ensuring the flatness of the polished face was of prime importance, as hand polishing tends to "round-off" the edges which in turn leads to parasitic reflections during optical microscopy. Consequently, several samples (up to 8) were blocked together as shown on Fig. 3.9 before grinding the resulting surface flat and polishing it using adhesive-lined sanding papers glued on an aluminium plate. To avoid surface scratches due to particles, the grinding and polishing were performed "wet", i.e. with water, down to a 3 µm grit silicon carbide / aluminium oxide sanding paper.

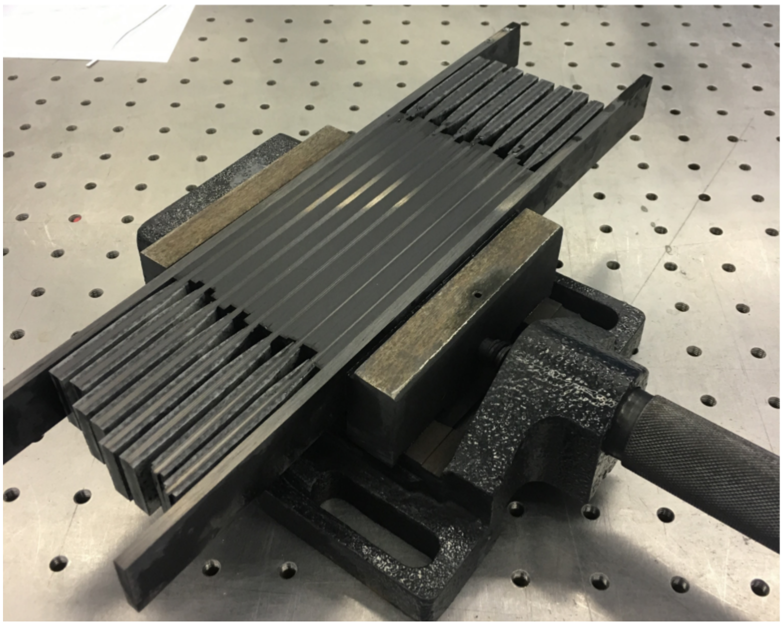

Figure 3.9: UNT samples polishing setup

3.3.3 Sample testing - Macroscopic damage characterisation

The tests were performed according to the ASTM D3039/D3039M-08 standard [98] on an axial-torsional MTS 809 tensile machine using a 100kN load cell. The strain was measured using HBM 1-LY-41-6/120 gauges placed in the center of the sample's gauge region. The signal was run through the strain-gauge amplifiers integrated in the MTS Flextest® 40 controller used do drive this tensile machine. The first sample of each batch was systematically fitted with two gauges, one on each side of the specimen, to check for the absence of bending and therefore warrant the correct alignment of the testing fixture as expected by the standard. One change from the standard was imposed due to the free edge observation procedure described in section 3.3.3.2, namely that the testing speed had to be slowed down to $0.125\,\mathrm{mm\,min^{-1}}$ instead of the recommended $2\,\mathrm{mm\,min^{-1}}$. This had some impact that will be discussed in section 4.2.1 especially for the systems using the TP80ep resin due to the viscous effect playing a much larger role at reduced testing speeds.

3.3.3.1 Acoustic emission monitoring

Acoustic emission monitoring similar to [5] was used to determine the onset of bulk damage, defined as a threshold of 10^{-15}J on the recorded cumulative acoustic emission energy. The acquisition was performed with a Physical Acoustics Corporation Mistras-2001 system using two NANO-30S probes with an appropriate Δt filter to limit the acquisition zone to the gauge length and a 65 dB acquisition threshold. This procedure was shown in previous work [5, 6, 34, 7] to reliably predict the onset of damage both by performing a sensitivity analysis on the threshold level and by comparison of the predicted onset of damage with open-hole fatigue tensile tests.

Whilst this procedure worked extremely well for prior characterisation work of several composite systems as well as for the M40JB-TP80ep system of the present work, a change in the resin used for the GFRP tabs provided by NTPT™ did prevent its successful application to the T800-based systems studied here. After extensive investigations, it turned out that a more brittle matrix was used for their manufacturing, leading to a strong acoustic emission activity within the tabs as early as 0.35% strain for T800-TP80ep and T800-TP175 samples of 150, respectively 134 gsm using the new tabs. As the definition of the rejection zone must take coarse finite values, reducing the Δt filter to avoid the tip of the tabs' taper resulted in an excessively small window of the gauge section to remain audible which did skew the results. Fortunately, both the T800-TP80ep and the T800-TP175 systems had been previously tested before the tab formulation was changed and the newly acquired results could thus be added to previously obtained data. This however meant that the free edge observations for these systems were not simultaneous with AE measurements any more, though the very similar strength recorded proves that a similar behaviour is to be expected.

3.3.3.2 Free edge observation

For the M40JB-based system, pictures of the polished free edge were recorded during the tensile test at a frequency of 1Hz, using a Guppy Pro F-146 CCD camera mounted either on an Olympus SZX12 stereo-microscope or on an Edmund Optics E-Zoom6V one. The slow acquisition speed, despite a fast shutter speed coupled with the slow loading speed, was required to be able to correct the focus during the test without significant loss of data due to the very limited depth of field. The size of the observation window ranged from 1.1x0.8mm for the 30 μm plies to 3.1x2.3mm for the 150 μm and 300 μm ones, corresponding to an optical magnification ranging from 2.5x to 6.5x depending on the ply thickness, and was located close to the center of the gauge region. The magnification was kept at 2.5x for the thicker plies in order to capture as much 90° ply length as possible. For the thinnest plies, the magnification was limited at 6.5x as the resulting depth of field would not have allowed a proper focus to be found with more zoom. This setup is shown on Fig. 3.10.

After testing, the free edges of selected specimen were observed under a higher magnification optical microscope and in SEM to ensure that the limited resolution of the optical equipment used in-situ did not prevent the observation of some smaller defects during the tests. The presence of free edge damage left tell-tale signs that could be very well picked up by the SE-detector, as shown on Fig. 4.6.

For the T800-based systems, a new Keyence VHX-5000 video microscope could be used instead of the Olympus stereo-microscope. On top of the already much larger depth of field offered by the VHZ20 lens due to its optical quality, the use of the real-time depth composition function totally solved the previously difficult focus determination at the expense of acquisition speed, which was reduced to 0.25Hz. However, every picture could be exploited which was not always the case with the prior setup, and a higher (digital) magnification could be used for the observation of samples made with the thinnest plies. An optical magnification varying between 2x for the largest ply thicknesses and 4x for the smallest ones was used, leading to an observation window varying between 3.5x2mm and 1.75x1mm, which is markedly bigger than with the previous setup. If the optical magnification is smaller than with the previous one, the nearly doubled pixel density, with individual pixels that are 21% larger than on the guppy camera, drastically improved the numerical zooming capability, resulting in much more detailed pictures on screen at an apparent (sensor vs. screen) magnification of 200x. This setup is shown on Fig 3.11, and the automation of the picture recording was handled by Tinytask [99].

When analysing the recorded images, the damage type was first assessed. Considering the predominance of the transverse cracking, this damage type was then quantified. The crack density throughout the test, defined as the number of cracks observed divided by the total length of observed 90° ply, was first recorded. A linear regression of the averaged crack density for a given specimen type was then performed to identify the strain at onset of damage, alleviating the potential issue of observing a zone that is not the first one to exhibit damage.

Figure 3.10: Free edge ISM setup using the Edmund Optics microscope

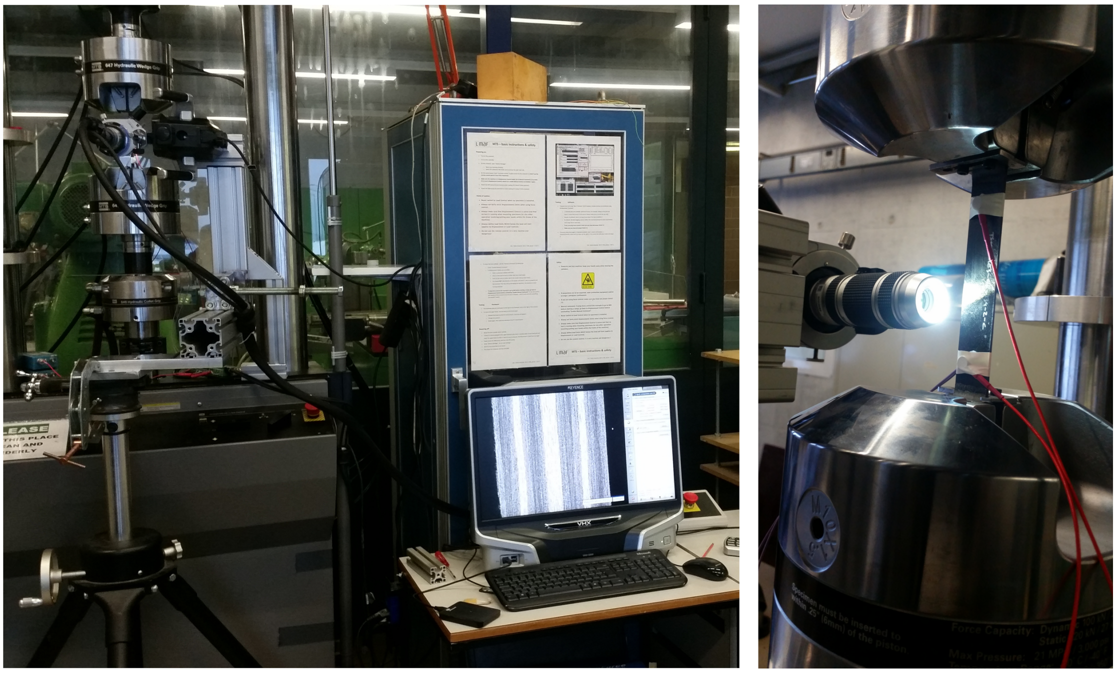

Figure 3.11: Free edge ISM setup using the Keyence VHX-5000

3.3.4 Interrupted testing - sample sectioning

Selected M40JB-TP80ep samples were used to study the propagation of the free edge cracks into the width of the sample by means of interrupted tests. The stress levels at which the loading was stopped were chosen according to the results presented in section 4.2 in order to be superior to the onset of free edge cracking but inferior to the AE onset, or superior to the AE onset. One issue with this approach was that the transverse cracks in the bulk of the samples did close again very cleanly when the loading was relaxed if the failure of the specimen was not reached. This implied that an apparatus was required to re-load the samples slightly under the microscope to reveal the existing transverse cracks.

Consequently, after the desired stress levels were reached, the loading was swiftly interrupted and the samples removed from the MTS tensile machine. A section of the gauge length was then cut out of the samples close to their center and cut through the middle of their width as shown on Fig. 3.12 using a diamond wire saw with a nominal wire diameter of 130 µm. The cut line revealing the middle of the samples was then polished on a Streuers® manual polishing machine, down to 4 µm grit silicon carbide polishing papers. A new set of tabs was then glued to the newly manufactured "partial samples", which were then finally reloaded in a small screw driven jig to reopen any crack present, at a loading inferior to 3kN. This loaded section was then observed under a Keyence VHX 500 microscope at an optical magnification of 15x, using a mix of concentric and ring lighting, over a length of approximately 10mm. The same observation procedure was applied to the original polished free edge of the sample. A reference line drawn across the width of the gauge length before the cut ensured that the observation at the free edge and in the newly revealed bulk could be spatially superimposed for comparison.

This procedure being very time consuming regarding sample preparation, the repetition of the observations at several sample depth for all the selected loading levels of all three systems studied was deemed most cumbersome and a better way to characterise the transverse crack propagation throughout the width of the samples was thus devised as discussed in the following section 3.3.5.

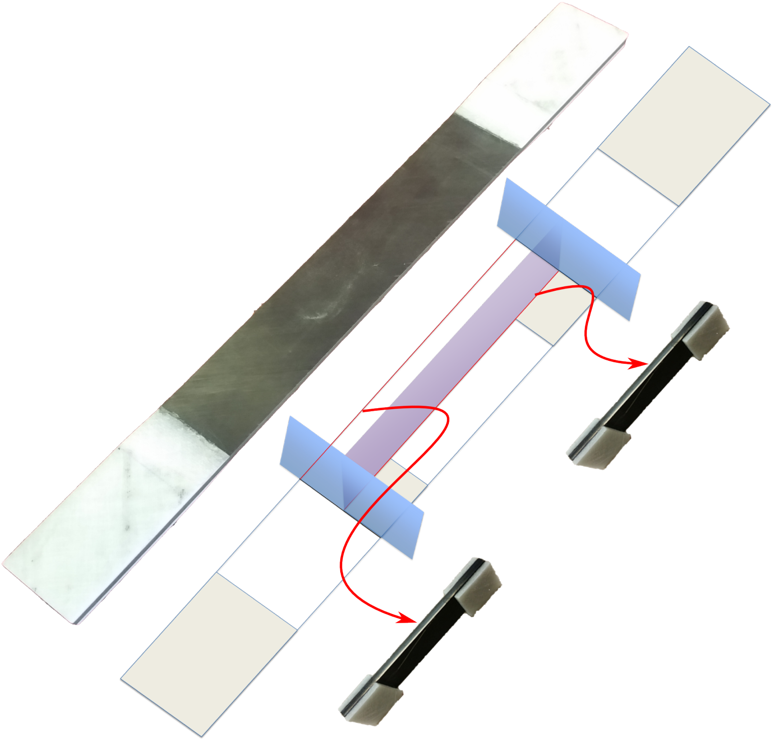

Figure 3.12: Schematic of the sample sectioning after the interrupted loading

3.3.5 Interrupted testing - X-ray tomography

Owing to the practical difficulties presented in the previous section 3.3.4, a similar interrupted testing procedure was developed in order to observe the crack propagation through the bulk of the specimen by means of X-ray tomography.

Once the interrupted UNT test had been performed, the samples were infiltrated with a ZnI_2-based penetrant solution which was shown to produce good contrast [46] and has the additional benefit to free the imaging process from time constraints as the iodide compounds formed in the solution stay in the sample even after evaporation of the solution. Its formulation is 60g ZnI_2 powder for 10ml ethanol, 10ml water and 10ml Kodak PhotoFlow 200. In order to ensure a good penetration of this contrasting agent, it was applied during 24 hours on slightly reloaded samples (typically 50 MPa) to reopen the cracks previously created during the test. This infiltration was performed in a machined UHD polyethylene sheath to reduce the required solution volume due to its cost, as shown on Fig. 3.13. This sheath was bonded to every sample using an urethane glue. After infiltration and prior to scanning, the samples were dried and slightly polished to remove any iodide compound deposited at the surface which would have created a very high contrast during tomography in places of no interest.

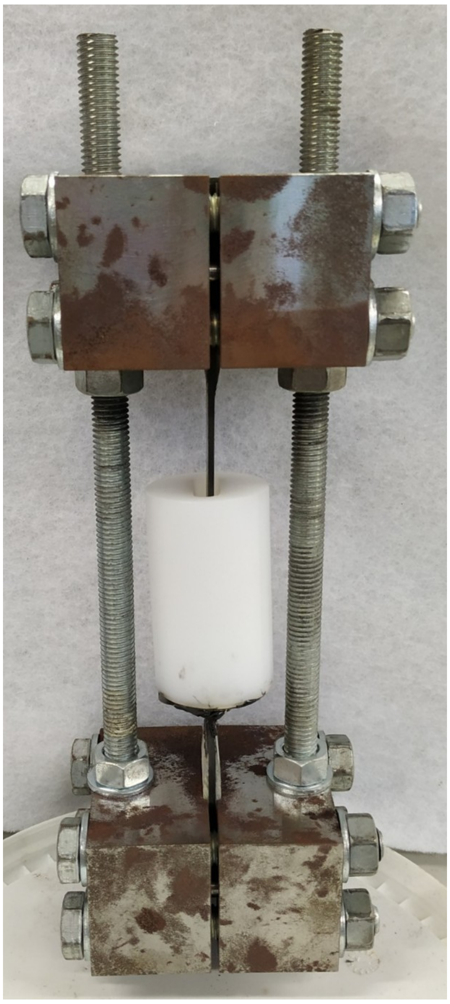

Figure 3.13: Infiltration setup, with the bonded polyethylene sheath and the reloading jig both shown.

An RX-Solutions Ultratom micro CT scanning device[1], shown on Fig. 3.14, was used to reveal the damage presence. A resolution of approximatively 7 µm per voxel allowed the observation of 10mm of gauge length over half of the width of the sample for each scan. It was shown [100] that the use of such contrasting agents permits the observation of features 5 to 10 times smaller than the actual voxel size, which suits the goals sought here.

The images obtained were used in two different ways. Firstly, "plunging" into the bulk of the specimen from its free edge by observing successive slices in the plane parallel to the free edge allowed the observation of the transverse crack shape. Secondly, using slices parallel to the top surface of the specimen, maximum intensity projection of all the slices laying in chosen plies allowed the count and length measurement of the cracks thus revealed, whilst also highlighting any delamination present if originating from the free edge. The required

---

[1] PIXE, https://pixe.epfl.ch/

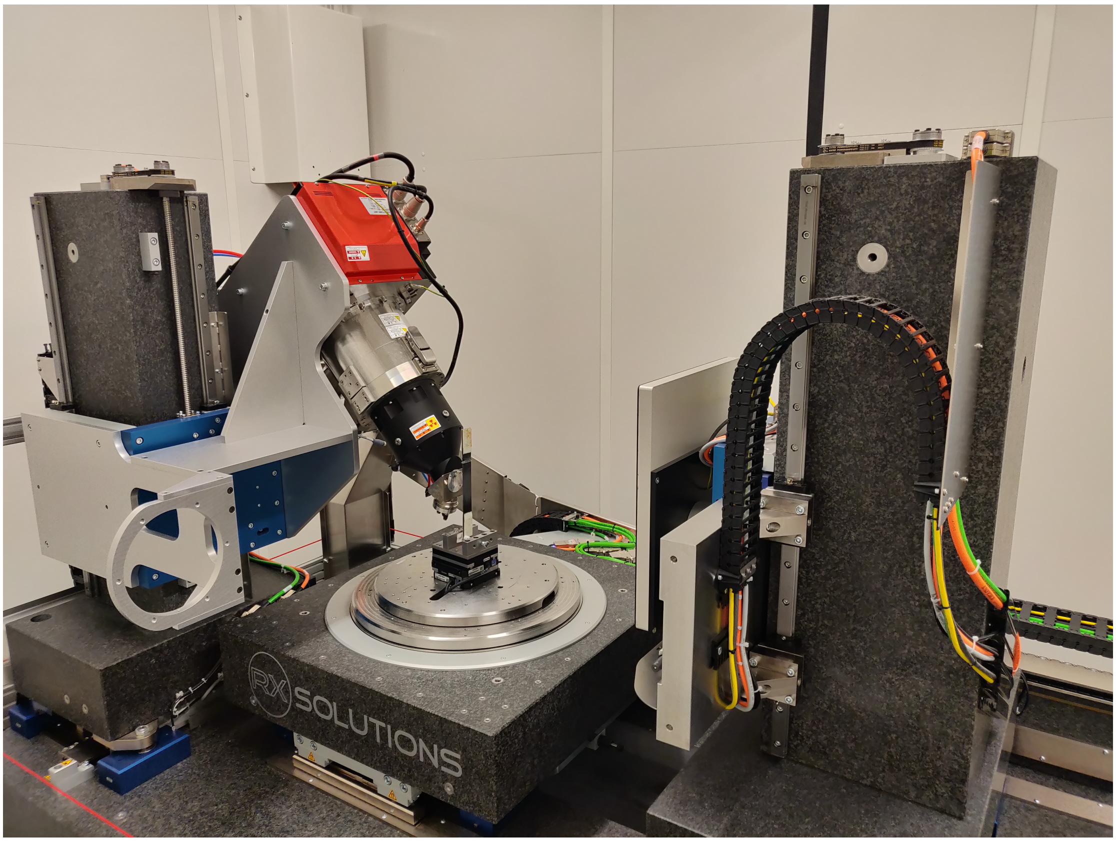

Figure 3.14: X-Ray tomograph

post-processing was performed with Fiji [101].

The absence of damage originating from the center of the sample was asserted by performing the infiltration process on a single M40JB-TP80ep sample discussed in more details in section 4.2.3. In this sample, a slit was machined in the center of the gauge length (Fig. 3.15) after the interrupted UNT test, allowing the infiltration solution to diffuse into any possible damage from the sample's center as well as from its free edge.

Figure 3.15: Machined sample to check for the presence of damage originating from the center rather than propagating from the free edge

3.4 Micro-UNT

In order to ensure that the resolution available when performing the free edge observations described in section 3.3.3 was not insufficient to observe relevant damage process initiations, it was deemed desirable to reproduce these tests on smaller scale specimen that would allow the same observations to be performed at a higher magnification. Early attempts to perform in-situ SEM experiments were not successful due to the visco-elastic / visco-plastic nature of the TP80ep resin used at the time, which meant that a strong stress relaxation and thus movement happened during the holding phase required for the specimen scanning. A different solution presented itself with the use of the Keyence VHX-5000 optical microscope, which drastically cut down the required imaging time whilst allowing for automatic focus tracking and depth of field reconstruction.

The use of this microscope allowed higher in-situ observation magnifications to be used, whilst the built-in stitching capability allowed the observation of a large enough zone. An Instron 5848 MicroTester with a 2 kN load cell and Instron mini wedge grips 2716-017 was used for testing, as it was possible to lay the machine flat and test the specimen horizontally which greatly simplified the observation. Furthermore, its electrical actuation gave it a lot more stability compared to the hydraulic actuation of the MTS 809 tensile testing machine used for the full-size samples, greatly helping with the focus of the images captured. The motorized z-stage head of the VHX-5000 was mounted on a custom manual translation stage, which allows the observation of the required length of the specimen at higher magnifications. The z-stage support on its translation stage is shown on Fig. 3.16 and the whole setup can be seen on Fig. 3.17. The size of the specimen obviously had to be adapted to the much smaller scale of the load cell, but it retained significant similarity to the full scale tests.

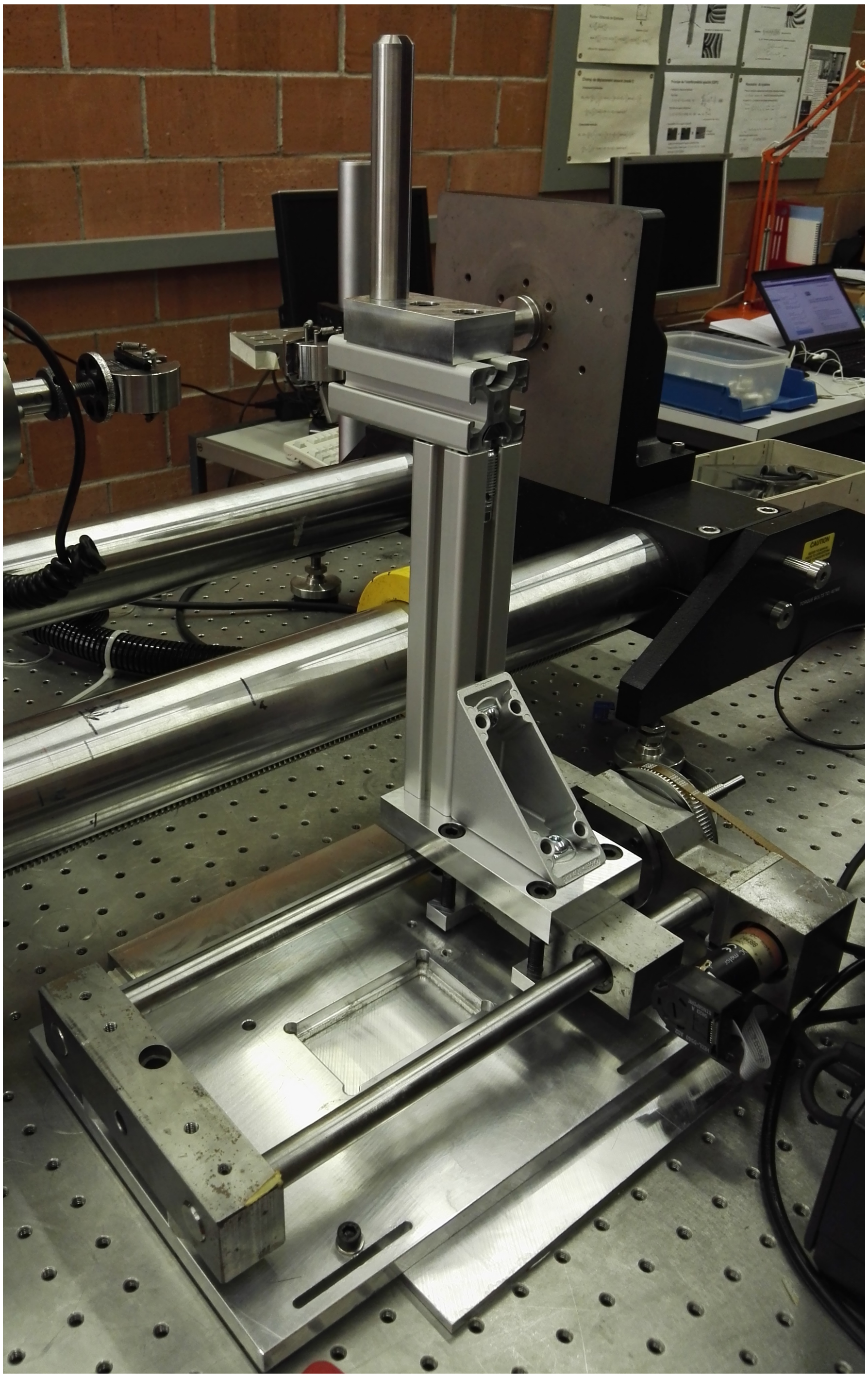

Figure 3.16: Micro-UNT displacement precision stage shown in the foreground, with the microscope head adapter mounted on it. The tensile machine is visible in the background with no specimen mounted.

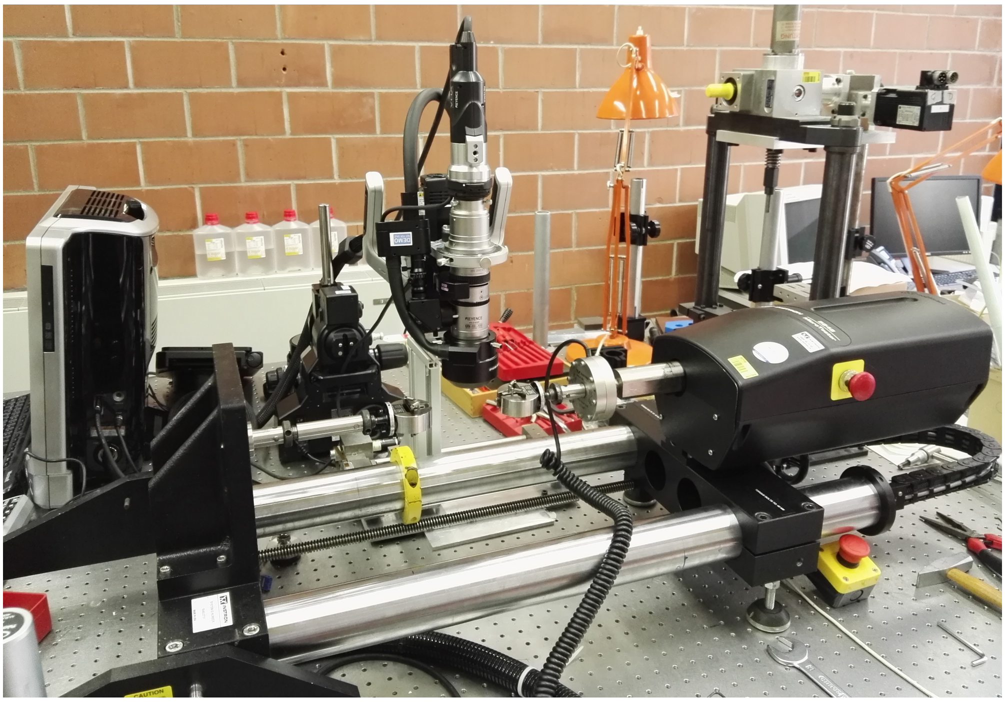

Figure 3.17: Micro-UNT global setup, with the microscope head mounted on its adapter to the displacement stage, and the tensile machine in the foreground. No specimen mounted.

3.4.1 Micro-specimen manufacturing

Small, very thin QI plates of M40JB-TP80ep and T800-TP175 material were manufactured for this study. The layup chosen is the same as for the full-scale specimen, and the dimensional details can be found in Table 3.5. Autoclave curing was performed as discussed in section 3.3 but the extremely thin plates did not warrant the use of spacers. QI stacking and resin formulations that do not bleed much warranted that reasonable fibre volume fractions were reached. The machining of the samples into 3x140 mm and 6x140 mm was performed on a 3-axis CNC milling machine using a 2mm diamond-coated mill-bit. The composite plates were glued ("white" or "paper" PVA glue) to 3mm plywood sheets on both sides to prevent machining damage and provide a mean of holding this sandwich structure to the mill's bed. The choice of PVA glue makes the post-machining removal of the wood layers easy, by simply wetting the wood and waiting for the glue to soften. It has also been proven strong enough to prevent any movement during machining.
One edge of each sample was polished to allow the ISM observation down to a 4000 grit SiC paper on a Streuers® manual polishing machine. The plywood was left glued to the carbon-epoxy composite during polishing to stabilize it as the specimen would otherwise have been too thin. Finally, the ±45° GFRP tabs used for the full-scale samples were cut and ground by hand to be glued with Loctite 401 cyano-acrylate adhesive, as shown on Fig. 3.18 in order to avoid stress localization in the grips of the tensile testing machine.

Figure 3.18: Micro-UNT sample

3.4.2 Micro-specimen testing

ISM optical micrography was performed in a similar manner to the full scale specimen but at a higher magnification on much smaller specimen. Due to the required displacement of the microscope to scan the required length in order to be statistically independent of the observation site, the loading had to be performed stepwise, and the pictures were recorded during holding phases. Due to the viscous effects present in the TP80ep resin, these tests were performed with a slight overshoot of the target load increments, followed by a controlled offloading back to the desired nominal load. This helped stabilise the specimen and reduce the creep during the imaging process. The loading steps as well as the overshoot magnitude are shown in Table 3.5. The microscope's head was manually moved along the specimen using the translation stage during the holding phases. Automated image stitching by DIC position recognition is offered by the microscope, and caters for the joining of the different pictures taken along the free edge for a given load step.

Table 3.5: Micro-UNT specimen and testing details

Material	M40JB-TP80ep			T800-TP175
t (µm)	30	75	150	67
length (mm)	140			
width	3mm and 6mm			
stacking	$[45/90/-45/0]_{2s}$	$[45/90/-45/0]_{s}$		
loading speed (mm/min)	0.5			
overload (N)	30 (3mm samples) / 60 (6mm samples)			
load step (N)	100 (3mm sample) / 200 (6mm samples)			
relaxation speed (mm/min)	0.1			
apparent magnification (x)	800	400	200	500

3.5 Fibre Characterisation

The CMM modelling discussed in chapter 5 requires the use of a more detailed representation of the fibres than what is available from the supplier's datasheets [102, 103, 104]. Many models have been proposed to predict the behaviour of UD lamina properties from the constituents, starting from the well know series and parallel or "rule of mixture" models (Voigt and Reuss) to full-blown homogenization models (Mori-Tanaka) and FE approaches. The inversion of such models to determine individual constituents properties from known lamina properties is however more challenging, as the sensitivity of certain parameters is very low. Considering that the most important requirement was to obtain realistic E_2^f values in order to not overestimate the stress concentrators at the fibre/matrix interfaces, the often used Chamis semi-empirical model [83] was used to deduce the fibre transverse properties from the identified UD lamina properties shown in Tables 3.1 and 3.2.

This model in its direct use allows the estimation of all five independent elastic properties of a lamina knowing those of its constituents and the fibre volume fraction, as shown in equations 3.5.1 to 3.5.5.

$$E_{11} = V^f E_{11}^f + V^m E^m \tag{3.5.1}$$

$$E_{22} = \frac{E^m}{1 - \sqrt{V^f}\left(1 - \dfrac{E^m}{E_{22}^f}\right)} \tag{3.5.2}$$

$$\nu_{12} = V^f \nu_{12}^f + V^m \nu^m \tag{3.5.3}$$

$$G_{12} = \frac{G^m}{1 - \sqrt{V^f}\left(1 - \dfrac{G^m}{G_{12}^f}\right)} \tag{3.5.4}$$

$$G_{23} = \frac{G^m}{1 - \sqrt{V^f}\left(1 - \dfrac{G^m}{G_{23}^f}\right)} \tag{3.5.5}$$

For the present use, the fibre longitudinal Young's modulus E_1^f was taken directly from the manufacturer's specification, as the individual certifications of the fibres used in our prepregs were available and supported them. G_{23} was estimated using $G_{23} = E_{22}/2(1+\nu_{23})$. These equations were therefore inverted to write

$$E_{22}^{f} = \frac{E^m \sqrt{V^f}}{\sqrt{V^f} + \dfrac{E^m - E_{22}}{E_{22}}} \tag{3.5.6}$$

$$\nu_{12}^{f} = \frac{\nu_{12} - (1 - V^f)\nu^m}{V^f} \tag{3.5.7}$$

$$G_{12}^{f} = \frac{G^m \sqrt{V^f}}{\sqrt{V^f} + \dfrac{G^m - G_{12}}{G_{12}}} \tag{3.5.8}$$

$$G_{23}^{f} = \frac{G^m \sqrt{V^f}}{\sqrt{V^f} + \dfrac{G^m - G_{23}}{G_{23}}} \tag{3.5.9}$$

$$\nu_{23}^{f} = \frac{E_{22}^{f}}{2G_{23}^{f}} - 1 \tag{3.5.10}$$

The typical limitation of this procedure is apparent when trying to compute the fibre transverse-transverse Poisson ratio ν_{23} as the result of 0.55 obtained for the M40JB fibres is not physical, and the value of 0.49 obtained for the T800 ones is barely acceptable. This value was therefore estimated at 0.45 for both fibres according to values found in [67], which conveniently also alleviated any potential numerical issue that could have been encountered with incompressible materials. The properties finally obtained can be found in Table 3.6.

Table 3.6: Fibre orthotropic properties deduced from the experimental lamina data

Property	M40	T800
E_{11}^{f} (GPa)	377	292
E_{22}^{f} (GPa)	11	10.4
E_{33}^{f} (GPa)	11	10.4
ν_{12} (-)	0.29	0.29
ν_{13} (-)	0.29	0.29
ν_{23} (-)	0.45	0.45
G_{12} (GPa)	44	26
G_{13} (GPa)	44	26
G_{23} (GPa)	3.7	3.49

The calculated fibre transverse moduli E_{22}^{f} fall within the standard deviation of the values obtained by nano-indentation on the same kind of fibres by Maurin et al. [84] which in turn were in good agreement with the generally accepted values found in Hughes [105].

4 Experimental results and analysis

The experimental results are presented in this chapter. Firstly, the results of the matrix characterisation are presented in section 4.1. The individual results for each composite system are then shown and discussed in sections 4.2 to 4.4. The different systems are then compared and their differences and similarities analysed in section 4.5. A summary of the different experimental findings is finally given in section 4.6

4.1 Matrix characterisation - experimental testing

4.1.1 Uniaxial compression tests results

Uniaxial compression tests performed as described in section 3.2.3.1 yield the two stress-strain curves shown on Fig. 4.1, allowing the identification of the compressive yield strength σ_c^y for both resins, of 80 MPa and 98 MPa at 0.05% strain for the TP80ep and TP175 epoxies, respectively.

The compressive elastic moduli are 11%, respectively 16.5% lower than those obtained from the tensile tests, which is a trend also observed in the literature for this class of materials [74].

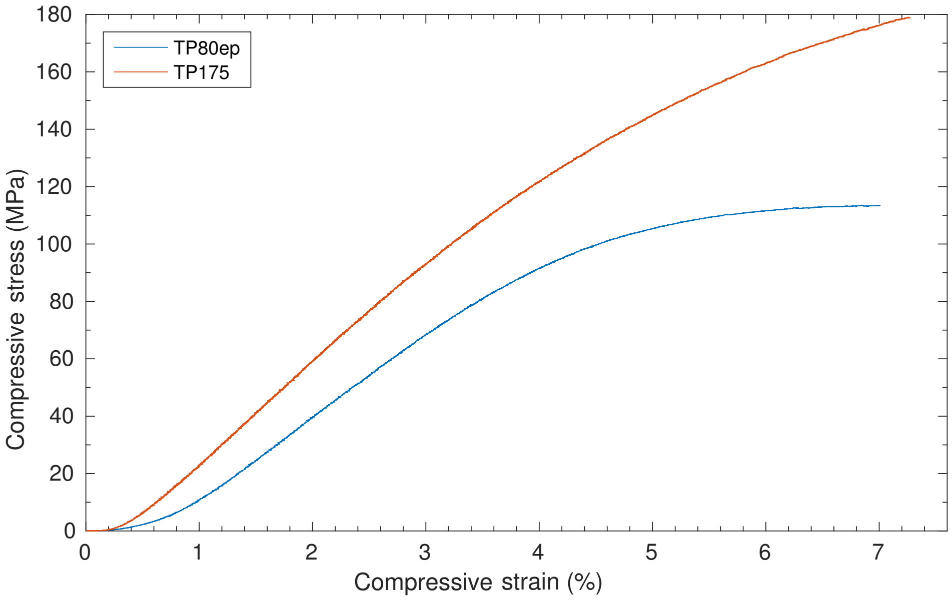

Figure 4.1: Bulk uniaxial compression stress-strain curve for both matrices

4.1.2 Nano-indentation test results

The nano-indentation curves obtained were useful to identify the ψ parameter of the Drucker-Prager models of the two epoxy matrices used in the present work, as will be discussed in chapter 5. The creep behaviour of both resins during the holding phase of the indentation can bee seen on Fig. 4.2. The difference in viscoplastic behaviour is shown on Fig. 4.3 where the respective normalized measured indentation moduli (EIT) are plotted as a function of the holding time for both resins, highlighting a much larger viscoplasticity in the TP80ep resin. This is typical of low temperature curing epoxies that are often undercured. The normalisation chosen simply divides the measured EIT of a given matrix subjected to a certain holding time by the EIT measured for that resin subjected to the longest holding time. Finally, a large difference in resin modulus is noticed when performing the nano-indentation in CFRP samples compared to neat resin, as shown on Fig. 4.4. An inverse identification scheme should be used to identify the underlying causes of this observed behaviour, such as load transfer to the adjacent stiffer fibres or size effects due to the resin confinement, but this fell out of the scope of the present work.

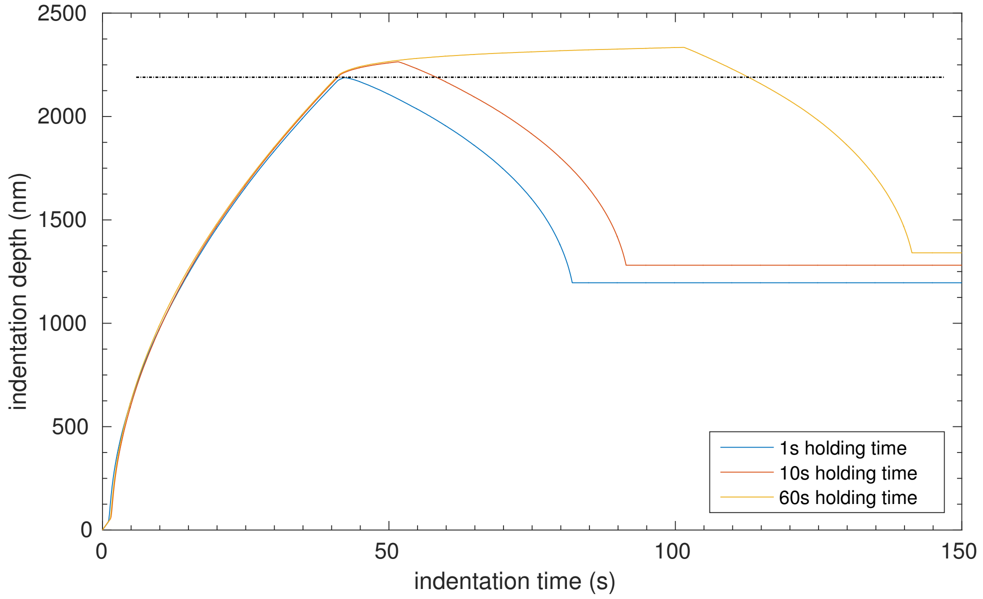

(a) TP80ep epoxy resin behaviour

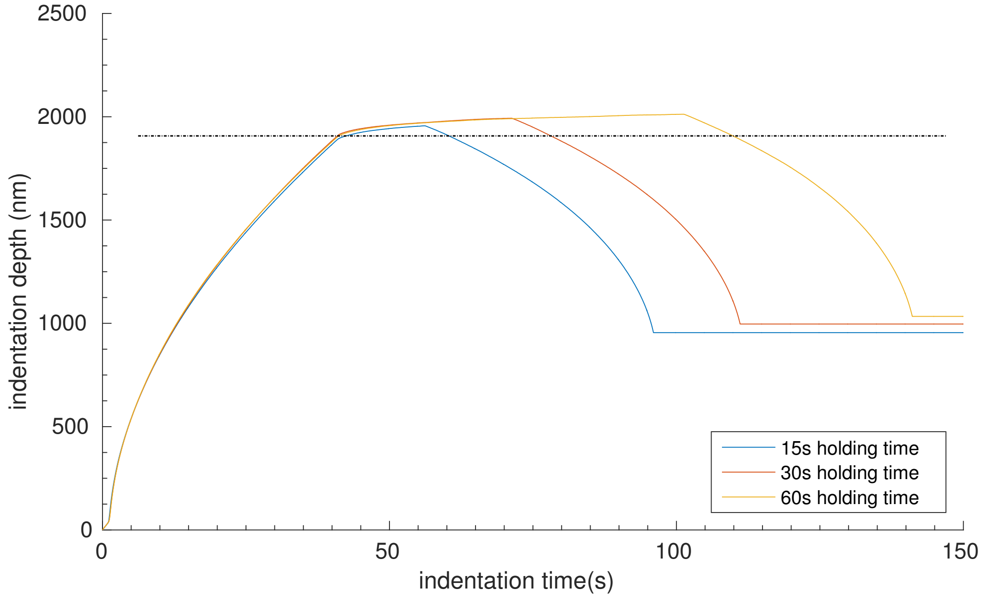

(b) TP175 epoxy resin behaviour

Figure 4.2: Creep behaviour of the resins during the nano-indentation holding phase. Dotted black lines show the indentation depth at the beginning of the holding phase

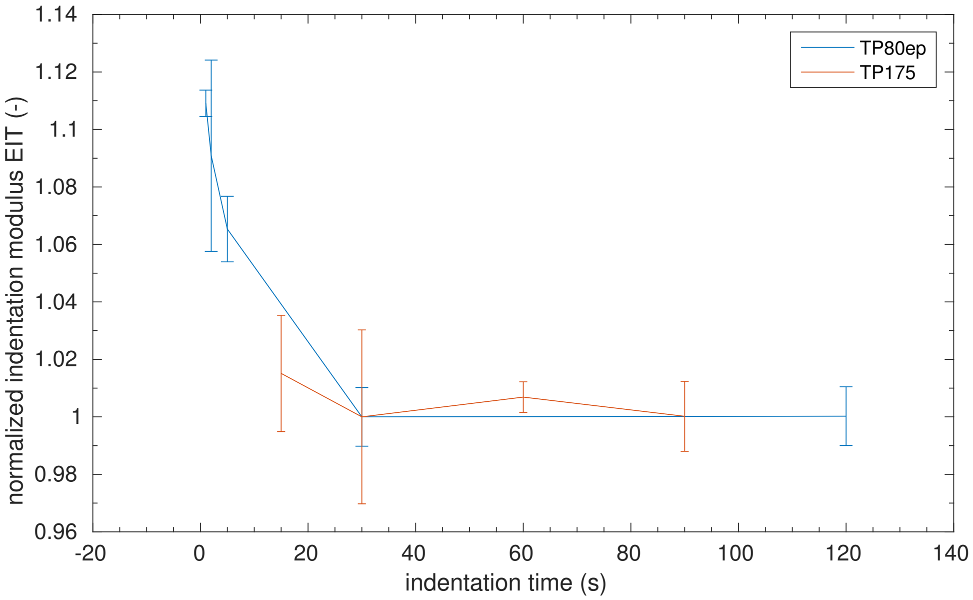

Figure 4.3: Viscoplastic behaviour of both resins. The indentation modulus (EIT) values measured are normalized for each resin by the EIT value measured for the longest holding time

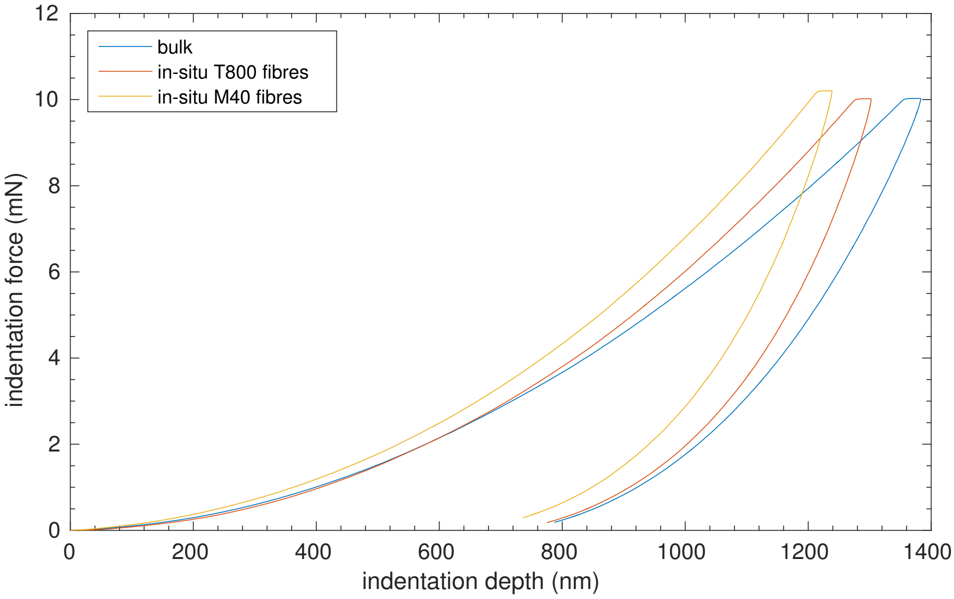

Figure 4.4: Difference between neat resin nano-indentation and in-situ CFRP measurements for TP80ep resin

4.2 M40JB-TP80ep system

4.2.1 Macroscopic UNT QI test results

4.2.1.1 Free edge damage observation

The typical development of free edge damage in M40JB-TP80ep composites can be found on Fig. 4.5, where a change in the damage mechanisms with decreasing ply thickness is observed. Samples made using the thickest (300 µm) plies exhibit the first transverse cracks between 0.3 and 0.32 % strain, which in a few instances appear simultaneously to free edge delamination and damage along the 90° plies. The tips of the transverse cracks then trigger a transverse cracking induced delamination (TCID) process from 0.5% strain until the failure of the specimen around 0.8 % strain. The specimen made with 150 µm plies have a higher onset of matrix transverse cracking at the free edge, first observed between 0.41% and 0.51 %. Some less extensive transverse cracking induced delamination then appears past 0.8% strain, but remains limited in length. The onset of transverse cracking is once again delayed in the samples made with 75 µm plies, with the first occurrences observed between 0.52% and 0.66%. However, this transverse cracking does not lead to any delamination with this ply thickness. Finally, for the samples manufactured using the thinnest (30 µm) plies, no damage can be observed at the free edge before the final failure. The post-mortem observation of selected samples, either using optical microscopy or in SEM as shown on Fig. 4.6 does not show any tell-tale signs of transverse cracking either. Although some smaller scale damage such as fibre-matrix debonding is not excluded from these observations, its detection cannot be performed at this magnification. It can also be observed that the transverse cracks at the free edges are inclined between 35° and 45° with respect to the loading direction, which can be attributed to the complex shear and transverse tensile stress state that develops in the 90° layers close to free edges.

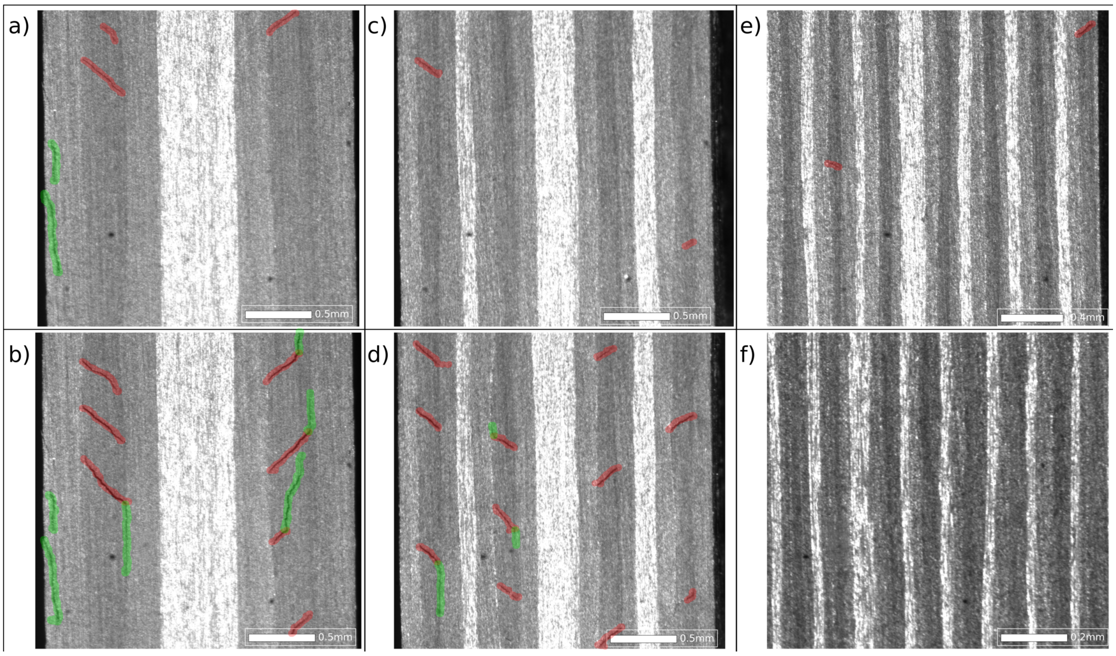

Figure 4.5: Optical in-situ micrographies showing the damage development at the free edges of selected M40JB-TP80ep specimen. Transverse cracking is highlighted in red and delamination in green. t=300µm at 0.31% strain in (a) and 0.55% strain in (b), t=150µm at 0.5% strain in (c) and 0.85% strain in (d), t=75µm at 0.9% strain in (e) and t=30µm at 1.05% strain in (f)

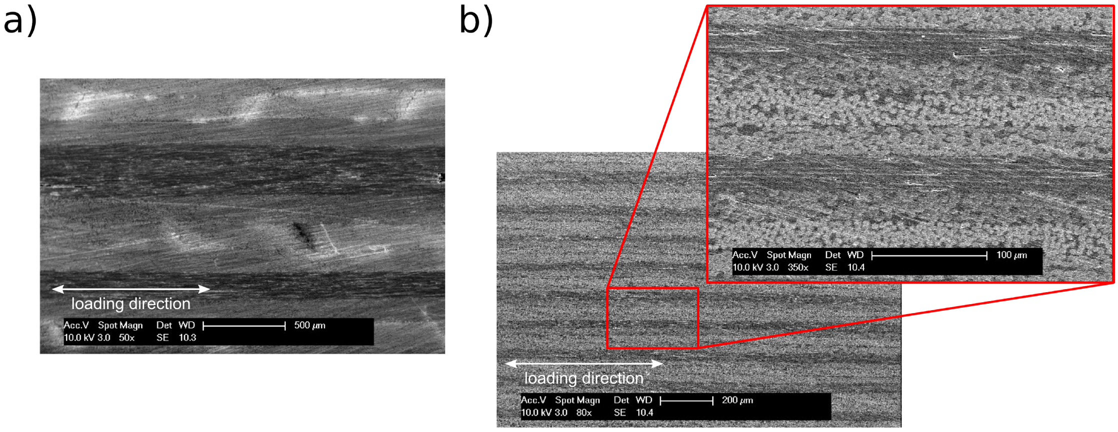

Figure 4.6: Post-mortem SEM picture of typical M40JB-TP80ep samples made with 150µm plies in (a) and 30µm ones in (b), both tested until failure. Transverse cracks in (a) are highlighted by a strong charging effect clearly observable using the SE detector, whereas no such sign is visible in (b).

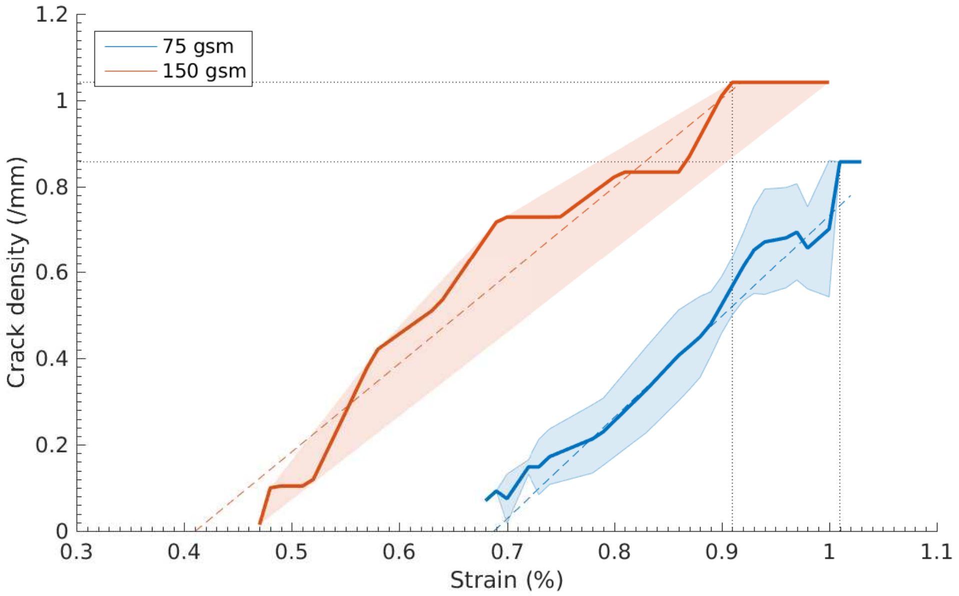

Figure 4.7: Free edge crack density for the M40JB-TP80ep system. The solid lines are interpolated average values for a given ply thickness and the light patch the corresponding standard deviation. The interrupted lines are a linear fit of the respective experimental averages. Doted black lines show the TC saturation and the strain at which it happens for all ply thicknesses. The t=30µm is not represented as no free edge cracks could be detected, nor is the t=300µm due to the occurrence of free edge delamination prior to TC onset in several samples

4.2.1.2 Acoustic emission

It is interesting to compare the strength and damage onset obtained by AE to the results in [5] on the same material batch, as shown on Fig. 4.8. The only controllable difference between both experimental data set is the strain rate used to perform the experiments. Most notably, the onset of damage defined by acoustic emission appears at a higher stress in the thicker (t=300µm & t=150µm) specimens tested at low strain rates (0.125 mm/min) than in the ones tested at a higher strain rate of 2 mm/min corresponding to the ASTM standard [98]. Considering the damage observations performed at the free edge in section 4.2.1.1 and in the bulk in section 4.2.3, this phenomenon can be explained by a larger stress relaxation due to viscoplastic flow in the highly loaded free edge region of the 90° ply region. The crack tip being blunted by this mechanism, the propagation towards the center of the sample is delayed and the AE onset is therefore measured at a higher stress. Indeed, for a viscoplastic material loaded with a controlled strain (as it is the case for 90° plies confined in the laminate), a lower strain rate leads to reduction of the apparent yield stress, which in turn promotes the development of plasticity in highly stressed regions and thus reduces stress concentrators. This rate dependent behaviour is not observed for lower ply thicknesses (t=75µm & t=30µm), which can be explained by a much lower sensitivity to edge damage with decreasing ply thickness, leading to a change in damage sequence. It should be noted that the two larger ply thicknesses are the only ones exhibiting significant free edge delamination. The fact that the strain-rate used for testing had such an effect on these ply thicknesses only further highlights the change in damage sequence with decreasing ply thickness, and the associated reduced sensitivity to free edge damage. Although the effect is much smaller, the opposite takes place for the low ply thicknesses. This can in turn be explained by the fact that without any significant free-edge effect, the creep experienced within the ply tends to locally overload the matrix, accelerating the localisation of damage.

If the measured ultimate strength of the tested laminates is marginally lower for all ply thicknesses loaded at a lower rate, the respective differences between the two data sets are lower than their standard deviation and no definite conclusion regarding the strain-rate effect on the ultimate tensile strength of the samples can thus be reached.

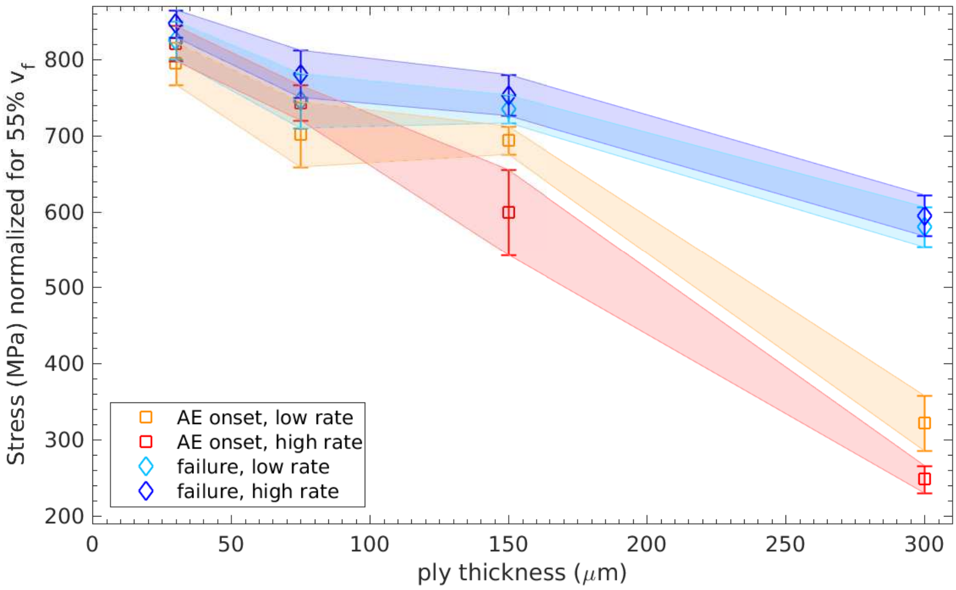

Figure 4.8: Comparison of the obtained AE and failure scalings (high rate values from [5])

4.2.1.3 Macroscopic damage scalings

The stress at which the first damage was observed at the free edge, as well as the onset of damage defined by acoustic emission and the ultimate strength of the different ply thicknesses tested are shown on Fig. 4.9. As no free edge damage could be observed for the samples made with 30µm plies until failure, the ultimate tensile strain value is reported instead of the free edge crack onset for this point. The high strain rate results have been used on Fig. 4.9 as they are less affected by the viscoplasticity of the matrix.

One striking feature of the comparison between the free edge observations and the acoustic emission measurements is the drastically different scaling exhibited by the free edge crack and the AE measurements. The observations performed at the free edge are in good agreement with a $\frac{1}{\sqrt{t}}$ scaling, as shown in green on Fig. 4.9. To the contrary, the onset of damage determined by acoustic emission increases much more linearly with decreasing ply thickness, as shown in red in the same figure. Furthermore, if the two onsets are nearly simultaneous for the thickest (t=300 µm) plies, the stress levels at which both are observed do change drastically for all smaller ply thicknesses, with free edge cracks appearing significantly earlier than the AE onset. Such a discrepancy between these two indicators can only be explained by different underlying mechanisms.

The hypothesis can be made that the behaviour of the samples manufactured using the thickest (t=300 µm) plies is dominated by the free edge, and that any damage appearing there immediately propagates into the bulk of the sample. This was confirmed by both the microscopy observation of sectioned samples (section 4.2.2) and the X-ray tomography of samples loaded to specific stress levels (section 4.2.3). With decreasing ply thickness, the onset of free edge damage is therefore not only delayed, but the ease with which free edge cracks can propagate towards the center of the sample is reduced. The onset of damage as recorded by AE therefore diverges from what is observed at the free edge, until a different failure mechanism such as translaminar fracture of the 0° plies becomes predominant. This is for instance the case for the t=30 µm samples, where the acoustic emission threshold is reached before free edge damage can be observed.

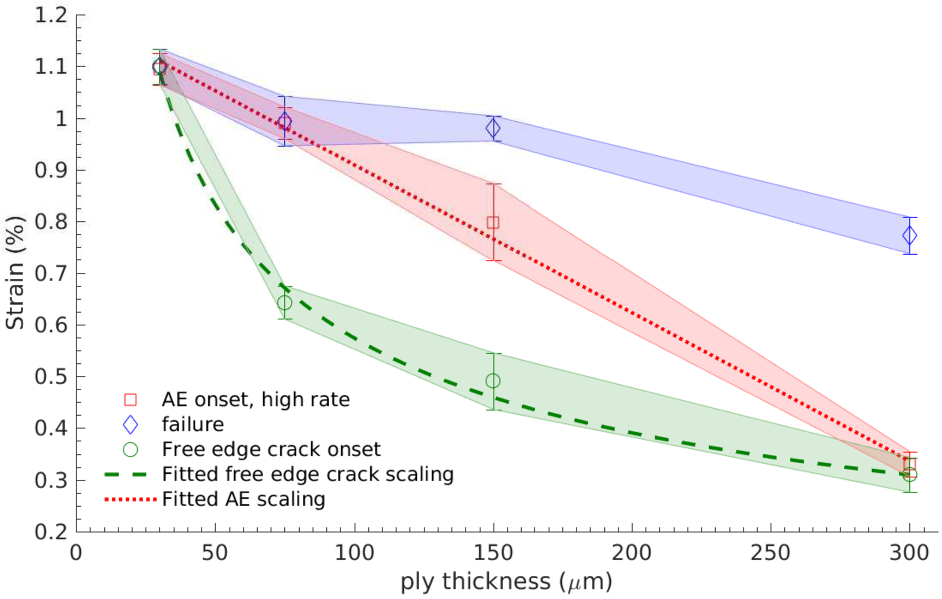

Figure 4.9: M40JB-TP80ep system: free edge crack and AE onset scalings with respect to ply thickness for QI samples

4.2.2 Sectioned samples (optical microscopy)

Partially loaded samples are observed ex-situ as described in section 3.3.4 to detect the presence of damage in the center of the samples. For the 150 µm ply specimen loaded at 500 MPa, before the AE threshold, no damage can be observed in the bulk of the sample, whereas the free edge shows obvious signs of transverse cracking, indicated in red on Fig. 4.10b. For a similar sample loaded at 700 MPa, past the AE threshold, the free edge reveals much more free edge damage as can be seen on Fig. 4.10a, with delamination (green) growing from the transverse cracks (red) and secondary damage (yellow) propagating into the ± 45° layers or growing within the 90° plies. At this stress, transverse cracks can be seen in the middle of the samples, and are superimposed in blue over the picture of the free edge. Finally, the sample manufactured with 75 µm plies is tested until close to the AE threshold without reaching it. It is shown on Fig. 4.10c, revealing a reduced free edge damage compared to the sample manufactured with 150 µm plies that is tested up to the same 700 MPa stress. Transverse cracking is the only observed damage mechanism, which is consistent with the observations made during the in the in-situ tests. Furthermore, no damage can be observed in the middle of this sample made with 75 µm plies. It could thus be established that the presence of transverse cracking in the bulk of the samples is linked to the crossing of the acoustic emission threshold as defined in this work.

It was noticed during the post-mortem (re)polishing of the sample's free edge that the crack density decreased markedly when grinding the free edge off, even within the first millimetre of gauge width. The transverse cracks in the bulk of the 150 µm sample are also truly transverse, normal to the loading direction, in opposition to their 45° angle at the free edge, due to the state of stress present there. Both these observations were confirmed by the X-ray tomography images discussed in section 4.2.3.

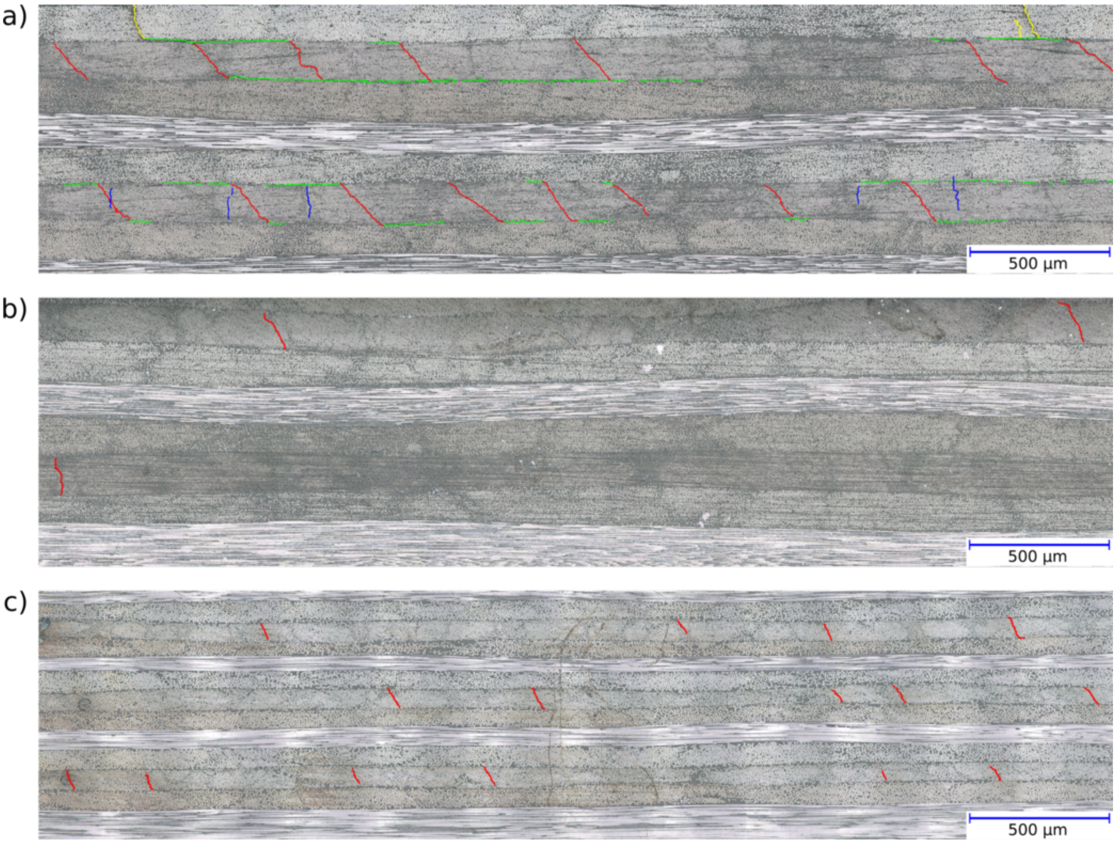

Figure 4.10: Free edge micrographs of the partially loaded specimen, t=150 µm tested at 700 MPa in (a), t=150 µm tested at 500 MPa in (b), and t=75 µm tested at 700 MPa in (c). Transverse cracks at the free edge are highlighted in red, the same damage type reaching the middle of the sample in blue, delamination in green and secondary damage in yellow

4.2.3 Tomography

Further evidence that the transverse cracks originate from the free edge of the samples and then propagate into the bulk at the onset of damage defined by AE is brought by the tomographic observation of partially loaded samples. These observations are performed for the selected ply thicknesses and loads described in Table 4.1. These loads are determined to always exceed the free edge transverse cracking onset, in order to ensure the presence of

Table 4.1: Summary of the different M40JB-TP80ep samples observed in X-ray tomography, indicating whether the AE threshold for their ply thickness had been exceeded or not, and whether transverse cracks were observed to propagate towards the center of the sample or not

sample ply t (µm)	Stress (MPa)	AE onset exceeded	TC propagation
150	500	no	no
150	700	yes	yes
100	550	no	no
100	650	no	no
100 (center slit) (2 samples)	650	no	no
100	700	yes	yes

damage, and either preceded or exceed the AE onset of damage, in order to highlight the mechanism responsible for the sudden increase of recorded AE energy.

Typical results can be seen on Fig. 4.11, representing a max intensity projection performed with Fiji [101] of all the slices laying in a typical 90° ply. It can be observed that in both the t=150 µm and t=100 µm samples, loaded to a stress inferior but close to the AE onset, no free edge crack propagates markedly into the bulk of the sample (Fig. 4.11a,b). To the contrary, in the samples of both 100 µm and 150 µm ply thicknesses loaded to a stress level superior to the acoustic emission threshold, transverse cracks clearly propagate into the bulk of the 90° plies (Fig. 4.11c,d).

In the case of the tests performed on samples with t=100 µm, there is a spread of only 50 MPa between crack confinement at the free edge and their propagation into the bulk. As the former had not reached the AE onset whereas the latter exceeded it, a very convincing case that the AE threshold corresponds to the propagation of free edge transverse cracks into the bulk can be made.

The presence of delamination is evident for the t=150 µm laminate tested at 700 MPa, but it is interesting to note that it does not extend far into the width of the sample despite a stress level very close to failure. This observation is compatible with delaminations originating from free edge transverse cracks (transverse cracking induced delamination) the extent of which remains limited to the vicinity of the free edges. Owing to the observation of the failure mode of these samples, it is most likely that the propagation of this delamination throughout the width of the sample is the last damage occurring and immediately leads to the complete failure of the specimen. No such delamination can be seen in the t=100 µm laminate despite having been subjected to the same stress level of 700 MPa. This corroborates the observations performed at the free edge reported in section 4.2.1.1.

Finally, it can be observed that the crack density in the bulk of the material at a given load is clearly smaller with the samples made of thinner plies (Fig. 4.11c,d).

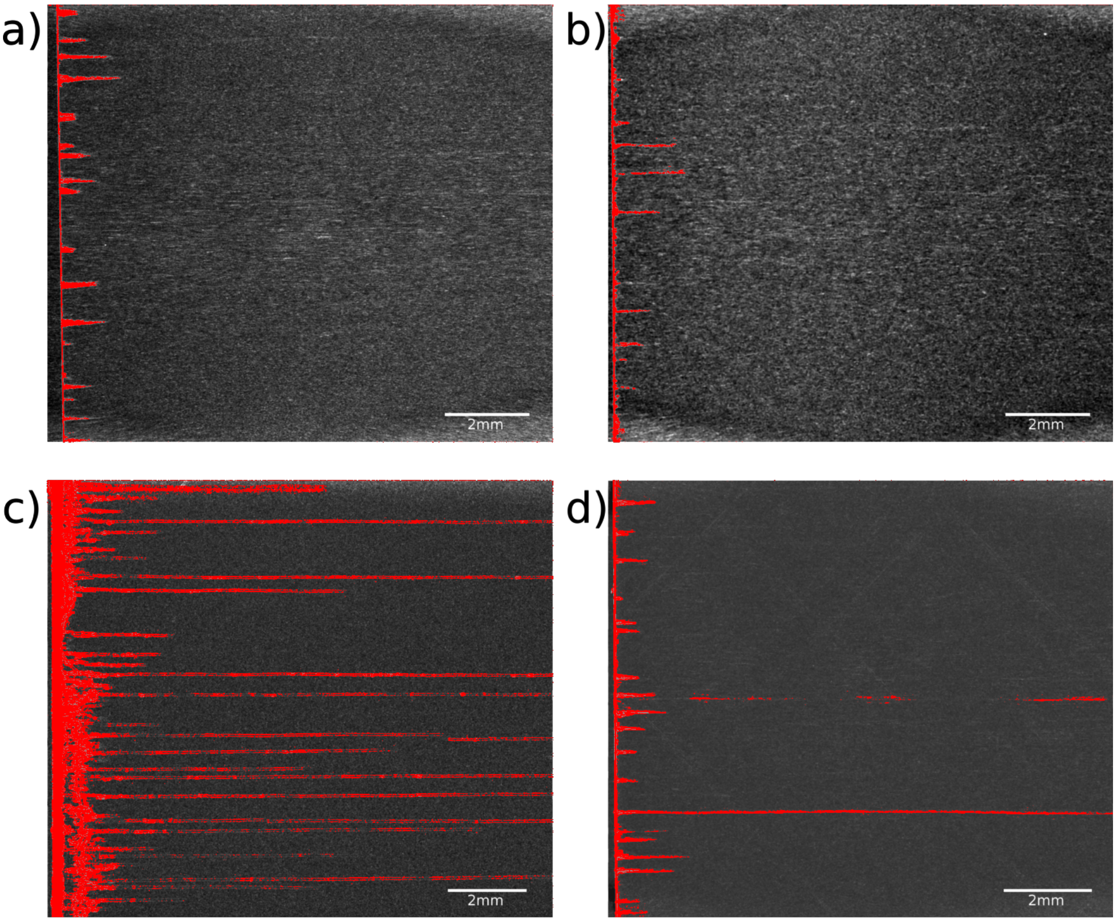

Figure 4.11: X-ray tomography of typical 90° plies of M40JB-TP80ep samples of: a) t=150µm tested at 500 MPa, b) t=100µm tested at 650 MPa, c) t=150µm tested at 700 MPa, d) t=100µm tested at 700 MPa.

The absence of damage originating from the center of the sample was examined by performing the infiltration process on a t=100µm sample loaded to 650 MPa like on Fig. 4.11c, but with a central slit machined in the sample after loading. The resulting image is shown on Fig. 4.12, and both the free edge of the sample and the slit edge can be clearly recognised. Transverse cracks are present at the free edge but no damage of any kind can be seen in the center of the sample.

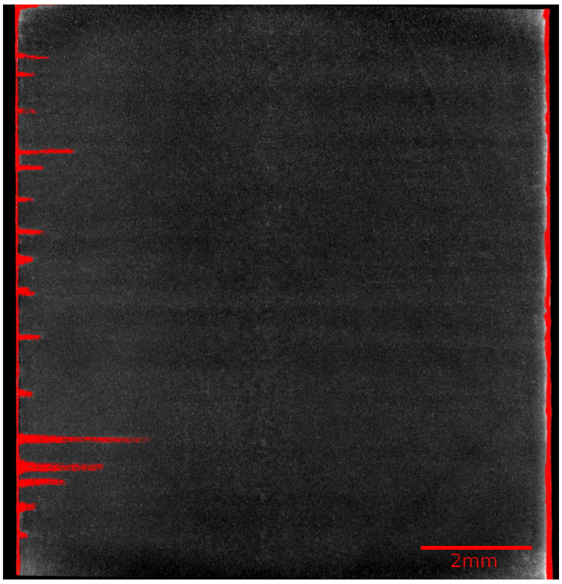

Figure 4.12: 90° ply of a 100 µm sample loaded to 650 MPa with a central slit machined before the infiltration process

4.2.4 Micro-UNT results

4.2.4.1 Mechanistic investigation

The same type of damage as observed on the full scale sample can be observed in the miniature micro-UNT tests, as shown shortly before specimen failure on Fig. 4.13. The free edge delamination and associated interlaminar debonding at the tips of transverse cracks, often seen in 300 µm full-scale samples, do show-up in the 150 µm case here, as seen on Fig. 4.13a. It must be mentioned that the samples made with plies of a 150 µm thickness did show some minor post-machining free edge damage despite extensive polishing, whereas this damage was absent of all samples manufactured with thinner plies. This means that the machining damage was much more pronounced in samples made with thicker plies, which corroborates the field reports of an improved machining quality with decreasing ply thickness. This behaviour can be related to the reduced sensitivity to free edge damage and delamination with decreasing ply thickness discussed previously.

The t=75 µm samples, as shown for instance on Fig. 4.13b do behave in a similar way to the t=75 µm and t=150 µm full scale samples, with the appearance of clear transverse cracking leading to interlaminar delamination at the crack tips. In the case of the 30 µm samples, just like in the full-scale ISM and post-testing SEM observations, no signs of matrix damage can be seen until specimen failure. However, the observation of these samples at a higher magnification than what is possible with the full-scale ones did reveal the presence of fibre-matrix debonding, as shown on Fig. 4.13c. This debonding was never observed in the micro-

UNT samples produced with thicker plies, which can be explained by the fact that the strain required to reach a debonding opening sufficiently large to be observed cannot be reached before localisation and specimen failure for the larger ply thicknesses.

4.2.4.2 Strength and specimen size effects

The damage sequence and change of mechanisms with decreasing ply-thickness observed in the micro-UNT experiments corroborate the observations performed at a higher scale. However, all samples failed much earlier than expected, as shown on Fig. 4.14.
If a general strength increase with decreasing ply thickness can once again be observed, it is not, however, of the same magnitude as for the full scale samples, but rather follows an asymptotic behaviour similar to the free edge damage onset scaling. The comparison of the micro-UNT failure stresses with the onset of free edge cracking in full scale samples is interesting, as it scales in a remarkably similar way with respect to ply thickness. Considering that the damage in the full scale samples are shown to originate from the free edges of the sample and propagate towards the center of the samples (see section 4.2.3), it is expected that a decrease in specimen width from 25 mm to 3 mm or 6 mm would reduce the strength of the micro-UNT samples. The fact that their respective failure stresses are only marginally higher than the free edge damage onset in the full scale samples corroborates this expectation, and leads to the conclusion that a strong specimen size effect is present when reducing the gauge width too far from the one recommended by the ASTM standard [98].

This specimen size effect coupled with the viscous behaviour of the matrix, which plays a major role during the holding phases required for the observations, were the two key reasons for the relative failure of the joint program initiated with D^{r} Federico Sket from IMDEA to perform in-situ observations of the crack propagation in the bulk of the material by using synchrotron tomography at the Paul Scherrer Institut. Its goal was to perform micro-UNT tests in-situ on small dogbone-shaped laminates similar to the ones tested for the part of the work described in this section. The same shortcomings were therefore revealed, with the very small samples size coupled to even longer holding times leading to an even quicker failure of the specimen, and no observable progression of TC into the bulk before specimen failure.

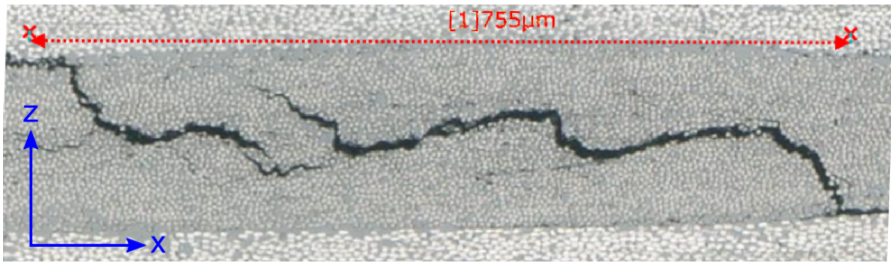

(a) t=150µm

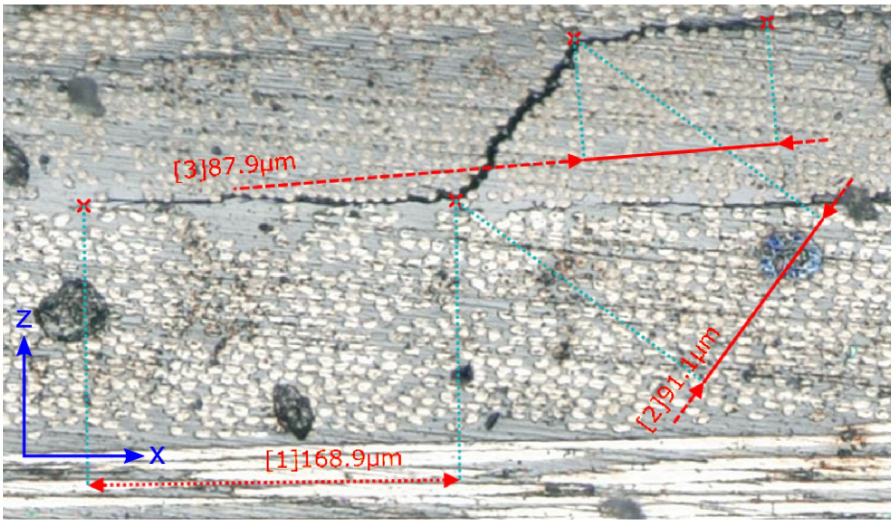

(b) t=75µm

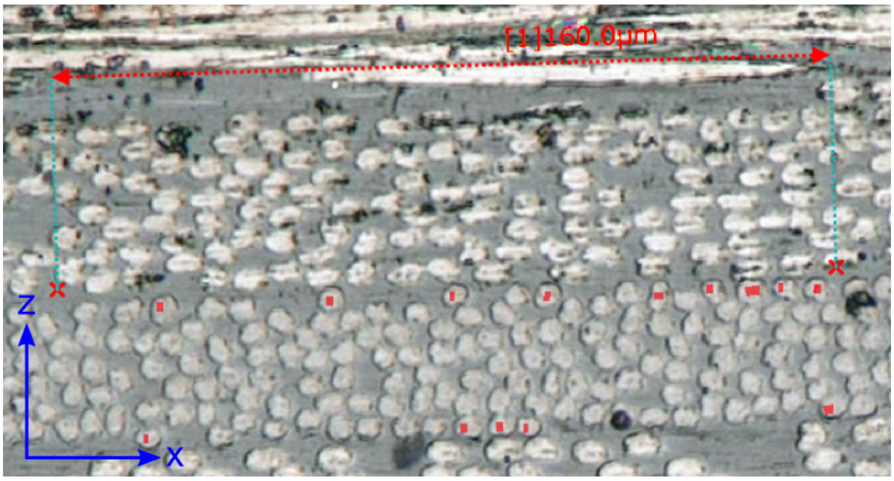

(c) t=30µm

Figure 4.13: Typical picture taken from the free-edge of micro-UNT samples close to failure. indicative measurements and dots highlighting debonded fibres shown in red. The loading direction is x and the stacking direction z.

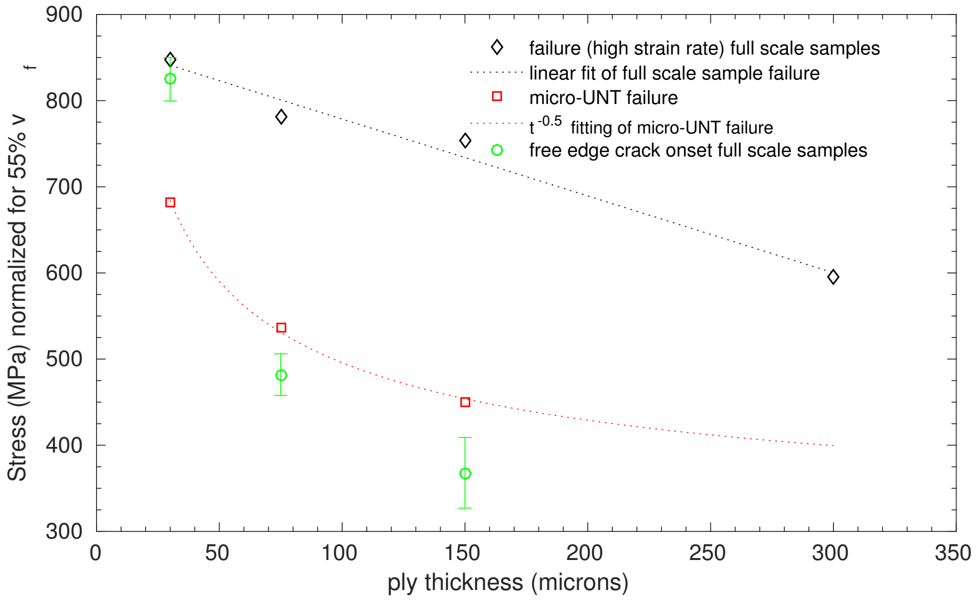

Figure 4.14: Failure stress comparison between micro-UNT (red) and full scale (black) samples. The free edge onset of the full scale samples (green) is added for comparison

4.3 T800-TP80ep system

4.3.1 Free edge damage observations

Typical free edge damage encountered in the T800-TP80ep system is shown on Figs. 4.15 and 4.16.

The t=300µm sample exhibit TC onset around 0.7% strain. unlike for the system using the same matrix with stiffer fibres, no free edge delamination is noticed prior to transverse cracking. Transverse cracking induced delamination appears aright after TC onset, though, growing in length as the TC density increases until about 1% strain. Further loading does not increase TC but increases TCID length until about 1.15% strain, where the extent of these delamination is so large that the outer ±45° degree layers are separated from the main laminate. From there on, the strain recorded obviously falls back to zero, but further delamination growth between the inner layers tend to split the 90° layers away from the laminate. Specimen failure due to the translaminar fracture of the 0° plies after large scale delamination has spread throughout the whole width and length of the sample eventually happens.

For the t=150µm samples, the onset of free edge TC is delayed until about 0.85% strain, and TCID do not appear before about 1.2% strain. From then on, TC density and TCID length both increase. From about 1.3% strain, some transverse cracking of the outer 45° plies is observed, leading to the longitudinal splitting of these layers away from the main laminate. The crack width observed is much smaller than in the t=300µm case, though, leading to the assumption that these delaminations do not propagate as far deep into the bulk of the samples. It must be said that the inner plies of the laminate do not split away one from the other at this point yet,

only the two outer layers do. TCID length and TC density both carry on increasing until about 1.45% strain when TC density saturates and the extent of TCID increases drastically, quickly separating inner layers and leading to failure around 1.6% strain.
The thinner samples, with t=75 µm, do not exhibit TC onset before about 1%, and some TCID appears at the TC's tips around 1.15% strain. It does however not increase much in length unlike for thicker plies, and remains constrained in close proximity to the TC's tip. Apart for some long TCID propagating between the outermost 45° degree plies and the 90° ones that are directly underneath them, the opening of which is strongly reduced compared to larger ply thicknesses, no TCID is observed until around 1.55% strain and only TC density increase is observed. From then on, TC density saturates and TCID growth is observed, but the opening of these delaminations remains once again very limited compared to what is observed in samples made with thicker plies. No complete ply separation is observed unlike the behaviour exhibited in laminates with t ≥ 150 µm. Finally, no damage of any kind is visible for samples with t=30 µm, as was the case with the other system using the same epoxy matrix.

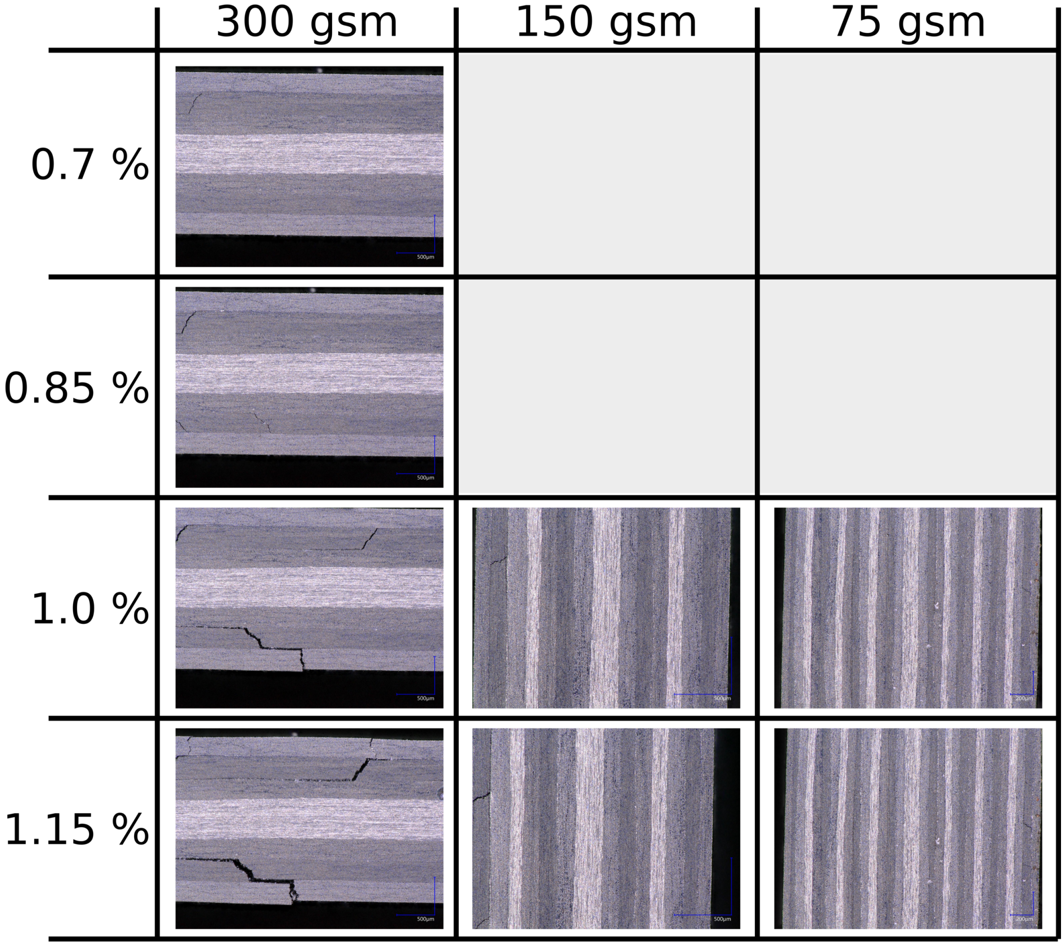

Figure 4.15: Optical in-situ micrographies showing the damage development at the free edges of chosen T800-TP80ep specimen at low strain.

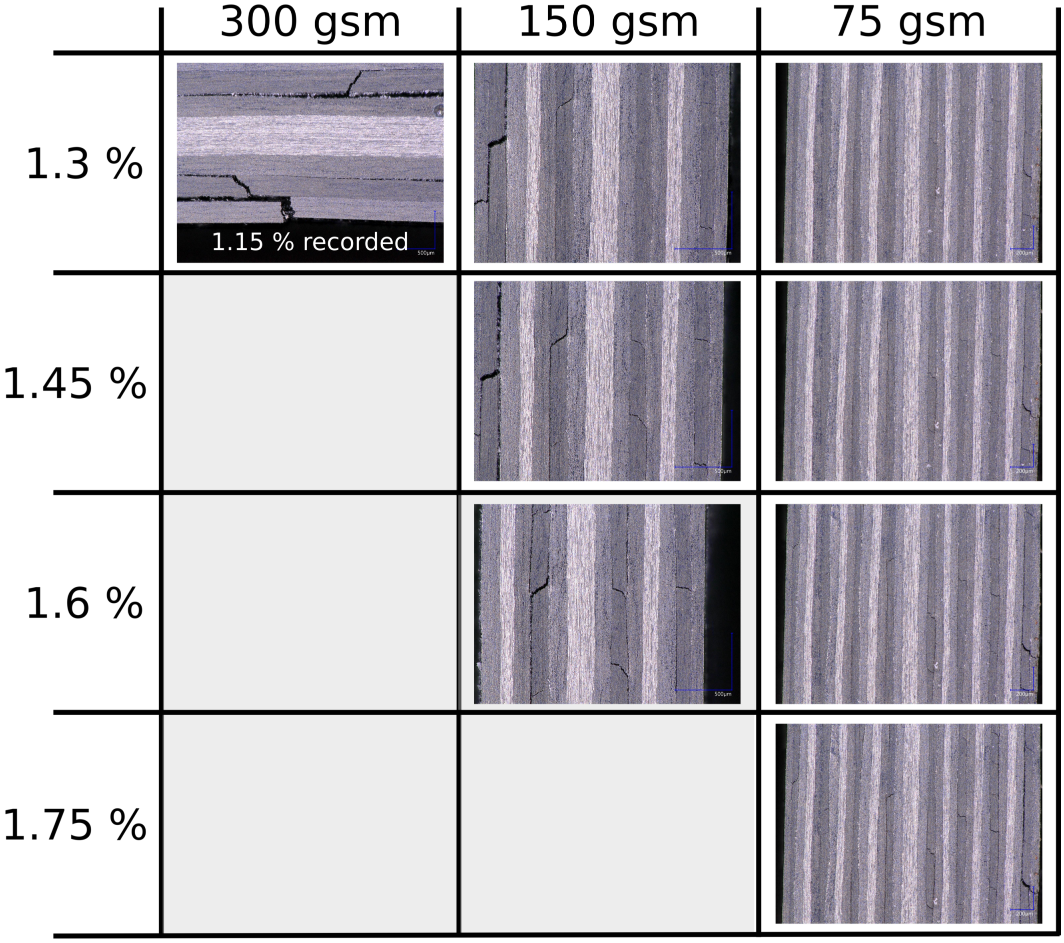

Figure 4.16: Optical in-situ micrographies showing the damage development at the free edges of chosen T800-TP80ep specimen at high strain. The recorded strain in the 300 µm samples does not increase past 1.15% due to the complete delamination of the outer plies and thus the separation of the strain gauge from the remaining load bearing part of the laminate

When plotting the average crack density variation with increasing applied strain, as shown on Fig. 4.17, it can be observed that the TC density rate of increase is remarkably similar for all ply thicknesses, and can be approximated by a linear fitting. Using the intercept of the linear fitting of crack density curve as an indicator, it can be observed that the strain at onset of free edge TC increases from 0.6% for t=300 µm specimen to 0.95% for t=75 µm specimen. If a saturation of transverse cracks is visible for the 75 µm samples, it is not the case for the two larger ply thicknesses. This is probably due to the absence of large delamination appearing during strain increase for the 75 µm samples. The 30 µm samples are not represented as no definite transverse cracks could be identified before specimen failure.

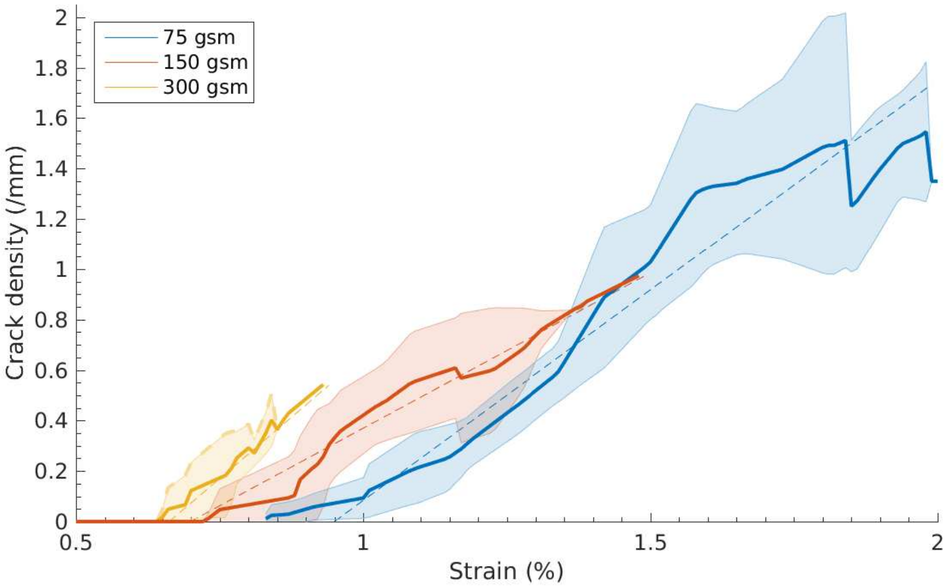

Figure 4.17: Free edge crack density for the T800-TP80ep system. The solid lines are interpolated average values for a given ply thickness and the light patch the corresponding standard deviation. The interrupted lines are a linear fit of the respective experimental averages

4.3.2 Macroscopic UNT QI test results

The tested specimens exhibit a strong ultimate strength scaling, as shown on Fig. 4.18. Comparing it to results previously obtained on a different batch of this material [7], a significant discrepancy is visible. Part of the explanation is due to the choice of T800S fibres for the 300 µm, 150 µm and 75 µm specimen used in this work, whereas T800H fibres were used in the previous batch, as is the case with the 30 µm samples of the present work. In order to take this into account, a tentative normalization by the relative fibre strength is proposed. The specimen manufactured with T800S fibres (2% failure strain) therefore see their measured ultimate tensile strain reduced by a factor of $\frac{1.77}{2}$ to approximate their response had they been manufactured with T800H fibres which have a 1.77% failure strain. This normalized strength is plotted in dotted lines on Fig. 4.18. The remaining noticeable increase in strength compared to prior measurements can be explained by two factors: a strain rate effect due to the viscoplastic behaviour of the resin, or a batch effect, attributed to the slightly different resin formulation used in this batch, the exact consequences of which were not known by the manufacturer.

A single sample of the batch used for this work with a ply thicknesses of t=75 µm was tested at a higher strain rate of 2 mm/min until failure, which happened at 1.82% strain, namely below the standard deviation of the tests performed at the slower 0.125 mm/min used for free edge ISM. An insufficient number of experiments were performed to be statistically representative, but no further samples were left to carry it out. However, it is most likely from this test that the

difference in testing strain rate had a significant influence on the results.
It is interesting to note that the strength of t=300µm samples using the new resin formulation is in good agreement with the values of the t=268µm samples of the previous batch, despite the difference in strain rate and irrespective of the normalisation due to fibre modulus. This points towards the importance of the viscoplastic flow on stress relaxation in the highly loaded free edge region in preventing damage progression into the bulk of the sample for intermediate ply thicknesses, whereas at very large ones, where the damage present at the free edge immediately propagates into the bulk, this plays no role. The much more noticeable effect of strain rate changes exhibited in this system compared to the M40JB-TP80ep material is certainly due to the much larger strains reached in the resin due to the change of fibres.

Comparing free edge TC onset to AE onset, the former is shown to precede the latter for all ply thicknesses used as was the case for the M40JB-TP80ep material. Their respective scaling with respect to ply thickness are however much more similar to each other than in the M40JB-TP80ep system. This can be explained by a similar propagation of the free edge damage into the bulk for all ply thicknesses, unlike the marked change in behaviour noted for the previous material.

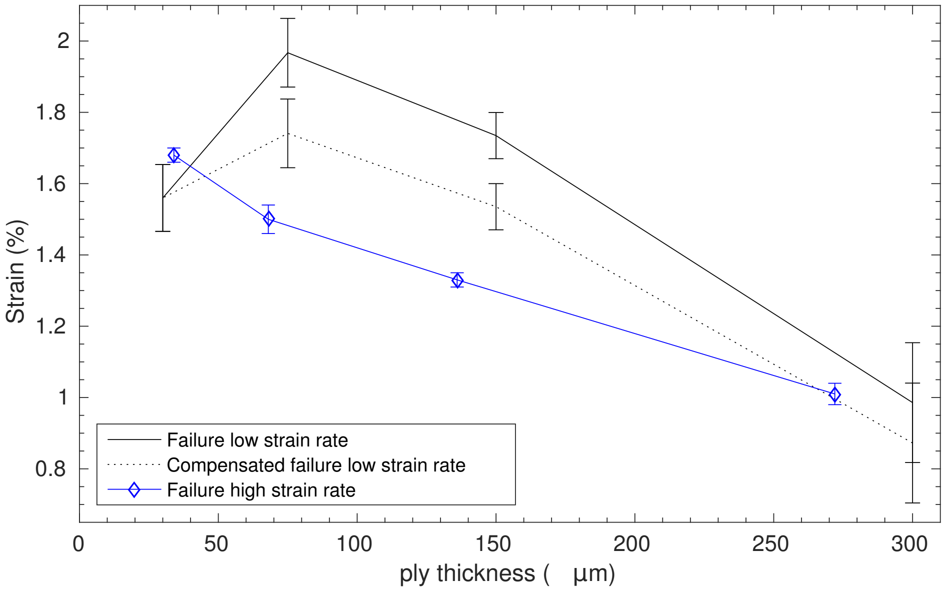

Figure 4.18: T800-TP80ep system comparison between failure strains when subjected to high strain rate and low strain rate. The dotted line accounts for the difference in fibre ultimate strain between batches tested at high and low strain rates.

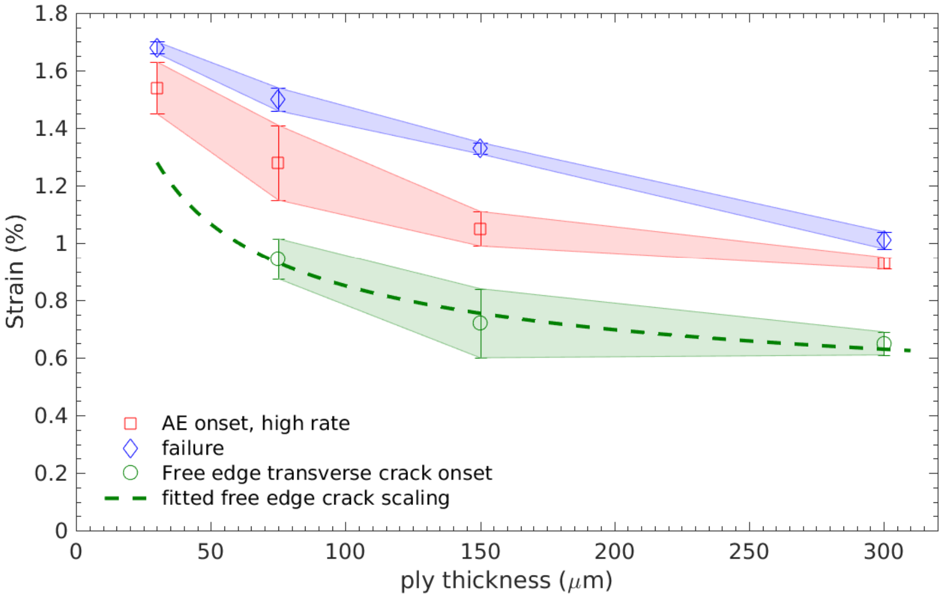

Figure 4.19: T800-TP80ep system free edge crack and AE onset scalings with respect to ply thickness. AE and strength values are taken from high strain rate experiments

4.3.3 Tomography

The tomographic imaging of selected T800-TP80ep samples loaded to predefined level allows once again some interesting comparisons to be drawn. Their loading is performed at low strain rate, in order to compare the propagation in the bulk of the material to free edge damage.

Fig. 4.20 shows the damage present in a typical 90° ply of selected specimen. The specimen on the left have been loaded until a stress inferior to the onset of damage defined by AE, whereas those on the right have been loaded until a stress superior to it, respectively within its standard deviation for the t=75µm sample due to the very small margin between this threshold and failure. Comparing the damage states before and after AE for both the t=150µm and t=75µm, it can be observed that the AE onset corresponds to the propagation of the free edge transverse cracks into the bulk. However, in contrast with laminates using M40JB fibres with the same resin, the transverse crack propagation at the AE onset is not fully developed. The large difference between the ultimate strength recorded between the batch tested and the one on which this AE threshold was defined, coupled with the low strain rate used for the loading of the samples used in tomography means that the AE threshold might have been different then expected. Due to the change of tab materials, AE could not be monitored during the partial loading of these samples, and no definite answer can thus be given. Despite this, a clear increase of crack propagation can be observed for the samples loaded at a higher stress level, with free edge delamination in the case of the t=150µm sample shown on Fig. 4.20d. A clear decrease of transverse crack propagation with decreasing ply thickness for a given stress level

is also observed when comparing the t=75 µm sample shown on Fig. 4.20a and the t=150 µm one shown on Fig. 4.20d, both loaded until 680MPa.
From the discussion above, it must be noted that although the exact strain at which full TC propagation is achieved is not perfectly identified here, the general damage progression and associated mechanisms remain the same as the ones observed for a similar ply thickness with the M40JB-TP80ep system

The ultimate strength of the t=300 µm samples being in good agreement with the t=268 µm samples of the previous batch as discussed above, it is interesting to note that the expected fully developed transverse crack propagation at higher stresses than the AE threshold is validated for this ply thickness, as seen on Fig. 4.21. It might suggest that the AE damage onset of damage for samples made with this new batch of material would have been higher than the one of samples made with the previous batch if it could have been measured.

A large delamination propagating as deep as the transverse cracks is also observed, which is in good agreement with the observations performed at the free edge. This demonstrates a reduced sensitivity of samples made with thinner plies to transverse cracking induced delamination, as the more heavily loaded t=150 µm and t=75 µm samples shown on Fig. 4.20 show much less, respectively no delamination in the bulk of the material.
Finally, and as was the case for the M40JB-TP80ep material, no sign of damage in the bulk of t=30 µm samples could be observed, even at stresses very close to specimen failure.

Considering the noticeable effect of strain rate, a comparison is made between two 150 µm samples loaded at the same stress level using different strain rates. As shown on Fig. 4.22, a larger amount of delamination and less transverse cracking constrained close to the free edge can be observed when decreasing the loading rate. As the damage extent at a given applied stress is notably changed with varying loading rate, it is indeed possible that the stresses at the tip of propagating transverse cracks is reduced by viscoplastic flow, thus delaying their critical propagation into the bulk and consequently contributing to a higher onset of damage as measured by acoustic emission.

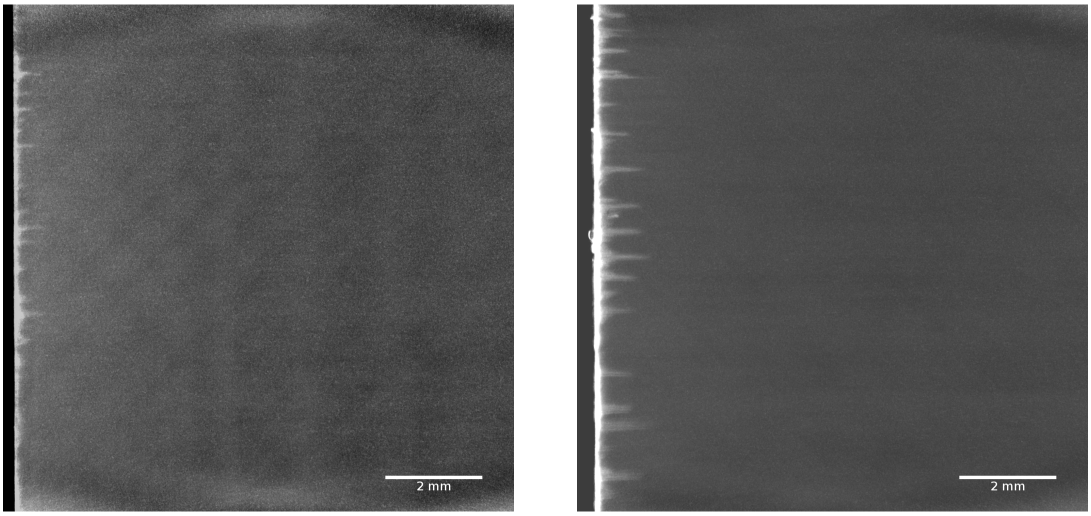

(a) 75 µm sample loaded until 680 MPa (pre-AE)

(b) 75 µm sample loaded until 740 MPa (post-AE)

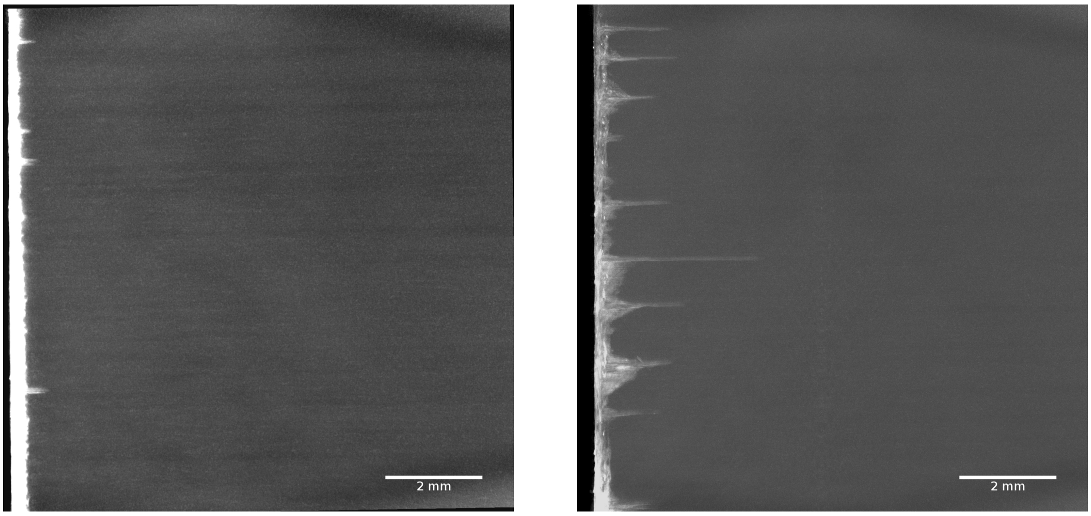

(c) 150 µm sample loaded until 440 MPa (pre-AE)

(d) 150 µm sample loaded until 680 MPa (post-AE)

Figure 4.20: Maximum intensity projection of a 90° ply region in selected T800-TP80ep specimen, highlighting the correlation with the AE threshold.

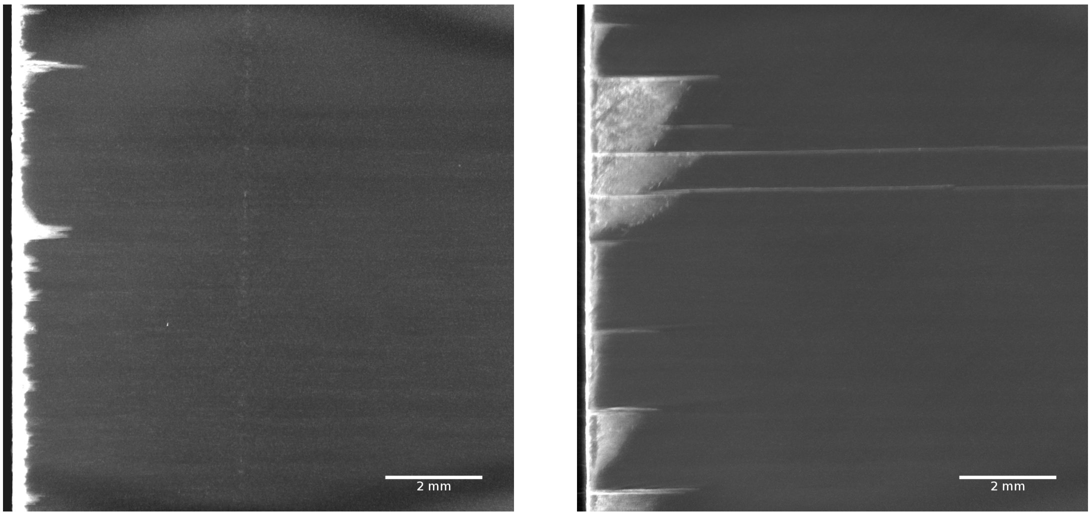

(a) 300 µm sample loaded until 400 MPa (pre-AE)

(b) 300 µm sample loaded until 526 MPa (post-AE)

Figure 4.21: Maximum intensity projection of a 90° ply region in two 300 µm T800-TP80ep specimen loaded until different stress levels

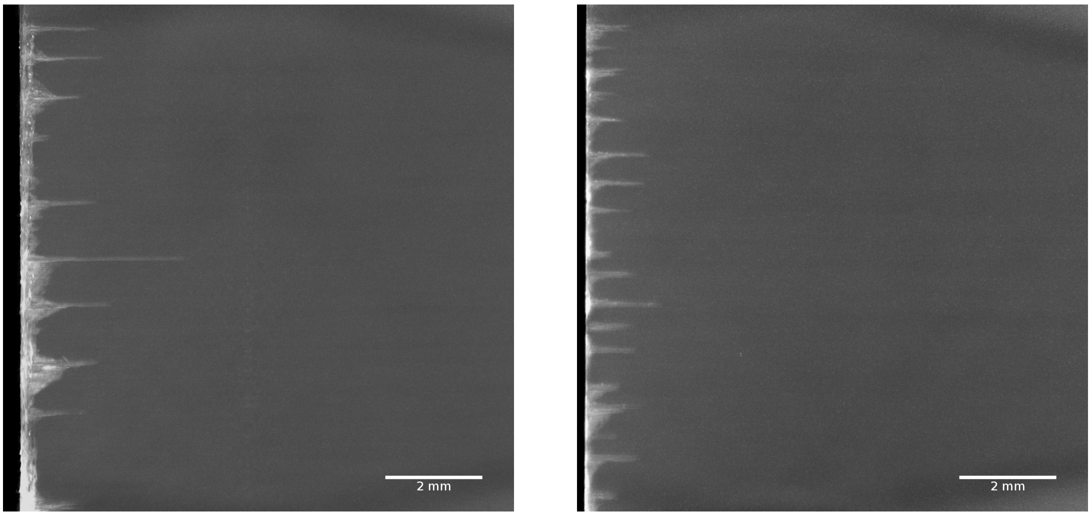

(a) specimen loaded at 0.125 mm/min

(b) specimen loaded at 2 mm/min

Figure 4.22: Maximum intensity projection of a 90° ply region in two 150 µm T800-TP80ep specimen loaded until 680 MPa at different strain rates

4.4 T800-TP175 system

4.4.1 Free edge damage observations

The typical damage development at the free edge of selected T800-TP175 samples is shown on Fig. 4.23 for strains ranging from 0.6% to 1.2%, and on Fig. 4.24 for those ranging from 1.4% to 1.93%. It can be observed that the generic mechanisms as well as their sequence and changes with respect to ply thickness are in agreement with the observations made for both systems using the TP80ep resin. In the thickest (t=268 µm) specimen, transverse cracks and in a few instances free edge delaminations in the resin rich zones between the restacked 90° layers appear around 0.55% strain. As low as 0.7% strain, transverse cracking induced delamination is triggered at the tips of the formed transverse cracks or where the free edge delaminations have grown up to the 90° ply interface. Secondary damage in the ±45° layers also starts appearing in this strain range. Whilst the transverse crack density increases with increasing strain, the delaminations also grow in size until one of the latter fully propagates through the width of the sample between 1.0% and 1.2%, leading to a specimen final failure due to longitudinal propagation of delamination cracks through the whole gauge length. The fact that the delamination has propagated throughout the whole width of the sample before failure could be asserted both in the microscopy images taken in-situ, where the part of the sample on one side of the delamination would exhibit a different displacement field as the one on the other side, as well as with the recorded strain values which would start to strongly diverge from the recorded machine displacement.

The samples made with plies of t=134 µm do start to exhibit transverse cracks around a similar strain to the t=268 µm samples, though no delamination is present simultaneously in this case. It only starts appearing as transverse cracking induced delamination around 0.75% strain, but remains much more limited in length than in the thicker samples. Some limited secondary damage in the ±45° layers also forms at the tips of some of these delaminations when they are present at the interface between the outermost ±45° layers of the laminate and the 90° layer directly underneath them. As these delaminations slowly grow, they start to coalesce around 1% strain, and carry on growing simultaneously with an increase of transverse crack density until specimen failure around 1.65%, without visibly splitting the whole sample as is the case in the thicker samples. The final failure type of these t=134 µm samples being dominated by delamination, it can be concluded that the final specimen failure must be caused by a sudden propagation of one of the larger delamination throughout the with of the samples, in a process that is quick enough to be invisible during the ISM observations.

In the case of the t=67 µm samples, the TC onset is delayed to around 0.8%. The small TCID appearing at the tips of some of the formed transverse cracks from 1.4% strain onwards remain very limited in length, and although they tend to grow and coalesce until specimen failure around 1.8%, their opening never grows as it does in the case of the samples made with

134 µm and 268 µm plies. Considering that a brittle transverse fracture failure of the samples is encountered at this ply thickness instead of the delamination dominated one of the samples made with thicker plies, it can be concluded that the free edge delamination observed for this ply thickness remains constrained at the free edge and never propagates throughout the width of the observed samples.

The transverse cracking onset observed in the case of the samples made with 34 µm plies is significantly delayed until over 1.1% strain. Unlike the two systems using the TP80ep resin, a clear transverse crack density increase can then be observed until the final failure of the samples at a strain statistically equivalent to the translaminar fracture of the 0° plies, without any sign of free edge delamination anywhere on the observed free edges.

Averaged transverse crack densities for all the observed samples of given ply thicknesses are reported on Fig. 4.25 together with their linear fitting. Considering the good agreement obtained by such a fitting, the strain at onset of free edge damage can be obtained as the intersection of the fitted curves of the respective crack densities with the abscissa. It can be observed that the rate of increase of crack density for the three thinnest ply thicknesses is quite similar. This highlights well the difference in damage mechanism encountered, as the 268 µm samples in which delamination is dominant exhibit a lower rate of increase in TC density with increasing strain, which could be attributed to an interaction between transverse cracks and delaminations. Furthermore, a clear TC density saturation can be seen for all ply thicknesses but the thinnest one, which is consistent with the translaminar fracture of the 0° plies taking place before full TC development is achieved. In the case of the 34 µm sample, as the transverse crack saturation is not reached before specimen failure, the ultimate tensile strain of the samples is used instead in the figures reporting TC onset.

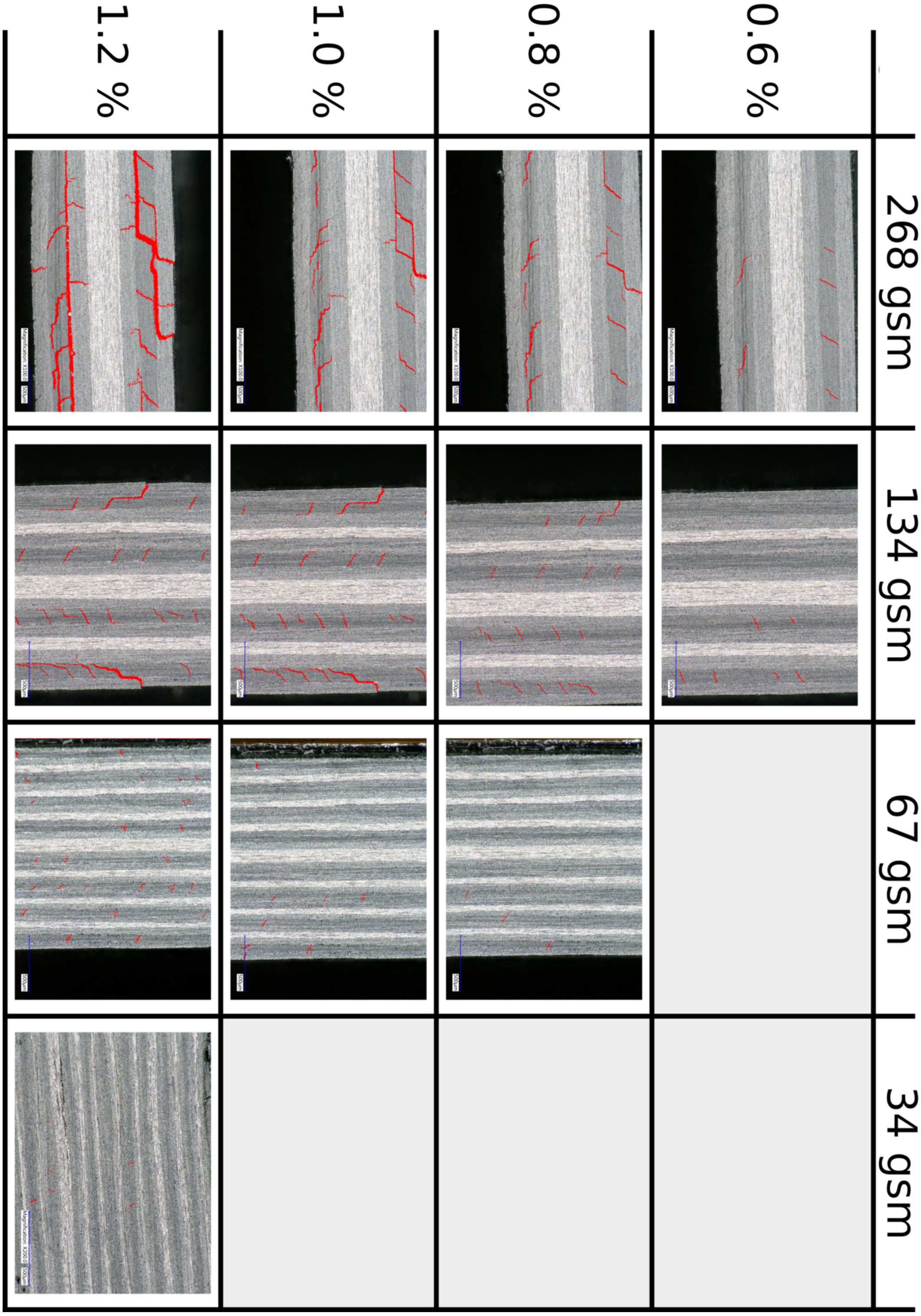

Figure 4.23: Optical in-situ micrographies showing the damage development at the free edges of chosen T800-TP175 specimen at low strain. Transverse cracking and delamination are highlighted in red.

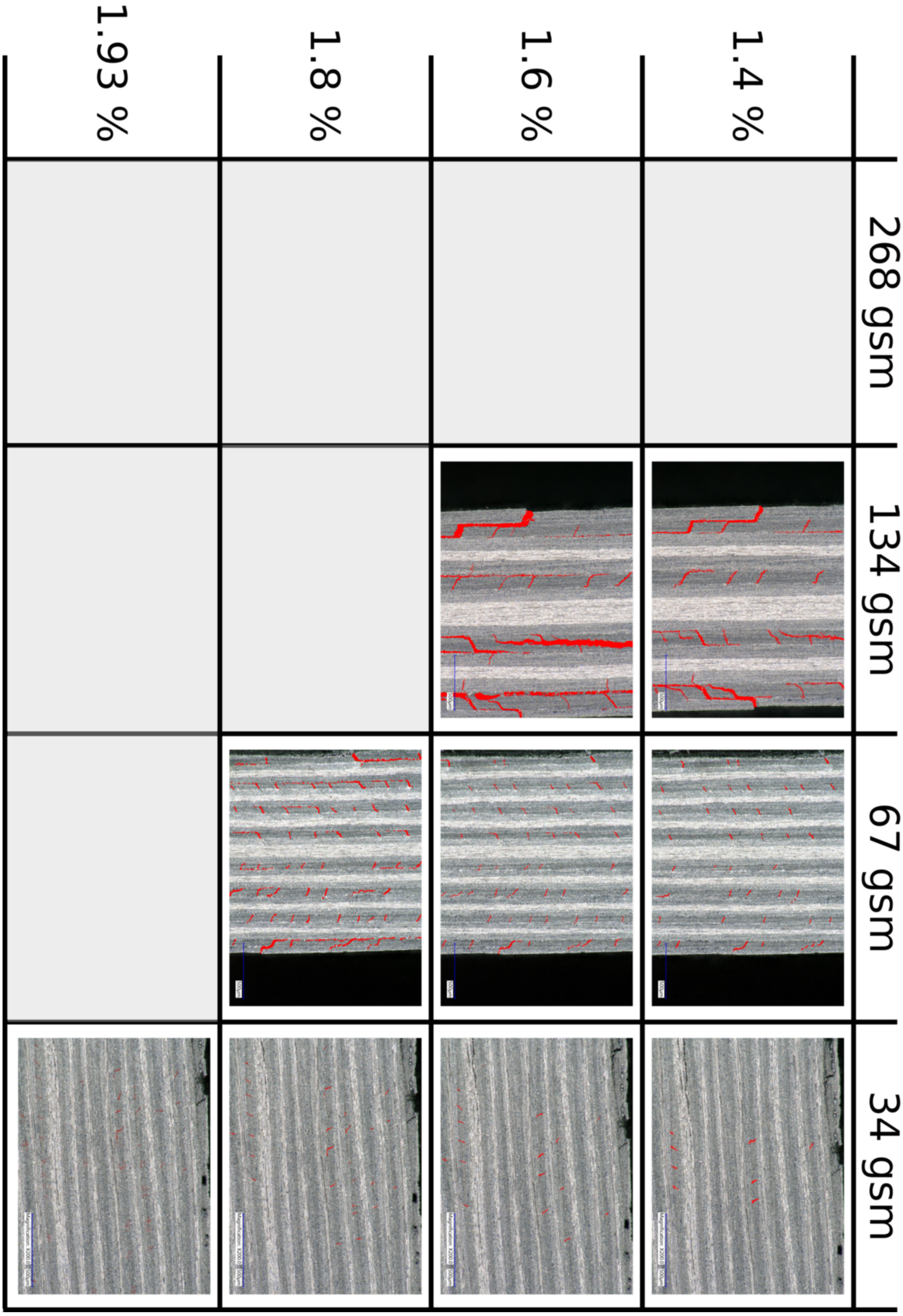

Figure 4.24: Optical in-situ micrographies showing the damage development at the free edges of chosen T800-TP175 specimen at high strain. Transverse cracking and delamination are highlighted in red.

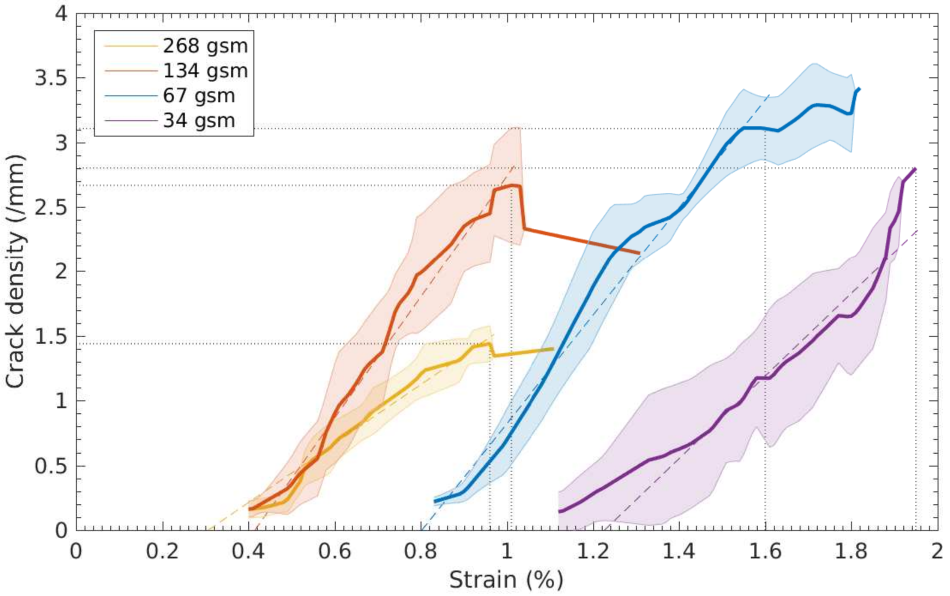

Figure 4.25: Free edge crack density for the T800-TP175 system. The solid lines are interpolated average values for a given ply thickness and the light patch the corresponding standard deviation. The interrupted lines are a linear fit of the respective experimental averages. Dotted black lines show the TC saturation and the corresponding strain for all ply thicknesses.

4.4.2 Macroscopic UNT QI test results

The free edge crack onset, AE onset and failure of the T800-TP175 samples are reported on Fig. 4.26. The free edge damage onset, identified on Fig. 4.25, can once again be fitted quite accurately by a $1/\sqrt{t}$ fitting, whereas the onset of damage obtained by AE is once again much more linear. As discussed in chapter 3, the AE measurements and free edge damage observations were taken from different samples, made with the same batch of prepreg, which makes their comparison valid despite the fact that they are not simultaneous observations as was the case with the M40JB-TP80ep system. The very large strain difference between both onsets proves once again that different damage mechanisms are at play at the free edge and in the bulk of these samples, their behaviour depending on ply thickness.

It is interesting to note that the strains at saturation of free edge TC, obtained from Fig. 4.25, showed an excellent agreement with the AE onset for the three ply thicknesses where transverse cracking or translaminar fracture of the 0° plies dominated the damage behaviour of the samples. In the t=34µm case, the latter was used instead of TC density saturation on Fig. 4.25 as the former was never reached. The AE onset of damage appears at a lower strain than the TC saturation for the thickest plies, indicating that the large delamination propagation observed at the free edge must have produced enough acoustic energy to reach the AE threshold before TC saturation was reached at the free edge.

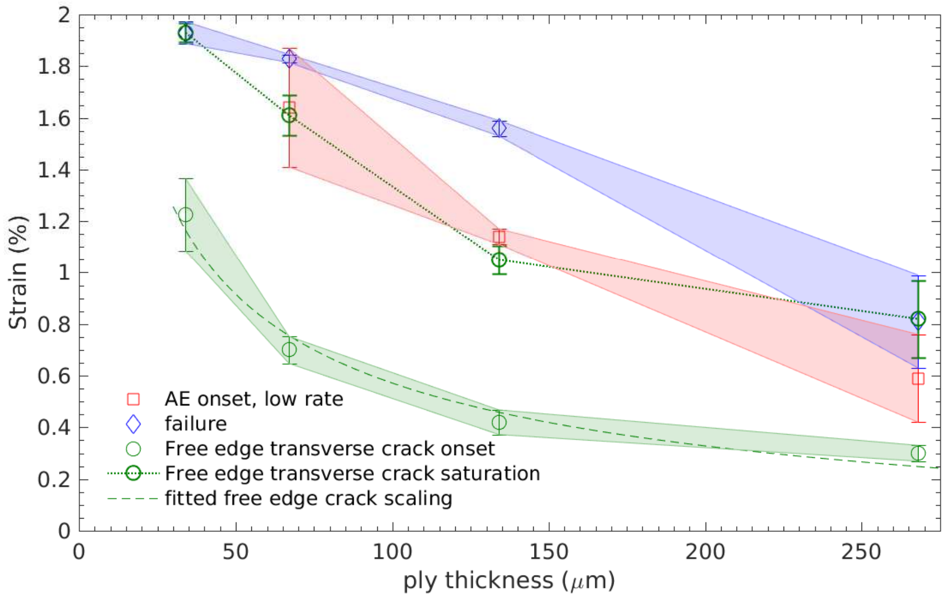

Figure 4.26: T800-TP175 system free edge crack and AE onset scalings with respect to ply thickness. The strain at which the transverse crack density saturates is superimposed to the AE onset for comparison

4.4.3 Tomography

The loading of the samples used for tomography was performed at low strain rate, in order to compare the propagation in the bulk of the material to free edge damage. No simultaneous AE recording was performed, and hence the AE threshold is only approximative. The t=268 µm samples exhibit no damage in the bulk shortly after TC onset at the free edge. At a stress level corresponding to the appearance of TCID at the free edge, and before TC density saturation, transverse crack start growing from the free edge into the bulk, as shown on Fig. 4.27a, eventually leading to fully propagated transverse cracks and large delamination zones at the interface between the 90° and the ±45° layers, as can be seen on Fig. 4.27b.

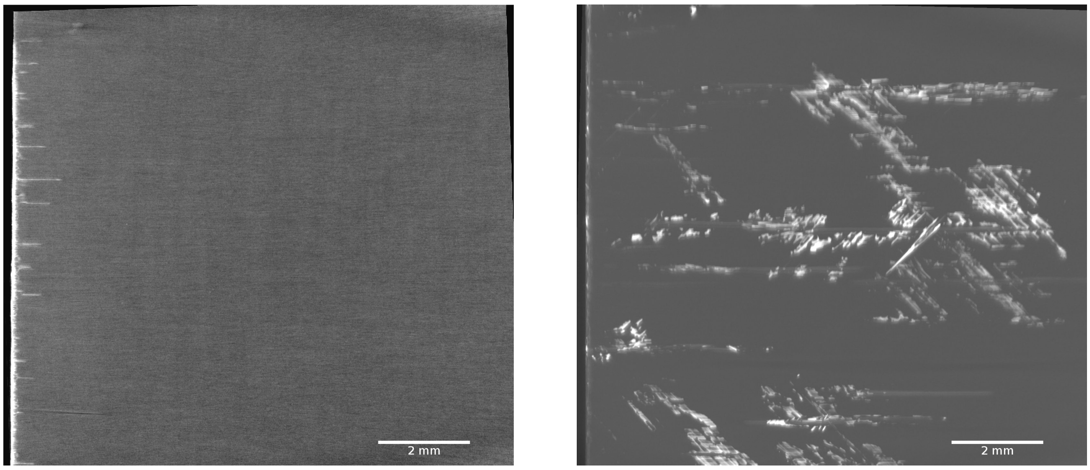

(a) 268 µm sample loaded until 380 MPa (pre-AE)　(b) 268 µm sample loaded until 460 MPa (post-AE)

Figure 4.27: Maximum intensity projection of a 90° ply region in two 268 µm T800-TP175 specimen loaded until different stress levels. At 460 MPa, the large delamination visible allows the TC to close back again, which makes them less obvious to see.

In the case of the 134 µm samples, a couple of fully propagated cracks appear fairly soon after the onset of free edge transverse cracking, as seen on Fig. 4.28a. This is a different mechanism than encountered previously, as a sample made with thinner plies (Fig. 4.28a) exhibits a full TC propagation into the bulk of the samples at a lower applied stress than a sample made with thicker ones (Fig. 4.27a). However, the early occurrences of propagated TC in the 134 µm ply sample look much thinner than the ones encountered in the 268 µm ply samples and are only encountered in a few random plies. Most of them are only present in the outermost 90° plies and could be attributed to porosity in the adjacent outer 45° plies. When present in the bulk, they are not fully bridging the ply thickness, as seen on Fig. 4.29. Considering the higher volume fraction of these samples (63%), it can be attributed to either manufacturing imperfections, or early matrix damage due to the thermal residual stresses in the highly packed fibre regions. These very thin propagated TC then multiply with applied strain as shown on Fig. 4.28b until shortly before the TC saturation and AE threshold. Once exceeding it, similar thin TC start to appear in the ±45° layers, as seen on Fig. 4.28d, whilst despite some small free edge delamination, none propagates into the bulk of the sample (Fig. 4.28c). At this stress level, the TC density in the bulk far exceeds what was measured in the system using the same fibres but the TP80ep matrix.

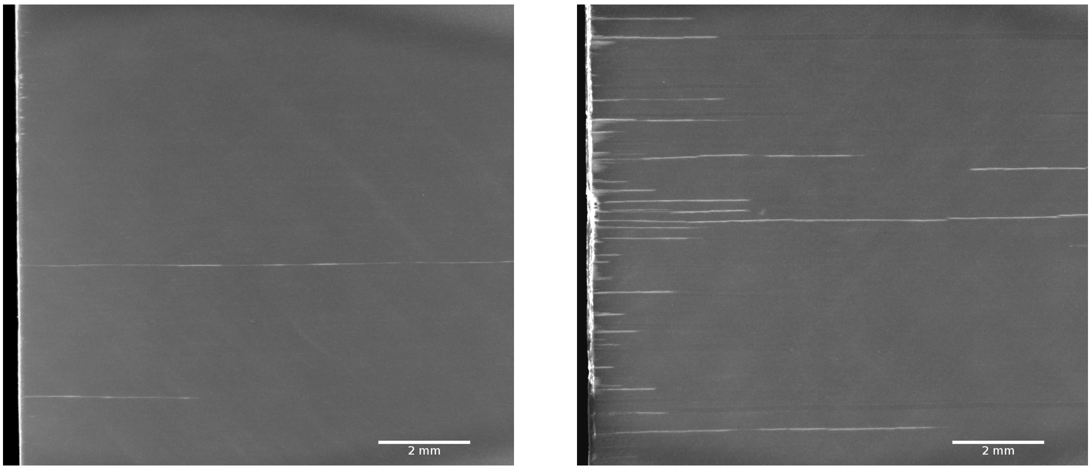

(a) 134 µm sample loaded until 300 MPa (pre-AE)

(b) 134 µm sample loaded until 500 MPa (at-AE)

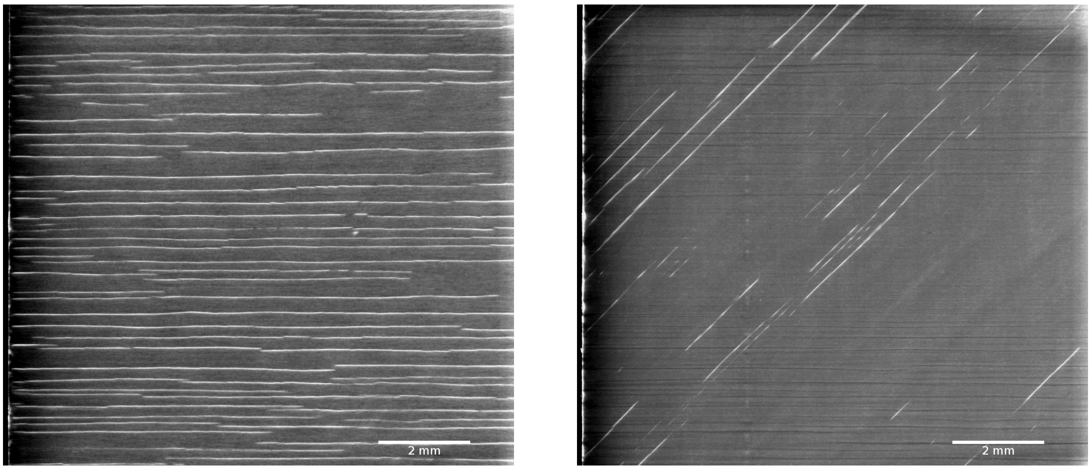

(c) 134 µm sample loaded until 650 MPa (post-AE), 90° ply

(d) 134 µm sample loaded until 650 MPa (post-AE), 45° ply

Figure 4.28: Maximum intensity projection of a 90° or 45° ply region in 134 µm T800-TP175 specimen loaded until different stress levels

The same sequence of damage is observed in the 67 µm ply samples, with thin fully propagated transverse cracks appearing soon after TC onset at the free edge, as shown on Fig. 4.30a. A strong increase in their density, coupled with the appearance of similar TC in the ±45° layers then develop at a strain level corresponding to the free edge TC saturation and AE onset, with no delamination visible in any ply orientation despite being very close to failure (see Figs. 4.30b and 4.30c). Based on CLT calculations, the transverse strain in the ±45° plies reaches its critical value soon after TC onset in the 90° plies. This causes the diagonal cracks visible on

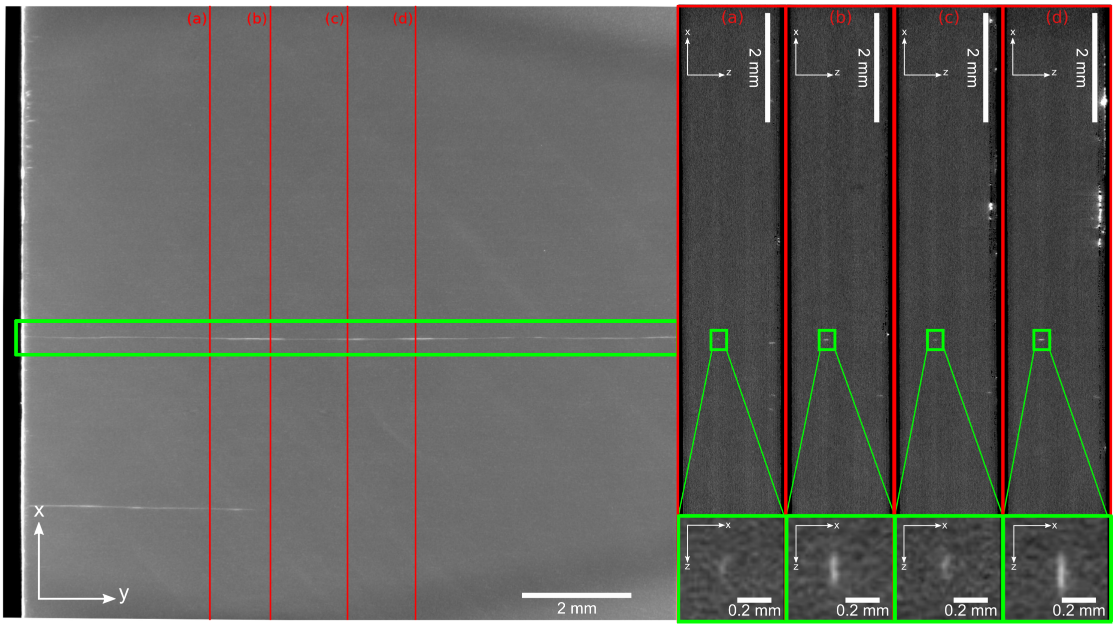

Figure 4.29: Plunging views (from the free edge into the bulk) of the t=134 µm loaded until 300 MPa, showing the varying TC length along the width of the sample. The loading direction is x and the stacking direction is z.

Figs. 4.28d, 4.30b and 4.30c for the same reason that causes the transverse cracks at a lower applied strain in the 90° layer.
Finally, comparing a t=34 µm sample shown on Fig. 4.30d with a t=67 µm one shown on Fig. 4.30c, both loaded at 940 MPa, it can be observed that a further reduction of ply thickness leads to a strongly reduced TC density, with no fully propagated crack in the bulk of the 34 µm ply sample and very little to no damage in the ±45° layers.

The proof that the early damage observed prior to AE onset in the samples made with this material is brought by the observation of the damage volume, as shown on Fig. 4.31. For both the 134 µm and the 67 µm samples, increasing the applied stress from the approximate AE level results in an exponentially larger volume of damage. This validates the use of the AE threshold as a good damage indicator despite some minor partially propagated TC prior or close to the AE threshold.

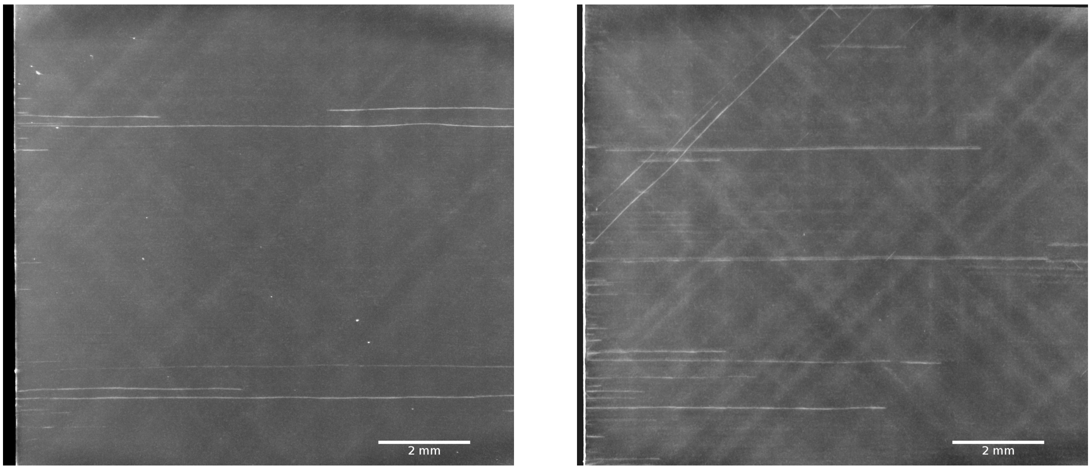

(a) 67 µm sample loaded until 500 MPa (pre-AE)

(b) 67 µm sample loaded until 800 MPa (at-AE)

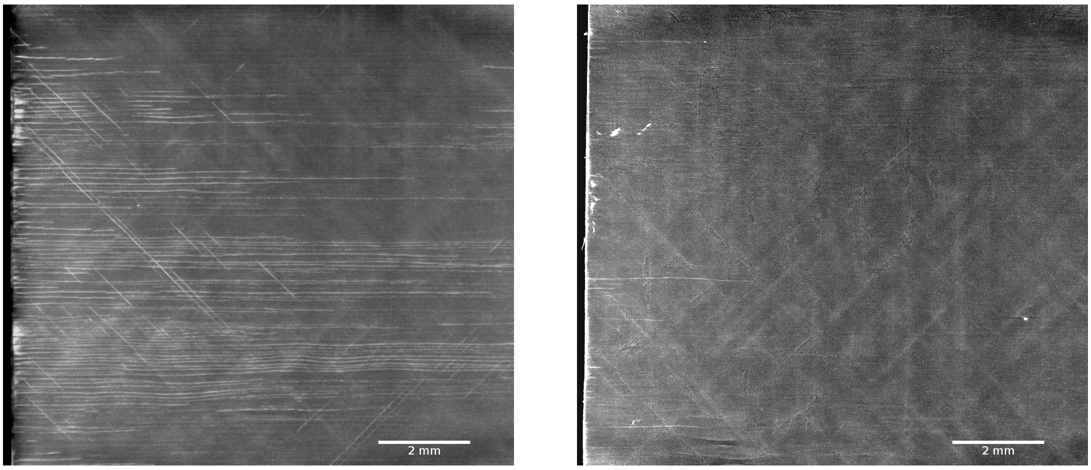

(c) 67 µm, 940 MPa load, 2 consecutive 90° & 45° plies superimposed (post-AE)

(d) 34 µm, 940 MPa load, 2 consecutive 90° & 45° plies superimposed (post-AE)

Figure 4.30: Maximum intensity projection of a 90° ply region or superimposed 90° and 45° in 67 µm and 34 µm T800-TP175 specimen loaded until different stress levels

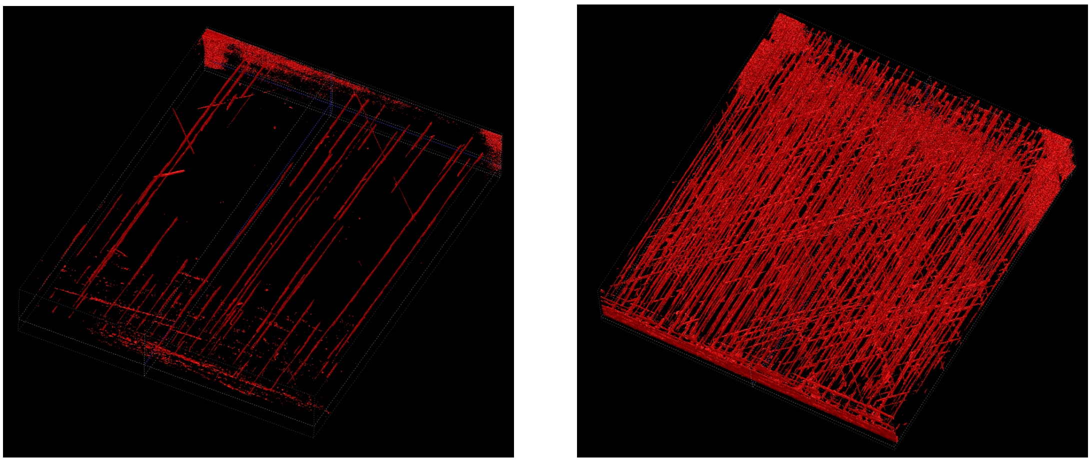

(a) 134 µm sample loaded until 500 MPa (at-AE)

(b) 134 µm sample loaded until 650 MPa (post-AE)

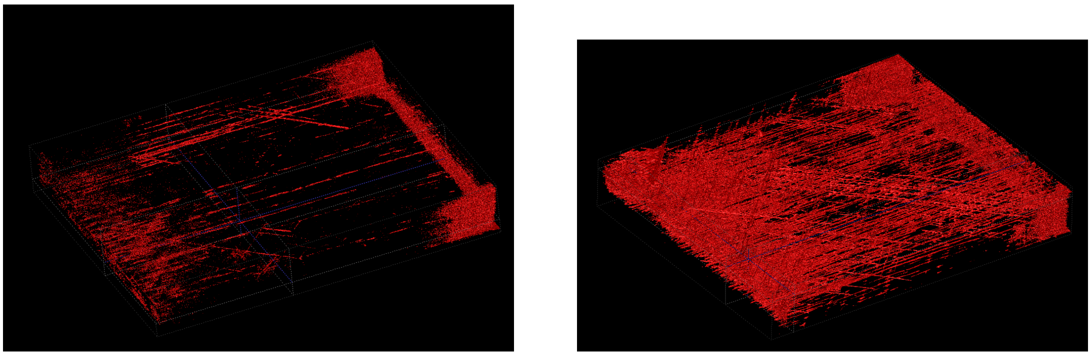

(c) 67 µm sample loaded until 800 MPa (at-AE)

(d) 67 µm sample loaded until 940 MPa (post-AE)

Figure 4.31: Damage volume at and post-AE threshold for T800-TP175 samples of 134 µm and 67 µm ply thickness. Considering the approximate estimation of AE in this case, the exponential increase in damage volume post-AE and hence applicability of AE threshold as a bulk damage onset criterion is evident

4.5 System comparison and mechanistic conclusions

4.5.1 Free-edge behaviour, bulk behaviour and mechanisms

At the free edges of the samples, the same mechanisms are observed for all three materials used in this work. For thick plies, transverse cracking first occurs in the 90° plies, often accompanied by intralaminar/free edge delamination in this same ply. This transverse cracking appears suddenly and fully bridges the ply width when it appears. The magnification used is not sufficient to measure fibre-matrix debonding, and thus a study of the transverse crack extension within the ply as defined in [23] is not possible here with the full scale samples. The coalescence of fibre-matrix debonding leading to transverse cracking cannot be observed in the micro-UNT experiments either, although the specimen size effect coupled with the use of a highly viscoplastic resin in a test requiring long holding times are the likely causes of the early propagation of free edge transverse cracks into the bulk in this latter case.
The transverse cracking in the 90° plies then quickly leads to transverse cracking induced delamination where the tips of the transverse crack reach the edges of the 90° ply. These delaminations then grow concomitantly with the appearance of new transverse cracks, until one delamination fully splits the sample lengthwise, leading to a final specimen failure dominated by delamination.

With decreasing ply thickness, namely for the t=150 µm and t=134 µm samples, the occurrence of free edge delamination is suppressed in all three materials, the growth of transverse cracking induced delamination is delayed, and the magnitude of the latter is reduced. The observed final failure is a mix of transverse fracture and large scale delamination. Decreasing the ply thickness further down to the 75 µm and 68 µm ply samples, the onset of transverse cracking is significantly delayed, and only minor transverse cracking induced delaminations can be observed in the samples using the T800 fibres, at strains exceeding 1.4%. The final failure mode is a transverse fracture of the specimen for all three systems, with no visible delamination at a distance from the specimen fracture zone.
Finally, the samples made with the thinnest plies do not exhibit any damage for the systems using the TP80ep resin, and a significantly delayed onset of transverse cracking for the T800-TP175 system, where the crack density at failure is actually lower than for the larger 67 µm ply samples, proving that the translaminar fracture of the 0° plies occurs before the full development of transverse cracking.

This damage sequence and the change of mechanism at the free edge associated with a ply thickness decrease from the t=150 µm to the t=75 µm range is similar to the results reported by Guillamet et al. [28] using non-crimp fabric carbon composite laminates. The two materials using T800 fibres also exhibit an increase of free edge transverse crack density at failure with decreasing ply thickness from the t=300 µm to the t=150 µm range (between 1.65 and 1.9 times higher density) which is consistent with the one reported by Sebaey et al. [25] using the same

fibres. This increase is however much less pronounced with the material using the stiffer and less ductile M40JB fibres where less than 10% increase in crack density is measured. This increasing critical crack density continues for the T800-based composites until the 75 µm range, whereas the M40JB-based samples show a decrease of critical TC density to a level lower than the one observed for the thickest plies.
For the thinnest plies, in the range of t=30 µm, no transverse cracks can be observed for the composites based on the TP80ep resin. For the system made with TP175 resin, a reduced crack density before final failure due to the fibres reaching their ultimate tensile strain is observed. Finally, the cracking parallel to the specimen's mid plane observed in [25] is only seen as free edge delamination in the sense of [28] for the thickest plies tested, but is totally absent as soon as ply thicknesses equal to or smaller than 150 µm are used.

Comparing the observations performed at the free edge with the AE measurements, which are shown by the tomographic observations to be a good indicator of bulk damage, very different onsets of damage are observed. For the thickest plies, both onsets are simultaneous for the M40JB-TP80ep material, and the AE onset closely follows the free edge transverse cracking onset for the T800-TP175 system. With decreasing ply thickness, these two onsets then drift further apart, indicating that the free edge damage is better constrained there, and its propagation into the bulk of the specimen more difficult. This highlights the presence of two different mechanisms at play in the bulk and at the free edge for the intermediate ply thicknesses. For the thinnest plies, the translaminar fracture of the 0° plies becomes dominant on the failure behaviour of the samples.

The difference between the shapes of the ply thickness scaling of AE onset and the free edge TC onset one is less pronounced for the T800-TP80ep system, but the AE onset reported should be taken with caution for the reasons put forth in section 4.3. In any case, the onset of damage at the free edge always notably precedes the AE onset for this material as well. Great care should therefore be exerted to ensure that damage at the free edge is indeed representative of bulk damage if free edge observations are to be used to validate thickness dependent first-ply failure criteria based on plane-strain assumptions.

Considering the mechanisms observed in the bulk of the samples by tomography, it is noticed that major delamination follows the transverse cracking propagation into the bulk of the thickest samples (t=300 µm range) for all materials, which is in agreement with the final failure mode exhibited by the samples.
In the t=150 µm range of the TP80ep-based systems, this delamination remains constrained at the free edge even close to specimen failure. The observed final failure mode of these samples suggests that an abrupt propagation of these edge delaminations into the bulk are the cause of the final specimen failure, but this process happens very abruptly at a load so close to the failure of the specimen that it is impossible to observe using the methods adopted in this

work.
For the t=75 µm range of these materials, transverse cracking propagation into the bulk is the only damage mechanism observed, whereas no damage is visible at all for the t=30 µm range. Interestingly, the transverse crack density of fully propagated transverse cracks actually decreases for a given load between the t=150 µm and the t=75 µm range, which is in good agreement with the observations of Yokozeki et al. [26], but the opposite trend to what is observed at the free edge (see chapter 2). This difference is a further proof that free edge damage initiation and bulk damage propagation are due to two different mechanisms.

The micro-CT observations of the samples manufactured with the TP175 resin show a propagation of a small number of very thin transverse crack in some limited 90° layers of both intermediate ply thicknesses (t=134 µm & t=67 µm) very shortly after the free edge transverse cracking onset, and before the AE onset. These small transverse cracks are attributed to early matrix damage and/or debonding due to the very high residual stresses present in this 180 °C cure system, possible bad interface bonding in highly packed regions due to the higher fibre volume fraction of these samples or limited manufacturing imperfection. These events are however not energetic enough to be acquired by AE, represent a very small damage volume, and are therefore considered as side effects. The AE threshold remains related to a strong increase of TC density in the 90° plies accompanied here by transverse cracking in the ±45° degree layers, without observable signs of delamination. Finally, no fully developed transverse crack is observed for the thinnest (t=34 µm) plies, though some constrained free edge TC is observed, in agreement with the free edge observations.

The larger TC density in the TP175 based samples compared to the two systems using the TP80ep resin could be due to the larger strains achieved before failure with this system. Two further hypotheses are envisaged, but additional experimental testing would be required to validate them. On one hand, the much larger residual stresses due to the higher curing temperature of this resin could cause matrix damage and/or debonding during the cooling, creating a few pre existing partial cracks through the composite within the closely packed fibre regions where these residual stresses are the largest. On the other hand, the higher fibre volume fraction of theses samples might have lead to impregnation defects and/or local porosity, which would also create cracks prior to sample loading, with the same result of promoting a larger crack density rather than a growth of fewer cracks.

Regarding the TC propagation from the free edge into the bulk, it is noteworthy that their orientation changes for all materials from the observed angled cracks at the free edge to true 90° cracks as early as 2 mm underneath the free edge. Furthermore, as the TC density at the free edge measured on the tomographic images is in good agreement with the one measured using ISM under similar loading conditions, and having observed that no TC nucleates within the bulk of the samples, it can be inferred that the cracks observed in the bulk are the same ones as those observed at the free edge and not separate damage events.

Finally, the scaling in laminate strength that can be observed for all systems studied can be directly related to the change of damage mechanisms observed. Generally speaking, translaminar fracture of the 0° plies is always the last damage mode observed prior to failure. The overloading of these 0° plies leading to failure is accelerated by large delamination growth which tends to split layers apart. For the 150 µm and 75 µm range, delamination growth being delayed significantly or even suppressed, the strength of the specimen is naturally increased. Interestingly a further increase in the laminate strength is observed for the 75 µm and the 30 µm range, which might be related to the interaction of the ply thickness with local stress concentrators around the end of the tapered tabs. With thinner plies, the volume of 0° plies present in the stress concentration region might be further decreased. Considering that the 0° ply failure is controlled by a Weibull process, the reduction of highly stressed volume could explain the further increase of ultimate strength observed.

4.5.2 In-situ strength prediction

If the underlying LEFM hypothesis are adopted, the in-situ strength model [13, 12] discussed in chapter 2 is expected to yield valid predictions of TC growth in the bulk (plane strain) of the composite, which as shown by the X-ray tomography corresponds to the onset of AE. The transverse tensile strength Y_T^{is}, corresponding to the longitudinal propagation of a transverse crack in a constrained 90° degree ply and shown here to correlate with the acoustic emission threshold, can thus be expressed as

$$Y_T^{\mathrm{is}} = \sqrt{\frac{8G_{1\mathrm{c}}}{\pi t \Lambda_{22}}} \tag{4.5.1}$$

where Λ_{22} represents the compliance of the ply in the transverse direction, defined as

$$\Lambda_{22} = 2\left(\frac{1}{E_T} - \nu_{LT} E_L\right) \tag{4.5.2}$$

which in the case of CFRP can be approximated by $\Lambda_{22} \approx E_T^{-1}$ with less than 1% error. $G_{1\mathrm{c}}$ represents the mode I critical energy release rate (ERR) associated to transverse cracking, and is actually used as a fitting parameter in the original article of Dvorak and Laws [12] to fit available experimental data.

A similar fitting approach is used in the present work. Assuming AE onset as a reliable indicator of TC propagation in the bulk, the transverse stress in the 90° layer corresponding to TC onset is calculated using CLT with the inclusion of thermal residual stresses. The Y_T^{is} values thus obtained can be used to identify the apparent in-situ toughness $G_{1\mathrm{c}}^{\mathrm{is}}$ for all ply thicknesses of the three composite systems studied in this work by inverting equation 4.5.1. The obtained values are shown on Fig. 4.32 and a very clear decrease of $G_{1\mathrm{c}}^{\mathrm{is}}$ with decreasing ply thickness can be observed. Such a phenomenon has already been considered by Saito et al. [23] who by an inverse FE method based on in-situ crack-growth measurements obtained critical ERR values in good agreement with the ones determined in the present work.

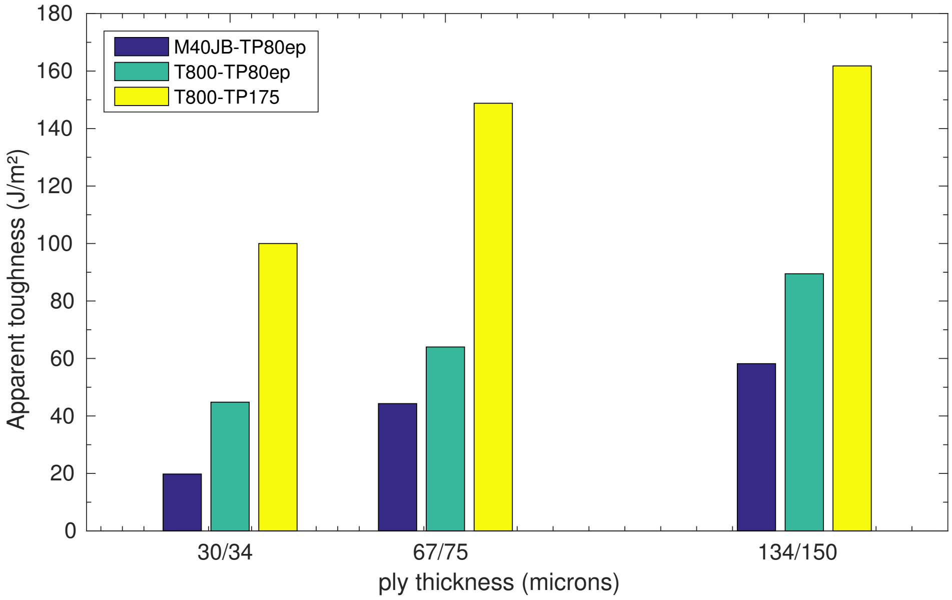

Figure 4.32: G_{1c}^{is} values for different materials and ply thicknesses

In terms of prediction, the fact that the apparent toughness related to TC seems to change with ply thickness strongly limits the use of equation 4.5.1 to generalize test data to different ply thicknesses, especially for plies of less than 100 µm thickness.

If one assumes that the hypothesis behind equation 4.5.1 are verified (material continuum, linear elasticity, plane-strain, no crack bridging), the fact that the apparent toughness is not constant with ply thickness can be directly inferred by the observed onset of TC propagation not following a scaling in $\frac{1}{\sqrt{t}}$. However, some of the validity conditions of 4.5.1 might not be verified in practice for very small ply thickness, for instance if distributed damage or plasticity can develop in the ply before TC propagation, which would thus render LEFM not applicable to this case. It can be envisaged that as the ply thickness is reduced close to the limit of the statistically representative volume element size, microscale effects could start being significant, for example distributed fibre matrix debonding, bridging effects or other size effects related to the interaction of damage localization with the neighbouring ply interfaces. These potential effects are addressed in chapters 5 and 6 by adopting a micromechanics perspective of the TC in a confined ply.

Should LEFM however be applicable, considering this reduction of toughness with decreasing ply thickness, a lower bound prediction on the in-situ strength of thin-ply laminates can be be proposed, where the G_{1c}^{is} of a given composite system is identified as proposed above using samples made with very thin plies. The identified G_{1c}^{is} value in such a case represents a lower bound of the value for all other ply thicknesses and thus can be used to replace G_{1c} in equation 4.5.1 to extrapolate a lower bound of the in-situ strength of this material for larger ply thicknesses.

This approach was applied to a wide range of CFRP materials in [7]. In order to compare different systems on the same graph, the in-situ strength is normalised as

$$Y_r = \sqrt{\left(\frac{\pi Y_{\mathrm{is}}^2}{4E_2 G_{\mathrm{app}}}\right)} \tag{4.5.3}$$

to obtain a master curve of the expected TC onset according to 4.5.1. The lower bound of the apparent toughness G_{1c}^{is} (G_{app} in [7]) is then determined for all the system studied as discussed above from the AE onsets measured on the thinnest ply thickness available for each system. The reduced in-situ strength Y_r is then calculated for all the measured ply thicknesses and reported on the master curve plot on Fig. 4.33.

Based on the results collected by LMAF so far and summarized on Fig. 4.33, the master curve derived from 4.5.1 using the apparent G_{1c}^{is} of the smallest ply thickness is providing a conservative lower bound for the onset of AE / TC propagation into the bulk. Interestingly, some systems, such as AS4/8552 exhibit a TC behaviour that nearly match the LEFM predictions whereas other ones such as those using the TP80ep or TP120 resins significantly deviate from this trend.

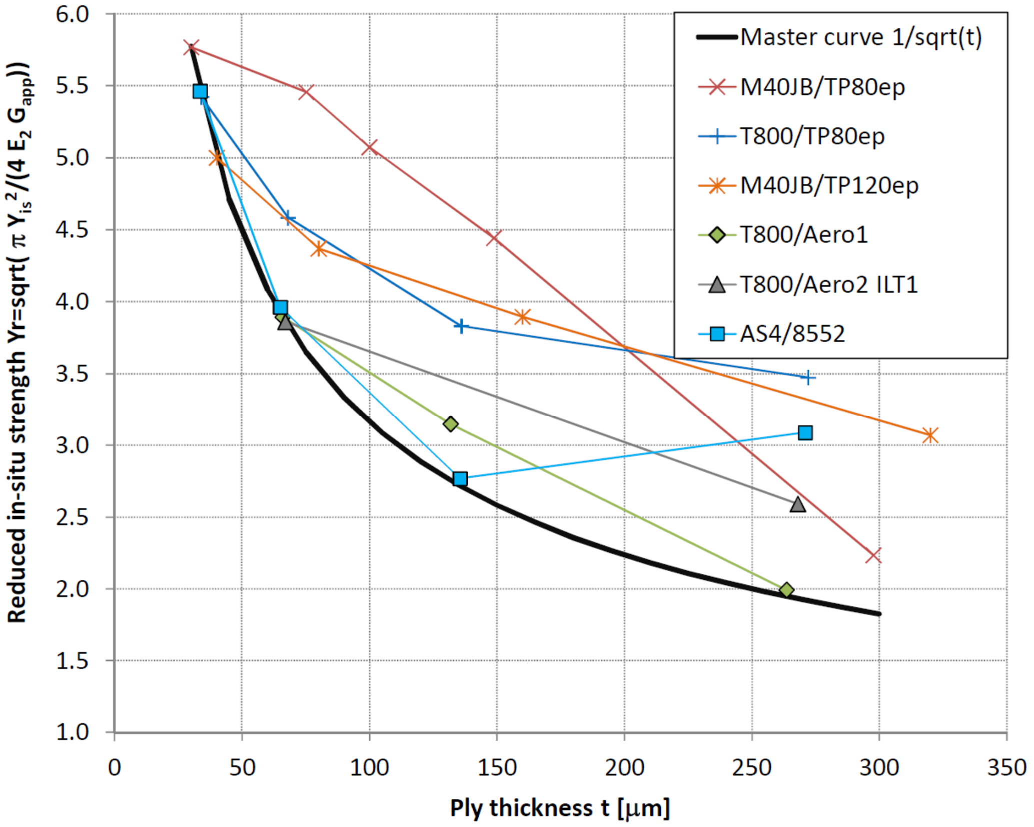

Figure 4.33: Comparison of Y_R^{is} as a function of ply thickness for different CFRP systems ([7])

4.6 Summary of experimental findings

Several key elements of this experimental work can be summarized here:

- The damage sequence observed at the free edge and its variation with respect to ply thickness is similar for all three materials tested. Transverse cracking induced delamination onset is delayed and its magnitude is reduced with decreasing ply thickness, until only transverse cracking can be observed. Further reduction of the ply thickness leads to the total disappearance of free edge damage for the systems using the TP80ep epoxy, and to a delayed onset of transverse cracking for the one using the TP175 resin. For the thinnest plies, the onset of damage is shown to be nearly coincident with the final failure and can reach values of up to 95% of the ultimate strain of the fibres.

- The onset of damage defined by AE is a good predictor of bulk damage, namely the propagation of transverse cracks that were constrained at the free edge into the bulk of the sample, and the additional appearance of transverse cracks in the ±45° layers for the TP175-based samples.

- Bulk damage is shown to be caused by the propagation of free edge transverse cracks towards the center of the samples only. No lamina-level damage originates within the sample.
- The onset of damage scaling in the bulk and at the free edge are shown to differ strongly for all three tested composite systems, indicating that different mechanisms are at play in both sites.
- Using CLT, the experimental AE onset and the inverted in-situ strength expression, it is shown that the apparent toughness values used in the in-situ strength expression decrease with reduced ply thicknesses. A lower bound estimate for this in-situ strength of thin-ply composites is thus proposed, only requiring the experimental acoustic onset of damage determination for one very thin ply sample of a given system to provide a safe lower bound of the in-situ strength for all ply thicknesses.
- To understand the root causes of the observed trends, it is required to go past the assumptions underlying the LEFM in-situ strength model and to study TC at the microscale.

5 Micromechanics numerical methods

In order to gain a better understanding of the mechanisms at play during the damage observed experimentally, a multiscale FE model was developed. Based on materials properties measured experimentally as well as real microstructures of the actual samples tested, the steps taken to ensure a good correlation with the experimental results yielded valuable informations regarding the mechanisms at play.

This chapter thus presents the different components of the final models, as well as the reason underlying some of the choices made. The first section discusses the numerical part of the matrix modelling and its validation. The simulation used to determine the fibre/matrix interface strength is then presented, before the actual multiscale model, its implementation and its calibration is discussed. Finally, the different procedures used to extract the results of interest for this work from the final models, which are presented in Chapter 6, are described.

5.1 Matrix modelling - numerical work

As discussed in chapter 3, the ductility of the matrix had to be extended from the experimentally obtained stress-strain curve and associated ultimate tensile strain to account for the larger ductility of epoxy at smaller length scales [74, 78, 75]. This became apparent when modelling systems using the T800 fibres, which have an ultimate tensile strain allowing the local matrix strain to exceed the experimentally determined ultimate strain of the matrix in a macro scale sample. Largely unnoticed in the case of the system using the high modulus M40JB fibres, the use of the experimentally determined macro scale ductility acted as a cap on the onset of damage predicted by the numerical model when simulating T800-based composites, with early matrix damage triggering localisation and early transverse cracking. The procedure outlined in section 3.2.2 was thus applied, extending the stress-strain curve to match experimental results on very small samples [74, 75] as used by Arteiro et al. [69, 70] in a similar numerical framework.

Once the parameters of the general exponent Drucker-Prager yield function were determined as described in section 3.2.3, the evaluation of the dilatation angle ψ for both resins were performed by comparing the experimental nano-indentation curves with the ones of the model described in section 5.1.1. The matrix thus modelled therefore presents a pressure dependant elasto-plastic behaviour with hardening. The agreement with the experimental data used to determine the numerical models was then validated with a single element numerical test as described in section 5.1.2.

Once the critical strain (or maximum plastic strain ε_p^D) of the matrix) is reached, a linear softening, energy based regularized damage model reduces the stiffness of the matrix elements. The damage variable SDEG is defined as the scalar stiffness degradation variable. (Ductile damage model in Abaqus [61])

5.1.1 Nano-indentation simulation

As mentioned in section 4.1.2, it became apparent that the numerical nano-indentation curve was highly sensitive to the ψ value used to model the matrix, as shown on Fig. 5.1. This leads to the desire to use the FE model to perform an inverse identification of this parameter when comparing it to typical experimental nano-indentation curves, as the elasto-plastic model is already defined and ψ is the only remaining undetermined variable of the matrix model.

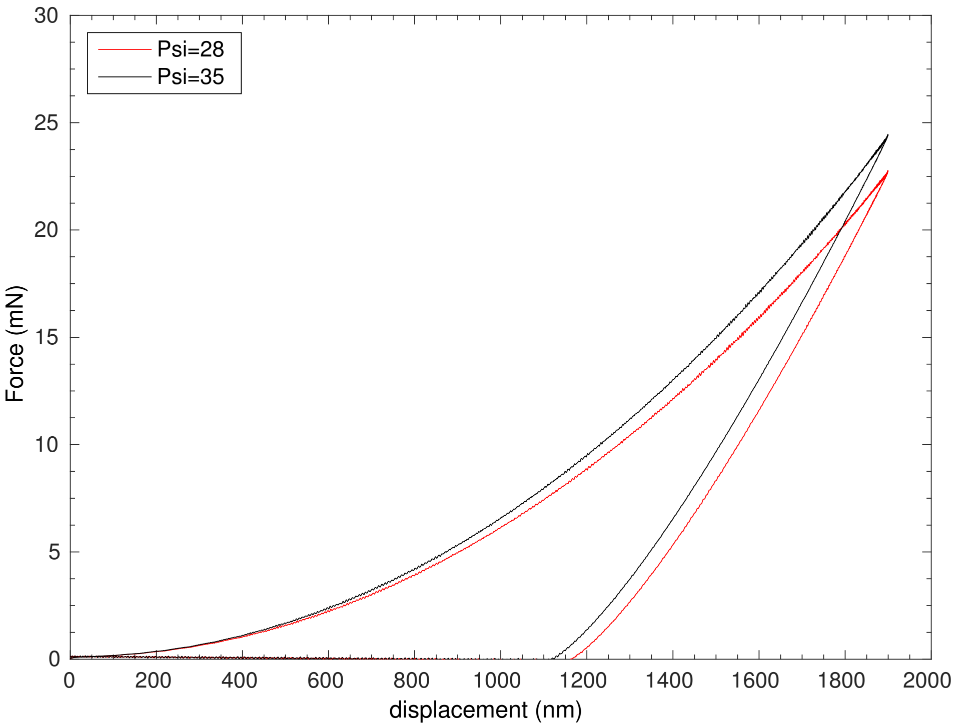

Figure 5.1: Effect of a variation of ψ on the nano-indentation simulation

An axisymetric 2D model of the nano-indentation process was thus created to replicate numerically the experimental test. As shown on Fig. 5.2, an equivalent angle of 70.3° is used to model the Berkovitch indenter tip as is usually done despite some controversy regarding this practice [106]. The matrix elastic properties are taken directly from the manufacturer's data shown in Table 3.3 whereas the yield function coefficients a and b as well as the hardening curve are defined as presented in section 3.2. The analysis is run in Abaqus Explicit for ease of convergence considering the large deformation as well as to be consistent with the multiscale model that uses this data. The elastic modulus of diamond is reduced to 500 GPa to minimise numerical issues due to the large mismatch of stiffnesses between the indenter and the matrix, and the size of the matrix zone is chosen to ensure that no edge effects is present. The Drucker-Prager eccentricity parameter is kept at its default value of 0.1, whereas the dilatation angle value ψ is initially chosen equal to the pressure dependency parameter β measured on the yield function at high confining pressure, as would be the case with an associated flow behaviour. Both mesh and mass-scaling convergence analysis are performed to ensure that the results obtained are converged.

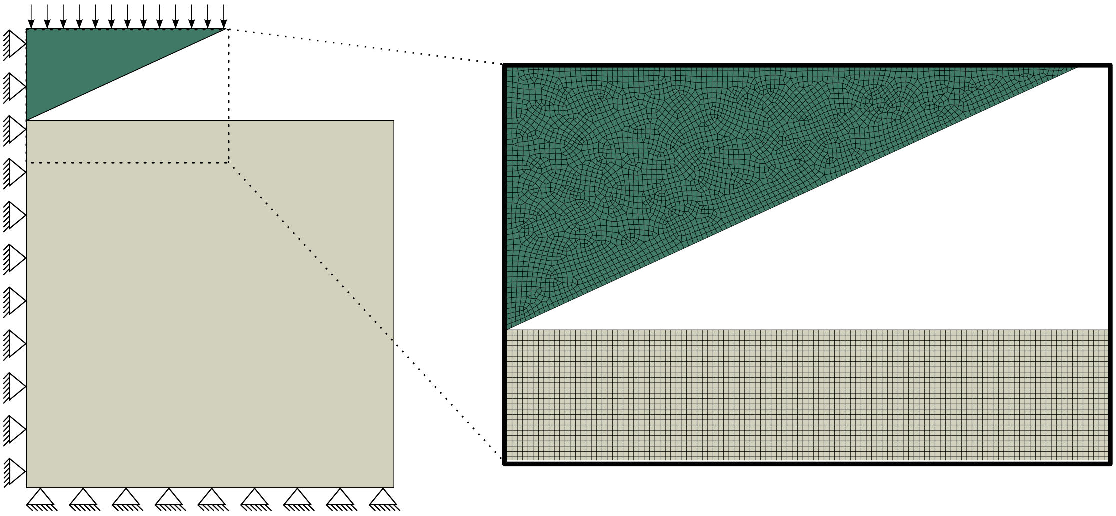

Figure 5.2: Nano-indentation FE model, mesh and boundary conditions. Diamond indenter tip in green and matrix in grey.

The numerical test was performed in displacement control up to the maximum indentation depth of the referenced experimental one, before returning the indenter to its original position. Both movements are performed using a smooth step function to ensure quasi-static conditions. To do so, the top surface of the modelled indenter is linked to a reference point via a kinematic coupling, where the displacement is imposed and the reaction forces are extracted to build the numerical indentation curve. This curve is then compared to the referenced experimental one where the "hold" section was suppressed. As no viscous effects are included in the matrix model, the creep behaviour cannot be captured and this suppression was therefore required.

Finally, the ψ parameter is varied until the best match is found. The results for both matrices used in this work can be found on Figs. 5.3a for the TP80ep epoxy resin and 5.3b for the TP175 one.

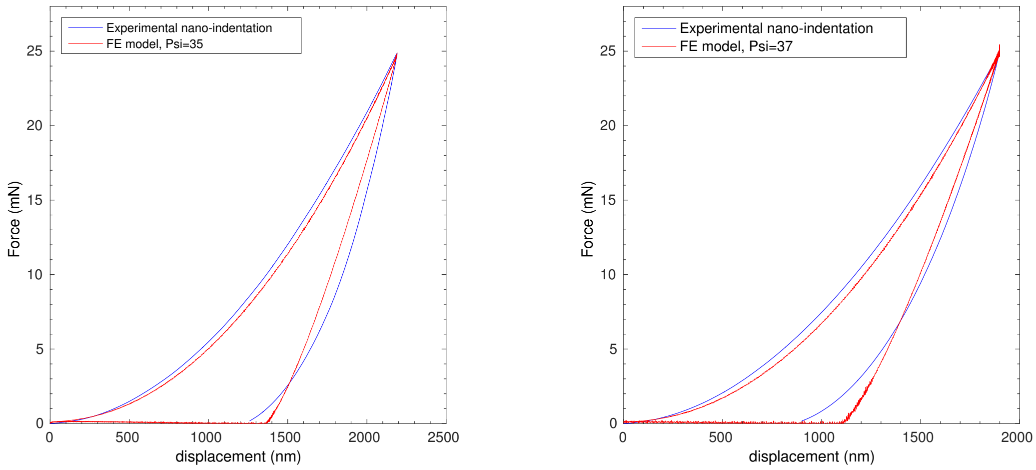

(a) TP80ep fitting

(b) TP175 fitting

Figure 5.3: Comparison of the experimental and numerical nano-indentation curves

Looking at the deformed (numerical) shape of the indenter's imprint into the resin, it can be recognised that the matrix thus modelled has a pile-up behaviour upon indentation which is explicitly described in Rodriguez et al. [80] as a condition where the Oliver and Pharr method [97] cannot be used, further validating the use of another calibration procedure for the yield function itself.

5.1.2 Model validation

Both the loading part of the nano-indentation curve as well as the beginning of its unloading part, where the modulus is measured, are in good agreement between model and experiment. However, the plastic deformation at the end of the indentation is overestimated in both cases. This is most likely due to an imprecise hardening curve extrapolation in the regime where no experimental data exists, combined with viscous effects that are unaccounted for. It would also have been interesting to study the effect of the plastic strain at onset of damage ϵ_p^D, which is defined as the plastic strain upon reaching the limit chosen on the ductility extension discussed in section 3.2.2. Reducing this value and modifying the hardening curve accordingly to achieve the same stress-strain curve would allow simultaneous plasticity and damage to take place. This did not fit in the scope of this work but would be interesting to study in the future. In any case, considering that the extreme compressive deformations encountered in such a test are very far from the tensile loads encountered in the embedded cell model where the matrix models are implemented in this work, the match is considered good enough and the matrix model therefore further validated on a single element test subjected to uniaxial tension and compression. The comparison between the numerical result and the experimental data can be seen on Fig. 5.4a and 5.4b, proving that the approach using simple uniaxial tests used here was able to provide results that are accurate enough for the expected low triaxial stress-state encountered in this work.

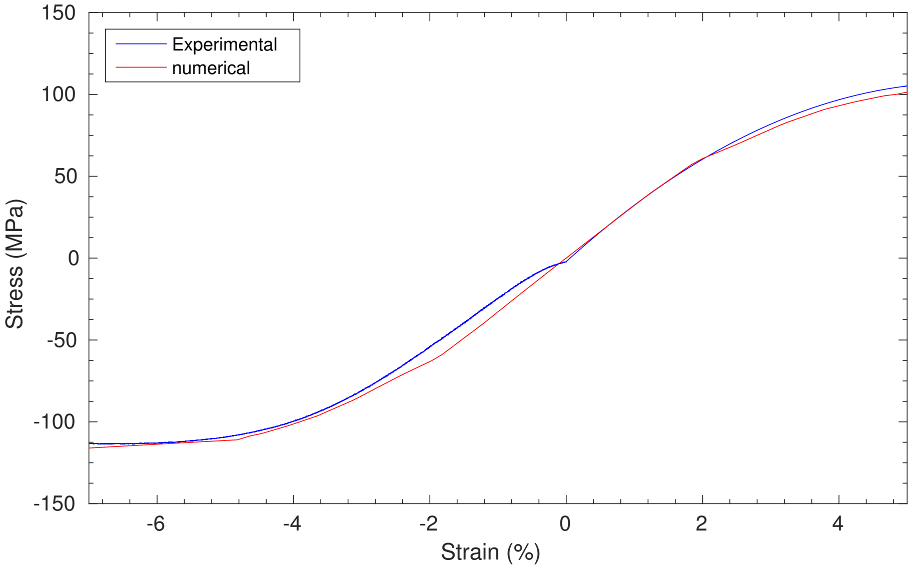

(a) TP80ep

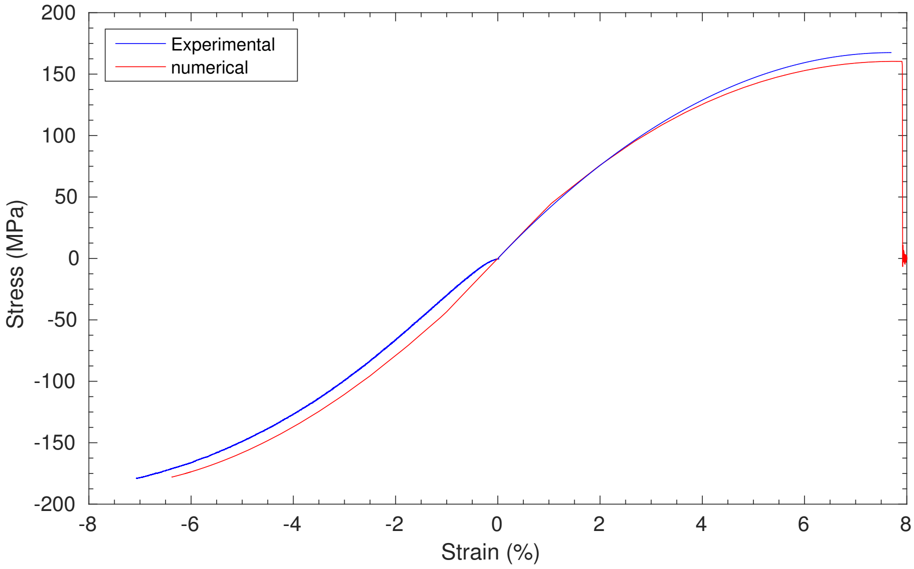

(b) TP175

Figure 5.4: Matrix models uniaxial tensile / compressive validation.

5.2 Embedded Cell modelling

As discussed in chapter 2, an embedded cell approach was chosen to perform the multiscale modelling, in order to relate simulations at the microscale, including the local damage process, to experimental macroscopic values such as an onset of damage at the free edge or in the bulk. The fibre material properties were taken from Table 3.6, and the matrix material properties were obtained as discussed in sections 3.2 and 5.1. The fibre-matrix interfaces modelling is discussed in section 5.3, and all the properties used in the final models are recalled in chapter 6, Tables 6.1 and 6.3.

5.2.1 Microstructure modelling

Optical microscopy images of chosen samples were used to model the finely discretised 90° ply region used in the micromechanical numerical models. Either manual fibre identification or an in-house Matlab script working through grey level thresholding, erosion and watershed algorithm were used to reconstruct the fibre centre locations. The fibre's cross section was then modelled as a circle. The diameter of the fibre is chosen as close as possible to the nominal fibre diameter, whilst allowing a fibre separation gap large enough to fit at least one properly conditioned matrix FE element (minimum 5% of the nominal diameter). An example for the T800-TP175 system with t=67 µm is shown on Fig. 5.5. The fibre center location and diameter thus defined were then fed to a parametric python script to create the model in Abaqus.

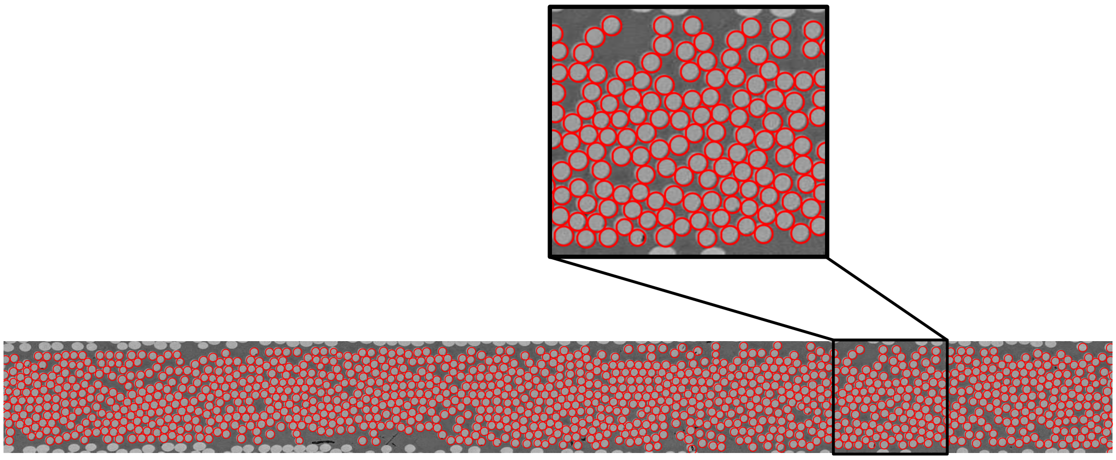

Figure 5.5: Example of an identified T800-TP175 t=67 µm microstructure using the Matlab script developed in-house

5.2.2 Multiscale embedded cell implementation

The micromechanical zone described above was embedded in a larger purely elastic continuum model of the laminate, as shown on Fig. 5.6. To avoid localisations at the interface between the elastic continuum model and the embedded cell, a transition zone with increasing matrix and interface strength and toughness was built-in at the edges of the latter, as shown on Fig. 5.7. The embedded cell boundaries are not simple straight edges but rather follow the outer fibres as this is a better representation of how two adjacent plies "interlock" in the actual samples, where no clear resin rich interply regions could be observed.
A [0/45/90/-45/0] stack was used to replicate part of the quasi-isotropic layup of the physical samples. The lamina properties were defined from experimental testing and classical homogenization equations. It was verified that this subjected the embedded cell to a similar stress-state than an internal 90° ply would be experiencing in the core of the laminate. A single element width 3D model representing a thin 4 µm slice of material was implemented and solved in a dynamic explicit solver (Abaqus explicit) with mass scaling recalculated at each increment to represent the quasi-static response of the material. Studies were performed on both the variable mass scaling's target stable time increment and on the mesh element size to ensure that the simulations were fully converged.

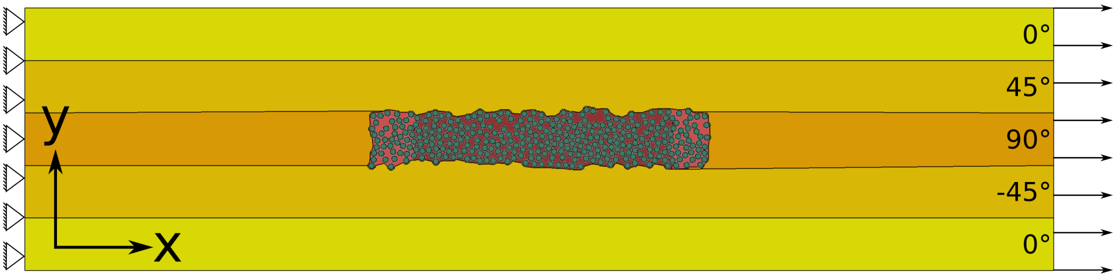

Figure 5.6: Embedded cell model example. The fibres are shown in green, the matrix in red and the homogenized plies in different tones of yellow depending on their orientation. The lighter red area highlights the transition zone compared to the darker red one which is the region where results are gathered

In the case of the M40JB-TP80ep system, no residual thermal stresses were taken into account due to the very small temperature differential. The loading of the FE model could thus be implemented as a displacement smooth step, with a converged stable time increment target of 5E-6. In the case of the T800-TP175 system however, an initial thermal step could not be avoided. This cooling step was defined with an amplitude of -125 °C as is proposed in the literature ([107]) for 180 °C cure systems to take into account the much larger matrix plasticity and reduced rigidity at elevated temperatures. The fibre and matrix CTE's were taken from manufacturer's data sheets or estimated from literature ([108, 109, 110, 111]) and the lamina CTE's calculated by simple series/parallel homogenization models from the constituent's ones. These various CTE's are presented in Tables 5.1 and 5.2.
Owing to the absence of external forces during the thermal step, the target stable time incre-

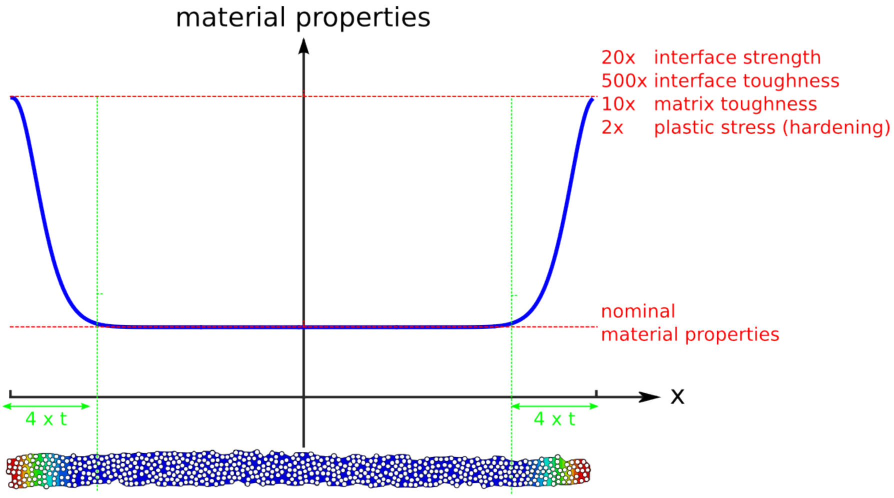

Figure 5.7: Example of the transition zone used to avoid localisation at the edges of the embedded cell

ment could be increased to 2E-5 to speed up the computation without any detrimental effect such as an increasing kinetic energy appearance. After the thermal step, a mechanical loading step is implemented.

Table 5.1: Coefficients of thermal expansion (CTE) used for components

Material	α_1^f (/K)	α_2^f (/K)	α^m (/K)
T800 + matrix	-0.4E-6	1E-5	6E-5
M40JB + matrix	-0.83E-6	1E-5	6E-5

Table 5.2: Coefficients of thermal expansion (CTE) used for plies

Lamina	α_L (/K)	α_T (/K)
M40JB - TP80EP	-4.025E-7	3.25E-5
T800 - TP80EP	1.469E-7	3.25E-5
T800 - TP175	3.0915E-7	3.25E-5

5.2.3 Boundary conditions

The experimental results highlighted an important difference in strength scaling and mechanisms between the damage observed at the free edge and in the bulk. Consequently, it seemed worthy to model both conditions and see how the model behaved in both cases. A set of plane-strain boundary conditions was therefore modelled to simulate the bulk behaviour, whereas a submodelling approach was used in the case of free edge.

In both cases, the load was imposed through a smooth step, in order to minimise the dynamic effects. The implementation of such a step is present in Abaqus, with the amplitude A varying throughout the step as

$$A(s) = A_0 \cdot s^3 \left(10 - 15s + 6s^2\right) \tag{5.2.1}$$

with A_0 the total desired amplitude at the end of the time step and s the step's time increment, if assuming $A(0) = 0$ and $0 \leq s \leq 1$. The 125 °C thermal step implemented for the TP175 simulations as well as a displacement amounting to 3% strain for the TP80ep embedded cell simulations were implemented in such a way.

In the case of the T800-TP175 system, however, a displacement boundary condition cannot be cleanly defined after the thermal step due to the global implementation of the displacement values in Abaqus, which would either lead to a restricted thermal shrinkage or to a jump in displacement. A velocity amplitude leading to the same displacement was therefore implemented in tabular form by differentiation of the displacement's amplitude previously used, namely

$$A_{\text{speed}}(s) = 30A_0 \cdot \left(s^4 - 2s^3 + s^2\right) \tag{5.2.2}$$

with the same A_0 as previously used, corresponding to a displacement amounting to 3% strain on the model. Both amplitudes are shown on Fig. 5.8.

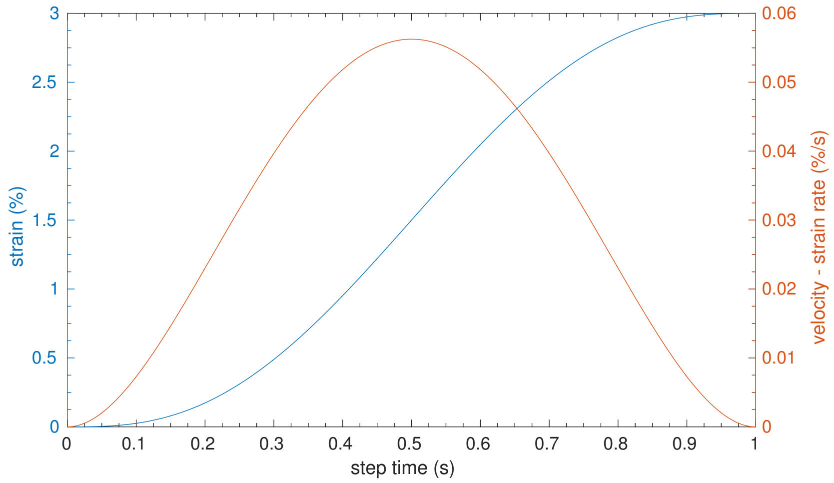

Figure 5.8: Smooth step amplitudes

5.2.3.1 Plain-Strain: Bulk simulation

The bulk of the material is simulated via plane-strain conditions, enforced by a symmetry plane on the front face of the model and by imposing the planarity of the back one, as shown on Fig. 5.9. Out of plane displacements due to Poisson effect are therefore not over-constrained, whilst the entire back face cannot deform but has to remain perfectly flat.

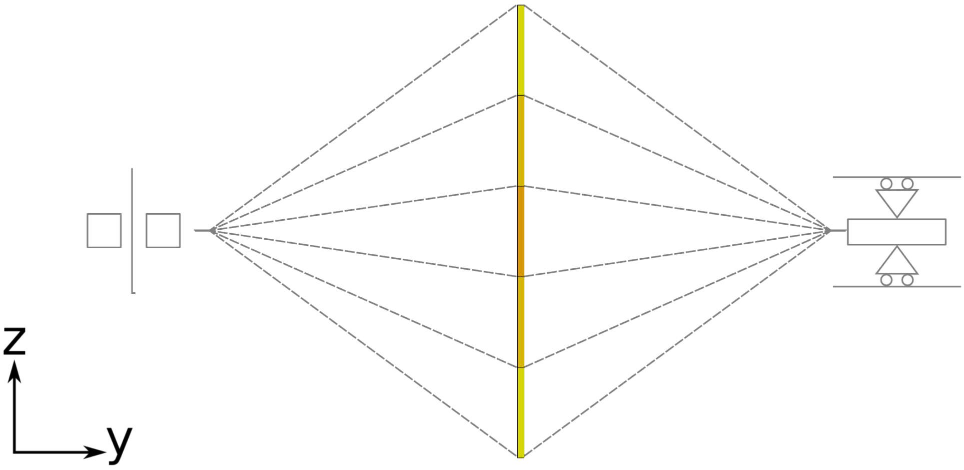

Figure 5.9: Plane-strain / bulk boundary conditions

5.2.3.2 Submodelling: Free edge simulation

An accurate description of the free edge would require a full 3D simulation, the computational cost of which was not deemed practical. In order to approximate it as closely as possible with a reduced computation time, a submodelling approach was chosen. This means that the continuum model extended to the half width (12mm) of the sample was first run in Abaqus Standard, with a symmetry plane in the same position as the geometric sample ones, thus accurately modelling half of the width of the sample as a homogenised linear elastic solid. A biased mesh with the finer end at the free edge was used, with the embedded cell zone replaced by its homogenized properties. The displacement field calculated in a zone determined around the embedded cell, shown on Fig. 5.10 can then be used as displacement boundary conditions for the thin single element slice of the embedded cell, thus imposing a realistic 3D displacement boundary condition on the submodel.

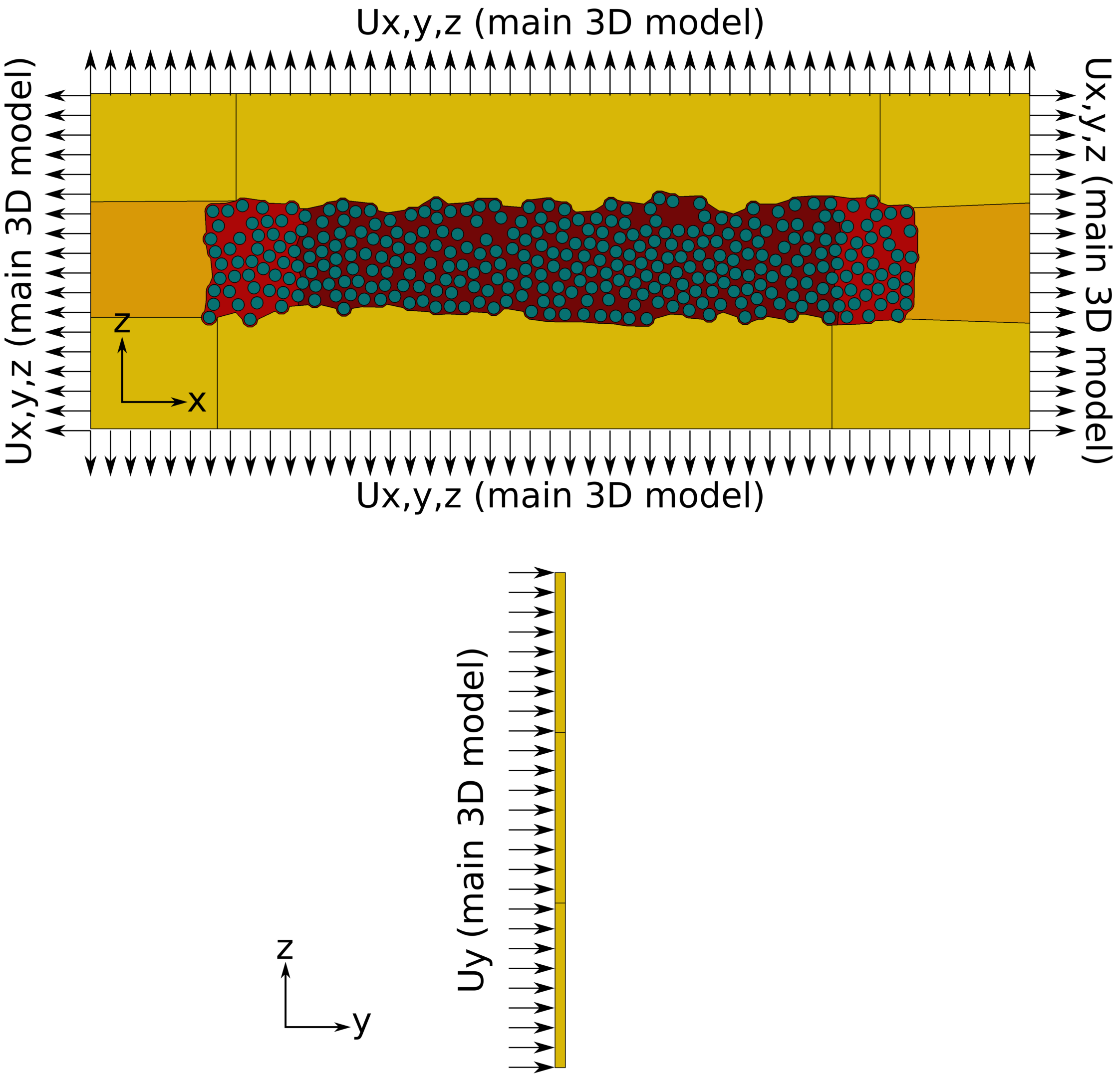

Figure 5.10: Boundary conditions enforced through the submodelling approach used for the free edge of the samples

5.2.4 Mesh

All embedded cell models rely on the C3D8R and C3D6 elements proposed by Abaqus Explicit. A typical element size of 20µm is used in the continuum regions, and a global size of 0.5µm in the embedded cell. The mesh is further refined around the fibres by the enforcement of a requirement to place 30 elements on the perimeter of each fibre or surrounding matrix zone. A single element is used in the depth of the model, resulting in meshes varying between 212k nodes for the smallest model and 1Mio nodes for the largest one. Such a mesh is shown on Fig. 5.11. Typical computation time varies between 24h and 120h on a single CPU.

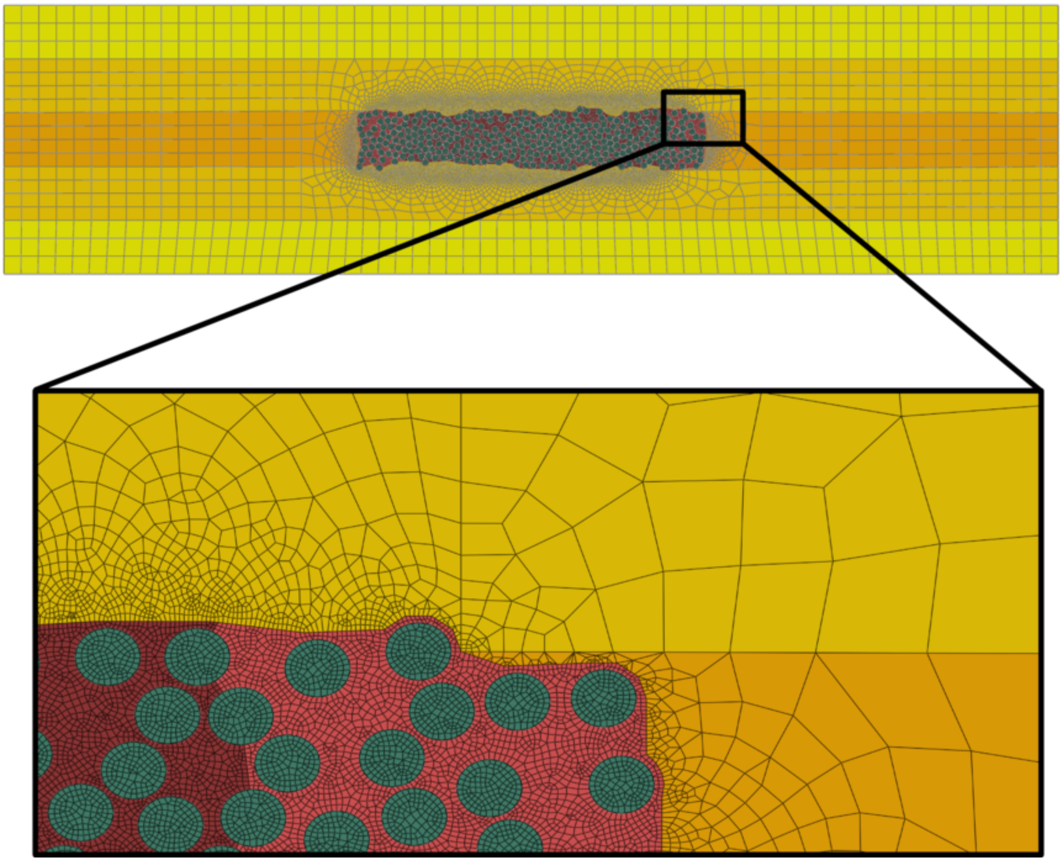

Figure 5.11: Example of embedded cell mesh

5.3 Interface modelling and calibration of its parameters

The fibre-matrix interfaces were modelled as cohesive surfaces with the linear softening, energy based model present in Abaqus, with a quadratic traction onset of damage criterion. The interface stiffness was set at the lowest value ensuring a converged force-displacement curve when performing a sensitivity analysis to this parameter on a small RVE containing a single fibre embedded in a small matrix cube and meshed similarly to the embedded cell model, as shown on Fig. 5.12.

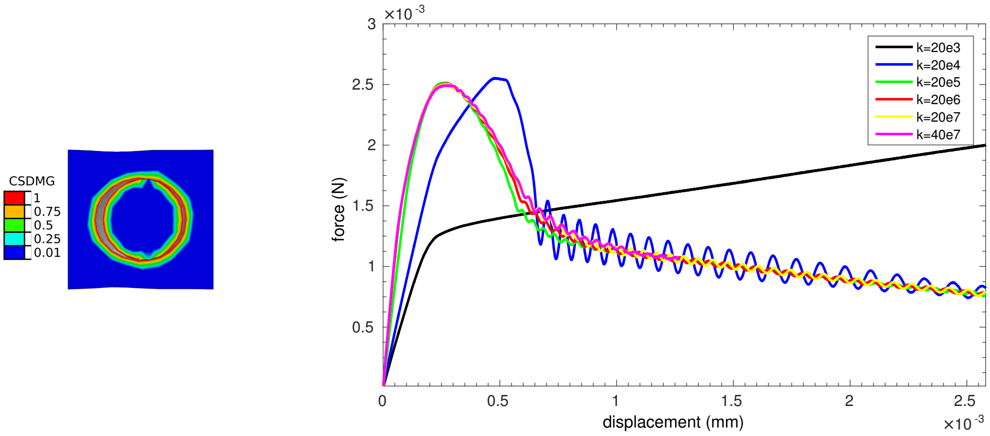

(a) contour plot of interface damage

(b) Force-Displacement curve

Figure 5.12: Sensitivity analysis of the interface stiffness, with the contour plot of the single fibre RVE subjected to uniaxial tension and the resulting force-displacement curves shown

The fibre-matrix interface normal strength τ_i^n and toughness G_i are notably difficult to determine experimentally, and no such data was available for our materials. A numerical inverse identification was therefore attempted, either directly in the embedded cell model at a given ply thickness, or using a simpler 90° ply model, shown on Fig. 5.13, in which the same type of mesh as in the embedded cell was used. For the interface toughness, the goal was to tune the parameters in such a way that the AE onsets for a given material could be replicated numerically. For the interface strength, the goal was to accurately predict the transverse tensile strength of the material, which was known from experimental UNT 90° tests as reported in Tables 3.1 and 3.2.

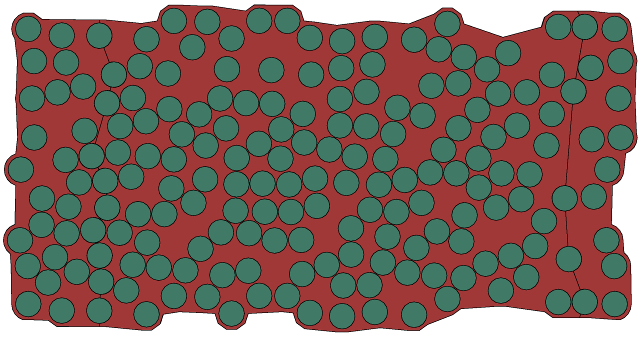

Figure 5.13: Transverse tensile (UNT90) FE model

To this effect, the UNT 90° model was subjected to transverse tensile loading, whilst the constituents parameters used were the same ones as for the embedded cell model. Only the interface parameters were varied in order to run a sensitivity analysis. To minimise the influence of the interface toughness on the UNT90° simulation, it was run in load control, so that when damage initiated, sufficient driving force was available to rapidly break the interface, thus giving a clear indication of the fracture of the model. Considering the fragile failure mode observed experimentally in UNT 90° tensile tests, this assumption would not make much difference compared with a physical test run in displacement control, and presented the advantage of reducing the coupling of two unknown interface parameters which required identification.

Several microstructures, either chosen as parts of the ones used in the embedded-cell models or randomly generated using Viper [112], were tried with no sensible effect on the result of the UNT 90° simulation, demonstrating an independence of the lamina transverse strength from the microstructure specificities as long as the volume fraction was kept constant. For the M40JB-TP80ep first used, variations of the interface toughness within a range able to markedly change the response of the embedded cell model ($2\mathrm{J/m^2}$-$5\mathrm{J/m^2}$) did only produce small variations on the UNT 90° model one. To the contrary, variation of the normal interface strength had a major effect on the UNT 90° response, as shown on Fig. 5.14, whereas the effect was much less marked for the embedded cell model. This demonstrated that the use of such a simulation was a good approach to obtaining the parameter sought.

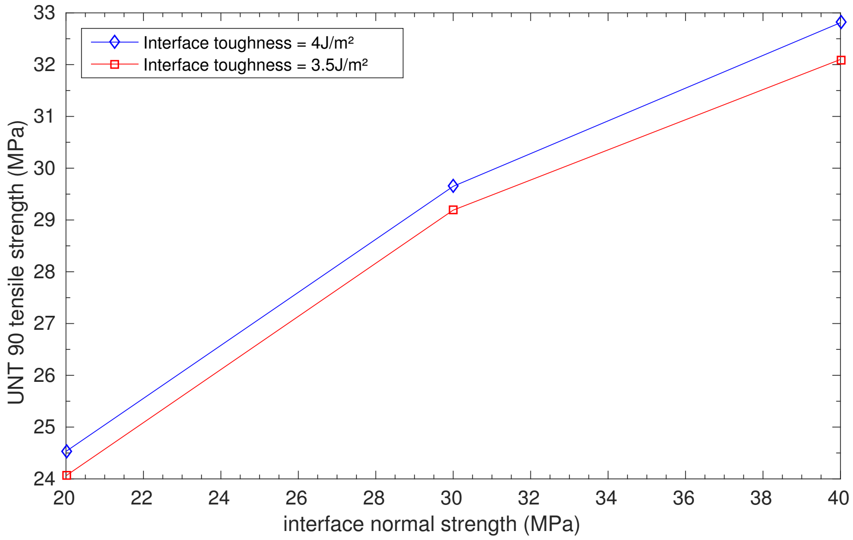

Figure 5.14: Interface normal strength and toughness sensitivity of the M40JB-TP80ep UNT90 model

The two interface shear strengths were defined as $\tau_i^s = \frac{3\tau_i^n}{2}$ as proposed in the work of Ogihara and Koyanagi [82], used by other authors ([64, 88]) in a similar situation. It was however verified numerically by a sensitivity analysis using the M40JB-TP80ep system properties, shown on Fig. 5.15, that these values played no major role in the overall lamina response of such a simulation.

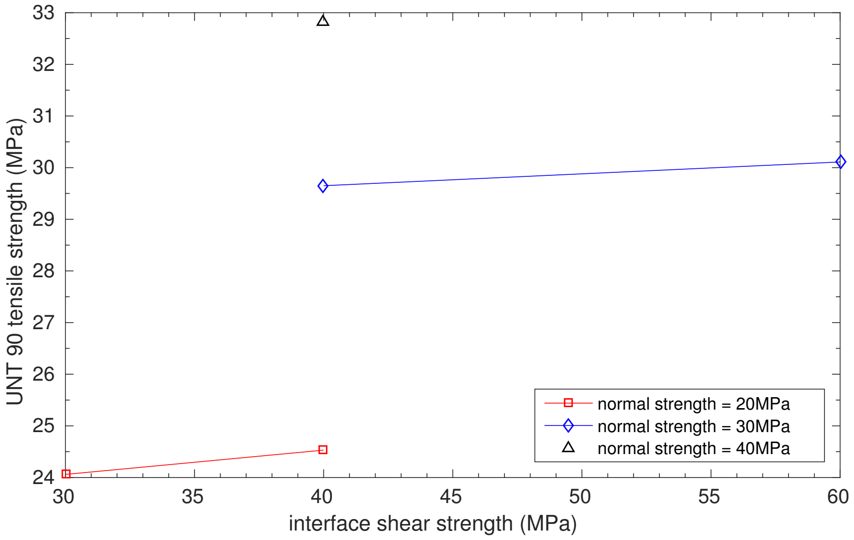

Figure 5.15: Interface shear strength sensitivity of the M40JB-TP80ep UNT90 model

5.4 Analysis techniques

In order to analyse the results of the numerical FE models, several analyses are performed, and the following sections highlight the key points of their implementation.

5.4.1 Crack definition

The numerical onset of damage is defined as the point at which the load bearing capacity of a zone spanning over 50% of the ply thickness is significantly reduced. This can easily be recognised by either looking at contour plots of S_{xx} within the embedded cell, as is typically shown on Fig. 6.4 or watching for the first drop in the averaged stress-strain curve of the embedded cell, as shown on Fig. 5.16.

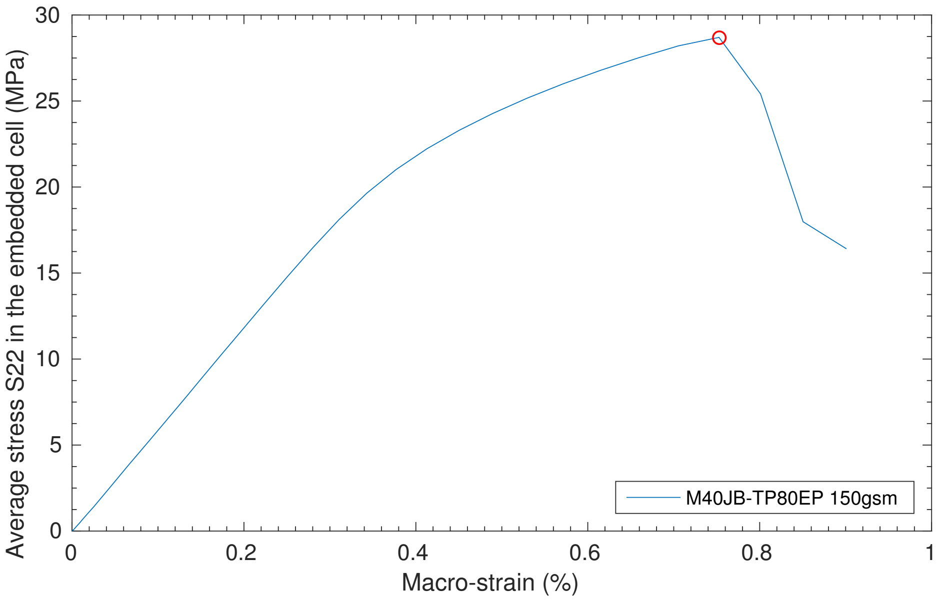

Figure 5.16: Averaged stress S_{22} in the embedded cell vs macro-strain, with crack onset shown in the red circle

5.4.2 Stress State

The triaxiality η of the stress state is important for the resin behaviour, and is therefore extracted from the embedded cell at different time steps, by dividing the p (pressure field) and q (von Mises stresses) stress invariants for each element, according to the definition of η. These values are normalized by their respective element volume when averaging over the whole embedded cell region.

5.4.3 Numerical transverse crack ERR

A clear reduction of the toughness associated to transverse cracking was noted in section 4.5.2 when identifying it from the experimental onset of damage values by inverting the in-situ strength equation. To investigate whether the same trend is present in the numerical model, the plastic and damage dissipation terms associated to the appearance of the first transverse crack(s) were therefore summed and this energy dissipation then divided by the surface of the said crack, defined as the model thickness multiplied by the distance separating the two transverse crack tips. As distributed plasticity and fibre-matrix debonding occur before the initiation of a transverse crack, the dissipated energy associated to transverse cracking is determined as the increment of dissipated energy over a segment of time corresponding to the initiation, growth and arrest of the transverse crack. This effectively defined a critical ERR associated to the transverse cracking of the numerical models. These two dissipative terms are shown on Fig. 5.17 in the case of the M40JB-TP80ep t=30 µm model, where the first transverse cracks form in the strain range highlighted in yellow.

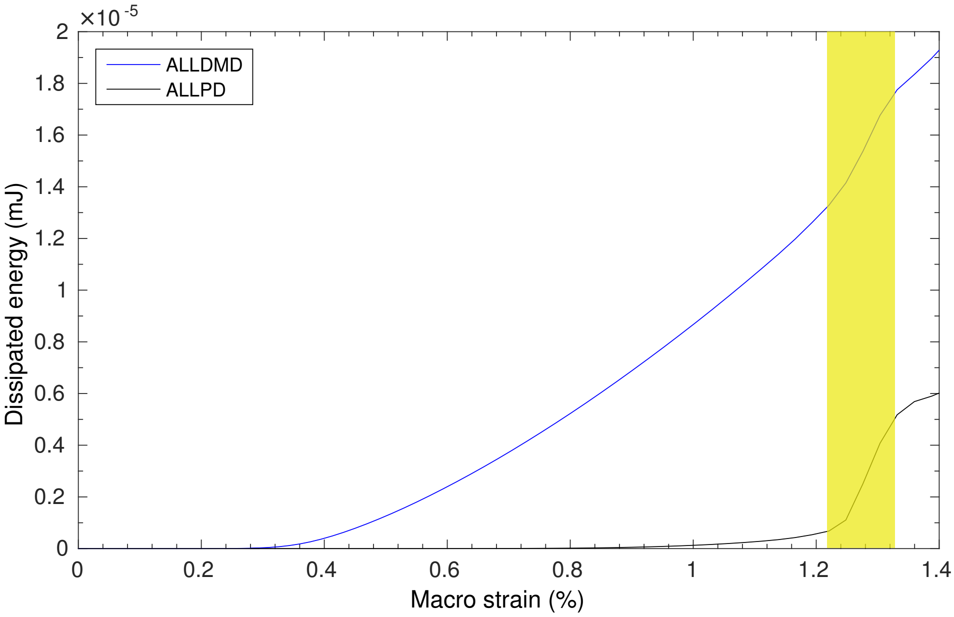

Figure 5.17: Damage (ALLDMD) and plastic (ALLPD) dissipation energy for the M40JB-TP80ep system with t=30 µm, where the energy increase corresponding to TC appearance is highlighted in yellow

6 Micromechanics numerical results and analysis

This chapter first considers the M40JB-TP80ep simulation results, including a description of how the interface parameters are defined, how the different boundary conditions lead to different results and how good a match with the experimental AE onsets can be obtained. The T800-TP175 system is discussed next; The plane-strain simulations run with the material properties of this second system, coupled with an analysis of the different issues faced when trying to define interface parameters as well as their effect on thermal residual stresses is presented. With the interface parameters allowing the numerical onset of transverse cracking to agree well with the experimental data being determined, the TC-related ERR is calculated and compared to the values obtained using the semi-analytical procedure, where the in-situ strength model is inverted. Finally, a short summary of the numerical results is presented.

6.1 M40JB-TP80ep system

6.1.1 Interface parameters calibration

Considering the low influence of the interface toughness on the results on the UNT90 simulation for this composite system, which are shown on Fig. 5.14, the strength of the interface was determined such that the results of this simulation matched the experimental transverse tensile strength of 24.5 MPa, leading to a normal interface strength value $\tau_i^n = 20\,\mathrm{MPa}$, and a corresponding shear strength $\tau_i^s = 30\,\mathrm{MPa}$. A parametric study is then run on the t=68 µm embedded cell model with boundary conditions enforcing a plane-strain state to determine the toughness G_i of the interface, by matching the numerical TC onset to the experimentally measured onset of damage determined by AE. The choice of using the 68 µm ply thickness for the interface toughness calibration is motivated by the fact that TC was shown in chapter 4 to be the clear dominant damage mechanism (no delamination observed and translaminar fracture of the 0° plies not reached) at that ply thickness. The numerical TC onset obtained is compared to the experimental AE onset as the latter is shown to be a correct indicator of TC growth in the bulk in chapter 4.

The results of the sensitivity analysis performed on the embedded cell model regarding interface parameter choice are shown on Fig. 6.1. As the experimentally determined strain at onset of TC in the bulk of the 75µm ply M40JB-TP80ep composite is 0.9%, the interface toughness was chosen at 3J/m^2 for this system. It is shown on an earlier version of this model [113] (6.2) that the variation of G_i shifts the total numerical scaling curve up and down but does not significantly affect its shape.

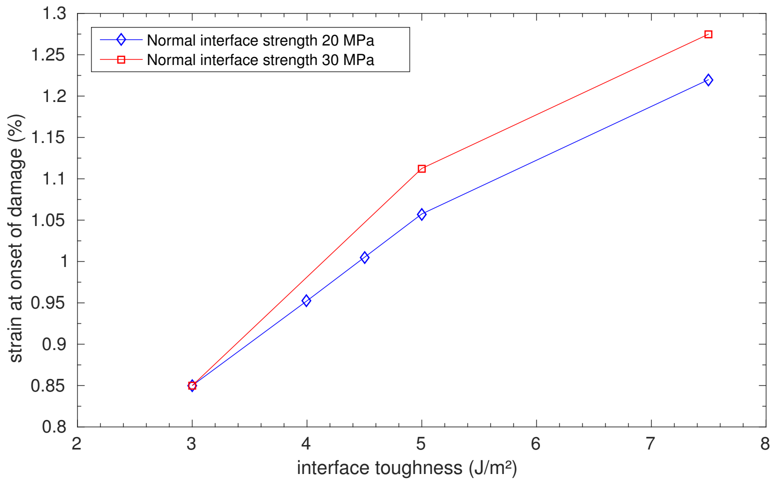

Figure 6.1: Sensitivity to interface normal strength τ_i^n and toughness G_i of the M40JB-TP80ep embedded cell model

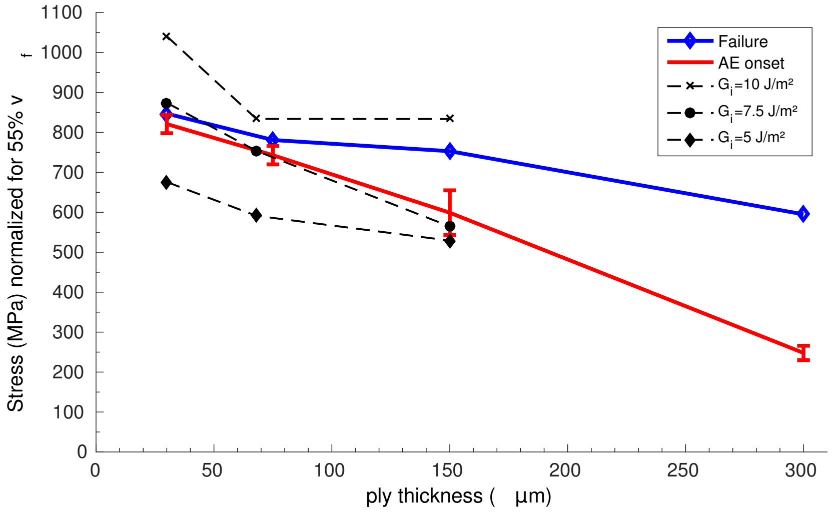

Figure 6.2: Sensitivity to G_i variations in a previous version of the model assuming isotropic fibres, adapted from [113]

6.1.2 Simulation parameters

The final simulations parameters used in the modelling of the M40JB-TP80ep system for all ply thicknesses and all boundary conditions are summarized in Table 6.1.

Table 6.1: Material properties used in the multiscale FE model for the M40JB-TP80ep system

UD lamina Properties	
Density (kg/m^3)	1500
Young's modulus E_{11} (GPa)	220
Young's modulus E_{22} (GPa)	7.01
Poisson ratio ν_{12} (-)	0.314
Shear Modulus G_{12} (MPa)	4661
Shear Modulus G_{23} (MPa)	2417
Fibre Properties	
Density (kg/m^3)	1750
Young's modulus E_{11}^f (GPa)	377
Young's modulus E_{22}^f (GPa)	11
Poisson ratio ν_{12}^f (-)	0.29
Poisson ratio ν_{23}^f (-)	0.45
Shear Modulus G_{12}^f (GPa)	44
Shear Modulus G_{23}^f (GPa)	3.5
Matrix Properties	
Density (kg/m^3)	1200
Young's modulus E_m (MPa)	3261
Poisson ratio ν_m (-)	0.35
Drucker-Prager parameter a	8.33
Drucker-Prager parameter b	2
Onset of damage compressive strain ε_c^c (%)	25
Onset of damage shear strain ε_s^c (%)	1.75
Onset of damage tensile strain ε_t^c (%)	1.75
Critical Energy Release Rate G_m (J/m^2)	64
Interface properties	
Normal interface Stiffness K_{nn} (N/mm^3)	2E7
Shear interface Stiffness K_{ss} & K_{tt} (N/mm^3)	4E7
Interface strength τ_1^0 (MPa)	20
Interface strength τ_2^0 & τ_2^0 (MPa)	30
Critical Energy Release Rate G_i (J/m^2)	3

6.1.3 Final numerical scaling and comparison with experimental results

Once the interface toughness is calibrated as described in section 6.1.1, a very good agreement between numerical and experimental results can be reached, as shown on Fig. 6.3. The high strain rate experimental acoustic emission threshold values is used for comparison with the plane-strain (bulk) simulation, as no viscous model is implemented numerically. The onset of free edge damage is used for comparison with the submodel (free edge) simulation.

It is interesting to note that the way transverse crack appear is very similar to the behaviour observed experimentally at the free edge and through the width of the sample: at 90° to the ply in the bulk simulations and at an an angle close to 45° in the free edge ones, as shown on Fig. 6.4. In the bulk model, cracks do nucleate indifferently throughout the thickness of the ply, depending on the local microstructure. To the contrary, in the free edge simulations, cracks do always start close to an edge of the RVE situated at the interface between the 90° ply and one adjacent ±45° ones due to the local stress-state. With interface properties set as low as is required here, the cracks do tend to propagate in a rather straight way, with some localised kinking in the t=150 µm model due to microstructure heterogeneity. However, with higher interface toughness values, a much larger kinking of the cracks around the fibres is observed.

Most importantly though, the change of boundary condition produced a change of transverse strength very similar to the one observed experimentally, lending further credit to the hypothesis that free edge cracking and bulk transverse cracking, due to very different stress-states, are two different mechanisms with different onsets. The predicted onset of damage for the thinnest plies exceeds the experimental values. However, because no translaminar fracture failure criterion is implemented in the 0° plies of these simulations, what is actually predicted by the t=30 µm model is that no TC is present before failure, which is in agreement with the experimental observations.

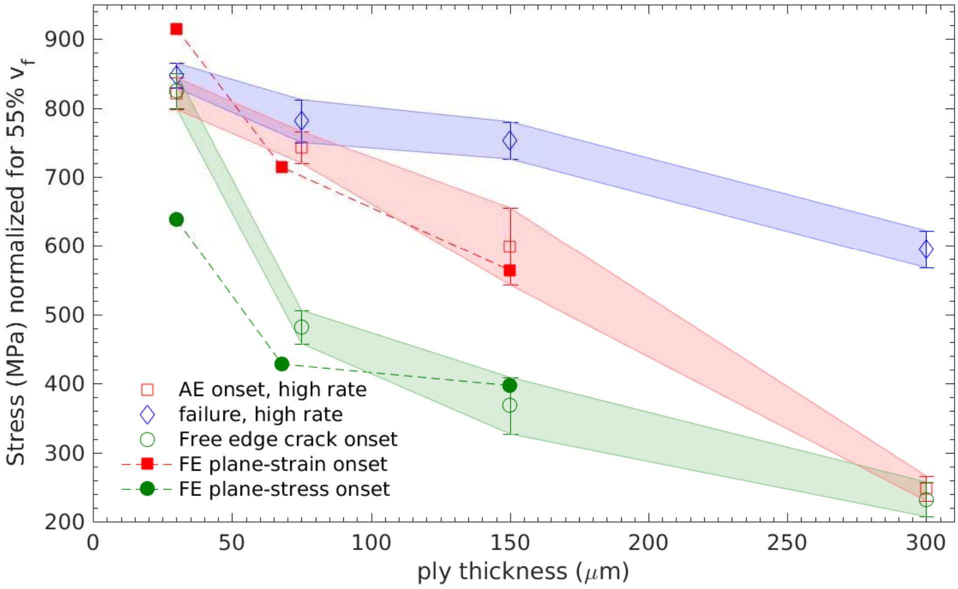

Figure 6.3: Comparison between FE predictions and experiments for the M40JB-TP80ep system

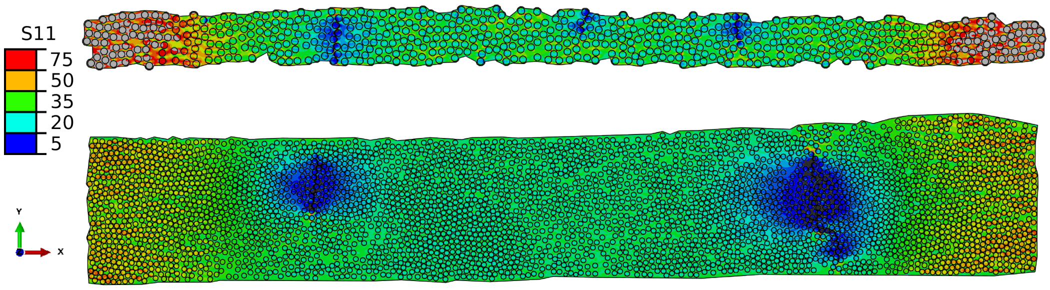

(a) Bulk / plane-strain

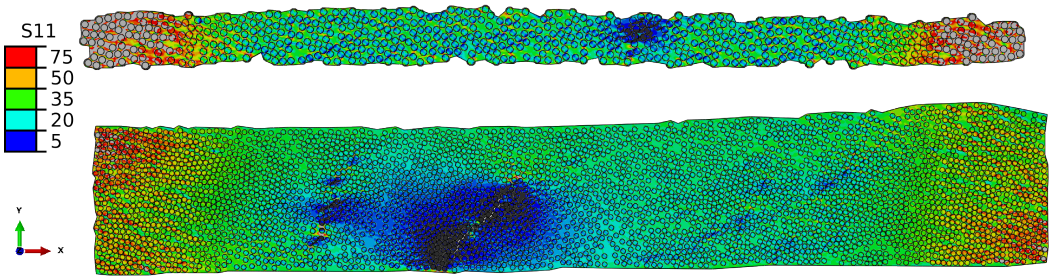

(b) Free-edge / Submodel

Figure 6.4: Crack onset contour plot for 150gsm and 30gsm M40JB-TP80ep system

6.1.4 Damage sequence observed in the simulations

The sequence of damage events in the plane-strain (bulk) simulations is remarkably similar for all three simulation. The first damage to appear is fibre-matrix debonding, which initiates for all ply thicknesses around 180 MPa applied stress in the laminate. This is consistent with the appearance of fibre-matrix debonding noted during in-situ SEM observations on this material using a CP laminate, and can be characterised as a weak interface as it is the first type of damage that develops. This debonding then leads to local stress concentrators in the matrix, plasticity damage accumulation and eventually transverse matrix cracking through coalescence of micro-damage. When this coalescence takes place, some matrix ligaments remain and bridge the two crack faces, being stretched as the crack further opens. It is interesting to note that this coalescence always starts in regions where the fibres are closely packed due to increased stress triaxiality. The main difference noted in the sequence of events between the three simulation is an increased capability to accumulate distributed damage before localisation with decreasing ply thickness. As seen on Fig. 6.5, the interface damage indicator (CSDMG) representing the loss of stiffness of the interface due to damage, show a very similar onset and initial increase for all ply thicknesses. However, as seen on the average equivalent plastic strain curves (PEEQ) in Fig. 6.5, large plastic strains only develop at a much higher strain for the thin ply laminate t=68 µm and t=30 µm. Indeed, it is only once coalescence is formed that the remaining matrix ligaments experience an increase of plasticity, quickly leading to the formation of a formed crack, where the local load bearing capability drops off. This typical damage development is shown on Fig. 6.6.

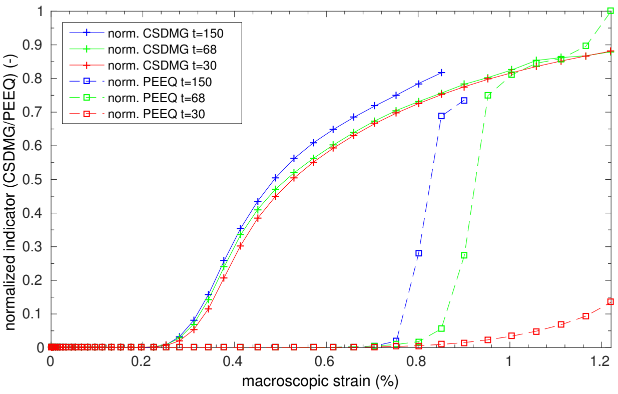

Figure 6.5: Average interfacial (cohesive) damage indicator CSDMG and equivalent plastic strain PEEQ for the three ply thickness modelled for the M40JB-TP80ep system

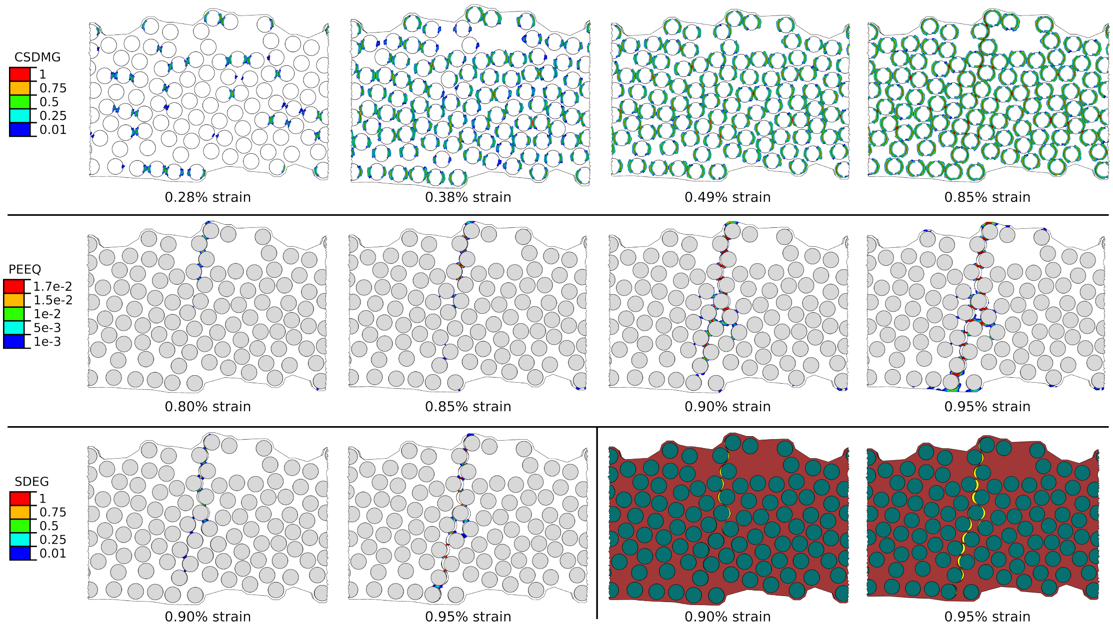

Figure 6.6: Damage evolution of a typical transverse crack in the 68 µm M40JB-TP80ep model. The PEEQ and SDEG contour plots highlight the matrix ligaments bridging the crack after coalescence of debonding has been reached. The two figures at the lower right corner highlight the crack opening with the formed void shown in yellow.

6.1.5 Stress-state at the free edge

The stress state at the free edge of the samples is analysed using the linear elastic homogenised 3D model used to drive the submodel to understand the reason for the angled TC observed at the free edges. No significant difference is noticed between the different ply thicknesses when computing the mean stress components in the microstructure zone. The t=68 µm model is analysed in detail, with the usual convention of the index 1 for the fibre direction and 3 for the stacking direction. At an applied strain of 0.95%, the mean transverse tensile stress $\overline{\sigma}_{22}$ in the 90° layer at the free edge is nearly doubled compared to the mean stress ontained from CLT prediction, with a mean value of 115 MPa. Simultaneously, the 90° ply at the free edge is under a tensile out of plane stress $\overline{\sigma}_{33}$ close to the same value, at a mean 102 MPa. This "through the thickness" stress tends to split the ±45° layers away from the 90° one and thus promotes delamination. Furthermore, the mean shear stresses $\overline{\tau}_{12}$ and $\overline{\tau}_{13}$ are negligible within the 90° ply, increasing only very close to the ply boundaries. However, the component $\overline{\tau}_{23}$ cannot be neglected, as it reaches a mean value of 75 MPa, as shown on Fig. 6.7. At the free edges, the 90° ply within the selected quasi-isotropic laminates is thus under combined bi-axial tension and transverse shear. It is this combined stress-state that is responsible for the angle of the transverse cracks observed at the free edge. With a principal stress analysis, the angle of the crack can be easily deduced, assuming that the crack is normal to the principal stress direction.

With the above mentioned values, it is possible to obtain the crack angle ϕ as

$$\phi = \frac{1}{2}\arctan\left[\frac{\overline{\tau}_{23}}{\left(\frac{\overline{\sigma}_{22}-\overline{\sigma}_{33}}{2}\right)}\right] = 42.5° \tag{6.1.1}$$

which is very close to what is observed experimentally.

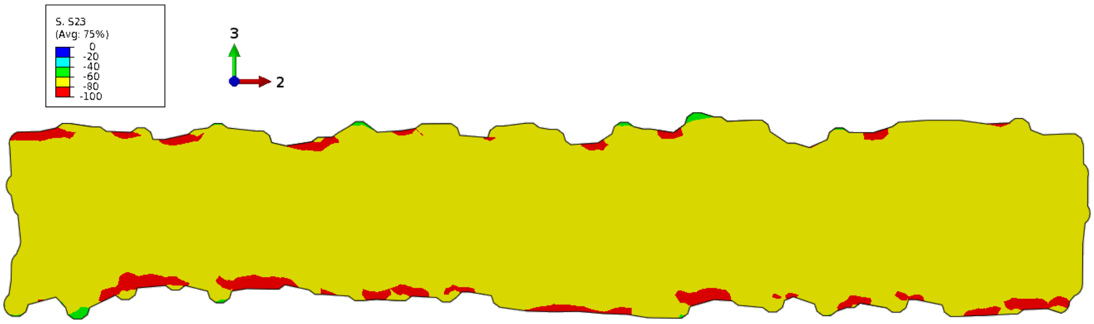

Figure 6.7: τ_{23} stress at the free edge of the t=68µm M40JB-TP80ep model

6.1.6 90° ply homogenisation

In order to ensure that the homogenised ply behaviour of the plies do not vary with ply thickness, their behaviour are numerically homogenized to extract average stress-strain curves, as shown on Fig. 6.8a. As the homogenized behaviour turns out to be equivalent in all three ply thicknesses but for the strain at which damage localisation happens, an attempt can be made to model the diffuse damage as a hardening behaviour in an elasto-plastic simulation. To this effect, the elastic modulus is measured at 6GPa, and the hardening curve defined as shown on Fig. 6.8b by measuring the plastic strain at several locations on the 30gsm curve shown on Fig. 6.8a. The resulting behaviour of the homogenised elastoplastic ply can then be measured by replacing the whole 90° layer of the simulated laminate, including the embedded cell by the newly defined elasto-plastic homogeneous material. Averaging its behaviour in all elements once again, it is shown on Fig. 6.8c to be in very good agreement with the mechanical response observed in the embedded cell until the respective damage localisation strains of the three simulated laminates.

The elastic modulus obtained from homogenisation is notably lower than the one measured experimentally and reported in Table 3.1, but much closer to the one predicted by the rule of mixture at the given fibre volume fraction. This can be explained by the fibre waviness due to the processing, locally changing the angle from the expected perfect 90° to the loading direction and thus increasing the sample's stiffness.

For continuum level laminate failure prediction, TC can therefore be modelled using either cohesive elements within the 90° plies or could be integrated as a ply thickness dependent ductility criterion on the transverse stress-strain relation of the ply.

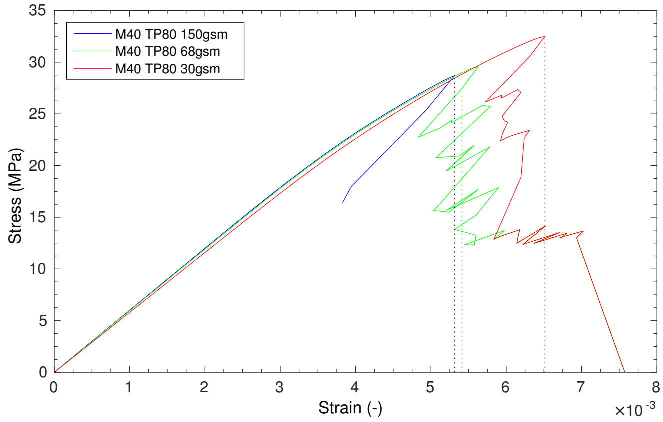

(a) Comparison of homogenised behaviour of M40JB-TP80ep system for the 3 ply thicknesses

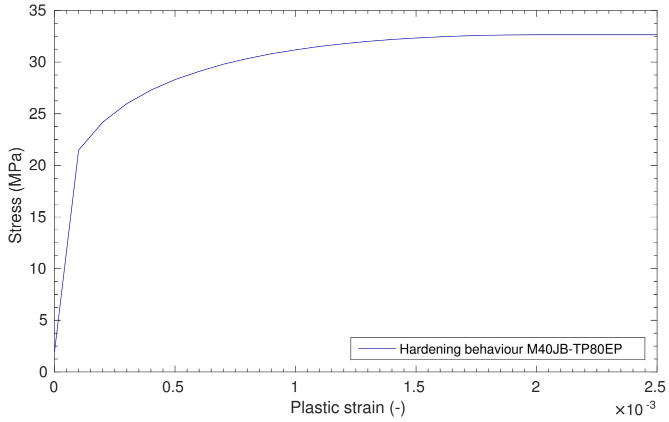

(b) Hardening curve computed from averaged stress-strain M40JB-TP80ep embedded cell models. The onset of plastic strain can be seen around 21 MPa.

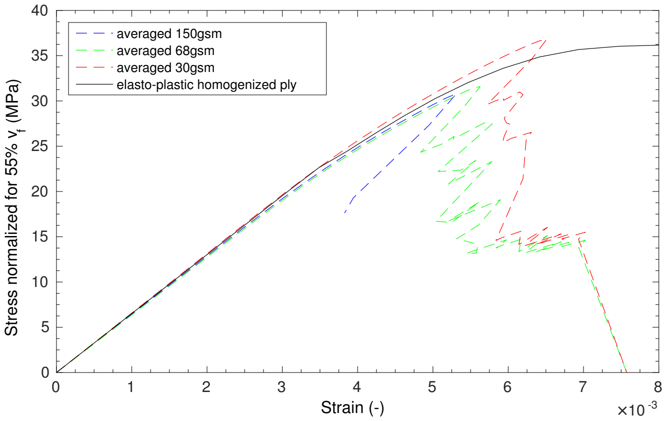

(c) Comparison between M40JB-TP80ep homogenized elasto-plastic ply behaviour and averaged micromechanical embedded cell behaviour for the same system

Figure 6.8: M40JB-TP80ep 90° ply homogenisation

6.2 T800-TP175 system

6.2.1 Microstructure considerations

In order to isolate the influence of the microstructure on the results and keep the comparison between constituent properties, the same microstructures as in the M40JB-TP80ep are used first, with the appropriate T800-TP175 material and lamina properties. They are later changed to the real identified or randomly generated T800-TP175 ones in section 6.2.6 to study the effects of microstructures with a given set of material parameters.
The thermal residual stresses do not seem to be affected by the ply thickness, as the mean values of all the stress components within the embedded cell, as well as their standard deviation are equivalent for all 3 ply thicknesses modelled for given microstructures and material parameters. Had there been a change in the local stress concentrators due to ply thickness, the standard deviations at least would have changed significantly. This is not all too surprising, as the critical close packing region will have similar fibre distributions for all ply thicknesses, the perfect hexagonal packing being their natural limit.

6.2.2 Interface parameter calibration

In this instance, the use of the UNT90 RVE model did not prove successful, despite taking into account the thermal stresses. The use of an interface strength/toughness pair allowing the transverse tensile strength of the material to be replicated numerically during a UNT 90° simulation lead to a large underestimation of the onset of damage in the bulk as predicted by the embedded cell, plane-strain model, as shown on Fig. 6.9. With the high size effect present in such experimental UNT90 tests, it is very likely that early localisation takes place in some part of the laminate due to edge effects, manufacturing imperfection or local matrix damage, leading to the early propagation of a critical crack due to the unconstrained nature of this test. Such a mechanism cannot be accurately captured by an RVE approach.

Consequently, a sensitivity analysis was performed directly on the embedded cell with t=68 μm, as shown on Fig. 6.10. The results demonstrate that the onset of damage predicted by the plane-strain model can be matched to the AE onset for that ply thickness either by increasing the strength or by increasing the toughness of the interfaces, with a noticeable difference in the local 90° ply maximum S_{22} stress reached depending upon the pair of parameters chosen.

Increasing the interface toughness with a low interface strength value allows a higher macroscopic strain at onset of damage to be reached with lower local transverse stresses in the 90° layer than if the interface strength was increased instead. This is due to the early diffuse debonding happening during the simulation of the thermal step due to the low interface strength, which reduces the ply stiffness. To the contrary, increasing the strength of the interface leads to a more fragile behaviour, with a linear elastic local stress-strain behaviour until localisation and abrupt ply fracture. This is shown in Fig. 6.11 where simulations with lower

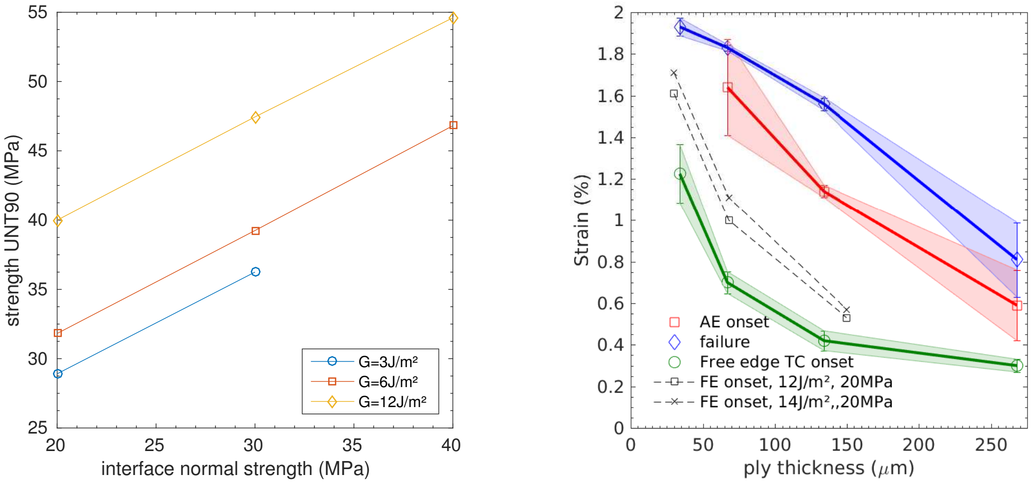

(a) UNT90 model sensitivity, 41.5 MPa UNT 90 strength targeted

(b) embedded-cell model scaling

Figure 6.9: Interface strength and toughness identification using the UNT90 degree simulation, and its resulting scaling compared to the experimental results.

interface strength exhibit a strong reduction of the transverse modulus after the thermal step. For a given interface strength, the toughness is shown to control the onset of localization (load drop).

It is interesting to note that for a given interface toughness of G_i= 14 J/m^2, the initial increase in interface strength from 20 MPa to 40 MPa actually reduce the transverse strength of the embedded 90° ply (see Fig. 6.10b). This can be explained by the transition from a weak interface behaviour where debonding occurs everywhere in the embedded cell, as was the case for the M40JB-TP80ep system, to a stronger interface behaviour which is dominated by plastic strain and damage localisation. As local stress concentrators are larger in the latter case, localisation is more easily achieved, leading to the observed reduction of the ply's transverse tensile strength. Further increase in interface strength do however lead to higher transverse tensile strength as the behaviour type does not change any more.

Considering the change in average ply modulus, experimental in-situ strain measurements could allow the correct strength/toughness pairing to be determined, and would be a much easier solution to implement than in-situ push-in or push-out tests. Although thin-ply laminates are too thin for this, FBG sensors could be embedded in a transverse ply of a t=150 μm laminate for local strain measurements. However, as this is not within the scope of the present work, further simulations using the same interface toughness as determined for the M40JB-TP80ep system were performed, and their relative scalings shown on Fig. 6.12. Clearly, comparing the strength values required to match the experimental AE onset when using such low toughness values to the UNT90 sensitivity analysis shown on Fig. 6.9a, the simulated transverse tensile

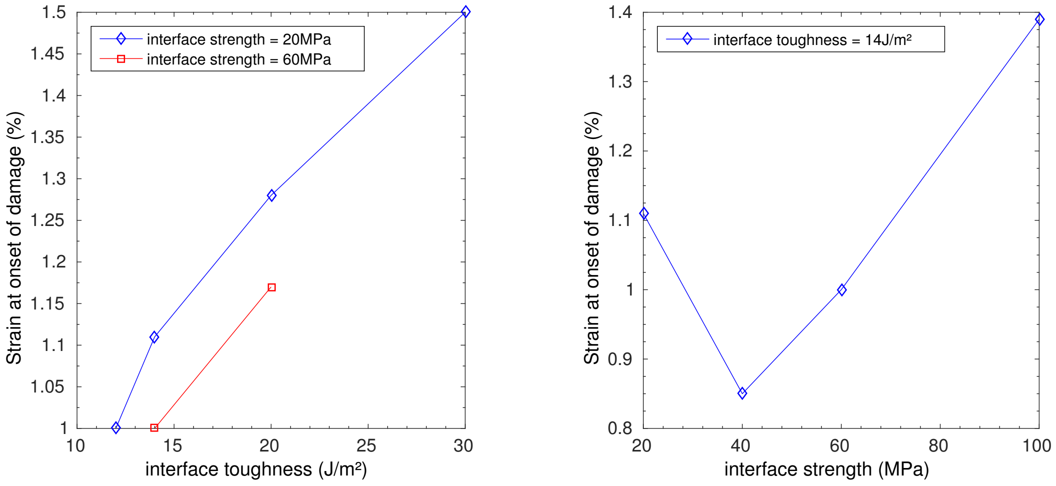

(a) sensitivity to interface toughness (b) sensitivity to interface strength

Figure 6.10: Interface strength and toughness sensitivity analysis performed on the t=68 µm embedded cell model for the T800-TP175 system. Strain at onset of damage refers to TC onset as defined in section 5.4.1.

strength using the UNT90 RVE will be overestimated compared to the experimental UNT90 tests results performed on thick 90° UD specimen. This difference leads to the postulation that the behaviour of UD transverse tensile specimen is controlled by the weakest point of the specimen, which would suggest a Weibull type of size effect, such as the one observed for neat resin tensile tests [74, 78] or laminates [114].

From this sensitivity analyses performed on the t=68 µm embedded cell model, it is observed that numerous interface strength/toughness combinations can be found that will allow a good match with the experimentally measured AE onset at a given ply thickness. It is therefore very interesting to compare the influence of the different pairings on the scaling of the onset of TC with respect to ply thickness. Consequently, three sets of simulations are performed, as described in Table 6.2. Their homogenised transverse behaviour are shown on Fig. 6.13, and their respective onset of damage scaling with decreasing ply thicknesses shown on Fig. 6.14.

Table 6.2: Chosen interface parameter pairs to study the scaling of bulk damage onset with respect to ply thickness

property/scenario	strong interface	tough interface	mix
G_i (J/m^2)	3	36	14
τ_i^n (MPa)	200	20	130
AE onset t=68 µm (%)	1.56	1.56	1.56

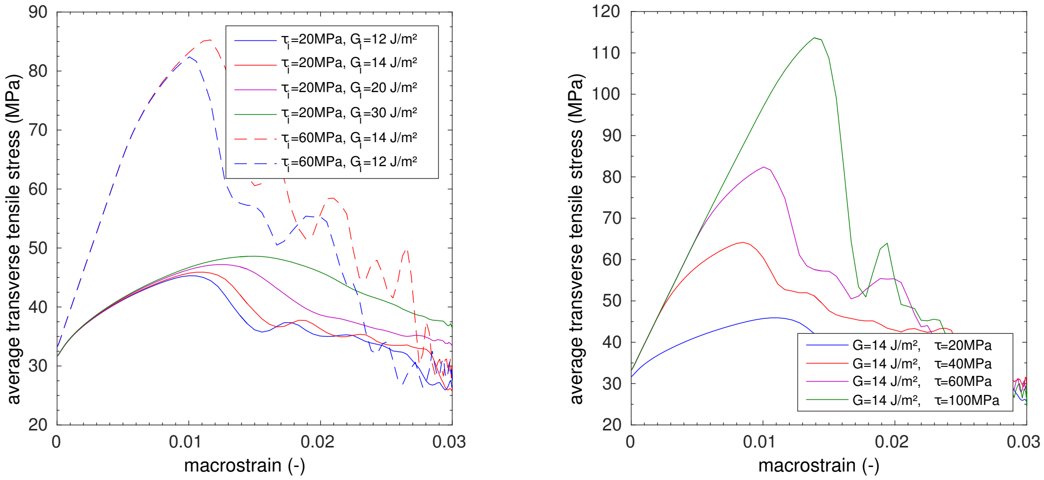

(a) sensitivity to interface toughness

(b) average 90° ply S_{22} vs applied strain

Figure 6.11: Interface strength and toughness sensitivity analysis performed on the t=68 µm embedded cell model for the T800-TP175 system showing the respective average 90° ply transverse tensile stresses vs applied strain

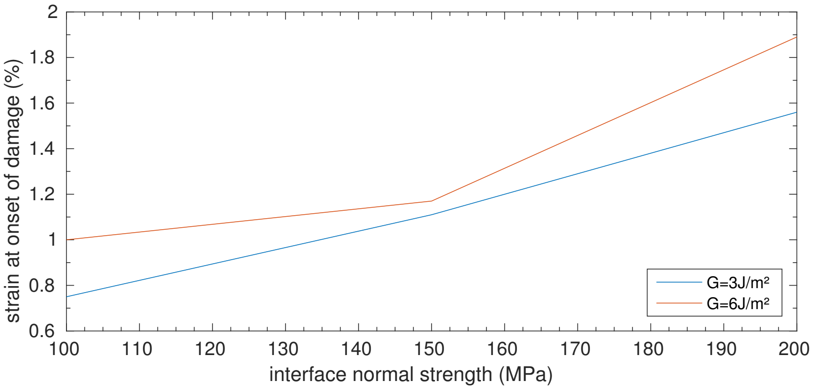

Figure 6.12: Sensitivity analysis performed on the t=68 µm embedded cell model with high interface strength and low interface toughnesses

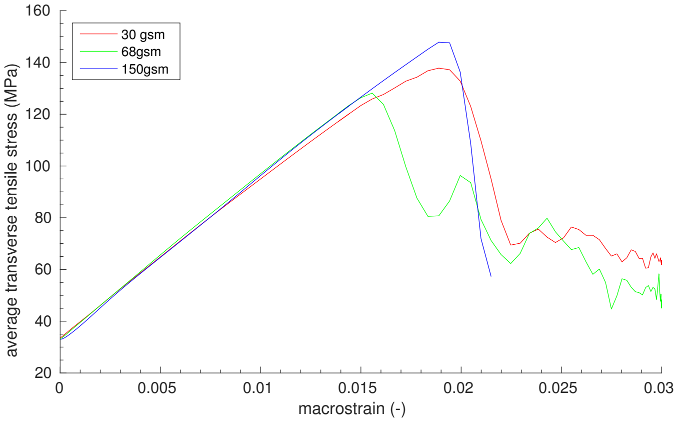

(a) strong and brittle hypothesis

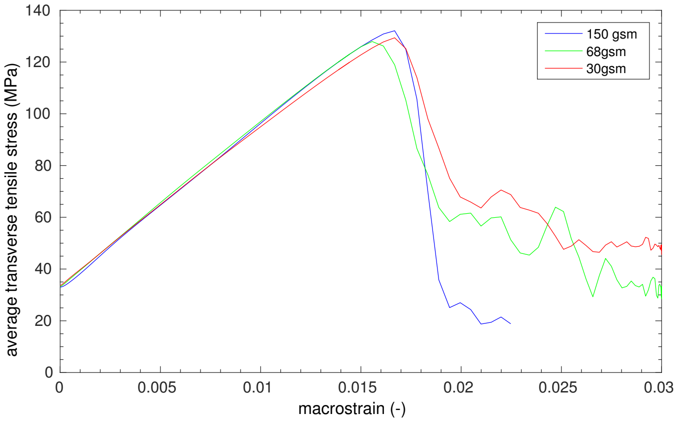

(b) mixed hypothesis

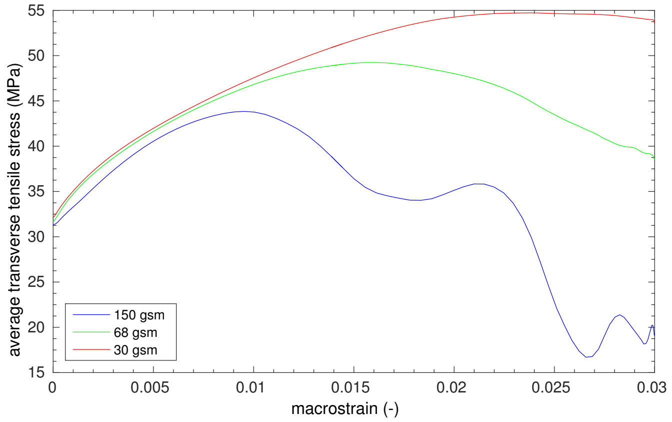

(c) tough and weak hypothesis

Figure 6.13: Average transverse tensile behaviour for the 3 different interface hypotheses

In the strong interface model shown on Fig. 6.13a, a sudden localization in the t=68 µm RVE is not coherent with ply thickness scaling observed experimentally. This can be attributed to a "weak" point due to very close packing, which is magnified by the very high stresses developed when no debonding can occur and thus lead to early localisation. In a model with mixed properties, as shown on Fig 6.13b, no clear evolution of onset of TC with ply thickness can be seen. This shows that scaling actually depends on both interface strength and toughness and thus would require more in depth experimental characterization to improve the model. Most likely, the 130 MPa interface strength is still too high to allow debonding to occur early enough to trigger localisation. However, it was low enough to allow stress relaxation in the close packing region of the t=68 µm model compared to the strong and brittle interface hypothesis, or the toughness was high enough to accommodate an interface breakage without triggering localisation. Finally, if a weak but tough interface is modelled, as shown on Fig 6.13c a logical scaling compared to the experimentally observed AE onset is recovered where reduction of ply thickness increases the onset of TC very significantly.

As discussed above, depending on the chosen interface properties identified on the 68 µm ply thickness, the predicted scaling of TC onset can vary very significantly and could completely differ from the observed experimental scaling for other ply thicknesses, as shown on Fig 6.14. Accurate, experimentally determined interface properties are thus very important to improved numerical prediction of TC.

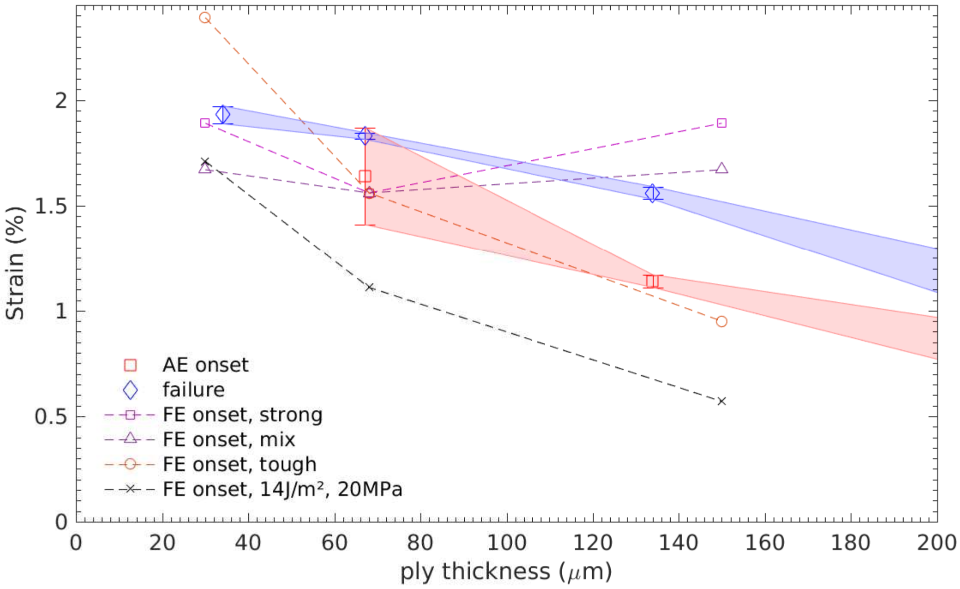

Figure 6.14: TC onset scaling under several interface hypotheses

Most importantly, the onset of TC differs strongly depending on whether the interface strength or the interface toughness is increased. As mentioned for the M40JB-TP80ep system, increasing only the interface toughness from the 14 J/m^2 to 36 J/m^2 results in a translation of the curve to higher strains without affecting its shape markedly. To the contrary, increasing the strength of the interface delays the appearance of TC irrespective of the ply thickness, as by preventing debonding it also delays the ulterior coalescence of debonds required to grow a transverse crack. In practice, matrix damage might control the crack formation in such a case, but the very high matrix ductility and toughness values used in these simulations do prevent it. No sensitivity analysis was performed on the matrix parameters to this effect considering that the fibre-matrix interface is generally regarded as weaker than the matrix itself.

The major reason for the much increased interface properties required in the simulations of this system is the thermal step predicting the residual thermal stresses. The average residual stresses shown on Fig. 6.15a reach between 12 MPa to 39 MPa, but local stresses can peak at much higher values in regions of strong resin confinement. It is thus no surprise that advanced thermoplastic toughened epoxy blends are needed to reach high performance in high Tg composites. Without such reinforcements, the composites would crack right after curing. A directly proportional dependence of the temperature differential on the onset of TC is shown on Fig. 6.15. Considering that the fibre-matrix bonding process as well as the matrix thermo-mechanical properties during composite curing are not well understood yet, applying a 125 °C temperature differential might overestimate the residual stresses, which would have a direct impact on the identified interface properties. Residual stress measurements & model validation are therefore critical to obtain good predictions.

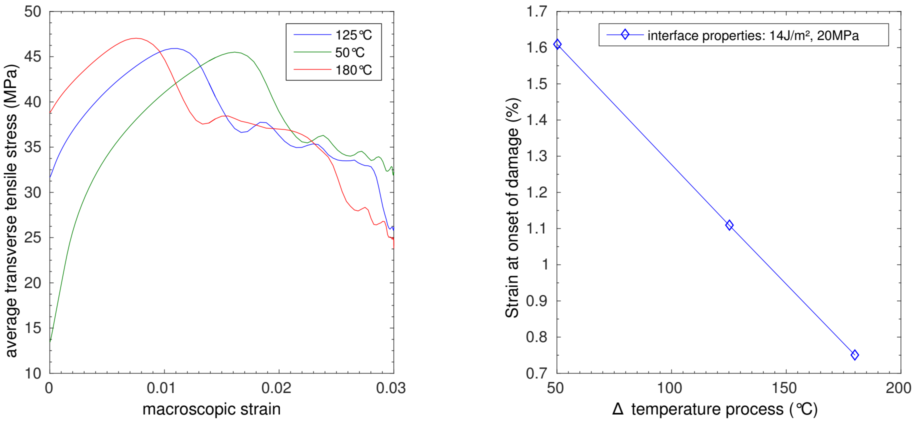

(a) average 90° ply S_{22} vs applied strain

(b) onset of damage scaling with temperature

Figure 6.15: Average transverse tensile stress versus applied strain curves for three different temperature differentials and their associated predicted onset of damage.

It should be noted that, because of the multiscale nature on the model used, two levels of thermal stresses are accounted for in the micro structured region. Firstly, the continuum level residual stresses in the 90° ply are represented by the overall stress transferred to the microstructured region by the neighbouring continuum regions. Secondly, the local (micro fluctuation) thermal stresses are modelled as well by the difference of CTE between the resin and fibres. It is interesting to note that in a classical CLT calculation of residual stresses, only the homogenized residual stresses are captured which are significantly lower than the local ones developed at the micro scale, for example at the fibre-matrix interface. Indeed, once averaged, the micro fluctuations of residual stresses should cancel out and would not appear at the continuum level. This reasoning could explain why such high values of fibre-matrix interface stresses were obtained and why it was necessary to significantly increase the interface properties of the TP175 system to get close to the experimental observations. Further investigations on the actual thermal residual stress build-up at the microscale would be necessary to enhance the fidelity of the model, for example through measurement using embedded FBG sensors.

Based on the results of the present parametric study, it can be concluded that the interface strength for this material has to be comprised between 20 MPa and 130 MPa. Indeed, the latter value is shown to prevent the formation of debonds and thus their coalescence into transverse cracks for all ply thicknesses. On the other hand, the highly ductile behaviour of the transverse ply and the extent of interfacial damage prior to loading with the low bound value is judged unlikely.

Further simulations, complemented by an experimental characterization of the interfacial shear strength by push-in test such as proposed by Rodriguez et al. [81] would give more insight into this behaviour. Consequently, despite the difficulties encountered in the calibration of the interface properties, the tough interface hypothesis is used to show the scaling that can be reached.

6.2.3 Simulation parameters

The final set of simulations parameters used in the modelling of the T800-TP175 system for all ply thicknesses, leading to the predicted onset of damage in the bulk of the material shown on Fig. 6.16, are summarized in Tables 6.3 for the mechanical properties, whilst the thermal properties can be found in Tables 5.1 and 5.2.

Table 6.3: Material properties used in the multiscale FE model for the T800-TP175 system

UD lamina Properties	
Density (kg/m^3)	1500
Young's modulus E_{11} (GPa)	163
Young's modulus E_{22} (GPa)	7.77
Poisson ratio ν_{12} (-)	0.314
Shear Modulus G_{12} (MPa)	5572
Shear Modulus G_{23} (MPa)	2680
Fibre Properties	
Density (kg/m^3)	1750
Young's modulus E_{11}^f (GPa)	292
Young's modulus E_{22}^f (GPa)	10.4
Poisson ratio ν_{12}^f (-)	0.29
Poisson ratio ν_{23}^f (-)	0.45
Shear Modulus G_{12}^f (GPa)	26
Shear Modulus G_{23}^f (GPa)	3.49
Matrix Properties	
Density (kg/m^3)	1200
Young's modulus E_m (MPa)	3261
Poisson ratio ν_m (-)	0.35
Drucker-Prager parameter a	6.29
Drucker-Prager parameter b	2
Onset of damage compressive strain ε_c^c (%)	25
Onset of damage shear strain ε_s^c (%)	3.74
Onset of damage tensile strain ε_t^c (%)	3.74
Critical Energy Release Rate G_m (J/m^2)	256
Interface properties	
Normal interface Stiffness K_{nn} (N/mm^3)	2E7
Shear interface Stiffness K_{ss} & K_{tt} (N/mm^3)	4E7
Interface strength τ_1^0 (MPa)	20
Interface strength τ_2^0 & τ_2^0 (MPa)	30
Critical Energy Release Rate G_i (J/m^2)	36

6.2.4 Final numerical scaling and comparison with experimental results

Once the interface parameters have been set according to the previous discussion (assumption of a weak but tough interface), the simulated onset of damage in the plane-strain model can be compared to the AE onset measured experimentally, as shown on Fig. 6.16.

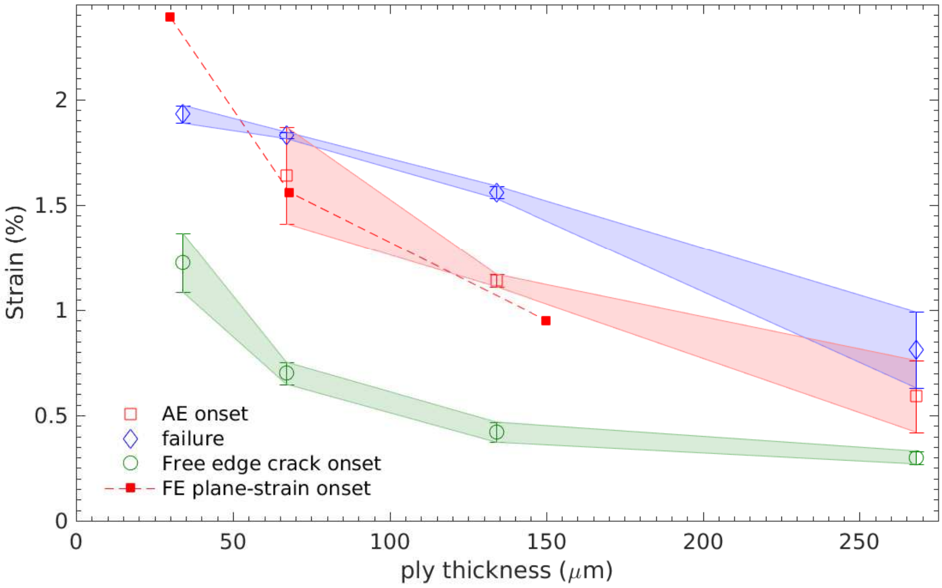

Figure 6.16: Comparison between FE predictions and experimental results for the T800-TP175 system

Comparing the plan-strain (bulk) simulations to the AE onset of damage, a very good agreement is noted for the two intermediate ply thicknesses. The t=30µm simulation overestimates the onset of damage strain, but this is due to the lack of translaminar fracture of the 0° plies in the simulations. It was shown experimentally that both AE onset and translaminar fracture happen statistically simultaneously at that ply thickness, the former most likely caused by the latter instead of TC propagation. Taking this failure mechanism into account would therefore have capped the simulations at the correct onset of damage strain if it had been implemented. As mentioned in section 6.2.2, the interfacial strength is not yet well determined in this simulation, and further work is needed to obtain a truly predictive model of TC with independent measurement of interface properties. Nevertheless, the present results show that, if the interface is assumed weaker than the matrix, a relatively accurate scaling of TC onset can be obtained with the embedded cell model.

6.2.5 Damage sequence observed in the simulations

Assuming the tough interface hypothesis (see Table 6.2), the damage sequence observed is similar to the one exhibited by the M40JB-TP80ep, with the slight difference that distributed debonding has already occurred during the simulation of the thermal residual stresses and that distributed plasticity in the matrix ligaments can therefore develop from the beginning of the loading. This is not the case when a stronger interface is modelled, as the strength of the interface obviously defines the applied strain at which debonding appears. The normalised average equivalent plastic strain development, shown on Fig. 6.17 for the weak but tough interface, slows down with decreasing ply thickness, as was very visible in the case of the t=30 µm M40JB-TP80ep simulation shown on Fig. 6.5. The debonding after simulation of the residual stresses and its increase during loading is also limited with decreasing ply thickness.

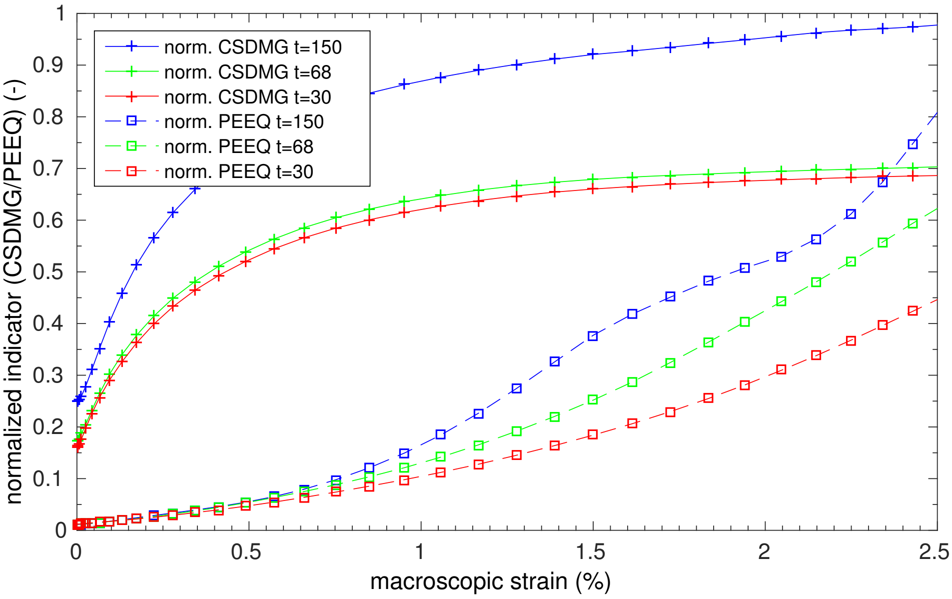

Figure 6.17: Average interfacial (cohesive) damage indicator CSDMG and equivalent plastic strain PEEQ for the three ply thickness modelled for the T800-TP175 system

Finally, it should be noted that due to the residual thermal stresses, the matrix has on average already exceeded its yield strength before loading begins. This is shown on Fig. 6.18a where the average pressure and von Mises stresses are plotted for both systems modelled, together with their respective yield function. It can also be seen in the contours plot shown on Fig. 6.18b, where the higher triaxiality in the densely packed fibre regions can be recognised. The ductile behaviour of the matrix in stress-states presenting a triaxiality $0.6 \leq \eta \leq 1$ therefore plays a major role, and the absence of experimental test for this kind of loading in this work calls for some caution to be exerted in the analysis of the results. Should the ultimate strength of the resin be reached before damage localisation in some area, it would lead to early matrix cracking without prior debonding. This is one of the reason which could explain the early TC observed in tomography for this system. (see section 4.4.3)

Whether this local damage then triggers an early TC or remains limited depends on the local microstructure and stress-state. It is therefore possible that cavitation failure of the matrix in some densely packed region could have triggered small premature low energy TC or allowed the contrastant to penetrate into the width of the samples through the damaged matrix without the presence of an actual fully extended TC.

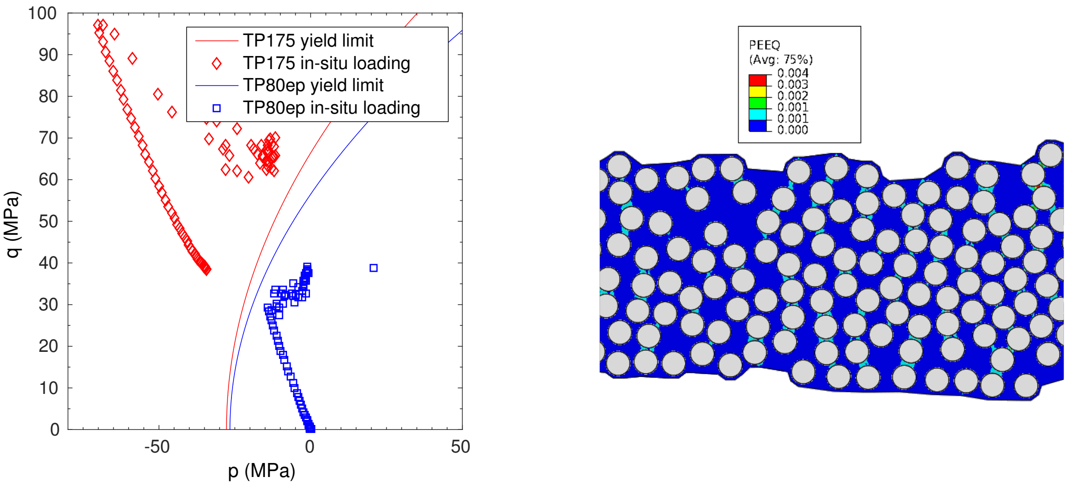

(a) Matrix P-Q graph (b) T800-TP175 PEEQ contour plot

Figure 6.18: Matrix plasticity due to thermal residual stresses, shown in contour plots before loading on the right and on its P-Q plot during loading compared to the TP80ep resin with no residual stresses on the left

6.2.6 Effect of microstructure variations

Changes in the microstructures of the models using the same material and interface properties yield interesting changes. Using the Random Sequential Adsorption (RSA) algorithm implemented in Viper [112] to generate several microstructures of equivalent statistical fibre diameter, ply thickness and fibre volume fraction to the ones measured experimentally, the applied strain at TC onset is on average 7.3% higher to the one obtained using the M40JB-TP80ep microstructure for the t=34 µm models, increased by 12.2% for the t=67 µm and increased by 24.8% for the t=134 µm one, as shown on Fig. 6.19. For all ply thicknesses, the simulations using the actual identified T800-TP175 microstructures yield TC onsets which are equivalent to the low end of the standard deviation of those obtained using the RSA algorithm.

Considering the discussion in section 6.2.2, the scaling obtained using the correct microstructures for this material points towards a slight overestimation of the interfacial toughness and a slight underestimation of the interfacial strength. A new calibration of interface parameters using these microstructures should therefore be performed to obtain the best interfacial prop-

erties. However, for the purpose sought here, the differences in TC onset noted when changing the microstructure demonstrate that it has a non-negligible effect, and actually allow a better agreement with the experimental data for the interface properties used here.
Furthermore, the importance of inter-fibre distance is highlighted by performing simulations on a subset of the previously computed ones, where the fibre radius is reduced by 5% for all fibres. The strains at onset of TC thus obtained are on average 21.8% higher for the t=34 µm models, 15.5% higher for the t=68 µm models and 21% higher for the t=134 µm models, as shown on Fig. 6.19. The sensitivity to closely packed fibre regions observed in the previous simulations is thus verified.

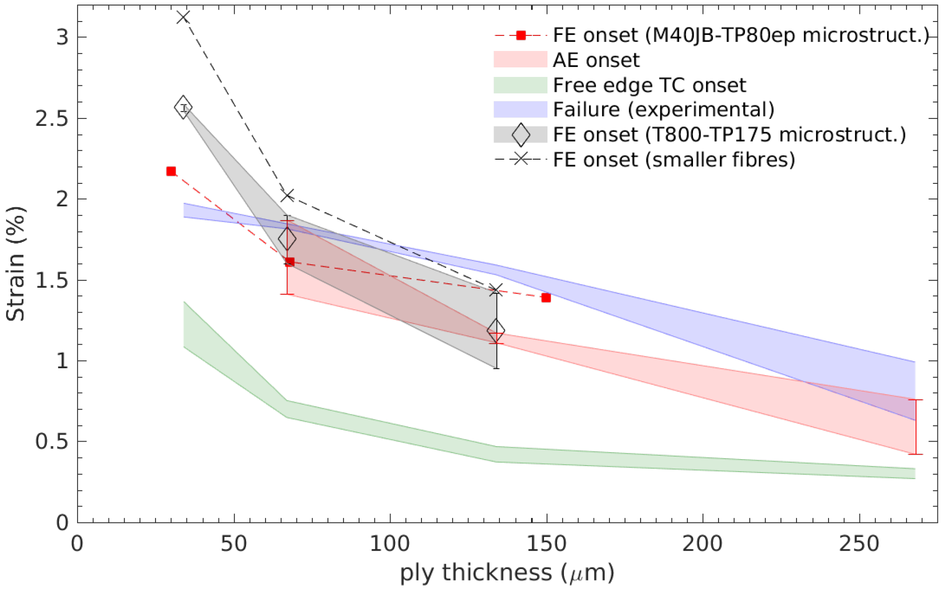

Figure 6.19: Scaling obtained when using the microstructures identified on the actual T800-TP175 samples. The grey standard deviation patch represents the different results obtained using randomly generated microstructures. The effect of fibre radius and thus inter-fibre distance is highlighted.

6.3 Comparison of both systems and result analysis

The damage sequence observed in the predictions of the bulk damage for both systems is in good agreement with prior experimental observations [41] and numerical simulations [41, 55, 56, 69]. Furthermore, the scaling of damage onset with respect to ply thickness is in good agreement with both the experimental observations performed as well as with the numerical in-situ transverse strength prediction of Arteiro et al. [69] in the same ply thickness range.
The very good agreement obtained between AE onset and plane-strain simulation allow to attribute the critical damage mechanism in this ply thickness range to transverse cracking, as

observed experimentally in tomography. The same damage sequence is present in these simulations, and the localisation of the critical damage is delayed with decreasing ply thickness.

The importance of the matrix ductility and fibre-matrix interface, highlighted in previous work [7], is shown here to have a very important impact on the simulated TC onset in the presence of large residual stresses. Indeed, these thermal residual stresses could exceed the yield limit of the matrix before mechanical loading. The absence of a beneficial "thin-ply" effect in the standard low toughness 180 °C curing system noted in [7] can now be attributed to matrix damage during the cooling phase of the curing. The damaged material zones promote further damage growth during loading, facilitating the appearance of transverse cracks with lower driving force. Localisations of damage could therefore be present prior to loading if a more brittle resin is used, which would explain the lack of increase of in-situ strength with decreasing ply thickness.

6.4 Critical ERR calculations

The critical ERR attributed to the first TC appearance is computed from the embedded cell simulations for both systems as discussed in section 5.4.3 and shown on Fig. 6.20. Both systems show the same tendency of a decreasing toughness with decreasing ply thickness, as was the case for the experimental values shown on Fig. 4.32. This phenomenon as well as the critical ERR levels obtained are in good agreement with the previous work of Saito et al. [23] where a range of $20\mathrm{J/m^2}$ to $40\mathrm{J/m^2}$ was computed for cross ply-laminates of similar ply thicknesses. It should be reminded that the computed critical ERR is based on the sudden increment in energy dissipation developed during the propagation of the TC in the FE results. The part of energy dissipated prior to localization by distributed debonding and plasticity is not taken into account in this measure.

It is particularly interesting to note that the fact that the microscale FE prediction shows a decreasing trend in apparent toughness while using the same material properties is a strong hint towards the justification of a ply thickness dependent toughness for TC. Indeed, whilst the validity of linear elastic fracture mechanics could be questioned when estimating the apparent toughness by inverting the in-situ strength model in section 4.5.2, the microscale FE simulations used in this chapter provide a fully non-linear, highly detailed representation of the mechanisms at play in the composite. The fact that such a complex model shows a similar trend to that of the LEFM expression seem to demonstrate that the distributed damage and plasticity in the ply does not necessarily affect the damage localization that controls TC development and its scaling with ply thickness.

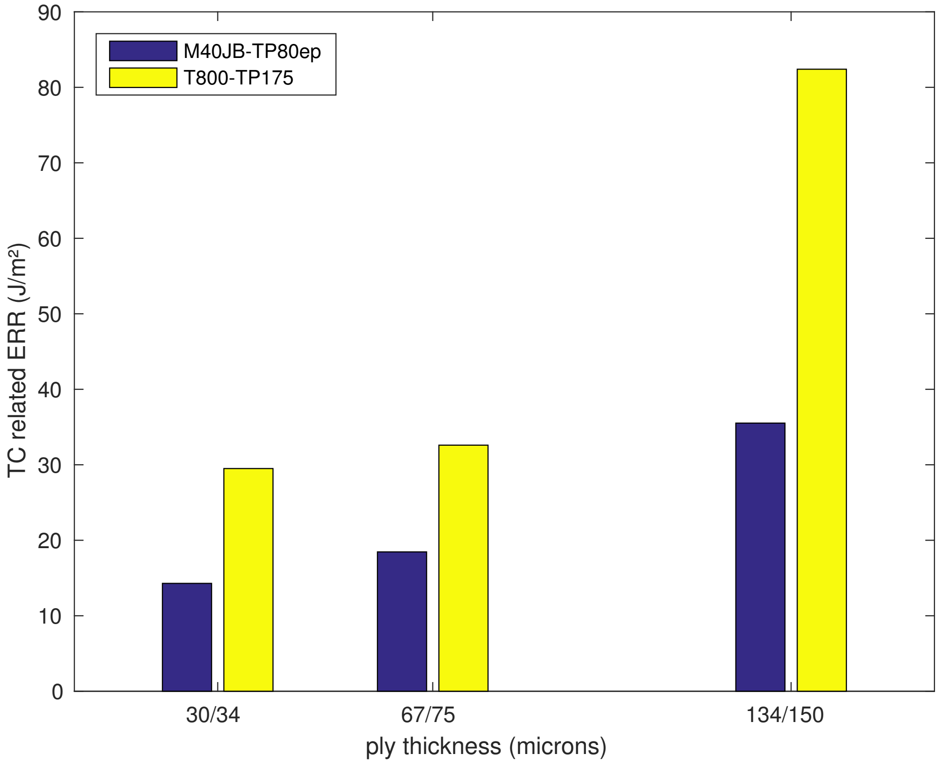

Figure 6.20: Numerical critical ERR for both simulated systems (plane-strain simulation)

6.5 Summary of numerical findings

- The damage progression for both materials is shown to start by distributed fibre-matrix debonding, until coalescence is reached in a fibre-rich region, at a strain depending on ply thickness. As further strain is applied, the remaining matrix ligaments that are still bridging the crack are stretched and deform plastically until the ply loose its load bearing capability.

- The importance of interface properties have been highlighted. For an interface strength assumed too low, the thermal residual stresses lead to early debonding. If it is assumed too high, the transverse cracking onset is delayed for all ply thicknesses. Variations in interface toughness are shown to shift the scaling curve vertically without much effect on its shape.

- The high influence of thermal residual stresses for high temperature systems was highlighted. Large tensile stresses are imposed to the resin, and a linear dependence of the damage onset to the temperature jump imposed is observed during the sensitivity analysis on one ply thickness.

- Due to the effects of the thermal residual stresses, a high matrix ductility is crucial to avoid matrix damage during the manufacturing process. Very low ductility epoxies with good fibre-matrix interface should sustain the matrix stresses present before debonding. Otherwise, early TC due to matrix failure will dominate the behaviour of the 90° ply instead of those due to coalescence of interface damage and matrix ligament extension.

- A similar reduction of critical ERR with smaller ply thicknesses to the experimentally observed one was demonstrated, which further suggests that the apparent toughness associated to transverse cracking of very thin-ply composite varies with ply thickness.

7 Simulation at the lamina level

7.1 Hypothesis

Considering the decrease of critical ERR related to transverse cracking observed both numerically in section 6.4 and semi-experimentally in section 4.5.2, it seems that the $G_{1\mathrm{c}}$ value used in LEFM models is to be considered as a ply-thickness dependent property. Inspired by the work of Herraez et al. [88] discussed in chapter 2, as well as by the results of Saito et al. [23], a hypothesis is formed that the reduction of ply thickness, whilst contributing to the increase of transverse tensile strength through crack confinement as predicted by LEFM, has a second effect that has not yet been taken into account when modelling this phenomenon. It would be this second effect that is leading to the observed reduction in critical ERR related to transverse cracking.

A variation of toughness depending upon a geometrical feature is basically an R-curve behaviour. However, reasoning in such terms presents the disadvantage that the crack extension a into the bulk of the material is required, which cannot be easily obtained experimentally (no in-situ tomography) or numerically (full 3D multiscale model required). This TC extension a is however directly related to the TC crack opening displacement δ through elasticity relations [115] depending upon the laminate stacking sequence and ply thickness. In this work, a formalism based on COD will thus be preferred, leading to a cohesive traction-separation representation of the TC mechanism instead of an R-curve formulation.

As suggested by the small scale matrix ligament bridging highlighted in the work of Herraez [88] and similarly observed in the embedded cell simulations of this work (see chapter 6), the hypothesis of a laminate toughness following an increasing R-curve effect seems reasonable. Actually, to create a transverse crack, it was observed that a process zone needs to be formed, in which the composite is only partially fractured and bridging tractions are significant. This process zone need to grow until it reaches a fully developed state corresponding to the steady state toughness of the ply. Due to bridging traction development, the critical ERR increases during the process zone development. As the process zone develops, the COD increases progressively and reaches a critical value corresponding to the COD at the end of the fracture process zone. Cohesive models relating the cohesive traction to the COD are an appropriate representation of such an effect. In the case of transverse cracks confined within a thin-ply laminate, the width of a transverse crack is limited by the ply's thickness. Practically, this means that for small ply thicknesses, the maximum COD (and therefore the crack length a) achievable could be limited to values smaller than the ones required to reach a fully developed process zone and thus the steady state critical ERR of the 90° plies. This would explain the reduction of apparent critical ERR G_{1c}^{is} observed both experimentally and numerically with decreasing ply thickness, and could be a physical explanation of the deviation between the observed transverse strength scaling compared to LEFM based in-situ strength theory.

An initial evaluation of this hypothesis was performed by simulating a plane-strain, linear elastic model of the same 3 laminates as had been used in the M40JB-TP80ep multiscale models, and introducing a single transverse crack in the middle of their respective 90° layers. Loading the 3 laminates until their respective AE onset strain, δ was measured and shown to be strongly reduced with decreasing ply thickness, from δ=1.85 µm for the t=150 µm simulation to δ=0.57 µm for the t=30 µm one, which was an encouragement to proceed with this approach. Compared to the results obtained by Herraez et Al. [88], where the critical COD at the end of the process zone are of the order of 8 µm, such low values of achievable COD in thin-ply composite would clearly support the hypothesis of a partial process zone development corresponding to the observed decrease of apparent toughness for lower ply thicknesses.

7.2 Modelling strategy and traction-separation curve identification

If the hypothesis presented above is valid, it ought to be possible to lump all of the damage into a cohesive zone corresponding to a transverse crack in an otherwise fully linear elastic, ply-level model of the laminate. Considering that the geometry of the model controls the relationship between a and δ, it is possible to reformulate the R-curve effect, formulated based on crack length, into an energy dissipation potential function (EDP) formulated in terms of COD and defined as

$$EDP(\delta') = \int_0^{\delta'} \sigma_{COH}(\delta)\,\mathrm{d}\delta \tag{7.2.1}$$

with σ_{COH} the cohesive stress and δ the COD of the TC [116, 117]. The EDP is thus an energetic view of a cohesive traction-separation model $\sigma_{COH}(\delta)$ as it represents the work of the dissipative cohesive forces up to a given COD. Conversely, the cohesive traction-separation law can be retrieved simply by differentiation of the EDP.

With this formalism, the reduction of the apparent critical ERR associated to TC when decreasing ply thickness can simply be modelled through the reduction of the crack opening displacement δ at onset of transverse cracking caused by geometrical constraining of the transverse crack. On the one hand, for thick plies, the bounds of the integral (equation 7.2.1) are larger than the critical COD for a fully developed process zone and the apparent ERR given by the EDP is constant for all ply thickness considered thick. On the other hand, for low ply thickness, the COD becomes smaller than the critical COD for a fully developed process zone and thus only a fraction of the steady state fracture energy can be dissipated: the EDP integral is truncated, and the resulting apparent ERR decreases. A reduction of COD at onset of TC with ply thickness combined with a cohesive traction-separation model would thus allow the modelling of the apparent decrease of ERR with ply thickness under a certain threshold of ply thickness while maintaining a constant ERR for thicker plies.
To do so, an appropriate (unique for all ply thicknesses) cohesive traction-separation law or its EDP counterpart need to be identified for a given composite. Once identified, it would allow the onset of damage to be correctly predicted for all ply thicknesses and all stacking sequences where TC is the dominant failure mode observed.

7.2.1 Identification concept

The aim of the mesoscale model developed is to capture the finite fracture process zone and its incomplete development in highly confined thin-ply composites by means of a single cohesive zone model applicable to transverse cracking in all ply thicknesses, as discussed above. To do so, a single cohesive law for all ply thicknesses has to be identified. Considering the results and discussions presented in chapter 4 and 6, this model has to be representative of bulk damage and thus compared to the onset of damage measured by AE. For a given composite system, the data obtained for the ply thicknesses where delamination does not dominate its damage behaviour can be used for the identification of its cohesive law. In the case of the M40JB-TP80ep and and T800-TP175 systems used in this chapter, it is the 30 µm, 75 µm and 150 µm ply thicknesses for the former and the 34 µm, 68 µm and 134 µm ply thicknesses for the latter.

7.2.2 FE model used for identification

Regarding the traction-separation model used, two main mechanisms are shown to be at play in the development of transverse cracking according to the multiscale model results discussed in chapter 6, namely debonding and small-scale bridging of matrix ligaments. Following [88], each of these mechanisms is described by an independent linear traction-separation law, as shown on Fig. 7.1. Their summation leads to a bilinear traction-separation law shown to be able to accurately predict the R-curve behaviour of this class of material for a SENB test [88] and for the longitudinal fracture of Compact Tension specimen [89].

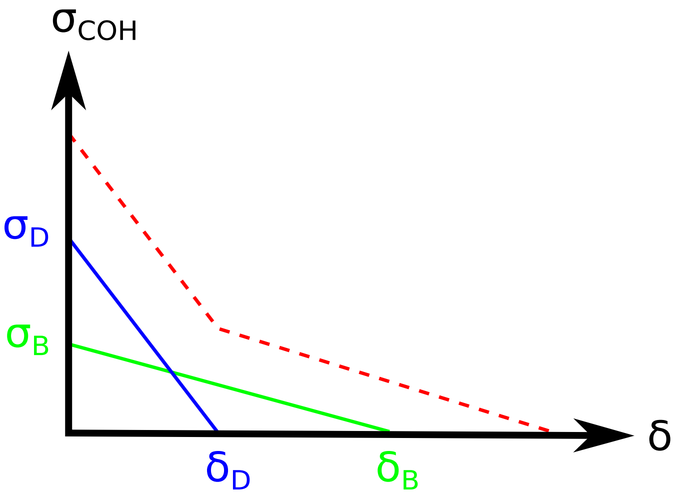

Figure 7.1: Cohesive parameters that are being identified. σ_D and δ_D are the strength and maximal opening of the cohesive elements related to debonding. σ_B and δ_B are their equivalents related to matrix micro-filament bridging. The bilinear law resulting from their superposition is shown in red

A 2D plain-strain, ply-by-ply model is therefore developed with very similar geometry to the one used for the embedded cell model, as shown on Fig. 7.2. The homogenized ply properties used are the same as the ones used previously in the surroundings of the embedded cell model, as are the boundary conditions imposing a state of plane-strain. A single transverse fracture is modelled within the 90° ply as two superposed cohesive layer with cohesive traction separation laws representing debonding and matrix bridging, respectively.

In order to be compared to bulk (AE) experimental data, plane-strain boundary conditions are used, as in the CMM model. The stacking sequence used is the same one too, namely [0/45/90/-45/0]. The length of the model is dictated by the requirement to obtain a homogeneous stress-state in the cohesive zone.

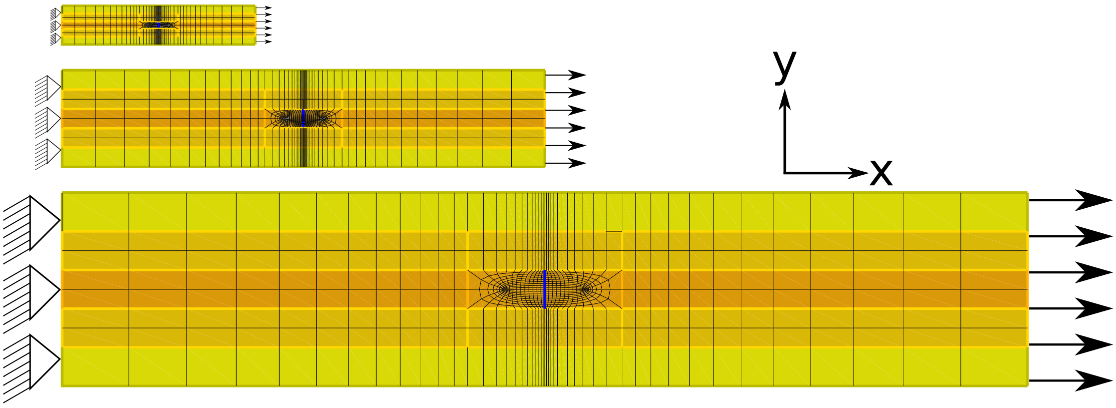

Figure 7.2: Description of the homogenized model for traction-separation laws identification

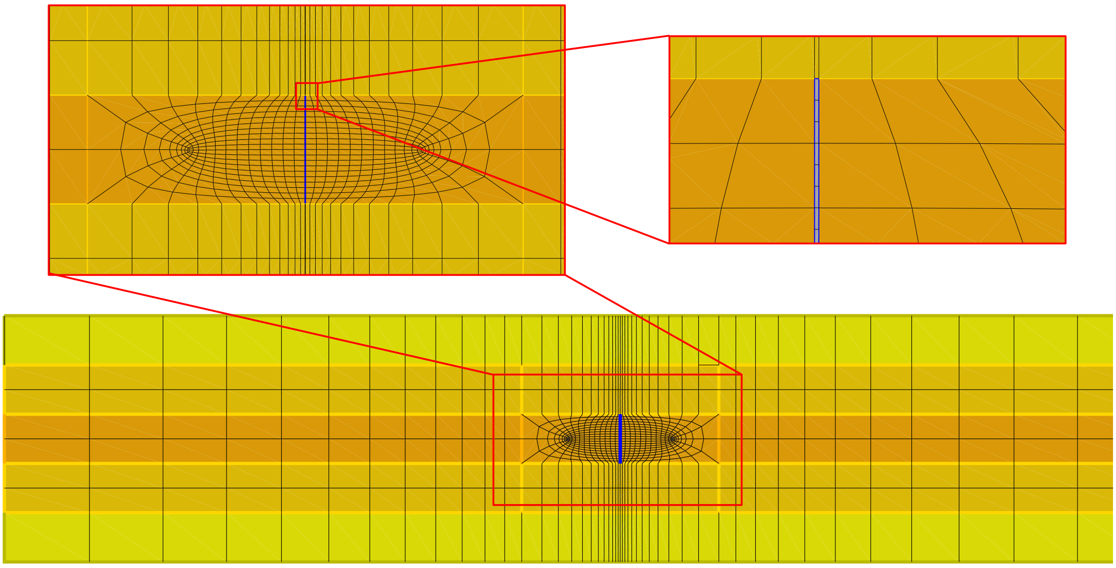

Figure 7.3: Mesh used for the traction-separation laws identification. The superimposed cohesive elements are shown in blue and are 3 times smaller than the surrounding elements.

The three ply thicknesses modelled are run simultaneously in a single simulation, with scaled element size and boundary conditions. The mesh consists of 2574 C3D8R and 360 COHD8 elements and comprises 7080 nodes in total, and is shown in Fig. 7.3. The problem is solved using an explicit solver (Abaqus Explicit) with mass scaling recalculated at each increment to represent the quasi-static response of the material. It is validated that at the mass scaling's desired stable time increment set at 5E-6, as used in the CMM model, the kinetic energy is negligible compared to the work of external forces.

A transverse crack in these models is deemed fully developed when the integration point located at 1/6 of the ply's thickness in an element adjacent to the cohesive zone sees its transverse stress drop below a set threshold, as shown on Fig. 7.4. This is consistent with the observations made in the multiscale FE model, where a crack was defined as the local loss of load bearing capability, despite some local matrix zones (around not debonded fibres and in the ligaments bridging the crack) not being fully damaged. There is therefore no need to reach the critical opening of the cohesive elements to deem the ply cracked. An optimisation scheme is then used to identify the traction-separation parameters (strength and maximum crack opening) of both mechanism that allow the AE onset of damage measured experimentally to be replicated.

Obviously, only the bulk TC damage onset can be captured with the present approach. This is however much more interesting as a design criterion anyway, as it can directly be transposed into multilayer shell or CLT models of the laminate. Furthermore, as the free edge behaviour was shown to be a local effect, it is of much less importance for onset of damage predictions.

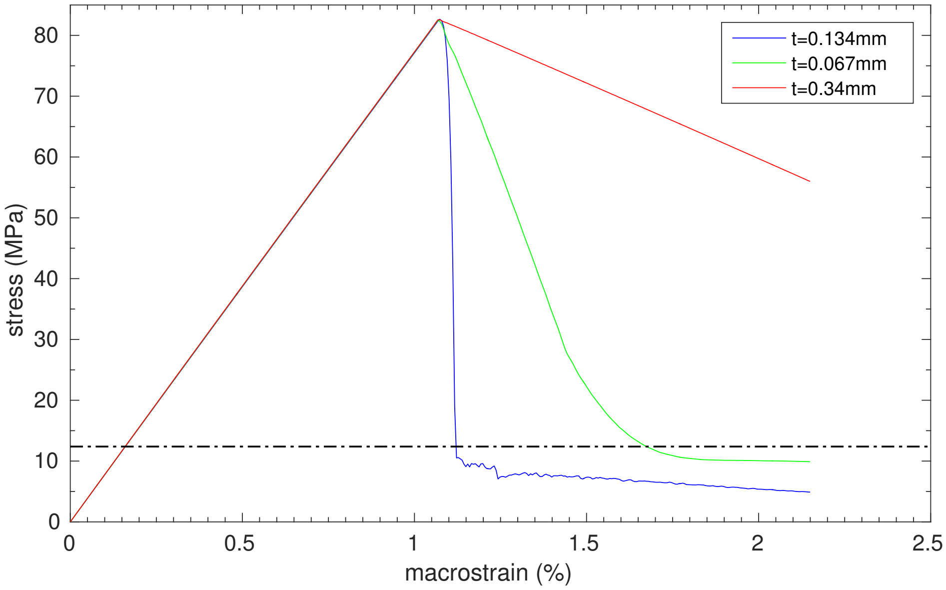

Figure 7.4: S_{22} in an element adjacent to the cohesive zone, located at 1/6th of the ply thickness, plotted for the three ply thicknesses. Threshold set shown in black.

7.2.3 Optimisation scheme

The parameter identification scheme is performed by coupling the Abaqus FE solver with a Matlab non linear least square optimization solver running the Levenberg Marquardt algorithm without strict bounds set on the parameters. The parameters being identified are the critical stress σ and COD δ of both linear cohesive laws, which are shown graphically on Fig 7.1. "Soft bounds" are implemented in the error vector to penalise the result when approaching non-physical values. The main error vector represents the mismatch between the model prediction and the recorded AE onset for the 3 ply thicknesses modelled, and is defined as

$$\xi = \left[\frac{\left(\min\left(\epsilon^{\mathrm{n}}_{30}, \epsilon^{\mathrm{UTS}}_{f}\right) - \epsilon^{\mathrm{e}}_{30}\right)}{\epsilon^{\mathrm{e}}_{30}} + \frac{\left(\min\left(\epsilon^{\mathrm{n}}_{75}, \epsilon^{\mathrm{UTS}}_{f}\right) - \epsilon^{\mathrm{e}}_{75}\right)}{\epsilon^{\mathrm{e}}_{75}} + \frac{\left(\min\left(\epsilon^{\mathrm{n}}_{150}, \epsilon^{\mathrm{UTS}}_{f}\right) - \epsilon^{\mathrm{e}}_{150}\right)}{\epsilon^{\mathrm{e}}_{150}} \right] \quad (7.2.2)$$

with $\epsilon^{\mathrm{n}}_{t}$ the macroscopic strain values at detected onset of TC extracted from the numerical simulation for a given ply thickness t (the macro-strain value at which the threshold is crossed, as shown on Fig. 7.4) and $\epsilon^{\mathrm{e}}_{t}$ the strain at AE onset measured experimentally in laminates with ply thickness t. The norm of this error vector is defined as the objective function for the non-linear minimisation problem.

To take into account the translaminar fracture of the 0° plies, numerically extracted strains at TC onset are limited to the fibre ultimate strain ϵ_f^{UTS}. Practically, this means that on Fig. 7.4, even though the t=0.34mm curve has not crossed the threshold at 2% macrostrain, the ply is considered cracked anyway as the translaminar fracture of the 0° plies at this strain does lead to the failure of the specimen.

The macroscopic strain values at onset of TC for the three simulated ply thicknesses are extracted from the simulation, and compared to the experimental AE onset strains for the same ply thickness in order to build the error vector described in equation 7.2.2. The values of the 4 traction-separation parameters are then iteratively optimised until a minima of the error vector is found, as shown on Fig. 7.5. As some initial parameter lead to local minima of the objective function, an exploration of the parameter space is performed around a first set of initial values chosen based on the multiscale modelling interface parameters values. All physically possible combination of doubling and halving these 4 initial guesses are tried to ensure a total coverage of the parameter space around them. The local minima that can be encountered are mostly due to initial parameters chosen too far off the optimal solution, leading to a total absence of sensitivity to their variation, thus not allowing the calculation of an initial gradient to initialise the optimisation scheme.

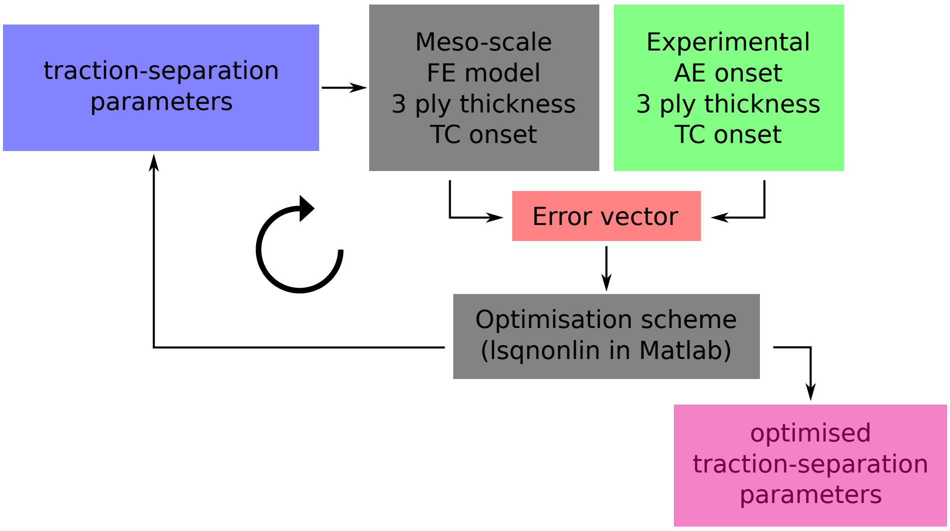

Figure 7.5: Optimisation scheme schematic, showing that the FE model yields TC onset values for each ply thickness from a set of traction-separation parameters. These parameters are optimised to replicate the AE TC onset values.

Local minima typically present an error vector norm equal or larger to 30%. A set of several converged simulations always present error vectors smaller than 1%, which are retained. Within this set, even though the individual traction-separation values are slightly different, the EDP curves obtained are largely similar. Having identified the macroscopic stain at failure from the simulation, the measurement of the numerical δ on the simulation and integration of the optimised traction-separation laws until this point allows the calculation of the critical

ERR for all three ply thicknesses. A comparison can thus be made between this approach and the semi-experimental or the micromechanical modelling ones.

A sensitivity analysis is performed on the stress threshold values used to define the TC onset (fully developed crack criterion). If chosen too low, it might never be crossed for any applied strain. In such a situation, the optimisation scheme has no sensitivity to changes in cohesive parameters, which is undesirable. To the contrary, if set too high, the ply might be deemed cracked before actually losing its load bearing capability. Optimised EDP curves obtained from different initial points with such an overestimated threshold typically start to diverge for larger δ values.

Trial and error and the observation of the S_{22} curve for the largest ply thickness (see blue curve on Fig. 7.4 is required to set the threshold. The post-TC load bearing capability of the plies observed during initial testing of this method seems to be lightly sensitive to the defined cohesive strength. Initial testing indicates that a normalised stress value of 0.15 times the cumulated strength of both cohesive elements used for the simulation is likely to yield an appropriate threshold.

7.3 M40JB-TP80ep system

Three simulations using the M40JB-TP80ep material properties and AE onsets converge towards results with less than 1% error. The resulting traction-separation and EDP curves are shown on Figs. 7.6a and 7.6b. The COD at crack onset for these simulations is measured at 0.22 µm, 0.55 µm and 0.90 µm for the 30gsm, 75gsm and 150gsm models, respectively, leading to the critical ERR shown on Fig. 7.7 for comparison with the values obtained for this material by the numerical micro-mechanics model and by the semi-experimental identification. The traction-separation parameters of the three simulations retained and the cohesive toughness thus defined are recalled in Table 7.1. The average value for each parameter is also calculated for comparison purposes.

Table 7.1: σ-δ parameters for the cohesive elements in the M40JB-TP80ep simulation, with the computed associated toughness. Average of each parameter computed for comparison between systems

Parameter	σ_D (MPa)	δ_D (µm)	G_D (J/m^2)	σ_B (MPa)	δ_B (µm)	G_B (J/m^2)
	33.4	0.9	15.6	17.5	1.1	10
	41.2	0.9	19.5	9.7	1.3	6.1
	44.1	1.0	21	6.6	1.4	4.7
Average	39.6	0.9	18.7	11.3	1.3	6.9

The obtained results show a similar trend as observed previously both numerically and experimentally. The underestimation in the case of the t=30 µm model has to be considered with caution, as the model isn't very sensitive for such low ply thicknesses. Indeed, due to the fact that crack onset and failure at this ply thickness are for all intent and purpose simultaneous, it is only possible to ensure that no underestimation of crack onset is present. In such a case, the optimisation scheme will try to find a set of parameters to reach a better fit. It will however be incapable of detecting parameters leading to an overestimation of the TC onset, due to the fact that the error vector takes into account that translaminar fracture of the 0° ply would have occurred by that strain. the numerator of the error term t=30 in equation 7.2.2 will therefore stay pegged at 0 no matter what the parameters are changed to. This means that the error vector is insensitive to variations of the input when parameters leading to an overestimation of TC onset are defined for the t=30 µm case. An over-estimation of TC onset due to this can lead to a lower critical COD due to excessive cohesive forces, and might therefore lead to an under-estimation of the critical ERR. (The δ' value in Eqn. 7.2.1 is underestimated, leading to an underestimation of EDP(δ'), the critical ERR) Considering that the critical ERR value obtained by the embedded cell FE model for this ply thickness was actually predicted at a higher strain than the fibre ultimate strain, such an underestimation of critical ERR for t=30 µm is possible.

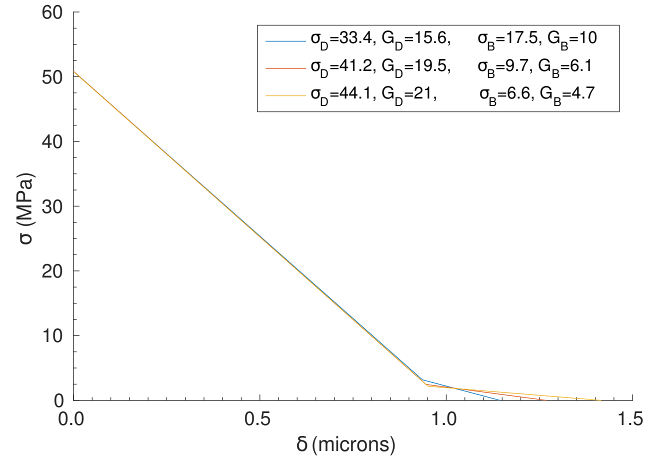

(a) traction-separation laws

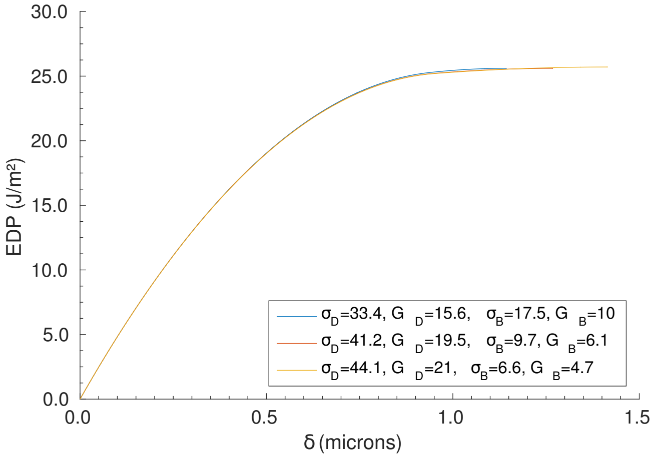

(b) EDP-curve

Figure 7.6: Traction-separation laws and related EDP curve identification for the M40JB-TP80ep system. The figure legend states the strength of the debonding mechanism σ_D and of the small scale bridging σ_B in MPa, as well as the toughness of the debonding G_D and of the small scale bridging G_B in J/m^2

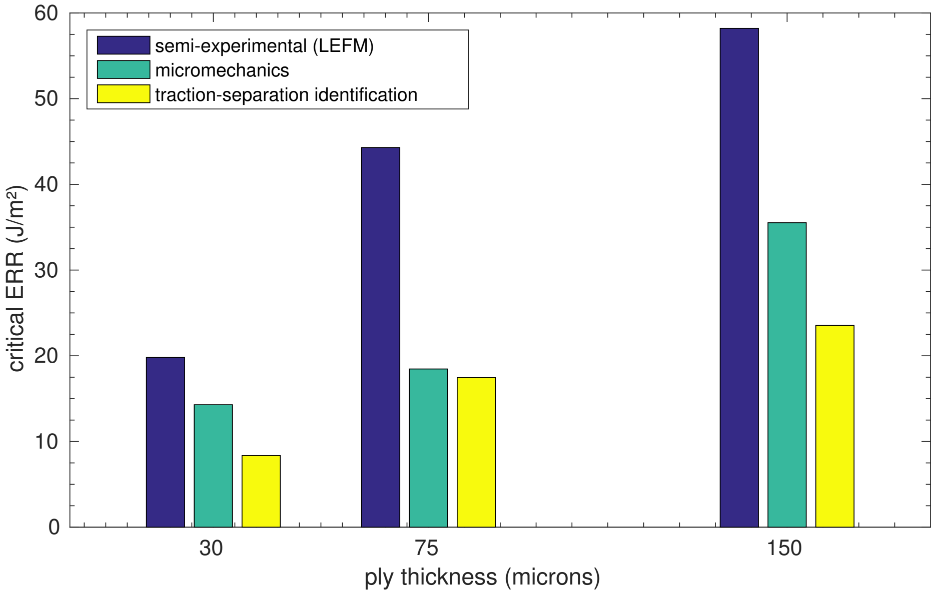

Figure 7.7: Critical ERR comparison for M40JB-TP80ep system

7.4 T800-TP175 system

Five simulations using the T800-TP175 material properties and AE onsets converge towards results leading to less than 1% error. The resulting traction-separation and EDP-curve are shown on Fig. 7.8a and 7.8b. The COD at crack onset for these simulations is measured at 0.26 µm, 0.49 µm and 0.941 µm for the 34gsm, 68gsm and 134gsm models, respectively, leading to the critical ERR shown on Fig. 7.9 for comparison with the values obtained for this material by the numerical micro-mechanics model and by the semi-experimental identification. The traction-separation parameters of the five simulations retained and the cohesive toughness thus defined are recalled in Table 7.2. The average value for each parameter is also calculated for comparison purposes.

Table 7.2: σ-δ parameters for the cohesive elements in the T800-TP175 simulation, with the computed associated toughness. Average of each parameter computed for comparison between systems

Parameter	σ_D (MPa)	δ_D (µm)	G_D (J/m^2)	σ_B (MPa)	δ_B (µm)	G_B (J/m^2)
	62.1	1.5	46.4	20.1	2.9	28.9
	65.5	1.6	53.6	16.5	2.4	19.7
	60.5	1.6	47.9	21.8	2.4	25.7
	65.7	1.6	53.2	16.5	2.4	20.1
	52.8	1.6	43.5	29.2	2.0	29.2
Average	61.3	1.6	48.9	20.8	2.4	24.7

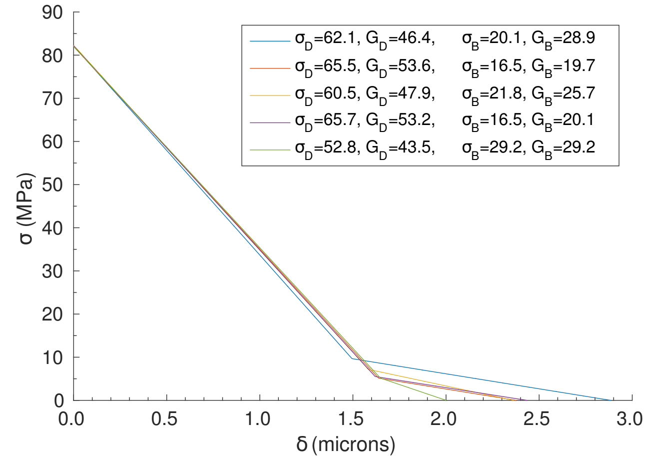

(a) traction-separation laws

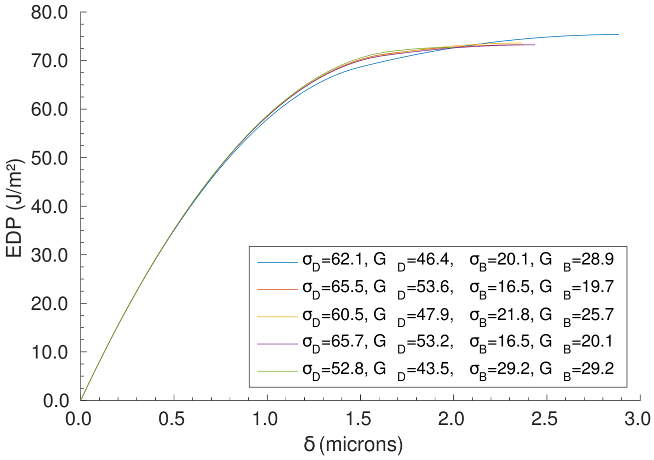

(b) EDP-curve

Figure 7.8: Traction-separation laws and related EDP curve identification for the T800-TP175 system. The figure legend states the strength of the debonding mechanism σ_D and of the small scale bridging σ_B in MPa, as well as the toughness of the debonding G_D and of the small scale bridging G_B in J/m^2

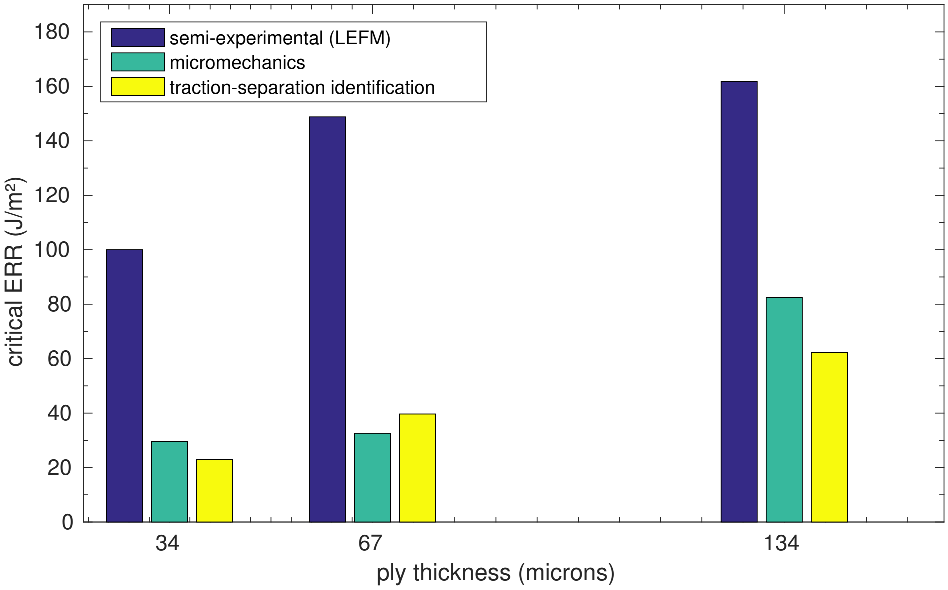

Figure 7.9: Critical ERR comparison for T800-TP175 system

7.5 Discussion

The same trend of a decreasing critical ERR with decreasing ply thickness can be well captured by the traction-separation law identification scheme presented in the present section. For the M40JB-TP80ep system, the critical ERR obtained is closely comparable to the results obtained via the embedded cell micromechanical simulation, as shown on Fig. 7.7. A value of $40\mathrm{J/m^2}$ is in good agreement with the ones computed by Saito [23].

Looking at the strength and opening values of the cohesive element representing the debonding mechanism, the value obtained for the T800-TP175 system is 2.6 times larger than in the M40JB-TP80ep one, which makes sense since the TP175 is an aerospace grade highly modified and toughened epoxy resin. The average decohesion strength is estimated close to 40 MPa and 60 MPa, respectively, which is in line with the range of interface strengths identified in chapter 6 for the micro-mechanics FE model.
A dominance of decohesion over ligament bridging is present in both cases but with much higher values of critical COD in the case of the TP175 system. In both cases, the critical ERR was reduced by about 65% between the t=150 µm and the t=30 µm simulations.

Interestingly, if the critical ERR values obtained using the traction-separation parameter identification method are very close to the ones obtained with the micro mechanics model, the values obtained by inverting the LEFM in-situ strength model lead to much higher values of apparent toughness. This discrepancy is quite surprising as both the FE model used for identifcation and LEFM assume linear elasticity outside of the process zone. The difference is therefore attributed to the assumption of no bridging tractions used in the LEFM expressions which assumes a negligible process zone whereas the micro and continuum FE simulations show that the process zone is indeed of comparable size to the ply thickness, for ply smaller than 150 µm.
Further improvement of the in-situ LEFM expressions to account for the required crack opening profile bridging tractions when considering a finite process zone, coupled with energy calculation seem a promising approach to capture analytically the TC scaling with ply thickness.
It should finally also be noted that in both systems studied herein, matrix ligament bridging seem to play a secondary role. Consequently, the proposed identification and cohesive modelling approach proposed in this chapter could be simplified by using a single linear degradation term only. A difference would only start to appear at larger δ values, close to the steady state of the EDP function, which corresponds to thicker plies. For these thicker plies, the importance of the TC is reduced anyway as delamination starts to play a preponderant role in the onset of damage of the laminates, as was shown in chapter 4. The loss of accuracy would therefore be minimal.

Considering the mechanisms underlying the in-situ strength effect, the results obtained in this chapter highlight the fact that reducing the ply thickness opposes two effects: On one hand, and as expected by LEFM-based models, it increases the transverse strength due to confinement, which can be observed here as a reduction of crack opening displacement for a given applied strain, even in the absence of cohesive elements. On the other hand, due to the finite size of the process zone, the transverse fracture toughness is decreased, which is identified by the loss of load bearing capability at smaller crack opening displacements. It is the superposition of these two effects that explains the difference observed between experimental results and the transverse tensile strength predicted by LEFM-based models.

Overall, the fact that a simple linear cohesive law can predict the observed scaling of TC onset is remarkable as it opens the way for further development of improved in-situ strength models that could properly account for the finite size of the process zone without requiring a much larger experimental dataset. To do so, it would nonetheless be necessary to test several ply thicknesses of a given material, as two parameters need to be identified (strength and critical COD or toughness of the cohesive elements). Based on the experimental observations performed, the measurement of TC onset by AE in a UNT test on QI laminates could be an efficient method to experimentally determine the onset of TC.

Using a similar identification method as proposed in this chapter, TC cohesive law parameters can be identified relatively quickly and implemented for TC prediction in a wide variety of analytical or numerical models at the continuum scale. As shown on Fig. 7.10, once the traction-separation law pertaining to the TC of a transverse ply in a given material is identified, it would be trivial to modify the lamina-level model to represent any laminate under review. An accurate prediction of the applied strain at TC onset could thus be obtained for any ply thickness and stacking sequence, which could then be implemented in any existing continuum failure criterion.

Finally, if an improved analytical model for the ERR of a confined transverse crack subjected to a linear degradation large scale process zone was developed, the whole identification and prediction process could be computed analytically, which would open the way to very efficient prediction tools for thin-ply composite laminates.

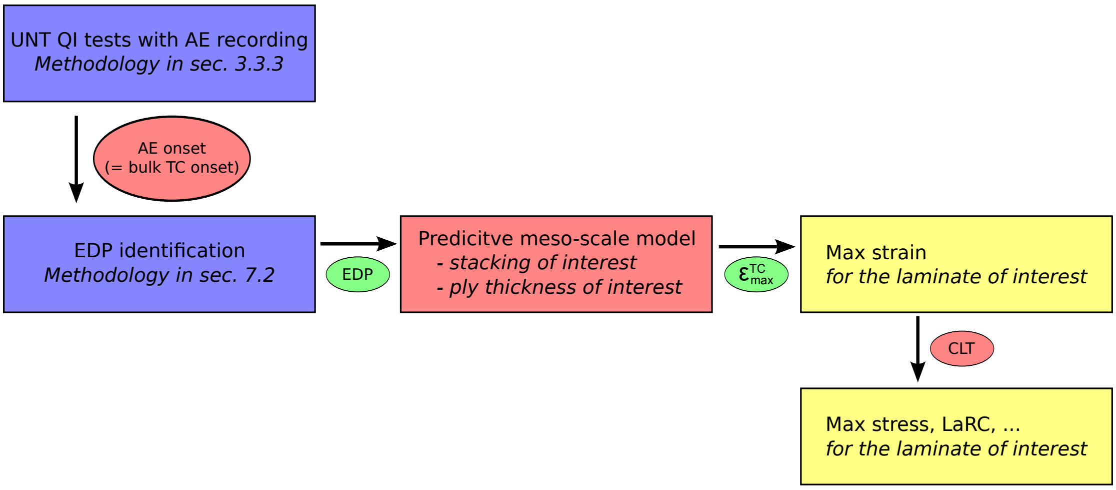

Figure 7.10: Flowchart of a TC prediction tool for a given material

8 Summary, conclusions and future outlook

8.1 Summary and conclusion

In this work, the ply thickness dependency of three different thin-ply carbon fibre reinforced polymers quasi-isotropic laminates was investigated experimentally. The choice of their constituents was performed in order to be representative of a wide array of materials. Observations performed at the free edge using optical and SEM imaging techniques were compared with bulk measurement relying on acoustic emission measurements, post-testing optical microscopy imaging of sectioned samples and computed X-ray tomography.

All materials exhibited a change of damage behaviour at the free edge of the samples with decreasing ply thickness. Whilst delamination was shown to dominate the behaviour of the thick ply samples, transverse cracking was observed to be the dominating damage mechanism for ply thicknesses equal to or smaller than 150 µm, with the translaminar fracture of the 0° plies triggered first for some of the thinnest plies tested (t≈30 µm).

It was shown that the onset of damage in the bulk of the samples always took place at larger strains than at the free edges. The acoustic emission threshold used to determine this onset was shown through tomography to be related to the propagation of major transverse cracking from the free edge into the bulk. In accordance with the literature, transverse crack density at the free edge before failure was observed to increase with decreasing ply thickness for both materials using high strength fibres. A similar increase in transverse crack density when changing from thick to intermediate ply thicknesses with the material using high modulus fibres was also observed. Simultaneously, the transverse crack density recorded shortly before failure in the bulk of the material was shown to decrease, which is also in good agreement with previous works. At the free edge, the strain at onset of transverse cracking was shown to increase in a nearly hyperbolic way for low ply thicknesses and could be fitted with a $1/\sqrt{t}$ dependency. However, in the bulk, the scaling was shown to be much more linear and thus deviated from LEFM predictions.

Assuming linear elastic fracture mechanics hypotheses, the apparent toughness of the three materials tested was computed by inverting the in-situ strength model. To do so, the average transverse tensile in-situ stress of the 90° ply was computed through CLT from the recorded laminate strain at AE onset. The in-situ strength equation could then be inverted to obtain an estimate of the critical energy release rate related to the transverse cracking of constrained 90° plies, which was shown to decrease with reduced ply thickness.
This property allowed a conservative estimation of the in-situ strength of intermediate ply thickness laminates to be performed. Applying the LEFM expression whilst using the apparent toughness identified for the thinnest plies available for a given material defined a lower strength bound that could safely be used for design, as demonstrated by the reduced in-situ strength master-curve.

To gain a better understanding of the intricate damage process happening within a ply, a multiscale embedded cell FE-model was developed, and applied to the two systems with the most contrast in constituent properties, namely a high modulus, low curing temperature system (M40JB/TP80ep) and a highly toughened aerospace grade high Tg system (T800/TP175). All material properties were obtained or derived from experimental tests, except for the fibre-matrix interface. Transverse cracking for both materials was shown to be caused by interfacial damage coalescence until localisation, whereupon the matrix ligaments bridging the two crack faces were strained, causing plastic dissipation and damage. The dominance of interface properties on the final transverse crack development was highlighted, as were the importance of thermal residual stresses which induce high triaxiality local stresses in regions of close fibre packing. The magnitude of these stresses was shown to be large enough to trigger interface or matrix damage in composites that are not produced with a ductile enough matrix or with poor fibre bonding strength. Furthermore, for given material properties, the curing temperature differential was shown to have a direct inversely proportional effect on the transverse tensile strength. In-situ residual stress measurements would be required to validate this claim, as the curing and bonding process is not well understood yet in this regard, and the current model might thus overestimate the severity of the issue. It should however be kept in mind for processing.

A very good agreement between the numerical predictions of the embedded cell model with the experimentally measured AE onset of transverse cracking could be reached for both materials when applying plane-strain boundary conditions. When using a submodelling approach to impose boundary conditions assimilated to free edge, a change in damage onset and transverse crack morphology was observed, both being in good agreement with the experimental observations at the free edge. Transverse cracking could thus be validated as the dominating damage mechanism for ply thicknesses ≤150 µm and the high importance of edge effects on the damage mechanisms taking place at the free edge reproduced numerically. The large difference in transverse crack onset between both boundary conditions, observed both numerically and experimentally, should therefore lead to increased caution when comparing plane-strain models of transverse cracking to experimental free edge observations, especially for stacking sequence promoting high free edge stresses.

When used to measure the plastic and damage energy dissipated during a transverse cracking event, the calibrated micromechanical models exhibited a similar reduction of critical ERR with decreasing ply thicknesses than observed experimentally, further suggesting that the apparent toughness associated to transverse cracking of very thin-ply composite is a ply thickness dependent property.

In light of these results, a mesoscale model was proposed where all the damage was lumped into a single thin transverse crack modelled using two superposed cohesive elements with linear traction-separation behaviour. The first was related to fibre-matrix debonding whilst the second was related to the small scale bridging of matrix filaments. An optimisation scheme was used to identify the strengths and maximal openings of both elements to match the AE onset for the three ply thicknesses where transverse cracking was shown experimentally to be the dominating damage mechanism. The maximal cohesive stresses thus obtained were in good agreement with the interface strength properties used in the micro mechanics model, and the critical ERR predictions of both numerical approaches were also in good agreement. Fibre-matrix debonding was shown to be the dominating mechanism, to the point where the applicability of a single linear traction-separation relation could be considered. Finally, the absence of decoupling between process zone size and ply thickness could be inferred from the large discrepancy observed between the semi-experimentally obtained critical ERR values and the ones identified numerically. Using the mesoscale model as presented in this work together with the proposed identification scheme and related experimental characterisation, the introduction of a transverse cracking induced critical stress/strain in all existing continuum failure criterion is made possible for all ply thicknesses, down to the smallest ones that can be produced.

8.2 Future outlook

On the experimental and micromechanical modelling front, further work ought to be carried out pertaining to the characterisation of interface properties and thermal residual stresses to validate the current model and increase its fidelity. Push-in tests using a flat punch nano-indenter tip and in-situ strain measurements using FBG's are two methods mentioned in this work that could be put to good use in this regard.

Novel in-situ observations of the damage propagation from the free edge into the bulk could be envisaged in order to gain further knowledge regarding this process that could only be observed at frozen intervals in the present work. The increasingly small resolution available in micro X-ray tomographs is of great help in this regard. True in-situ observations couldn't possibly be performed in tomography due to the required acquisition time, but using Xenon gas as the contrastant and observing the samples using radiographic scans only might yield some useful pieces of information.

Regarding the upscaling from the micromechanical modelling, the application of the traction-separation law identification presented in this work should be extended to the other materials that have been tested to extend the database, thus further validating the applicability of the method. The good qualitative agreement between interface properties used in the micromechanical model and the critical cohesive strengths obtained via the traction-separation relation identification demonstrated here could also be used to improve the estimate of interface properties for the microscale model and should be compared to the additional experimental data discussed above. The application of the traction-separation laws identified to a numerical model of a full sample where a known crack density could be introduced using cohesive elements could be used for further validation with the experimental data set, both at the free edge and in the bulk.

The consideration of the bridging tractions present on the crack profile, required to properly account for the finite size of the process zone demonstrated in this work, and their induced effect on the energy release rate, were shown to be required. It is remarkable that a simple linear cohesive law could predict the observed scaling of TC onset, as it allows a very promising way to analytically capture the transverse cracking onset scaling with respect to ply thickness to be inferred: If the linear stiffness degradation large scale process zone demonstrated in this work was implemented in an analytical solution to the elasticity problem of a constrained transverse crack, an analytical expression could be derived to accurately predict the in-situ strength of thin-ply composites. This opens the way for further development of improved analytical in-situ strength models without requiring a much larger experimental dataset.

Bibliography

[1] M. Kühnel. The global cfrp market 2016. In *Experience Composites, Augsburg, September 21st 2016*, 2016.

[2] M. Holmes. Global carbon fibre market remains on upward trend. *Reinforces Plastics*, pages 38–45, November/December 2014.

[3] M. Kühnel, M. Sauer, and E. Witten. Composites - marktbericht 2018. 2018.

[4] P. Fonta. Pushing the technology envelope. In *ICAO environmental report 2010*, chapter 2, pages 72–78. ICAO, 2010.

[5] R. Amacher, J. Cugnoni, J. Botsis, L. Sorensen, W. Smith, and C. Dransfeld. Thin ply composites: Experimental characterization and modeling of size-effects. *Composites Science and Technology*, 101:121–132, 2014.

[6] R. Amacher, W. Smith, C. Dransfeld, J. Botsis, and J. Cugnoni. Thin ply: From size-effect characterization to real life design. In *CAMX 2014 - Composites and Advanced Materials Expo: Combined Strength. Unsurpassed Innovation.*, pages –, 2014.

[7] J. Cugnoni, R. Amacher, S. Kohler, J. Brunner, E. Kramer, C. Dransfeld, W. Smith, K. Scobbie, L. Sorensen, and J. Botsis. Towards aerospace grade thin-ply composites: Effect of ply thickness, fibre, matrix and interlayer toughening on strength and damage tolerance. *Composites Science and Technology*, pages –, 2018.

[8] G. Frossard. *Fracture of thin-ply compositeseffects of ply thickness.* PhD thesis, EPFL, 2018.

[9] M. Jalalvand, G. Czél, and M. R. Wisnom. Damage analysis of pseudo-ductile thin-ply ud hybrid composites: A new analytical method. *Composites Part A: Applied Science and Manufacturing*, 69:83–93, 2015.

[10] A. Parvizi, K. W. Garrett, and J. E. Bailey. Constrained cracking in glass fibre-reinforced epoxy cross-ply laminates. *Journal of Materials Science*, 13(1):195–201, 1978.

[11] S. Sihn, R. Y. Kim, K. Kawabe, and S. W. Tsai. Experimental studies of thin-ply laminated composites. *Composites Science and Technology*, 67(6):996–1008, 2007.

[12] G. J. Dvorak and N. Laws. Analysis of progressive matrix cracking in composite laminates ii. first ply failure. *Journal of Composite Materials*, 21(4):309–329, April 1987.

[13] P. P. Camanho, C. G. Dávila, S. T. Pinho, L. Iannucci, and P. Robinson. Prediction of in situ strengths and matrix cracking in composites under transverse tension and in-plane shear. *Composites Part A: Applied Science and Manufacturing*, 37(2):165–176, 2006.

[14] J. E. Bailey, P. T. Curtis, and A. Parvizi. On the transverse cracking and longitudinal splitting behaviour of glass and carbon fibre reinforced epoxy cross ply laminates and the effect of poisson and thermally generated strain. *Proc R Soc Lond A Math Phys Sci*, 366(1727):599–, July 1979.

[15] R. G. Krueger. Apparatus and method for spreading fibrous tows into linear arrays of generally uniform density and products made thereby, 1999.

[16] M. S. Irfan, V. R. Machavaram, R. C. Murray, F. N. Bogonez, C. Wait, S. Pandita, M. A. Paget, M. Hudson, and G. Fernando. *The design and optimisation of a rig to enable the lateral spreading of fibre bundles*, volume 48. June 2013.

[17] K. Kawabe, T. Matsuo, and Z. Maekawa. New technology for opening various reinforcing fiber tows. *JOURNAL-SOCIETY OF MATERIALS SCIENCE JAPAN*, pages 727–734, 1998.

[18] G. Catalanotti. Prediction of in situ strengths in composites: Some considerations. *Composite Structures*, 207:889–893, 2019.

[19] M. R. Wisnom, B. Khan, and S. R. Hallett. Size effects in unnotched tensile strength of unidirectional and quasi-isotropic carbon/epoxy composites. *Composite Structures*, 84(1):21–28, 2008.

[20] R. Amacher, J. Cugnoni, and J. Botsis. Thin ply composites: Experimental characterization and modeling. volume 2013-July, pages 4364–4376. International Committee on Composite Materials, 2013.

[21] B. Koetter, D. Polyak, J. Koerbelin, and B. Fiedler. Influence of ply thickness on failure initiation, propagation and mechanical properties in cfrp laminates. International Conference on Fatigue of Composites, 2018.

[22] F. E. Oz, N. Ersoy, M. Mehdikhani, and S. V. Lomov. Multi-instrument in-situ damage monitoring in quasi-isotropic cfrp laminates under tension. *Composite Structures*, 196:163–180, 2018.

[23] H. Saito, H. Takeuchi, and I. Kimpara. Experimental evaluation of the damage growth restraining in 90° layer of thin-ply cfrp cross-ply laminates. *Advanced Composite Materials*, 21(1):57–66, 2012.

[24] H. Saito, H. Takeuchi, and I. Kimpara. A study of crack suppression mechanism of thin-ply carbon-fiber-reinforced polymer laminate with mesoscopic numerical simulation. *Advanced Composite Materials*, 48(17):2085–2096, 2014.

[25] T. A. Sebaey, J. Costa, P. Maimí, Y. Batista, N. Blanco, and J. A. Mayugo. Measurement of the in situ transverse tensile strength of composite plies by means of the real time monitoring of microcracking. *Composites Part B: Engineering*, 65:40–46, 2014.

[26] T. Yokozeki, Y. Aoki, and T. Ogasawara. Experimental characterization of strength and damage resistance properties of thin-ply carbon fiber/toughened epoxy laminates. *Composite Structures*, 82(3):382–389, February 2008.

[27] T. Yokozeki, A. Kuroda, A. Yoshimura, T. Ogasawara, and T. Aoki. Damage characterization in thin-ply composite laminates under out-of-plane transverse loadings. *Composite Structures*, 93(1):49–57, 2010.

[28] G. Guillamet, A. Turon, J. Costa, J. Renart, P. Linde, and J. A. Mayugo. Damage occurrence at edges of non-crimp-fabric thin-ply laminates under off-axis uniaxial loading. *Composites Science and Technology*, 98:44–50, June 2014.

[29] A. Arteiro, G. Catalanotti, J. Xavier, and P. P. Camanho. Notched response of non-crimp fabric thin-ply laminates. *Composites Science and Technology*, 79:97–114, 2013.

[30] G. Frossard, J. Cugnoni, T. Gmür, and J. Botsis. Mode i interlaminar fracture of carbon epoxy laminates: Effects of ply thickness. *Composites Part A: Applied Science and Manufacturing*, 91:1–8, 2016.

[31] G. Frossard, J. Cugnoni, T. Gmür, and J. Botsis. Ply thickness dependence of the intralaminar fracture in thin-ply carbon-epoxy laminates. *Composites Part A: Applied Science and Manufacturing*, 109:95–104, 2018.

[32] A. Wagih, P. Maimi, E. V. González, N. Blanco, J. R. Sainz de Aja, F. M. de la Escalera, R. Olsson, and E. Alvarez. Damage sequence in thin-ply composite laminates under out-of-plane loading. *Composites Part A: Applied Science and Manufacturing*, 87:66–77, 2016.

[33] T. A. Sebaey and E. Mahdi. Using thin-plies to improve the damage resistance and tolerance of aeronautical cfrp composites. *Composites Part A: Applied Science and Manufacturing*, 86:31–38, 2016.

[34] R. Amacher, J. Cugnoni, J. Brunner, E. Krammer, C. Dransfeld, W. Smith, K. Scobbie, L. Sorensen, and J. Botsis. Towards aerospace grade thin-ply composites. In *ECCM 17*, number aid951_c11448893625, 2016.

[35] M. Jalalvand, G. Czél, and M. R. Wisnom. Numerical modelling of the damage modes in ud thin carbon/glass hybrid laminates. *Composites Science and Technology*, 94:39–47, 2014.

[36] M. R. Wisnom, G. Czél, Y. Swolfs, M. Jalalvand, L. Gorbatikh, and I. Verpoest. Hybrid effects in thin ply carbon/glass unidirectional laminates: Accurate experimental determination and prediction. *Composites Part A: Applied Science and Manufacturing*, 88:131–139, 2016.

[37] J. D. Fuller, M. Jalalvand, and M. R. Wisnom. Combining fibre rotation and fragmentation to achieve pseudo-ductile cfrp laminates. *Composite Structures*, 142:155–166, 2016.

[38] G. Czél, M. Jalalvand, and M. R. Wisnom. Design and characterisation of advanced pseudo-ductile unidirectional thin-ply carbon/epoxy - glass/epoxy hybrid composites. *Composite Structures*, 143:362–370, 2016.

[39] G. Czel, M. Jalalvand, M. R. Wisnom, and T. Czigany. Design and characterisation of high performance, pseudo-ductile all-carbon/epoxy unidirectional hybrid composites. *Composites Part B: Engineering*, 111:348–356, 2017.

[40] J. Rupil, S. Roux, F. Hild, and L. Vincent. Fatigue microcrack detection with digital image correlation. *The Journal of Strain Analysis for Engineering Design*, 46(6):492–509, June 2011.

[41] T. Hobbiebrunken, M. Hojo, T. Adachi, C. De Jong, and B. Fiedler. Evaluation of interfacial strength in cf/epoxies using fem and in-situ experiments. *Composites Part A: Applied Science and Manufacturing*, 37(12):2248–2256, 2006.

[42] C. González and J. LLorca. Mechanical behavior of unidirectional fiber-reinforced polymers under transverse compression: Microscopic mechanisms and modeling. *Composites Science and Technology*, 67(13):2795–2806, 2007.

[43] L. P. Canal, C. González, J. Segurado, and J. LLorca. Intraply fracture of fiber-reinforced composites: Microscopic mechanisms and modeling. *Composites Science and Technology*, 72(11):1223–1232, 2012.

[44] L. P. Canal, C. González, J. M. Molina-Aldaregua, J. Segurado, and J. LLorca. Application of digital image correlation at the microscale in fiber-reinforced composites. *Composites Part A: Applied Science and Manufacturing*, 43(10):1630–1638, October 2012.

[45] J. Rannou, N. Limodin, J. Rethore, A. Gravouil, W. Ludwig, M.-C. Baietto-Dubourg, J.-Y. Buffiere, A. Combescure, F. Hild, and S. Roux. Three dimensional experimental and numerical multiscale analysis of a fatigue crack. *Computer Methods in Applied Mechanics and Engineering*, 199(21-22):1307–1325, April 2010.

[46] F. Sket, A. Enfedaque, C. Alton, C. González, J. M. Molina-Aldareguia, and J. Llorca. Automatic quantification of matrix cracking and fiber rotation by x-ray computed tomography in shear-deformed carbon fiber-reinforced laminates. *Composites Science and Technology*, 90:129–138, 2014.

[47] A. J. Moffat, P. Wright, J.-Y. Buffiere, I. Sinclair, and S. M. Spearing. Micromechanisms of damage in 0° splits in a [90/0]s composite material using synchrotron radiation computed tomography. *Scripta Materialia*, 59(10):1043–1046, 2008.

[48] C. Kottler, V. Revol, R. Kaufmann, and C. Urban. Dual energy phase contrast x-ray imaging with talbot-lau interferometer. *Journal of Applied Physics*, 108(11):–, 2010.

[49] D. Paganin, S. C. Mayo, T. E. Gureyev, P. R. Miller, and S. W. Wilkins. Simultaneous phase and amplitude extraction from a single defocused image of a homogeneous object. *Journal of microscopy*, 206(1):33–40, 2002.

[50] F. Hild, A. Fanget, J. Adrien, E. Maire, and S. Roux. Three-dimensional analysis of a tensile test on a propellant with digital volume correlation. *Archives of Mechanics*, 63(5-6):459–478, 2011.

[51] E. Farmand-Ashtiani, J. Cugnoni, and J. Botsis. Specimen thickness dependence of large scale fiber bridging in mode i interlaminar fracture of carbon epoxy composite, 2014.

[52] E. Farmand-Ashtiani, J. Cugnoni, and J. Botsis. Semi-experimental investigation of bridging tractions in delamination. In *2013 Annual Conference on Experimental and Applied Mechanics*, volume 6, pages 197–204, Lombard, IL, 2014.

[53] L. P. Canal, J. Segurado, and J. LLorca. Failure surface of epoxy-modified fiber-reinforced composites under transverse tension and out-of-plane shear. *International Journal of Solids and Structures*, 46(11-12):2265–2274, 2009.

[54] H.-Y. Jeong. A new yield function and a hydrostatic stress-controlled void nucleation model for porous solids with pressure-sensitive matrices. *International Journal of Solids and Structures*, 39(5):1385–1403, 2002.

[55] T. J. Vaughan and C. T. McCarthy. Micromechanical modelling of the transverse damage behaviour in fibre reinforced composites. *Composites Science and Technology*, 71(3):388–396, 2011.

[56] T. J. Vaughan and C. T. McCarthy. A micromechanical study on the effect of intra-ply properties on transverse shear fracture in fibre reinforced composites. *Composites Part A: Applied Science and Manufacturing*, 42(9):1217–1228, 2011.

[57] A. R. Melro, P. P. Camanho, F. M. Andrade Pires, and S. T. Pinho. Micromechanical analysis of polymer composites reinforced by unidirectional fibres: Part i-constitutive modelling. *International Journal of Solids and Structures*, 50(11-12):1897–1905, 2013.

[58] A. R. Melro, P. P. Camanho, F. M. Andrade Pires, and S. T. Pinho. Micromechanical analysis of polymer composites reinforced by unidirectional fibres: Part ii-micromechanical analyses. *International Journal of Solids and Structures*, 50(11-12):1906–1915, 2013.

[59] F. Naya, C. González, C. S. Lopes, S. Van der Veen, and F. Pons. Computational micromechanics of the transverse and shear behavior of unidirectional fiber reinforced polymers including environmental effects. *Composites Part A: Applied Science and Manufacturing*, 92:146–157, 2017.

[60] J. Segurado and J. Llorca. A numerical approximation to the elastic properties of sphere-reinforced composites. *Journal of the Mechanics and Physics of Solids*, 50(10):2107–2121, 2002.

[61] Dassault Systemes. *Abaqus 6.12 Online Documentation.* 2012.

[62] D. C. Drucker and W. Prager. Soil mechanics and plastic analysis or limit design. 10(2):157–165, 1952.

[63] C. G. Davila, P. P. Camanho, and C. A. Rose. Failure criteria for frp laminates. *Journal of Composite Materials*, 39(4):323–345, 2005.

[64] F. Naya, M. Herráez, C. S. Lopes, C. González, S. Van der Veen, and F. Pons. Computational micromechanics of fiber kinking in unidirectional frp under different environmental conditions. *Composites Science and Technology*, 144:26–35, 2017.

[65] G. Soni, S. Gupta, R. Singh, M. Mitra, W. Yan, and B. G. Falzon. Study of localized damage in composite laminates using micro-macro approach. *Composite Structures*, 113(1):1–11, 2014.

[66] G. Soni, R. Singh, M. Mitra, and B. G. Falzon. Modelling matrix damage and fibre-matrix interfacial decohesion in composite laminates via a multi-fibre multi-layer representative volume element (m2rve). *International Journal of Solids and Structures*, 51(2):449–461, 2014.

[67] M. Herráez, D. Mora, F. Naya, C. S. Lopes, C. González, and J. LLorca. Transverse cracking of cross-ply laminates: A computational micromechanics perspective. *Composites Science and Technology*, 110:196–204, 2015.

[68] F. Naya, J. M. Molina-Aldareguia, C. S. Lopes, C. González, and J. LLorca. Interface characterization in fiber-reinforced polymer-matrix composites. *JOM*, 69(1):13–21, 2017.

[69] A. Arteiro, G. Catalanotti, A. R. Melro, P. Linde, and P. P. Camanho. Micro-mechanical analysis of the in situ effect in polymer composite laminates. *Composite Structures*, 116(1):827–840, 2014.

[70] A. Arteiro, G. Catalanotti, J. Reinoso, P. Linde, and P. P. Camanho. Simulation of the mechanical response of thin-ply composites: From computational micro-mechanics to structural analysis. *Archives of Computational Methods in Engineering*, pages –, 2018.

[71] L. Zubillaga, A. Turon, P. Maimi, J. Costa, S. Mahdi, and P. Linde. An energy based failure criterion for matrix crack induced delamination in laminated composite structures. *Composite Structures*, 112:339–344, 2014.

[72] L. Zubillaga, A. Turon, J. Renart, J. Costa, and P. Linde. An experimental study on matrix crack induced delamination in composite laminates. *Composite Structures*, 127:10–17, 2015.

[73] G. Guillamet, A. Turon, J. Costa, and P. Linde. A quick procedure to predict free-edge delamination in thin-ply laminates under tension. *Engineering Fracture Mechanics*, 168:28–39, 2016.

[74] B. Fiedler, M. Hojo, S. Ochiai, K. Schulte, and M. Ando. Failure behavior of an epoxy matrix under different kinds of static loading. *Composites Science and Technology*, 61(11):1615–1624, 2001.

[75] T. Hobbiebrunken, B. Fiedler, M. Hojo, and M. Tanaka. Experimental determination of the true epoxy resin strength using micro-scaled specimens. *Composites Part A: Applied Science and Manufacturing*, 38(3):814–818, 2007.

[76] J. Misumi, R. Ganesh, S. Sockalingam, and J. W. Gillespie. Experimental characterization of tensile properties of epoxy resin by using micro-fiber specimens. *Journal of Reinforced Plastics and Composites*, 35(24):1792–1801, September 2016.

[77] M. Romanowicz. Determination of the first ply failure load for a cross ply laminate subjected to uniaxial tension through computational micromechanics. *International Journal of Solids and Structures*, 51(13):2549–2556, 2014.

[78] J. Chevalier, X. P. Morelle, P. P. Camanho, F. Lani, and T. Pardoen. On a unique fracture micromechanism for highly cross-linked epoxy resins. *Journal of the Mechanics and Physics of Solids*, 122:502–519, 2019.

[79] J. Chevalier, X. P. Morelle, C. Bailly, P. P. Camanho, T. Pardoen, and F. Lani. Micromechanics based pressure dependent failure model for highly cross-linked epoxy resins. *Engineering Fracture Mechanics*, 158(Supplement C):1–12, 2016.

[80] M. Rodríguez, J. M. Molina-Aldareguía, C. González, and J. LLorca. Determination of the mechanical properties of amorphous materials through instrumented nanoindentation. *Acta Materialia*, 60(9):3953–3964, May 2012.

[81] M. Rodriguez, J. M. Molina-Aldareguia, C. González, and J. LLorca. A methodology to measure the interface shear strength by means of the fiber push-in test. *Composites Science and Technology*, 72(15):1924–1932, 2012.

[82] S. Ogihara and J. Koyanagi. Investigation of combined stress state failure criterion for glass fiber/epoxy interface by the cruciform specimen method. *Composites Science and Technology*, 70(1):143–150, 2010.

[83] R. Younes, A. Hallal, F. Fardoun, and F. H. Chehade. *Composites and Their Properties*, chapter Comparative Review Study on Elastic Properties Modeling for Unidirectional Composite Materials,. 2012.

[84] R. Maurin, P. Davies, N. Baral, and C. Baley. Transverse properties of carbon fibres by nano-indentation and micro-mechanics. *Applied Composite Materials*, 15(2):61–, 2008.

[85] K. Fujita, Y. Sawada, and Y. Nakanishi. Effect of cross-sectional textures on transverse compressive properties of pitch-based carbon fibers. *J-Stage*, 50(6Appendix):116–121, 2001.

[86] H. Miyagawa, T. Mase, C. Sato, E. Drown, L. T. Drzal, and K. Ikegami. Comparison of experimental and theoretical transverse elastic modulus of carbon fibers. *Carbon*, 44(10):2002–2008, 2006.

[87] J. Reinoso, G. Catalanotti, A. Blázquez, P. Areias, P. P. Camanho, and F. Paris. A consistent anisotropic damage model for laminated fiber-reinforced composites using the 3d-version of the puck failure criterion. *International Journal of Solids and Structures*, 126-127:37–53, 2017.

[88] M. Herráez, C. González, and C. S. Lopes. A numerical framework to analyze fracture in composite materials: From r-curves to homogenized softening laws. *International Journal of Solids and Structures*, 134:216–228, 2018.

[89] C. G. Davila, C. A. Rose, and P. P. Camanho. A procedure for superposing linear cohesive laws to represent multiple damage mechanisms in the fracture of composites. *International Journal of Fracture*, 158(2):211–223, 2009.

[90] T. Okabe, S. Onodera, Y. Kumagai, and Y. Nagumo. Continuum damage mechanics modeling of composite laminates including transverse cracks. *International Journal of Damage Mechanics*, 27(6):877–895, June 2017.

[91] G. Frossard, J. Cugnoni, T. Gmür, and J. Botsis. An efficient method for fiber bridging traction identification based on the r-curve: Formulation and experimental validation. *Composite Structures*, 175:135–144, 2017.

[92] M. Jing, T. Tan, C. Wang, Z. Feng, Y. Yang, and Y. Pan. Comparison on the micro-structure of toray t800h and t800s carbon fiber. *Cailiao Kexue yu Gongyi/Material Science and Technology*, 23:45–52, 2015.

[93] Iso 527-2:1993: Plastics – determination of tensile properties – part 2: Test conditions for moulding and extrusion plastics.

[94] N. W. Tschoegl. Failure surfaces in principal stress space. *Journal of Polymer Science Part C*, 32:239–267, 1971.

[95] T. S. Gross, H. Jafari, J. Kusch, I. Tsukrov, B. Drach, H. Bayraktar, and J. Goering. Measuring failure stress of rtm6 epoxy resin under purely hydrostatic tensile stress using constrained tube method. *Experimental Techniques*, 41(1):45–50, 2017.

[96] Standard test method for compressive properties of rigid plastics, 2015.

[97] W. C. Oliver and G. M. Pharr. An improved technique for determining hardness and elastic modulus using load and displacement sensing indentation experiments. 7(6):1564–1583–, 1992.

[98] Test method for tensile properties of polymer matrix composite materials, 2008.

[99] Tinytask. https://www.tinytask.net/index.php, 09 2018.

[100] P. J. Schilling, B. P. R. Karedla, A. K. Tatiparthi, M. A. Verges, and P. D. Herrington. X-ray computed microtomography of internal damage in fiber reinforced polymer matrix composites. *Composites Science and Technology*, 65(14):2071–2078, 2005.

[101] J. Schindelin, I. Arganda-Carreras, E. Frise, V. Kaynig, M. Longair, T. Pietzsch, S. Preibisch, C. Rueden, S. Saalfeld, B. Schmid, J.-Y. Tinevez, D. J. White, V. Hartenstein, K. Eliceiri, P. Tomancak, and A. Cardona. Fiji: an open-source platform for biological-image analysis. *Nature Methods*, 9:676–, June 2012.

[102] Inc. Toray Composite Materials America. M40j datasheet. https://www.toraycma.com/file_viewer.php?id=5086, April 2018.

[103] Inc. Toray Composite Materials America. T800h datasheet. https://www.toraycma.com/file_viewer.php?id=5121, April 2018.

[104] Inc. Toray Composite Materials America. T800s datasheet. https://www.toraycma.com/file_viewer.php?id=5126, April 2018.

[105] J. D. H. Hughes. The carbon fibre/epoxy interface - a review. *Composites Science and Technology*, 41(1):13–45, 1991.

[106] S. Swaddiwudhipong, J. Hua, K. K. Tho, and Z. S. Liu. Equivalency of berkovich and conical load-indentation curves. *Modelling and Simulation in Materials Science and Engineering*, 14:71, 2006.

[107] C.-H. Shen and G. Springer. Effects of moisture and temperature on the tensile strength of composite materials. *Journal of Composite Materials*, 11:2–16, 1977.

[108] K. F. Rogers, L. N. Phillips, D. M. Kingston-Lee, B. Yates, M. J. Overy, J. P. Sargent, and B. A. McCalla. The thermal expansion of carbon fibre-reinforced plastics. *Journal of Materials Science*, 12(4):718–734, 1977.

[109] C. Pradere and C. Sauder. *Transverse and Longitudinal Coefficient of Thermal Expansion of Carbon Fibers at High Temperatures*, volume 46. November 2008.

[110] Z. H. Karadeniz and D. Kumlutas. A numerical study on the coefficients of thermal expansion of fiber reinforced composite materials. *Composite Structures*, 78(1):1–10, 2007.

[111] D. E. Bowles and S. S. Tompkins. Prediction of coefficients of thermal expansion for unidirectional composites. *Journal of Composite Materials*, 23(4):370–388, April 1989.

[112] M. Herráez, C. González, C. S. Lopes, R. Guzman de Villoria, J. LLorca, T. Varela, and J. Sanchez. Computational micromechanics evaluation of the effect of fibre shape on the transverse strength of unidirectional composites: An approach to virtual materials design. *Composites Part A: Applied Science and Manufacturing*, 91:484–492, 2016.

[113] S. Kohler, J. Cugnoni, R. Amacher, and J. Botsis. Damage mechanisms in thin-ply composites : Free edge/bulk measurements and multiscale modelling. pages –. European Conference on Composite Materials, ECCM, 2016.

[114] M. R. Wisnom. Size effects in the testing of fibre-composite materials. *Composites Science and Technology*, 59(13):1937–1957, 1999.

[115] C. T. Sun and Z.-H. Jin. *Fracture mechanics.* Elsevier Ltd, 2012.

[116] B. F. Sørensen and T. K. Jacobsen. Determination of cohesive laws by the j integral approach. *Engineering Fracture Mechanics*, 70(14):1841 – 1858, 2003. Cohesive Models.

[117] K. Park, G. H. Paulino, and J. R. Roesler. A unified potential-based cohesive model of mixed-mode fracture. *Journal of the Mechanics and Physics of Solids*, 57:891–908, 2009.

Sébastien Kohler

Allée de la Luzerne 3
CH-1844 Villeneuve
☎ *+41 79 727 05 33*
✉ *sebastien.kohler@alumni.epfl.ch*
in *sebastienkohler*

EDUCATION

2014-2018	**PhD in Solid Mechanics**, *École Polytechnique Fédérale de Lausanne*.
2008-2014	**MSc in Mechanical Engineering**, *École Polytechnique Fédérale de Lausanne*.
2006-2008	**National Diploma in Motorsport Engineering**, *Wiltshire College*, England.
2003-2006	**Bilingual High school Diploma (FR-D)**, *Gymnase de Morges*, Switzerland.

PROFESSIONAL EXPERIENCE

2014-2018	**Doctoral assistant**, *EPFL*, Lausanne. Research in the area of composite damage mechanics at the meso and micro scales, including experimental and numerical (FE) characterization for thin-ply CFRP laminates. Teaching duties for the courses "Mechanical vibrations", "Finite element modelling and simulation" and for the mechanical vibration lab (modal analysis). 4 master semester projects supervised.
2013-2014	**Intern**, *Georg-Fischer*, Schaffhausen. 6 month master project in industry, studying specific vibrational issues in automotive drive trains (NDA).

LIST OF PUBLICATIONS

Kohler S, Amacher R, Cugnoni J, Botsis J, *Transverse cracking in the bulk and at the free edge of thin-ply composites: experiments and multiscale modelling*, Submitted manuscript to Composites: Part A, 25. Octobre, 2018

Kohler S, Cugnoni J, Botsis J, *Effect of ply thickness and constituents on the transverse crack propagation of thin-ply composites: Damage progression and modelling*, 18. European Conference on Composite Materials, Athens, 2018

Cugnoni J, Amacher R, Kohler S, Brunner J, Kramer E, Dransfeld C, Smith W, Scobbie K, Sorensen L, Botsis J, *Towards aerospace grade thin-ply composites: Effect of ply thickness, fibre, matrix and interlayer toughening on strength and damage tolerance*, Composite Science and Technology 2018; 168: 467-477

Kohler S, Cugnoni J, Amacher R, Botsis J, *Damage mechanisms in thin-ply composites: Free edge/bulk measurements and multiscale modelling*, 17. European Conference on Composite Materials, Munich, 2016

LIST OF CONFERENCE PARTICIPATIONS

Kohler S, Cugnoni J, Botsis J, *Crack propagation in thin-ply composites: Experimental observations and multiscale modelling*, 55. Annual Technical Meeting of the Society of Engineering Science, Madrid, 2018

Kohler S, Cugnoni J, Botsis J, *Effect of ply thickness and constituents on the transverse crack propagation of thin-ply composites: Damage progression and modelling*, 18. European Conference on Composite Materials, Athens, 2018

Kohler S, Cugnoni J, Botsis J, *3D microcracking evolution in thin-ply composites under tensile loading: Experiments and Analysis*, 8. ComptTest, Leuven, 2018

Kohler S, Cugnoni J, Amacher R, Botsis J, *Damage mechanisms in thin-ply composites: Free edge/bulk measurements and multiscale modelling*, 17. European Conference on Composite Materials, Munich, 2016

SELECTED PROJECTS

2014-2018 **Multiscale characterisation and modelling of transverse cracking in thin-ply composites**
PhD Thesis presented at EPFL's mechanical engineering doctoral school program

2013 **Modelling of ply thickness effects in scarf joints**
Development of a parametric finite element model of a composite scarf joint including damage models of the interfaces and ply failure.

2012 **High speed drilling z-axis development**
Development of a technical solution for a Z-axis supporting ultra-high speed spindles to bore 75 micron holes at a speed higher or equal to 25Hz.

2012 **Finite element analysis of an eye implant**
Finite Element Analysis of the influence from the tack insertion angle used to pin an existing retinal implant during surgery on the distance between the electrodes and the retina once the optical prosthesis is installed.

PERSONAL INFORMATION

age	30 years old
nationality	Swiss citizen
languages	French C2 (mother tongue) English C2 German C1